The Pennsylvania State University

The Graduate School

Intercollege Graduate Program in Materials

REAL-TIME SPECTROSCOPIC ELLIPSOMETRY AND ITS APPLICATION TO THE PROCESSING OF $YBa_2Cu_3O_{7-\delta}$ FILMS BY MOLECULAR BEAM EPITAXY

A Thesis in
Materials

by
Brady J. Gibbons

Submitted in Partial Fulfillment
of the Requirements
for the Degree of

Doctor of Philosophy

August 1998

UMI Number: 9901035

UMI
300 North Zeeb Road
Ann Arbor, MI 48103

We approve the thesis of Brady J. Gibbons.

Date of Signature

Susan Trolier McKinstry
July 15, 1998

Susan Trolier-McKinstry
Associate Professor of Ceramic Science and Engineering
Thesis Adviser
Chair of Committee

Darrell G. Schlom
July 15, 1998

Darrell G. Schlom
Associate Professor of Materials Science and Engineering

Robert W Collins
July 15 1998

Robert W. Collins
Professor of Physics and Materials Research

July 16, 1998

Xiaoxing Xi
Assistant Professor of Physics

Robert N. Pangborn
July, 16, 1998

Robert Pangborn
Professor of Engineering Mechanics
Head of Intercollege Program in Materials

ABSTRACT

The major issues which currently limit the use of $YBa_2Cu_3O_{7-\delta}$ (YBCO) in commercial devices based on Josephson junction technology are related to the properties of the interfaces between YBCO and other materials. Specifically, oxygen deficiency at the interface severely degrades the properties of a junction. Thus, what is desired is a tool which can characterize this on a very small depth scale. In this thesis, both *ex situ* and real-time spectroscopic ellipsometry (SE and RTSE) have been explored for use as tools to garner such information.

Initially, the sensitivity of SE to the oxygen content in the near surface region of a YBCO film was studied. This was done using SE modeling code that included the ability to model a concentration gradient of oxygen at the film surface. It was found that for atomically smooth *c*-axis oriented YBCO films, SE is sensitive to the oxygen concentration within one unit cell, even when the profile is graded. The sensitivity to small changes in the surface concentration of oxygen was also determined. The minimum detectable change was found to be between 0.016 and 0.023 (in δ), depending on the starting value. For *a*-axis films, SE is sensitive to the oxygen content to within 10 Å. The minimum detectable change in the surface concentration was between 0.023 and 0.078. Finally, the same calculations were made for YBCO films with a 4 nm layer of $SrRuO_3$ (a metallic oxide) on the surface to simulate an S-N junction. For both film orientations, the sensitivities did not change significantly.

In order for SE to be useful as a characterization method for YBCO films, optical property information must be available for the substrates that are commonly used. Thus, SE was used to determine the reference dielectric function data for five common YBCO substrate materials; $LaAlO_3$, $NdGaO_3$, $(LaAlO_3)_{0.3}$-$(Sr_2AlTaO_6)_{0.7}$, $LaSrGaO_4$ and 9.5 mol% Y_2O_3-ZrO_2. Also, data for one known reaction layer material, $BaZrO_3$, was determined.

Subsequently, a real-time spectroscopic ellipsometer was constructed for a molecular beam epitaxy (MBE) deposition system for observation of the processing of YBCO and one of its constituent oxides. This was the first time that RTSE has been utilized as a tool to monitor the deposition of oxides by MBE. The RTSE was used to calibrate the substrate temperature by using critical point analysis of the Si dielectric function. The instrument was then used to monitor the deposition of Y_2O_3 on Si. The thickness derived from the RTSE measurement showed excellent agreement with the thickness determined by *in situ* flux measurements (i.e., atomic absorption and quartz crystal monitor), as well as with Rutherford backscattering spectroscopy. From comparison of the cation incorporation vs. the arrival rate, a sticking coefficient of $= 1.00 \pm 0.07$ was obtained for Y under the deposition conditions utilized.

Finally, SE was used to study the diffusion of oxygen in YBCO. Initial experiments using single wavelength *ex situ* SE showed dramatic changes in the ellipsometric parameters as a YBCO film was heated in flowing Ar up to 530 °C. These changes were associated with reduction of the film. To minimize the impact of the reactions between YBCO and ambient air, similar experiments were conducted using the RTSE and the MBE chamber. First, the optimal wavelength ranges were determined for

observation of oxidation and reduction kinetics in YBCO films. It was found that wavelengths between 550 and 650 nm provided the best combination of oxygen sensitivity and minimal temperature dependence at an angle of incidence of 80°. Next, the activation energy (E_a) for the diffusion of oxygen in YBCO was found by heating an initially oxygen deficient film at 1, 3, 5, 10 and 15 °C/minute in a 10% O_3/90% O_2 atmosphere and observing the temperature at which oxidation was completed. E_a was between 0.43 and 0.52 eV, which compares very well with values for other activated oxygen species. Last, the reactivity of ozone as compared to molecular oxygen was found by comparing SE spectra at various ozone pressures. At 500 °C, ozone is at least 2000 times as reactive as O_2.

TABLE OF CONTENTS

LIST OF TABLES

LIST OF FIGURES

ACKNOWLEDGMENTS

In my six years at Penn State University. I have had the pleasure of meeting and working with some of the brightest people I am sure I will ever meet. Of those people. there are two in particular that have affected me most profoundly. First. I would like to acknowledge my advisor, Dr. Susan Trolier-McKinstry. Throughout my Master's and my Ph.D. research. she has been a constant source of guidance, support and knowledge which I will always appreciate. Second. I would like to acknowledge Dr. Darrell Schlom. His undying enthusiasm and his willingness to show rather than tell meant a great deal to me. The opportunities that these two people afforded me can never be repaid. I would also like to thank Dr. Robert Collins and Dr. Xiaoxing Xi for serving on my committee.

Over these past six years, the most important person in my life has been my soon-to-be wife. Heather Hawkins. The support and love that she has offered me throughout this entire effort has been extraordinary. I can only hope to do the same for her when it is her turn.

I must also extend my sincerest thanks to others at the MRL; Jon-Paul Maria. Dave Cann and Joe Shepard. in particular. It has been my pleasure to work with these people, through which we have become close friends. The support and technical staff at MRL also deserve my thanks, specifically I would like to thank Herb McKinstry. Away from Penn State, I must thank Marilyn Hawley at Los Alamos National Laboratory and Chang-Beom Eom at Duke University.

Finally, I must remember the people who taught me what it meant to succeed in life. It isn't what you have, it's how you live. Thank you Mom, Dad, and Sarah.

Chapter 1

INTRODUCTION

1.1 Introduction to the Problem

Josephson-effect devices utilizing high transition temperature (T_c) superconductors such as $YBa_2Cu_3O_{7-\delta}$ (YBCO), have demonstrated tremendous potential for improving devices such as superconducting quantum interference devices (SQUIDs) and ultra-fast digital electronics. For example, a promising architecture for ultra-fast analog-to-digital (A/D) converters and other digital electronics is rapid single-flux quantum (RSFQ) logic.[1] RSFQ circuits using low-T_c junction technology have achieved speeds of 100 GHz with a power dissipation of less than 0.1 μW per junction.[2] SQUIDs are based on the macroscopic long-range interference effect that occurs when a dc magnetic field is applied through a circuit containing two Josephson junctions. Low-T_c based SQUIDs are the most sensitive detectors of magnetic flux currently available. They can be used to measure magnetic field, magnetic field gradient, current, voltage, displacement and magnetic susceptibility.[3] The development of a reliable high-T_c Josephson junction technology would make high-speed RSFQ digital circuitry, as well as SQUID technology, possible at easily accessible liquid nitrogen temperatures, eliminating the requirement for liquid helium cooling. Despite this promise, there are significant materials and processing challenges involved in the fabrication of reliable high-T_c Josephson junctions.

After a decade of intensive research on high-T_c Josephson-effect devices, YBCO has emerged as one of the primary superconducting materials because of the extensive database of material properties that exists and because a relatively mature processing technology has been developed for it, compared to other high-T_c superconductors.[4] Because of the short superconducting coherence length intrinsic to YBCO (as well as the other high-T_c materials), superconductor-normal metal-superconductor (SNS) junctions based on the proximity effect are preferred over tunnel junctions for high-T_c Josephson-effect devices. However, due to this short coherence length, even the fabrication of SNS proximity effect junctions is extremely challenging. In particular, high performance devices require preparation of junctions with pinhole-free interlayers ≤ 4 nm in thickness.[4] This, in turn, requires the fabrication of atomically smooth films in which the superconductor is fully oxidized immediately up to the interface. Currently, the processing conditions with which this can be achieved are unknown. In addition, the detection of oxygen non-stoichiometry at the interface on a length scale comparable to the coherence length is beyond the reach of most existing techniques.

In a recent review of YBCO based SNS junction technology by Delin and Kleinsasser,[4] they concluded that the majority of reported SNS junctions displayed no evidence of true proximity effect behavior. They found that much of the data reported in the literature is dominated by pinholes through the interlayer or interfacial layer effects between the superconductor and normal metal. At the interface, oxygen deficiency on a scale of the coherence length results in a "dead" layer of non-superconducting material, or material with depressed superconducting properties. Thus, the thickness of the N layer is increased and the properties of the junction are significantly degraded (since the junction critical current decays exponentially as the thickness of the N layer increases). Therefore, at this point, the key roadblocks to the implementation of this technology are: 1) excessive interfacial roughness between the YBCO and the normal metal, and 2) oxygen non-stoichiometry at the interface.

What is desired is a tool which can characterize these effects in YBCO-based junctions on a very small depth scale in a controlled environment. This thesis is based on the use of spectroscopic ellipsometry (SE) for this purpose. SE is a light reflection technique which is capable of depth profiling samples with a resolution generally in the angstrom range (dependent on the dielectric functions of the materials being studied). In addition, it is non-destructive and non-invasive. Thus, it is an ideal tool to observe the processing of YBCO films in real-time.

SE has been used to characterize the dielectric function of YBCO by several researchers.[5,6] It was found that the dielectric spectra are both anisotropic and strongly dependent on the oxygen stoichiometry. Thus, if there is oxygen-deficient material at the surface of a YBCO film, it will be manifested in the SE data. Prior to this thesis, the sensitivity limits with which SE can detect oxygen deficiency were unknown. Thus, the use of SE to address the current roadblocks to the implementation of high-T_c junction technology needed to be investigated. To do so, molecular beam epitaxy (MBE) was employed to deposit YBCO films (and one of its constituent oxides) and real-time SE was used to observe the processing of these films in terms of oxygen content and diffusion in controlled environments. Through this, a powerful tool allowing an improved understanding of the processing conditions required to form YBCO films for junction devices was obtained.

1.2 Thesis Objectives

The objectives of this thesis were four-fold:

1) To construct a real-time spectroscopic ellipsometer (RTSE) and adapt it to the existing oxide molecular beam epitaxy (MBE) system. MBE was used to deposit films due to the extreme flexibility of growth conditions that was available using this technique. In addition, cooperative *in situ* deposition monitors such as atomic absorption flux monitoring (AA) and reflection high-energy electron diffraction (RHEED) augmented the RTSE for characterization of film growth. This combination enabled a determination of the cation incorporation rate as a function of the arrival rate during oxide film deposition.
2) To determine the applicability of RTSE as a characterization tool during MBE deposition of oxide thin films. RTSE has never been applied to the deposition of oxide thin films by MBE, thus it was important to determine how it could be used, its limitations, as well as how it complemented the other *in situ* monitoring techniques.
3) To determine the sensitivity with which SE could depth profile the oxygen content in YBCO-based junction devices. As described above, due to the dependence of the YBCO dielectric function on the oxygen content, SE can be used to quantify the extent of oxygen deficiency at the surface/interface of a YBCO thin film. However, in calculating the sensitivity to oxygen deficiency, it is important to consider the case where the oxygen content is graded.[7] This has never been previously reported.

4) To observe the oxidation behavior of YBCO thin films during processing and cooldown in the MBE chamber at various temperatures and pressures of oxygen and/or ozone. The ability to do these experiments in a controlled environment eliminated artifacts associated with surface layers due to corrosion of the film by the ambient atmosphere. In addition, it was desired to quantify the relative reactivity of ozone with respect to molecular oxygen. This information should assist in determining the optimum processing/cooldown procedures in order to obtain high quality YBCO thin films.

Chapter 2

BACKGROUND

2.1 $YBa_2Cu_3O_{7-\delta}$ (YBCO)

In 1986, Georg Bednorz and Alex Müller discovered superconductivity at 30 K in the La-Ba-Cu-O system.[8,9] The superconducting phase was found to be $La_{2-x}Ba_xCuO_4$. Subsequently, other researchers began to explore the effects of elemental substitutions on the structure and properties of this phase. As a result of that research, in 1987 Wu *et al.*[10] discovered superconductivity at 90 K in the Y-Ba-Cu-O system. Soon after, the superconducting phase was determined to be $YBa_2Cu_3O_7$ ($YBCO_7$).[*]

Fig. 2.1 shows the unit cell of $YBCO_7$. It is related to a cubic perovskite with the *c*-axis tripled in length. In the basic perovskite structure (i.e., ABO_3) the *A* site lies at the center of 8 corner-sharing octahedra with anions at the vertices. The *B* site lies at the center of those octahedra. For YBCO, the larger Y and Ba atoms are in the *A* sites and the smaller Cu ions are at the *B* sites. Ordering of the Y and Ba ions on the *A* sites accounts for the tripling of the unit cell length in the *c*-direction. That is, the top and bottom sub-cells have a Ba ion at the center, while the middle cell holds a Y ion.

For an ideal tripled perovskite unit cell, the structure should have 9 oxygen ions. Thus, $YBCO_7$ is an oxygen-deficient modification of the perovskite structure. The unit cell is orthorhombic with dimensions of a = 0.382 nm, b = 0.388 nm and c = 1.168 nm.[11] The source of the orthorhombic distortion was revealed through Rietveld refinements on

---

[*] The actual formula is $YBa_2Cu_3O_{7-\delta}$ where $0 \leq \delta \leq 1$. In this work, when referring to a specific oxygen content, the number will be given as a subscript following YBCO (i.e., $YBCO_7$).

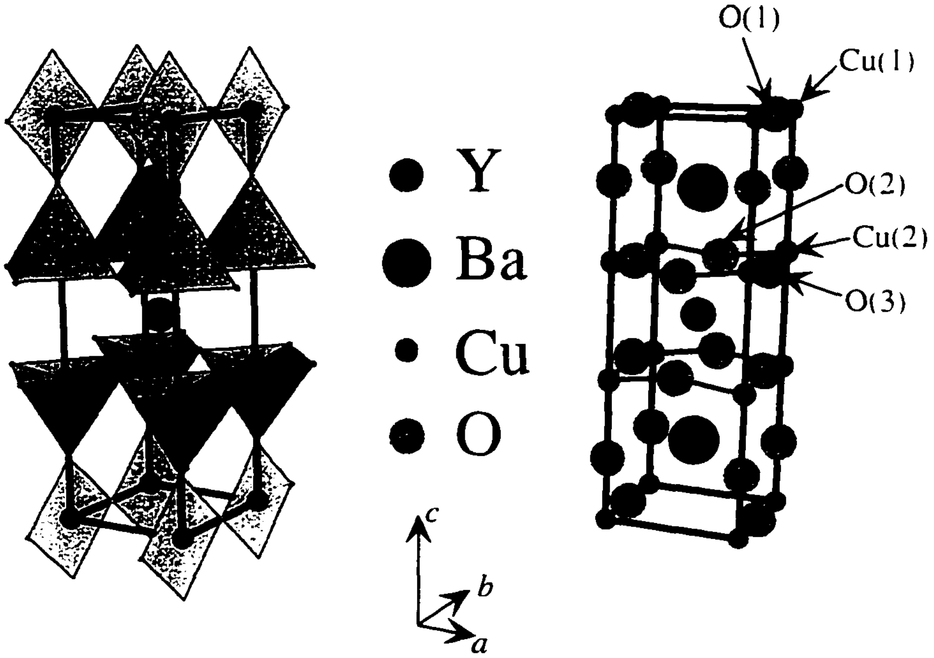

Figure 2.1 : The structure of YBCO shown in two forms: polyhedral and ball & stick models.

neutron diffraction experiments, as well as TEM measurements.[12-14] It was shown that the oxygen ions in the basal copper plane of the unit cell (O(1) in Fig. 2.1) were ordered in the orthorhombic structure and the material contained almost seven oxygen ions per unit cell. The ordering in the basal plane leads to occupation of one of the oxygen sites along a cell edge (O(1)), while the other site is left vacant. The cell edge with the occupied site is lengthened (the *b*-axis). The corner-linked square planar arrangements of Cu and O ions in the basal planes are known as "chains," whereas the Cu and O that form the base of the square pyramidal arrangement in the structure are linked together to form "planes." These sites are called the Cu(1) site and the Cu(2) site, respectively.

The superconducting state is an ordered state of the conduction electrons of the metal. The order is in the formation of loosely associated pairs of electrons below the superconducting transition temperature (T_c); they are disordered above T_c. Two important parameters that describe every superconductor (both low and high-T_c) are the

London penetration depth (λ_L) and the coherence length (ξ). The London penetration depth is a measure of how far a magnetic field can penetrate into the surface of a superconductor.[15] While to a first approximation superconductors are described as completely expelling magnetic flux for temperatures below T_c, in reality, the flux lines penetrate into the superconductor and decay exponentially.[16] The coherence length is a measure of the distance over which the superconducting electron pair concentration does not change drastically in a spatially varying magnetic field.[15] It can be thought of as the effective "size" of an electron pair.[16] In $YBCO_7$, due to the anisotropic nature of its crystal structure, the coherence length in the *a* and *b*-directions is much longer than in the *c*-direction ($\xi_{a,b}$ = 1-2 nm, ξ_c = 0.1-0.2 nm).[4] However both of these values are significantly smaller than their counterparts in low-T_c materials (i.e. ξ = 38 nm in Nb and ξ = 1600 nm in Al).[17]

2.1.1 Oxygen Content in YBCO

The chemical formula for YBCO is $YBa_2Cu_3O_{7-\delta}$, where $0 \leq \delta \leq 1$. The oxygen content in YBCO as described by the value of δ is a strong function of the processing conditions used.[18-20] $YBCO_7$ is only formed when the samples are cooled slowly in an oxygen-rich environment. Oxygen deficient structures can be obtained when the sample is quenched from a high temperature or cooled in a reducing environment. As oxygen is removed from the structure, an orthorhombic to tetragonal phase transformation occurs.[20-23] Oxygen is lost primarily from the O(1) site (see Fig. 2.1) in the Cu-O chains.[20] In YBCO$_6$, the O(1) site is completely empty. As YBCO is reduced, the unit cell parameters also change to $a = b = 0.3857$ nm and $c = 1.1819$ nm. The occurrence of this transformation is strongly dependent on the oxygen pressure as the material is being heated. Fig. 2.2 shows the lattice constants as a function of temperature for various oxygen partial pressures.[23] Neutron diffraction experiments showed that the oxygen arrangement changes from fully ordered at room temperature, to partially ordered at higher temperatures still in the orthorhombic phase and finally to completely disordered in the tetragonal phase.[20]

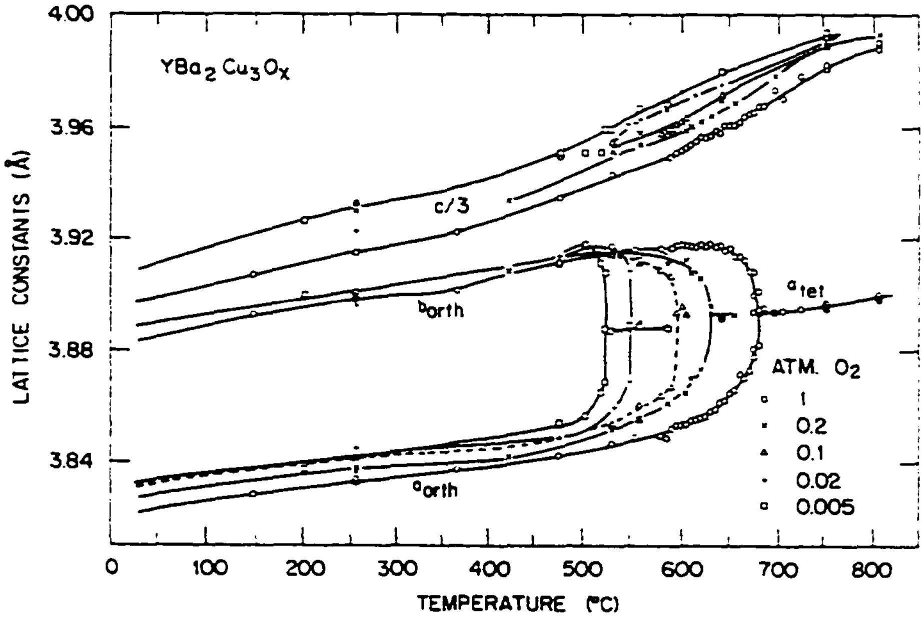

Figure 2.2 : Lattice constants a, b and $c/3$ under various O_2 atmospheres. The orthorhombic-tetragonal transformation temperature decreases with decreasing O_2 pressure. Lines are guides to the eye. From Specht *et al.*[23]

In addition to the structural changes that YBCO undergoes upon losing oxygen, the superconducting properties are largely controlled by the oxygen content and arrangement in the structure.[18,19,21,24,25] At the composition YBCO$_6$, the material is semiconducting, with antiferromagnetic order of the Cu spins. As the oxygen content increases above ≈ YBCO$_{6.4}$, the crystal becomes metallic (superconducting at low temperature) and non-magnetic. Fig. 2.3 shows the behavior of T_c as a function of oxygen content in the structure.[26]

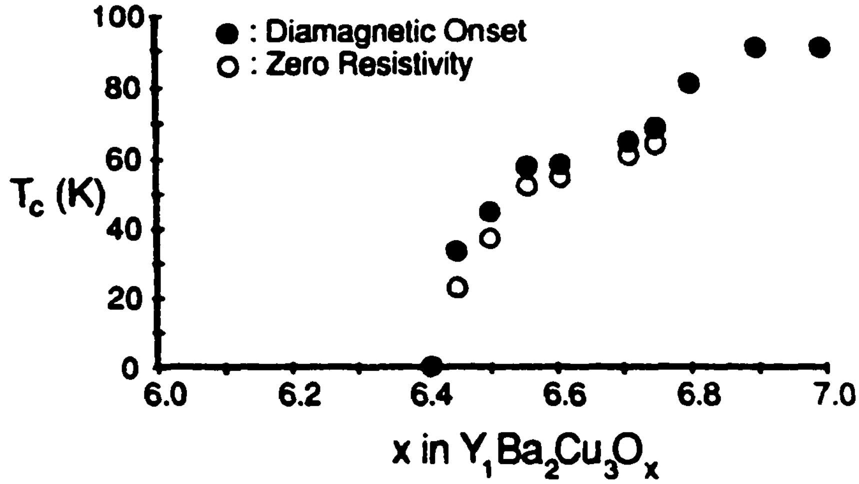

Figure 2.3 : Oxygen content dependence of the resistive superconducting transition temperature and the temperature of the onset of diamagnetism in YBCO for $6 \leq x \leq 7$. From Beyers *et al.*[26]

2.1.2 Thin Film YBCO

Both *c*-axis and *a*-axis oriented YBCO have been deposited in thin film form by several methods, including sputtering, evaporation, chemical routes, MBE, pulsed laser deposition (PLD) and others.[27,28] Substrates used for these depositions include $SrTiO_3$,[29-37] $LaAlO_3$,[30,35,36,38,39] $NdGaO_3$,[31] $LaSrGaO_4$,[40] $KTaO_3$,[41] MgO,[30,32,42,43] Al_2O_3 (with barrier layers),[29,44] $LiNbO_3$,[45] 9.5 mol% Y_2O_3-ZrO_2[46-49] and several others.[50] The choice of substrate is dictated by the necessity of chemical and structural compatibility with YBCO. Depending on the application, other factors such as dielectric constant, thermal expansion coefficient and high frequency dielectric loss must also be considered. From the above list, $SrTiO_3$ displayed the earliest success as a substrate for epitaxial growth of YBCO with high quality electrical properties.[50] The lattice mismatch to YBCO is 1.4% at room temperature and the thermal expansion coefficient is $11 \times 10^{-6}/°C$ (compared to $11 \times 10^{-6}/°C$ and $13 \times 10^{-6}/°C$ in the *a* and *b* directions of YBCO, respectively).[51] In addition, $SrTiO_3$ has the perovskite structure, providing for an ideal template layer to form epitaxial YBCO. All of the films studied in this work were deposited on $SrTiO_3$.

There are two different approaches to form epitaxial YBCO films.[24] The first involves depositing stoichiometric mixtures of the metallic elements at low temperatures to form amorphous films or finely dispersed particles, followed by annealing in an oxidizing atmosphere at 800 °C – 900 °C to form the desired phase. This is called the *ex situ* procedure. Films from this method often exhibit multiple crystallographic orientations and second phases within the film and on the surface.[24] The second method entails forming the YBCO phase directly on the substrate at temperatures of ≈ 700 °C, eliminating the need for a higher temperature annealing step. This is called the *in situ* method, and takes place under conditions which enable sufficient oxygen incorporation into the growing film. This is typically done under exposure to atomic oxygen or ozone. The advantages to the *in situ* method are lower processing temperatures, the ability to fabricate heterostructures with other materials and improved morphology. As will be discussed below, during *in situ* deposition of YBCO, the material grows oxygen deficient and must be cooled in an oxidizing atmosphere to obtain the superconducting phase, $YBCO_7$.

The oxygen pressure is a critical parameter when processing YBCO films, both *in situ* and *ex situ*. Hammond and Bormann[52] and Feenstra *et al.*[24] examined the effect of

The oxygen pressure is a critical parameter when processing YBCO films, both *in situ* and *ex situ*. Hammond and Bormann[52] and Feenstra *et al.*[24] examined the effect of oxygen pressure on the synthesis of YBCO thin films and based on a survey of available data, compiled an oxygen partial pressure versus temperature diagram showing liquid phase boundaries, stability criteria, the tetragonal to orthorhombic transition and lines of constant oxygen stoichiometry. This is shown in Fig. 2.4. From this diagram, it is clear that there is an intrinsic dependency of the oxygen stoichiometry on the growth conditions and care must be taken to ensure sufficient oxygen incorporation to obtain high quality YBCO films. Here it can be seen that at typical *in situ* deposition conditions, the material grows as $YBCO_{6-6.1}$ and is transformed to $YBCO_7$ on cooling in an oxidizing atmosphere.

2.1.3 YBCO Thin Film Surfaces

YBCO films that have been grown by these methods show very similar surface structures. Surface precipitates, surface degradation and other surface features will undoubtedly affect the usage of this material in Josephson junction applications. Given the high surface sensitivity of spectroscopic ellipsometry, these features can also complicate interpretation of SE data. Therefore, it is important to understand how these features develop and how they influence the resulting electrical and optical properties.

One of the most distinctive features of epitaxial *c*-axis oriented YBCO thin films is the presence of spiral features on the film surface. Examples of this are shown in Fig. 2.5.[53] These features were first reported in the work of Hawley *et al.*[54] and Gerber *et al.*[55] on magnetron-sputtered YBCO films deposited on $SrTiO_3$. These spirals have been

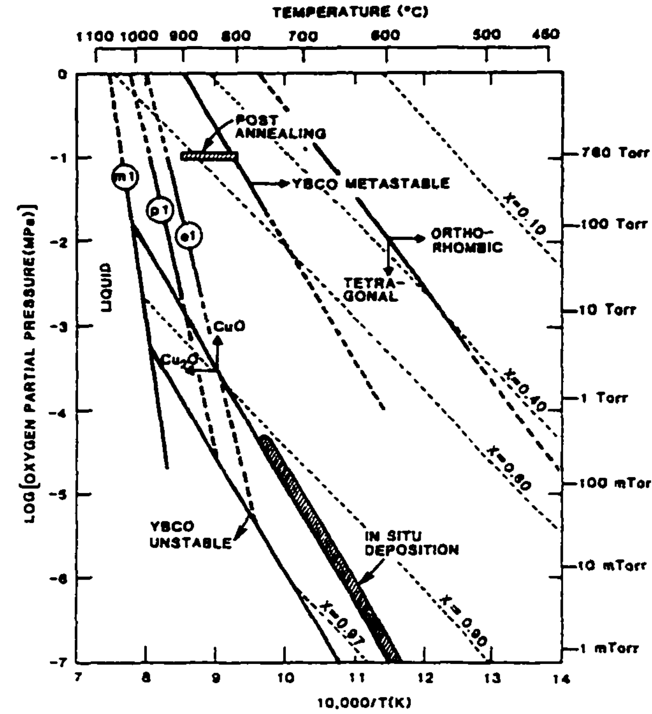

Figure 2.4 : Oxygen partial pressure vs. temperature diagram showing liquid-phase boundaries, stability criteria, tetragonal-orthorhombic transition line and lines of constant oxygen stoichiometry (x corresponds to δ). The CuO-Cu_2O-O_2 equilibrium line is also shown. The lines marked e1, p1 and m1 correspond to equilibrium lines for the eutectic composition $BaCuO_2$+CuO+YBCO⇔liquid, the peritectic composition CuO+YBCO⇔Y_2BaCuO_5+liquid and the melting point, respectively. Experimental and extrapolated ranges are indicated by solid and dashed lines, respectively. Processing conditions for *in situ* and *ex situ* film deposition are also shown. From Feenstra *et al.*[24]

observed on pulsed laser deposited and MBE deposited films, as well.[56-58] The individual step height between terraces was found to be between 1 and 2 nm, corresponding to the *c*-axis length of YBCO. The number of these features has been shown to decrease with increasing deposition temperature and substrate miscut,[53] as well as decreasing thickness.[55] It is accepted that these features originate at the intersection of screw dislocations with the growth surface. Schlom *et al.*[53] reviewed the possible causes of these dislocations and determined that only the meeting of incoherent growth fronts during deposition could account for the high densities of dislocations observed. In this case, the advancing growth front is forced to split at obstacles on the surface. The growth

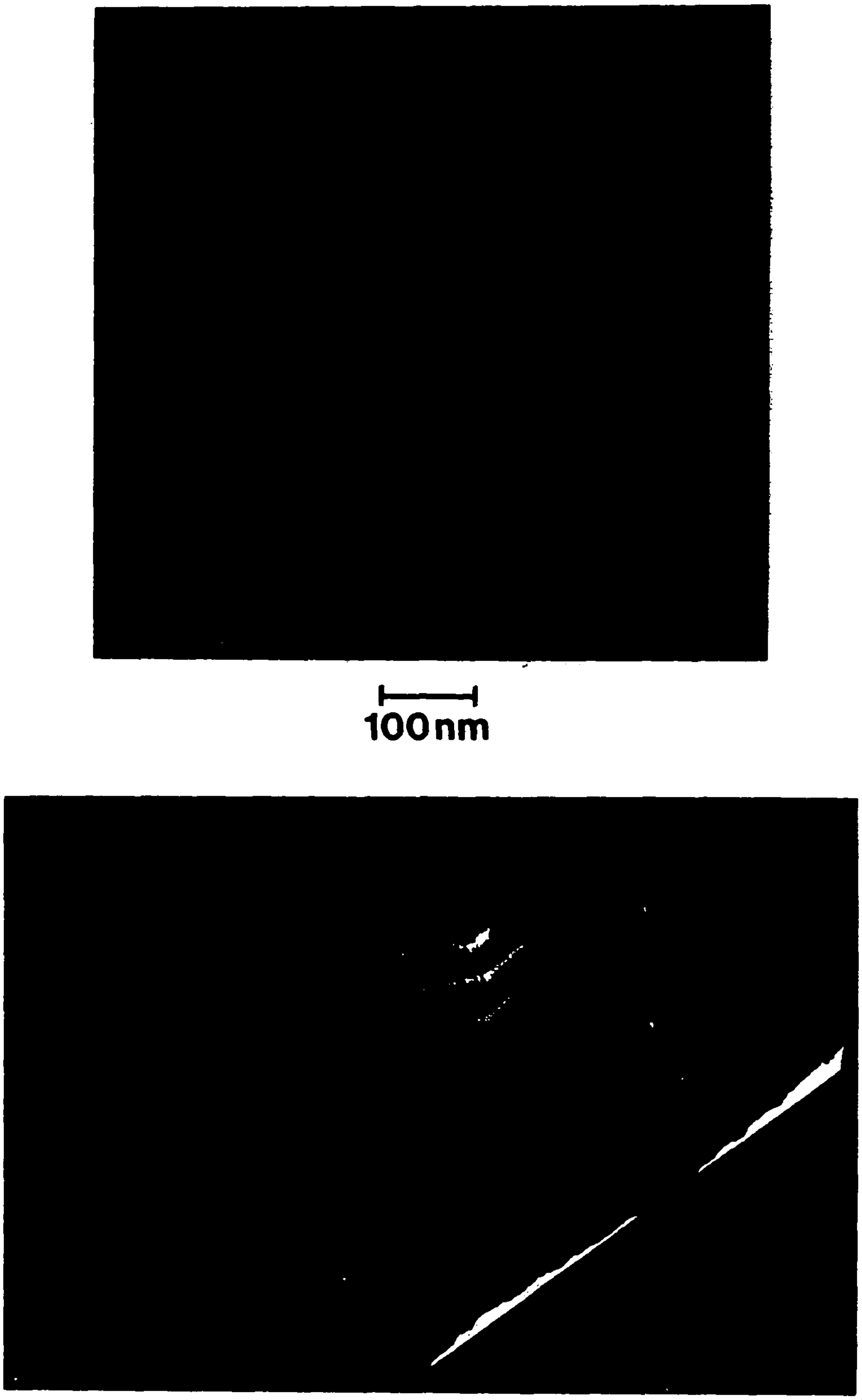

Figure 2.5 : STM images of a sputter deposited YBCO film on $SrTiO_3$. From Schlom *et al.*[53]

front eventually covers the obstacle, thus bending the layer, and further growth leads to the coalescence of two vertically misaligned growth fronts. This results in the formation of a screw dislocation. This conclusion was also reached by Stäuble-Pümpin *et al.*.[58] In later work, Catana *et al.*[59] proposed that the source of these obstacles was Y_2O_3 precipitates, which form epitaxially within YBCO. Alternatively, Aindow and Yeadon[60] suggest that these spiral features arise from dislocation half-loops which are nucleated in response to residual misfit at the interface.

In any case, as will be discussed below, a number of device applications demand smoother surface morphologies and less defective microstructures than can presently be achieved. The roughness of the smoothest YBCO film over a 1 μm × 1 μm region relevant for a device is about 5 nm for *c*-axis oriented films.[61] This is far rougher than what is necessary for devices such as Josephson junctions. One advantage of these spirals that has been discovered is that the critical current density (J_c) increases as the number density of the spirals increases.[62] It is proposed that the features act as flux pinning centers and thus raise the J_c. J_c values for epitaxial *c*-axis oriented films have reached as high as 8×10^6 A/cm^2 at 77 K.[55,63]

Analysis of the surface morphology on the scale described above has provided essential information for understanding YBCO film growth mechanisms. However, these films are also abundant in larger scale second phase surface precipitates, due to the small solid solubility region on the phase diagram. The ease with which these second phases can form is clear from analysis of the Y-Ba-Cu-O pseudoternary phase diagram. Fig. 2.6 shows the subsolidus phase diagram at 800 °C and ambient oxygen pressure.[64] As the

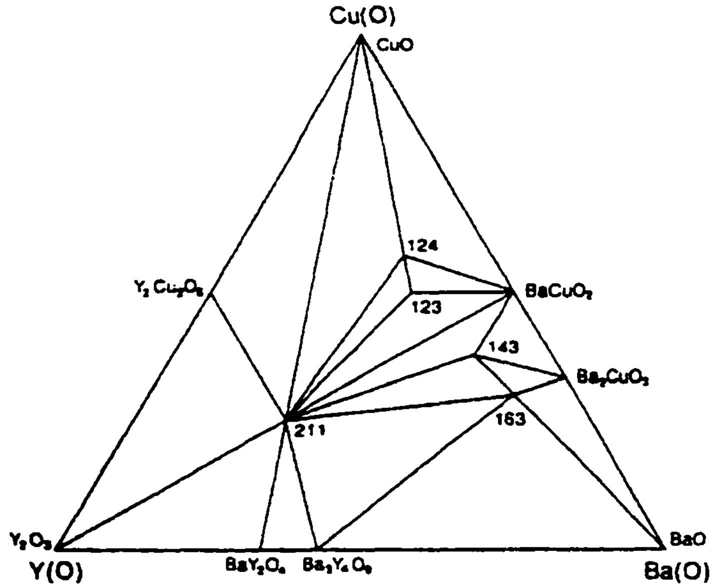

Figure 2.6 : The subsolidus ternary $YO_{1.5}$-BaO-CuO phase diagram at 800 °C in oxygen at ambient pressure. The numbers 123, 143, 163, 211 and 124 represent the compounds $YBa_2Cu_3O_{7-\delta}$, $YBa_4Cu_3O_{8.5+\delta}$, $YBa_6Cu_3O_{10+\delta}$, Y_2BaCuO_5 and $YBa_2Cu_4O_8$, respectively. From Karen *et al.*[64]

oxygen pressure is lowered at a fixed temperature, the phases and tie-lines in contact with YBCO change considerably. This is shown in Fig. 2.7, where at 850 °C, the $YBa_2Cu_3O_{7-\delta}$ phase is no longer stable below 0.3 Torr.[65] Previous studies have shown that precipitate formation is very sensitive to the deposition conditions and stoichiometry, as evidenced by Fig. 2.7.[66,67] Some of the precipitate compositions reported include: CuO and Cu_2O,[68-70] Y_2O_3,[59,68,71] $BaCu_2O_2$,[68] $YCuO_2$,[71,72] $Y_2Cu_2O_5$,[68] and $BaCuO_2$[70] among others. From the viewpoint of electronic devices, the existence of these precipitates can severely hinder the development of heterostructures such as superlattices and Josephson junctions. Fig. 2.8 shows an optical micrograph of an MBE-deposited 700 Å thick YBCO film with a number of surface precipitates. Comparison to previous research indicates that these outgrowths are Cu rich.[69,70] Note that the surface between the

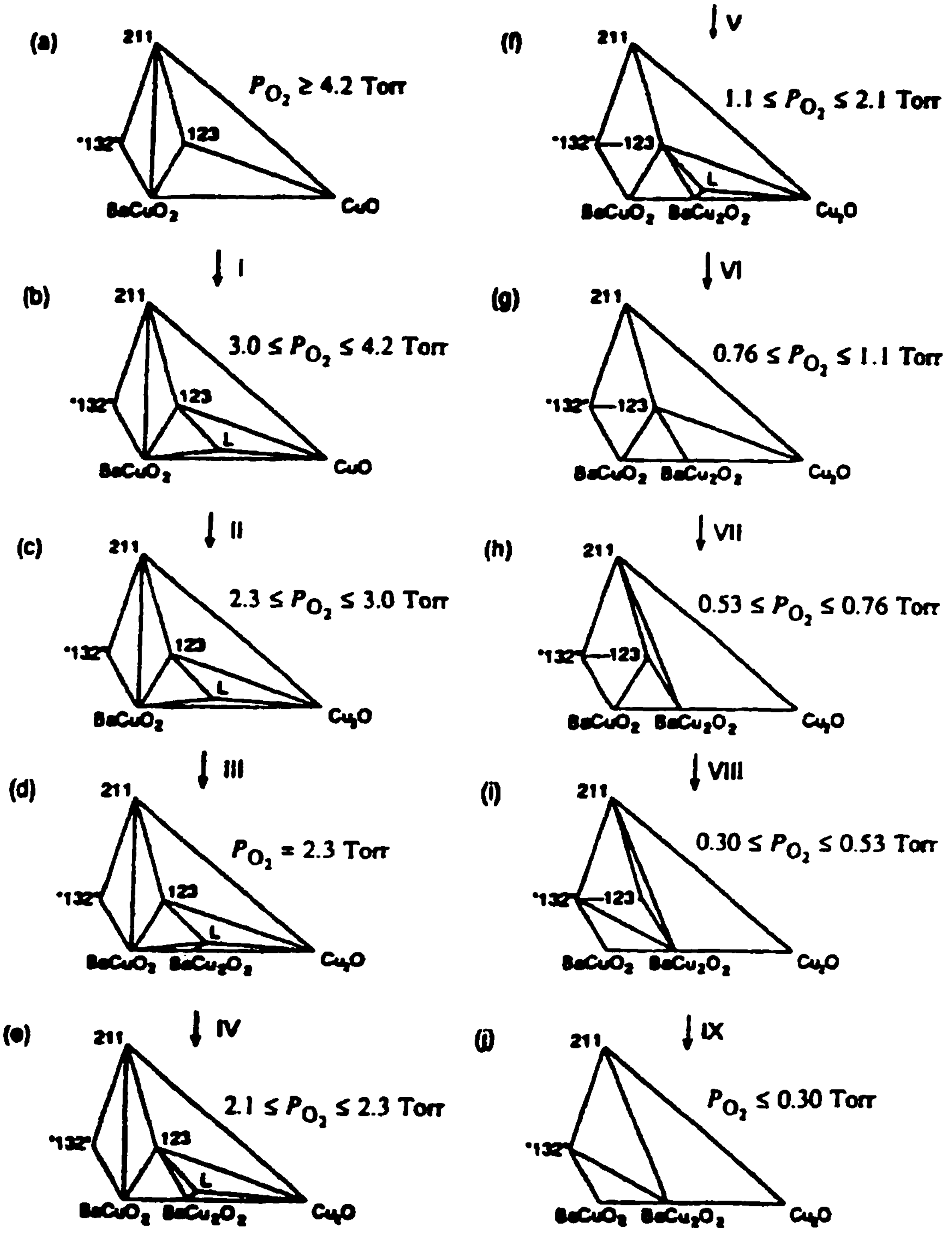

Figure 2.7 : The effect of oxygen pressure on the ternary Y-Ba-Cu-O phase diagram at 850 °C. (a) – (j) correspond to decreasing oxygen pressures. From Ahn *et al.*[65]

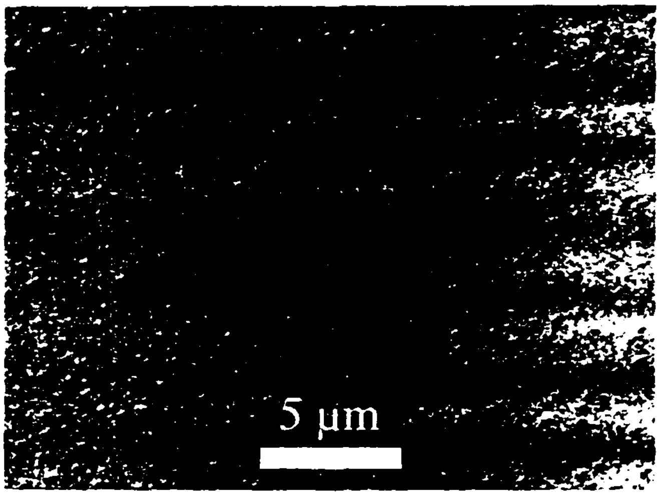

Figure 2.8 : Optical micrograph of an MBE deposited YBCO film on $SrTiO_3$.

precipitates is rather smooth, as has been seen by others.[61] It is also important to note that these precipitates are seen on films deposited by several methods.

In addition to the presence of surface structures and surface precipitates, YBCO film surfaces are inherently unstable and prone to corrosion. That is, a number of previous studies have shown that YBCO reacts with ambient air.[73-76] Specifically, reaction between YBCO and H_2O and CO_2 has been demonstrated. This reaction proceeds to form an overlayer of $BaCO_3$ mixed with $Ba(OH)_2$. Yan *et al.*[73] proposed the following mechanism for this formation, assuming some of the Cu^{3+} ions in the structure are reduced to Cu^{2+}:

$$3H_2O + 2YBa_2Cu_3O_7 \rightarrow Y_2BaCuO_5 + 3Ba(OH)_2 + 5CuO + 0.5O_2 \qquad (2.1)$$

$$Ba(OH)_2 + CO_2 \rightarrow BaCO_3 + H_2O \qquad (2.2)$$

Behner *et al.*[76] observed the development of this overlayer on *c*-axis oriented sputtered YBCO thin films after varying amounts of exposure to ambient atmosphere. Upon deposition, low energy electron diffraction (LEED) measurements showed a uniform termination on the top surface of the film, consisting of a BaO/CuO/BaO layer. After exposure to air, using x-ray photoelectron spectroscopy (XPS), they determined the time dependence of the thickness of the reaction zone. Assuming the diffusion of the reactants through the overlayer is the rate controlling step of the overlayer growth, the Tammann relationship can be used:[76]

$$d = k\sqrt{t} \tag{2.3}$$

where d is the thickness of the overlayer, k is the rate of formation and t is the time. From this, they extracted a rate constant of $k = 0.1$ nm/hr$^{0.5}$. This means that normal film corrosion due to exposure to ambient atmosphere proceeds very slowly. This was verified by measuring the critical temperature (T_c) and critical current (J_c) over time periods of up to 9 months and seeing no significant changes. They also proposed that patterning of the film could result in additional degradation along the *a/b* plane, which could have different corrosion kinetics. Alterovitz *et al.*[75] showed very similar results, however they proposed that the growth rate depends on the stoichiometry of the material on the top surface layer. Thus, the overlayer could grow much faster on films with a large amount of second-phase precipitates. McDevitt *et al.*[77] showed that this corrosion could be significantly reduced by modifying the surface of a YBCO film with linear alkylamines and fluorinated alkylamines reagents.

2.1.4 Josephson Junction Technology

Thin film YBCO has been proposed for many different electronic applications including SQUIDs, RSFQ-based ultra-fast digital electronics, microwave antennae arrays. microstrip resonators and others. A key component of some of these devices is a Josephson junction. The Josephson effect can be thought of as a small overlap of quantum-mechanical wavefunctions between two weakly coupled superconductors.[17,78,79] The coupling of the superconducting layers is obtained by separating them by some small distance. which is typically on the order of the superconducting coherence length (ξ). There are three primary results of this weak coupling: 1) The dc Josephson effect. where a lossless supercurrent flows across the junction in the absence of any electric or magnetic field. 2) The ac Josephson effect. where a dc voltage applied across the junction causes rf current oscillations across the junction and 3) Macroscopic long-range quantum interference. where a dc magnetic field applied through a superconducting circuit containing two junctions causes the maximum supercurrent to show interference effects as a function of magnetic field intensity.[15]

There are two basic types of Josephson junctions: a Superconductor-Insulator-Superconductor (SIS) junction and a Superconductor-Normal metal-Superconductor (SNS) junction. Other types do exist. including those with insulating barriers at the interfaces in an SNS junction (SINIS) and those with a semiconducting interlayer (SSmS). The principles of overlapping wavefunctions are different for the two basic types of junctions. In SIS junctions. the process is by tunneling of the superconducting electron pairs through the insulating interlayer. For SNS junctions. the coupling is produced by means of the "proximity effect." Much of the current research in high-T Josephson junction technology is focused on SNS type junctions,[4] since the short coherence lengths in high-T_c materials ($\xi_{a,b} \approx$ 1-2 nm. ξ_c = 0.1-0.2 nm) makes the fabrication of tunnel junctions extremely challenging. In SNS junctions, longer interlayer distances may be used due to the proximity coupling of superconductivity into the normal metal barrier. Thus, this discussion will focus on SNS type junctions.

The physical basis for the proximity effect is the leakage of Cooper pairs out of the superconductor and into the normal metal near an SN interface.[17] The electron pairs move through the N layer by metallic transport, in contrast to SIS junctions where the pairs are forbidden from the interlayer. A quantum-mechanical derivation of the results of overlapping electron pair wavefunctions shows that the current from one superconducting layer to the other is given by:[17]

$$I = I_c \sin \phi \qquad (2.4)$$

where I is the current across the junction, I_c is the maximum zero-voltage supercurrent that can be passed by the junction and ϕ is the phase difference between the electron pair wavefunctions in the two superconducting layers. Fig. 2.9 shows the current-voltage characteristic of a typical Josephson junction. With no applied voltage, a dc current will flow across the junction, with a value between I_c and $-I_c$, depending on the phase difference. The critical current of an SNS junction decays exponentially with increasing interlayer thickness, L, according to:[4]

$$I_c = I_{c0}\, e^{-L/L_0} \qquad (2.5)$$

where I_{c0} is an exponential prefactor and L_0 is the characteristic decay length. L_0 is typically on the order of the coherence length in the normal metal interlayer. The normal metal coherence length varies by material. For noble metals at 77 K, it is typically 15 – 30 nm, and for oxide normal metals, it is an order of magnitude smaller.[4]

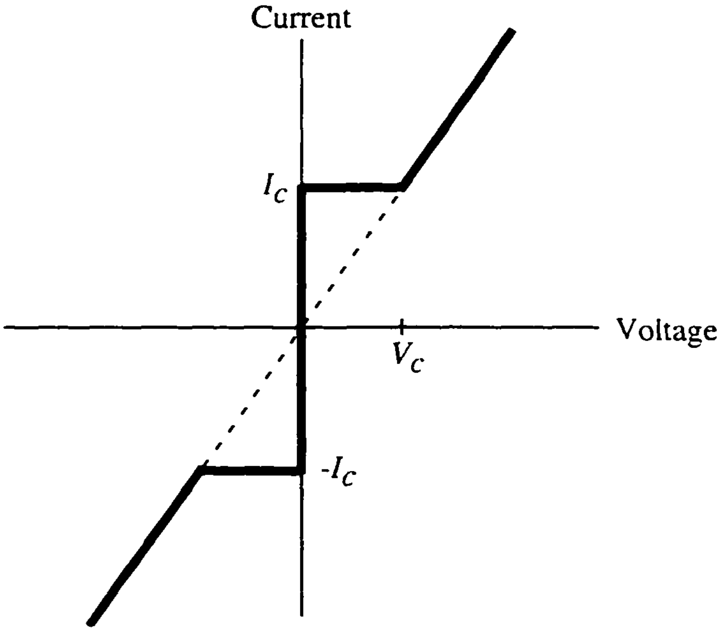

Figure 2.9 : Ideal current-voltage response of a Josephson junction.

The most important figure of merit for many applications involving Josephson junctions is the product of the critical current of the junction, I_c, and the normal state resistance of the junction, R_N.[17,80] Higher I_cR_N products make the circuits more immune to noise, which is important when operating at higher temperatures, due to the increased thermal noise floor. According to the theory of superconductivity developed by Bardeen, Cooper and Schrieffer,[81] this product can be calculated as:[17]

$$I_cR_N \approx {}^{2.8kT_c}\!/_{e} \qquad \text{at } T = 0 \tag{2.6}$$

where k is Boltzmann's constant, T_c is the superconducting transition temperature and e is the charge on an electron. Thus, the I_cR_N product should be much higher for high-T_c junctions than for low-T_c junctions. For YBCO-based SNS junctions, these values are calculated to be ≈ 17 mV from equation 2.6. The highest I_cR_N product reported as of 1996 in a high-T_c junction is 16 mV at 15 K and 1.5 mV at 77 K.[82] Much of the junction research has reported values in the 100 – 300 μV range at 77 K.[83-88] In addition to the importance of this figure of merit, the spatial uniformity of the I_cR_N product must also be good for these devices to be commercially viable (i.e., for superconducting circuits containing many junctions to have a reasonable yield).

There are two main geometries of Josephson junctions. They are the sandwich type and the edge, or ramp, type. Schematics of both are given in Fig. 2.10. For sandwich junctions, the YBCO layers can be either *a* or *c*-axis oriented. The advantage of *a*-axis oriented layers is the longer coherence length in the *a*/*b* direction. For edge type junctions, the transport across the interlayer occurs in the *a*/*b* plane (when the YBCO is *c*-axis oriented). Much of the published literature for YBCO-based devices is for edge junctions, since this geometry couples a relatively easily-grown YBCO orientation with a longer coherence length in the transport direction.[4] However, the fabrication process is complex and requires lithographic processing involving ion milling to establish the ramp, followed by epitaxial regrowth of the overlying barrier layer and YBCO. The ion milling step can result in a damaged interface; thus the resulting low I_cR_N products and inhomogenous interfaces are not surprising.[4] The sandwich type configuration is more easily fabricated, however the requirements for smooth, perfect interfaces as-deposited are more stringent than in ramp style junctions. As discussed below, it is believed that the surface and interface issues discussed above currently limit the quality of sandwich junctions.

Considerable effort has been devoted to the development of SNS junctions in both edge and sandwich configurations. A wide variety of normal metal materials have been utilized in these studies. Some of these include noble metals, such as Au,[80] Ag[80,89] and

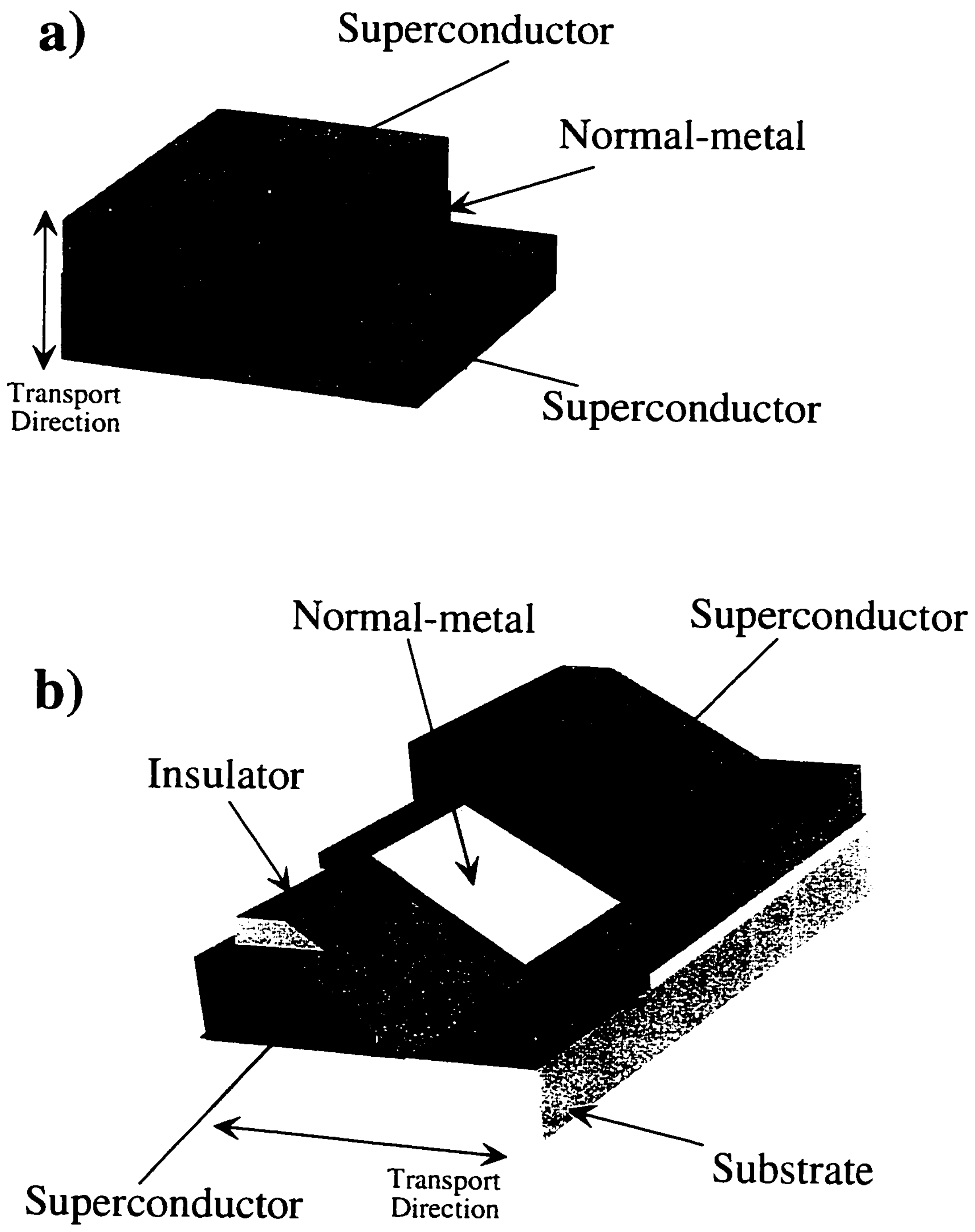

Figure 2.10 : Schematics of the two most common geometries of Josephson junctions, a) sandwich type and b) edge type.

Ag-Au alloys.[80,83] More recently, metallic oxide materials have been explored. Some of these include $CaRuO_3$,[86,90-92] $SrRuO_3$,[93] $La_{0.5}Sr_{0.5}CoO_3$,[86,93] Ca-doped YBCO,[86,87,94] Co-doped YBCO,[86-88,94] $La_{1.4}Sr_{0.6}CuO_4$,[86,94] Pr-doped YBCO,[95-97] and $PrBa_2Cu_3O_7$.[98-101] The junctions utilizing doped YBCO interlayers are known as SN'S junctions, denoting a superconductor above its transition temperature as the normal layer.

Despite these efforts, major materials-related issues remain to be overcome. Chief among these are interface issues. In a recent review of YBCO-based Josephson junctions, it was concluded that the majority of reported SNS junctions displayed no evidence of the proximity effect across the normal metal interlayer.[4] The authors showed that the behavior of most SNS junctions reported in the literature is dominated by pinholes through the N layer, as well as possible interfacial layer effects. Thus, based on these observations, the two major roadblocks to reliable high-T_c Josephson junction technology are: 1) Interface roughness for both *c* and *a*-axis oriented YBCO films. Smooth YBCO interfaces on either side of a thin (≤ 4 nm), uniform, pinhole-free interlayer are needed. 2) Oxygen non-stoichiometry in the vicinity of the normal metal interlayer. As described above, oxygen-deficient YBCO has very poor superconducting properties (if it is superconducting at all). Thus, any oxygen-deficiency near the interface results in a "dead layer" which increases the effective thickness of the interlayer and consequently decreases the junction critical current.[86,94] This thesis is directed towards developing a tool which will allow these effects to be discriminated.

2.2 Spectroscopic Ellipsometry (SE)

A complete discussion of spectroscopic ellipsometry (SE) is given in section 3.2. Here, a general overview of the technique will be given and its application to the study of high-T_c superconductors will be discussed.

SE is a light reflection technique which is capable of depth profiling samples with a resolution that depends somewhat on the material being studied, but is typically in the angstrom range. SE is non-destructive, non-invasive and requires no sample preparation. Basically, the measurement involves determining the change in polarization state of a light beam of known wavelength and polarization state upon reflection from the sample surface. This change is related to the depth profile of the dielectric function of the sample.[102] Computer modeling can then be utilized to obtain a best-fit description of the sample detailing the optical properties as a function of depth.[103-110] Excellent agreement between SE and other techniques such as cross-sectional transmission electron microscopy (TEM),[104] atomic force microscopy (AFM),[111,112] secondary ion mass spectroscopy (SIMS)[113] and Rutherford backscattering (RBS)[114] has been demonstrated. Originally, SE was used to study static materials with the goal of characterizing the depth profile and optical properties. With the advent of high-speed computers, and innovations in detector technology and usage, SE has been extended to the study of dynamic processes occurring during thin film deposition.

The technique of real-time spectroscopic ellipsometry (RTSE) has matured significantly since its development 10 years ago.[112,115-121] The ability to collect full spectroscopic spectra with an acquisition time of as little as 16 ms resulted in < 1 Å thickness resolution for growth rates up to 60 Å/s. With these capabilities, RTSE has been applied to characterization of the nucleation, coalescence and growth of amorphous, microcrystalline and polycrystalline thin films. In addition, the evolution of the optical properties of these materials as a function of thickness at different growth stages has been completed. Some materials that have been studied using RTSE include Al thin films,[122-125] crystal-Si,[126-128] amorphous-Si,[129-133] diamond films,[121,134] GaAs and related structures (such as $Al_xGa_{1-x}As$ and $In_yAl_xGa_{1-y-x}As$)[135-139] and CaF_2.[140]

2.2.1 SE Studies on YBCO

The application of SE to characterization of YBCO has been widely investigated.[5-7,109,141-159] Due to the significant optical anisotropy of YBCO, using SE is not straightforward; thus many of the first studies reported the pseudo-dielectric function for sintered polycrystalline samples. However, some of the initial studies were completed on single crystal samples or epitaxial thin films, thus the contributions from the *a*/*b* and *c*-axes dielectric functions could be separated (although the authors only reported data for the 001 surface).[141,142,145] Kircher *et al.*[6] were the first to report the dielectric function for the *c*, as well as the *a*/*b* axes (they assumed the *a* and *b*-axes to be optically equivalent). Later, Kotz *et al.*[150] used numerical analysis in combination with SE to extract ε_a and ε_b for two samples of varying, unspecified, oxygen content.

The most interesting feature noted in these early studies was the significant dependence of the YBCO dielectric function on oxygen content.[6,7,141,143,145] Fig. 2.11 shows the results from Kircher *et al.*[6] displaying this sensitivity, as well as the anisotropy

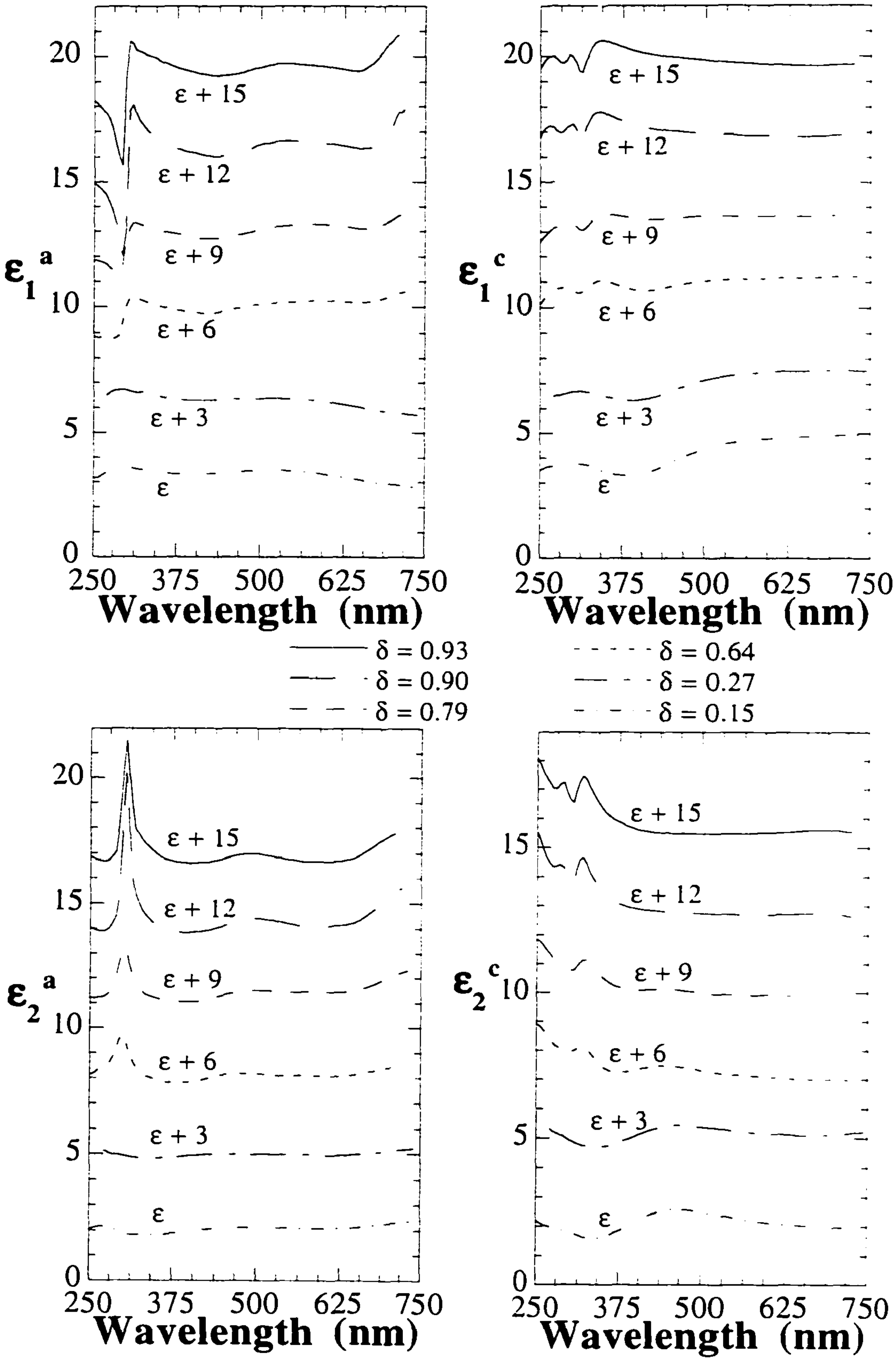

Figure 2.11 : YBCO dielectric function data from Kircher *et al.*[6] Note the anisotropy and the significant dependence on oxygen content (data are offset for clarity).

of the dielectric function. In that work, YBCO single crystals grown by the K_2CO_3 flux method[160] were examined using SE on both the (001) and (010)/(100) surfaces. The as-grown crystals were annealed in an oxygen atmosphere at 980 K for 13 hours and slowly cooled in order to obtain homogeneous $YBCO_7$ samples. Then, some of the samples were re-annealed in vacuum and quenched to obtain oxygen deficient samples. The weight loss of the sample was monitored during this process so the oxygen stoichiometry (δ) could be determined. Subsequently, ellipsometric measurements were taken and, using the two-phase model (see section 3.2), the dielectric function was calculated.

In the optical spectra in Fig. 2.11, the most obvious feature as a function of oxygen content is at $\approx$ 302 nm (4.1 eV) for both the *a*/*b*- and *c*-axes. There is also a feature in the spectra for the *a*/*b*-axes at $\approx$ 750 nm (1.65 eV) (only the shoulder is visible in these data). In order to gain some insight into the physical origins of these features, Kelly *et al.*[141] examined the optical properties of samples with different cation substitutions and oxygen concentrations. Substitution of Y by Er or Gd did not affect the spectra. Garriga *et al.*[143,145] substituted Y with Nd, Eu, Dy, Ho and Tm and again saw little change in the spectra. As δ approaches 1, nearly all of the oxygen is removed from the Cu(1) chains,[20] so the Cu(1) ions are bonded only to the two neighboring oxygen ions in the Ba planes. This results in an isolation of the O-Cu(1)-O clusters (or dumbbells as some researchers have named them). Kelly *et al.*[141] proposed that this localized electronic structure causes the appearance of the structure in the dielectric spectra at 302 nm (4.1 eV) as a function of oxygen content. Garriga *et al.*,[145] however, suggested that in addition to the O-Cu(1)-O transitions, the Ba-O transitions contributed to the

302 nm (4.1 eV) peak. This was due to the fact that BaO has similar transitions at 302 nm and 288 nm (4.1 and 4.3 eV). In later work, Kelly *et al.*[5] compared the optical spectra of several materials containing Cu-O structures, such as $YCuO_2$, Cu_2O and $La_2SrCu_2O_6$. There, they confirmed that the 302 nm (4.1 eV) absorption is related to the dumbbell structure described above. Kircher *et al.*[146] subsequently specified the structure to be due to $3d^{10} \rightarrow 3d^{9}4p$ transitions in the Cu ion of the O-Cu(1)-O dumbbell and to a minor extent from Cu-Ba charge transfer transitions.

The 750 nm (1.65 eV) feature has also been extensively investigated. Through Co doping on the Cu site (primarily Cu(1)), Kelly *et al.*[141] showed that this feature was strictly associated with the absence of metallic character. Later, Kelly *et al.*[5] ascribed this feature to the Cu-O perovskite planes, and showed that the existence of free carriers in these planes frustrates this bound excitation, thus the relationship with the metal-semiconductor transition. Garriga *et al.*[145] showed similar results. Finally, the broad structure at ≈ 445 nm (2.8 eV) has been observed in all of the copper oxide compounds (including the Bi based superconductors).[5,145] It is generally accepted that this structure is related to the copper-oxygen planes present in all of those materials.

The anisotropic nature of the YBCO dielectric functions has been exploited for characterization of the orientation of YBCO films by SE.[148,149,158] Sengupta *et al.*[148] deposited YBCO films on (100) and (110) oriented $SrTiO_3$ in order to deduce the effects of film thickness on the orientation. They observed that for films on (100) $SrTiO_3$, the film dielectric response became less metallic as the thickness increased. Thus, since the dielectric response of the *a*/*b*-directions is more metallic than that of the *c*-direction (as evidenced by the longer coherence length in the *a/b* plane). they attributed this change to a change in the orientation of the film. Habermeier *et al.*[149] used SE in combination with Raman scattering to characterize the orientation of (110) YBCO films deposited on (110) $SrTiO_3$. They measured the samples with either of two edges parallel to the plane of incidence. That is. in one direction pure ε_c could be measured and by turning the sample 90°. they measured a dielectric function that resembled a mix of ε_a and ε_b. The *c*-direction was determined to be that direction in which the broad peak at ≈ 2.8 eV was not present.

Due to the dependence of the YBCO dielectric function on oxygen content. Kelly *et al.*[7] proposed using SE to characterize the oxygen content of YBCO surfaces and YBCO interfaces with other materials. Their studies were done on ceramic samples alone (in air and in vacuum). and with thin layers of Al. In. Ag. Au. water and ethanol on the surface. With 40 Å and 65 Å thick Al layers deposited on the YBCO surface. ellipsometric spectra showed the existence of a peak at 4.1 eV. This suggested the Al had caused the interfacial region of the YBCO to become oxygen deficient. They attempted to model the ellipsometric spectra. without accounting for the optical anisotropy and the surface roughness, and obtained an approximate fit with a 15 – 20 Å thick layer of $YBCO_{6.33}$ on top of $YBCO_{6.85}$. Similar results were observed for a 25 Å thick In overlayer. Interestingly, in later work Kircher *et al.*[6] suggested an approximate resolution of SE of determining the oxygen content in YBCO of 0.15 in δ. In Kelly's work, he stated: "A more quantitative characterization of the interface can be sought by modeling the dielectric response. This is actually quite complicated because of the possible gradient of oxygen composition..." Thus, their results for the overlayer thickness and composition may be in error, but nonetheless they are indicative of what is happening at a very small scale near the interface.

The distinctive optical properties of YBCO (and many of the other CuO$_2$-based superconductors) make them ideal materials to be studied by many optical methods, in addition to ellipsometry. Reflectance measurements,[159,161-165] reflectance difference spectroscopy[159] and Raman spectroscopy[159,166-168] are some of the other measurements that have been completed.

2.3 Oxygen Diffusion in YBCO

As described above, both the normal state conductivity and superconductivity of YBCO depends strongly on the oxygen content.[18-20] Thus, control and monitoring of the oxygen content is an important issue for processing of these materials. The process of oxidation, subsequent to deposition, as well as the process of reduction must be understood in order to fabricate high quality YBCO films. There have been several studies on diffusion in bulk polycrystalline and single crystal samples,[169-189] as well as some on diffusion in oriented and epitaxial thin films.[152,167,187,190-196] These studies have attempted to determine the diffusion coefficients (both chemical and tracer) as a function of temperature and oxygen content or oxygen pressure and lattice direction, the activation energy for diffusion as a function of oxygen content and the modes of diffusion. Various methods have been used to observe the oxygen diffusion, including *in situ* resistivity (conductivity) measurements, thermogravimetry, SIMS profiles of tracer diffusion, electrochemical measurements, internal friction measurements and single wavelength ellipsometry. As a preface to this discussion, it should be noted that these studies were performed on samples of widely varying microstructural features, including porosity, grain size, twin density, orientation, sample surface area, impurity content and initial oxygen stoichiometry and homogeneity of oxygen distribution. Thus, the values that are reported in the literature can, and do, vary significantly.

2.3.1 Bulk YBCO

Tu *et al.*[169,170,172,174,177] used *in situ* resistivity measurements on ceramic YBCO pellets to observe the in and out diffusion of oxygen. The samples used showed grain sizes of about 10 µm and contained a large number of interconnecting pores. The experiments were done both isothermally and at constant heating rates. These measurements probe the entire sample's oxygen content. Fig. 2.12 shows the recovery of the resistivity beginning to occur at temperatures as low as 260 °C as an initially oxygen-deficient sample ($YBCO_6$) is heated in O_2. Based on Arrhenius fitting of the temperatures

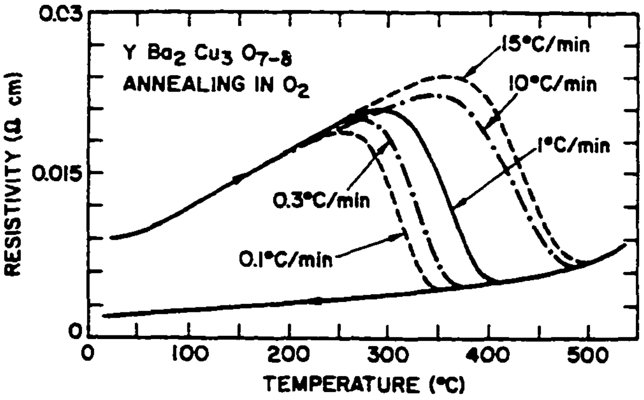

Figure 2.12 : A set of in-diffusion curves of oxygen-deficient samples (δ=0.4) upon annealing in ambient O_2 at various heating rates. From Tu *et al.*[177]

of the minimum or maximum in the resistivity as a function of heating rate, the authors extracted an activation energy for in-diffusion of 1.3 ± 0.1 eV. Based on this, they concluded that in the early state of in-diffusion, a near-surface layer saturated with oxygen forms and this layer limits further in-diffusion of oxygen with an activation energy of 1.3 eV. A schematic of this process is given in Fig. 2.13. This conclusion was also reached by Glowacki *et al.*[171] and later supported by Conder *et al.*[189] The authors then conducted an experiment to elucidate the effect of δ on the activation energy of oxygen in-diffusion. For this, they had to eliminate the formation of the oxygen-saturated surface layer. They found a significant dependence of E_a on δ: $E_a = 0.48$ eV for $\delta = 0.38$ and $E_a = 1.3$ eV for $\delta = 0$. That is, the activation energy is lower for oxygen diffusion when there is less oxygen in the structure.

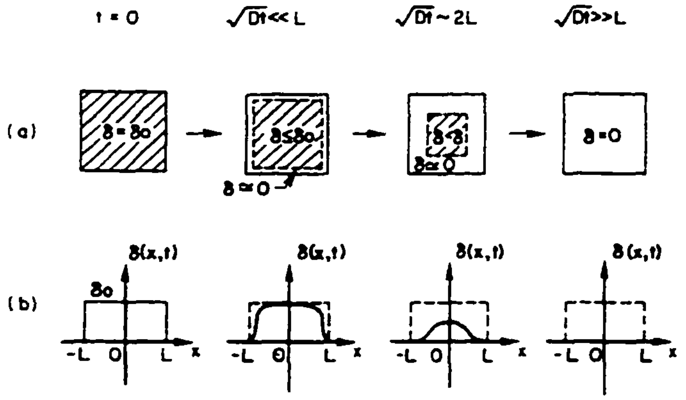

Figure 2.13 : (a) The time evolution of the oxygen distributions within a grain. Note that the outer portion of the grain reaches δ=0 much faster than the inner region. (b) The spatial variations of the oxygen content at constant temperature. From Yeh *et al.*[174]

Fig. 2.14 shows the results of sequential annealing in He and O_2 at 400 °C. From this, it can be seen that the in-diffusion behavior is faster than out-diffusion, which has also been noted by others.[190] In addition, the authors concluded that the rate of out-

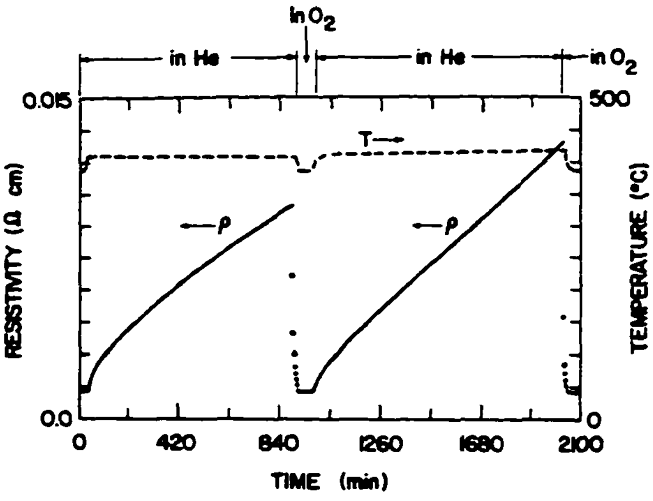

Figure 2.14 : A sequential anneal in He and O_2. The resistivity increases linearly and gradually in He but drops instantaneously in O_2. The dashed curve shows the temperature. From Tu *et al.*[177]

diffusion is independent of δ, and that this process is surface reaction limited (as opposed to diffusion limited). This resulted in samples with a homogeneous distribution of oxygen upon out-diffusion. They calculated activation energies of 1.7 – 1.75 eV for out-diffusion. Finally, assuming one-dimensional diffusion, they determined the diffusivity of oxygen into the oxide of $YBCO_7$ to be:

$$D = (0.035 \pm 0.005)\exp\left[\frac{-(1.3 \pm 0.1)\mathrm{eV}}{kT}\right]\mathrm{cm}^2/\mathrm{sec} \qquad (2.7)$$

In 1989, Rothman *et al.*[178] used SIMS to study the tracer diffusion of O^{18} in YBCO ceramics. The density of their samples was ≈99% of theoretical and the T_c was 90 K. They found that the diffusion of oxygen is strongly anisotropic, as is expected due to the anisotropic nature of the crystal structure. The faster component of the diffusion, associated with the *ab* plane, was found to have an activation energy of 0.97 ± 0.03 eV. The diffusion coefficients along the *c*-direction were approximately three orders of magnitude smaller than those in polycrystals. In addition, they found that D is not a strong function of oxygen pressure at 600 °C. These measurements only probe the near surface oxygen content due to the nature of the SIMS technique. In contrast, internal friction measurements completed by Tallon and Staines[181] showed that D decreased with oxygen pressure. In that work, an activation energy of 1.07 eV was obtained, correlating well with that of Rothman *et al.*

Tang and Lo[183] used thermogravimetry to measure the weight loss of powder samples on out-diffusion of oxygen. They found the process of out-diffusion to be diffusion limited, rather than surface reaction limited (in contrast to Tu *et al.*[177]). Also, an activation energy of oxygen diffusion of 1.4 eV for samples with $\delta \approx 0.1$ was determined. Since the weight loss of the entire sample was measured, the results are indicative of bulk diffusion.

Bredikhin *et al.*[185] studied the anisotropy of oxygen diffusion in YBCO single crystals. The experiments were conducted using O^{18} as a tracer and SIMS to characterize the depth profile. The diffusion coefficients at 400 °C and 800 °C were reported. According to their work, at 400 °C, $D_{a,b}$ is about 5 orders of magnitude larger than D_c and at 800 °C $D_{a,b}$ is about 2 orders of magnitude larger than D_c. The authors also determined the activation energies for diffusion and found that $E_c = 2.3$ eV and $E_{a,b} = 1.27$ eV. The value of $E_{a,b}$ corresponds well with the data of Tu *et al.*[177]

There are several other studies on oxygen diffusion in bulk ceramics, single crystals and powders. Table 2.1 is a summary of the above studies, as well as numerous others reporting similar data. The table lists the author, type of measurement, type of sample, temperature ranges of interest and other comments related to the work.

Table 2.1 : Summary of data from studies on diffusion of oxygen in bulk YBCO.

Group	Method	Sample type	Activation Energy	Diffusion coefficient (cm²/sec)
Tu *et al.*[177]	Resistivity	Ceramic	In-diffusion E_a=0.48 eV for δ=0.48 E_a=1.3 eV for δ=0 Out-diffusion E_a=1.7-1.75 eV	D(500 °C) = 1.2×10^{-10} D(400 °C) = 9×10^{-12}
Ikuma *et al.*[176]	Tracer diffusion Thermogravimetry	Powders	E_a=1.79 eV	D(400 °C) = 1×10^{-14}
Glowacki *et al.*[171]	Differential scanning calorimetry	Powders	In-diffusion E_a=1.47 eV	D(400 °C) = 3×10^{-11}
Brabers *et al.*[173]	Thermogravimetry	Powders	E_a=0.9 – 1.3 eV	----
Vischjager *et al.*[175]	Impedance spectroscopy	Ceramic	E_a=1.51 eV	----
Rothman *et al.*[178]	Tracer diffusion	Ceramic	E_a=0.97 eV (*ab* plane)	D(500 °C) = 6.7×10^{-11} D(400 °C) = 7.7×10^{-12}
Maier *et al.*[180]	Electrochemical	Ceramic	E_a=1.8 eV	----
Tallon *et al.*[181]	Internal friction	Ceramic	E_a=1.07 eV	D(500 °C) = 1.9×10^{-11} D(400 °C) = 1.7×10^{-12}
Scolnik *et al.*[182]	Electrochemical	Ceramic	----	D(room temp.) = 10^{-11} – 10^{-12}
Tang *et al.*[183]	Thermogravimetry	Powders	E_a=1.3 eV for $\delta\approx$0.1	D(500 °C) = 10^{-10} D(400 °C) = 6×10^{-12}
Bredikhin *et al.*[185]	Tracer diffusion	Single crystals	$E_{a,b}$=1.27 eV E_c=2.3 eV	$D_{a,b}$(400 °C) = 3×10^{-12} D_c(400 °C) = 4×10^{-17} $D_{a,b}$(800 °C) = 7.8×10^{-9} D_c(800 °C) = 6.2×10^{-11}
MacManus *et al.*[186]	Electrochemical	Ceramic	$E_{lattice\ diffusion}$=1.5 eV Out-diffusion E_a=1.4 eV In-diffusion E_a=1.76 eV	----
Krauns *et al.*[187]	Thermogravimetry	Ceramic	E_a=1.1 eV @ 400 °C E_a=0.3 eV @ 700 °C	D(500 °C) = 1×10^{-10} D(400 °C) = 3×10^{-11}
LaGraff *et al.*[188]	Resistivity	Single crystals and ceramics	----	D(700 °C) = 10^{-6}-10^{-7} for single crystals

2.3.2 Thin Film YBCO

Studies of oxygen diffusion in thin films of YBCO are not as widespread, and there are discrepancies between the reported results. Sageev Grader *et al.*[190] were the first to study the diffusion of oxygen in YBCO thin films. Their study compared bulk polycrystalline samples with both thick and thin film samples. The thin film samples were prepared by evaporation from separate metallic sources with a subsequent anneal in oxygen (*ex situ* prepared films). The diffusion was measured using resistivity measurements similar to the methods used for bulk samples described above. Using a one-dimensional diffusion model, and assuming a linear relationship between oxygen content and resistivity, the authors obtained diffusion coefficients of 4×10^{-11} to 1×10^{-12} cm^2/s for temperatures between 435 °C and 320 °C, respectively. A linear dependence was observed between the transient resistivity (the value for a given T and P) and the square root of time. Thus the authors concluded that the oxidation is diffusion controlled, not surface reaction limited as was seen in some of the studies on bulk material. In addition, the authors observed that in-diffusion of oxygen took place faster than the out-diffusion, as was seen in bulk material. It should be noted that only three data points were used to extract D and E_a, and no structural information was provided regarding the microstructural quality or orientation of the samples.

Yoshida *et al.*[191] examined the plasma oxidation of oxygen deficient YBCO. The films were deposited on MgO substrates by electron-beam evaporation from separate metallic sources and then annealed in oxygen at 900 °C. The films were *c*-axis oriented, but not epitaxial, with a T_c between 50 K and 70 K. The plasma oxidation process took place at 1 Torr and an rf power of 200 W. These experiments were done under no additional heating aside from the plasma, thus the temperature was kept below 160 °C. Assuming isotropic diffusion into a 460 nm thick film that is not surface reaction limited, the authors calculated an "effective" diffusion coefficient of 2.2×10^{-12} cm^2/s. The authors also noted that heat treatment of deoxygenated films at 230 °C in 1 torr of O_2 alone resulted in no change in the resistivity. Thus, the reactivity of atomic oxygen (present in the plasma) is shown to be much higher than that of O_2 by itself.

Based on the results of Yoshida *et al.*, Yamamoto *et al.*[193] extended the investigation of the oxidation kinetics of YBCO films in the presence of atomic or molecular oxygen using resistivity measurements. The films were deposited by off-axis magnetron sputtering (*in situ* deposited) on MgO, $LaAlO_3$ and yttria-stabilized zirconia (YSZ). T_c's were between 76 K and 89 K and the films were *c*-axis, *a*-axis and *a*+*c*-axis oriented. Assuming one-dimensional diffusion where D is not a function of oxygen content, the authors calculated $D = 3.8 \times 10^{-14}$ cm^2/s at 480 °C for *c*-axis oriented YBCO on MgO. Values on $LaAlO_3$ were similar while for YSZ the values were ≈ 50 times higher, which the authors attributed to a much poorer microstructure (more fast diffusion pathways). Activation energies were found to be ≈ 1.2 eV for all of the films. Experiments in atomic oxygen took place under an ECR generated plasma. The O flux was 2×10^{15} atoms/cm^{2}s. The diffusion coefficient for the film on MgO at 480 °C was calculated to be 7.8×10^{-13} cm^2/s, approximately 20 times higher than in molecular oxygen. The activation energy was 0.65 eV. The difference between atomic and molecular oxygen can be seen clearly in Fig. 2.15, where the conductance is plotted

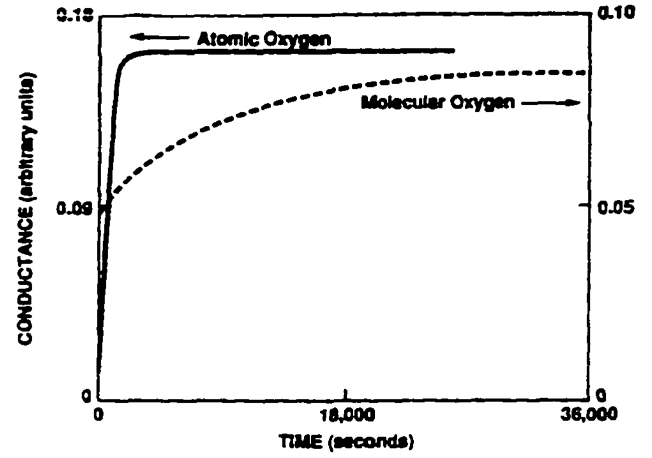

Figure 2.15 : The conductance of a *c*-axis film on MgO in the presence of atomic oxygen (solid line) and molecular oxygen (dashed line) as a function of time at 480 °C. From Yamamoto *et al.*[193]

versus time at 480 °C. The authors calculated the equivalent pressure of atomic oxygen (with respect to molecular oxygen), plotted in Fig. 2.16. It can be seen that the resistivity of the film at 0.2 mTorr of molecular oxygen plus the flux of 2×10^{15} atoms/cm^2s of atomic oxygen corresponds to the resistivity of the film in 200 mTorr of molecular oxygen alone. Thus the presence of an activated oxygen species during, or subsequent to deposition can significantly affect the final properties of the material.

Aarnink *et al.*[152] were the first to use ellipsometry to characterize the diffusion of oxygen into YBCO. The films were *in situ* off-axis sputter deposited onto YSZ substrates. Spectroscopic ellipsometry was used to determine the thickness of the films. This was done assuming no surface roughness and without accounting for the known $BaZrO_3$ reaction layer at the film/substrate interface.[46] Subsequently, the authors used single wavelength ellipsometry at 4.0 eV to observe the in-diffusion of oxygen. Based on an empirical equation relating the dielectric function at 4.0 eV to δ, and diffusion data

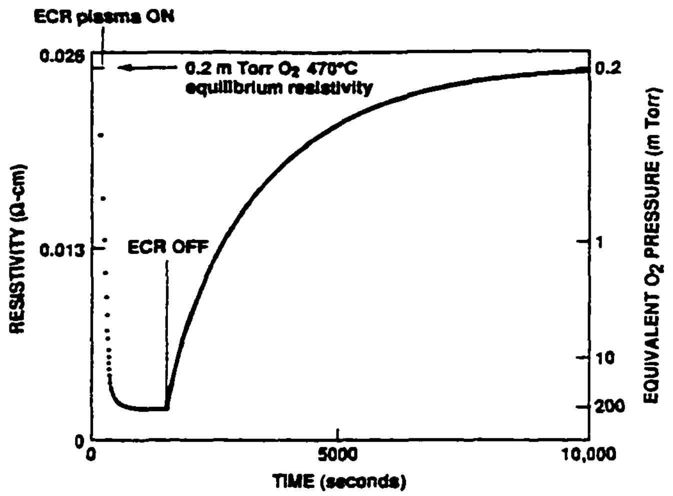

Figure 2.16 : Time dependence of the resistivity for an *a+c* mixed YBCO film before, during and after being exposed to an ECR plasma at 470 °C. On the right hand axis, the equilibrium resistivity for this film at several oxygen pressures is shown. From Yamamoto *et al.*[193]

from Rothman *et al.*[178,197] for bulk material, the authors compared their data to calculated data for one, two and three-dimensional diffusion models. It was determined that the two-dimensional model with short circuits (fast pathways) for diffusion in the *c*-direction fit the data best. The authors calculated the spacing of these short circuits to be 2.5 ± 0.2 μm, which corresponds to a number density of 1.6×10^{11} m^{-2}. This density was too low compared to that of the spiral surface features, so the authors attributed the short circuits to surface precipitates.

Lee *et al.*[194] used resistance changes to monitor the oxygen content in YBCO films during pulsed laser deposition. The substrates were $SrTiO_3$ and the deposition temperatures were between 560 °C and 700 °C. No structural information regarding the films was given. To monitor the *in situ* resistance during deposition, four strip electrodes were made on the substrate using silver paint and thin copper wires. No indication was given as to how these electrodes affected the growth of the film. Again, using a one-dimensional diffusion model, the authors determined diffusion coefficients from 3.1×10^{-11} cm^2/s at 450 °C to 6.3×10^{-11} cm^2/s at 600 °C with an activation energy of 0.33 eV. They obtained these values assuming that the oxygen distribution is not homogenous, that is they assumed that the sample had an oxygen rich layer on top of an oxygen deficient layer (see Yeh *et al.*[174]).

Other studies include Krauns *et al.*,[187] who also used resistance measurements to look at PLD films on MgO. They found a dependence of the diffusion coefficient and activation energy on oxygen content. D varied from 3×10^{-15} to 3×10^{-12} cm^2/s between 300 °C and 650 °C while E_a varied from 0.8 eV to 0.1 eV over the same temperature range. Li *et al.*[195,196] used SIMS and tracer diffusion for sputtered films on $LaAlO_3$. They saw O^{18} begin to migrate at temperatures between 250 °C and 300 °C and based on isotopic gas-solid exchange, they found a diffusion coefficient of 1.5×10^{-13} cm^2/s at 315 °C. Short circuit diffusion was found to play an important role in that work. Finally, Bock *et al.*[167] used laser Raman spectroscopy to monitor oxygen diffusion in YBCO films on MgO. Their results showed that out-diffusion began at temperatures as low as 220 °C at 4×10^{-6} Torr. Unfortunately, their results are complicated by the fact that the laser used caused local heating and thus oxygen migration.

From this discussion, it is clear that there are several points of disagreement throughout the literature. The main points are: the values of the diffusion coefficient as a function of temperature, whether the diffusion coefficient is sensitive to the oxygen content or oxygen partial pressure, the values of the activation energies for in and out-diffusion and whether these are dependent on oxygen content or partial pressure, and whether the diffusion is surface reaction limited or diffusion limited. Many of the studies used a one-dimensional Fickian model to calculate the diffusion parameters. This is most likely not entirely correct for all samples. Many of the bulk samples contained grain boundaries and second phases, while the films also were not all epitaxial and also contained second phases (and most likely some surface precipitates). This is shown in the data for the transition temperature and the x-ray measurements, when given. In addition, the lattice parameters of YBCO are sensitive to oxygen content, which should add strain terms to the diffusion model, providing another driving force for oxygen transport. These factors can all affect whether the assumption of Fickian diffusion is valid. The only consistent result from these studies is that oxygen uptake is observed to be more rapid than oxygen out-diffusion.

2.4 Molecular Beam Epitaxy (MBE)

Molecular beam epitaxy (MBE) was first developed by J.R. Arthur and A.Y. Cho[198,199] in order to grow GaAs and GaAs/$Al_xGa_{1-x}As$ structures. This technique exhibits several advantages over other methods such as pulsed laser deposition (PLD), sputtering, liquid phase epitaxy (LPE) and metal-organic vapor phase epitaxy (MOVPE). Some of these advantages include the ability to reproducibly control growth on the scale of atomic dimensions and to monitor this growth in real time. Also, with MBE it is possible to consistently deposit materials with impurity levels below ten parts per billion.[200]

MBE basically involves the generation of vapor fluxes of the constituent species and their subsequent reaction at the substrate surface to form an epitaxial layer.[200] If the precursor species are solid or liquid, they are heated to form a vapor. If they are gaseous, they are simply introduced into the system. The fluxes of these constituents can then be modulated, usually by physically blocking the beam using a mechanical shutter. This can yield rapid changes in the composition of the material being deposited or in the doping of the material. With the use of relatively fast shutters, the composition of each atomic layer can be adjusted. Thus, MBE can be thought of as atomic layer-by-layer engineering.[201]

The extremely high purity levels attainable via MBE are a result of the stringent vacuum conditions utilized. The addition of a load-lock to the MBE system ensures that the main deposition chamber is always maintained under ultra-high vacuum (UHV) conditions. Thus, substrates can be inserted or removed from the system and the quality of the deposited material is not compromised by outgassing from components in the main chamber exposed to air. Typically, pressures of approximately 10^{-10} to 10^{-12} Torr are desired for MBE of GaAs type structures in order to minimize impurities.[200]

A necessary condition for growth in MBE is that the mean free paths of the depositing species be longer than the source-to-substrate distance, since it is a "line of sight" technique. In typical machines, this distance is about 20 cm. A schematic of one type of MBE system design is shown in Fig. 2.17. Here, the relatively long distance between the sources and the substrate can be seen.

The fluxes of the species being deposited are usually formed from thermal effusion cells, often incorrectly referred to as Knudsen or K-cells. Some systems have up to 10 cells. In an effusion cell, the solid or liquid evaporant is contained in a crucible that is radiatively heated to form the vapor flux. In some cases, other types of sources can be used, such as electron beam evaporators or gas cracker sources.

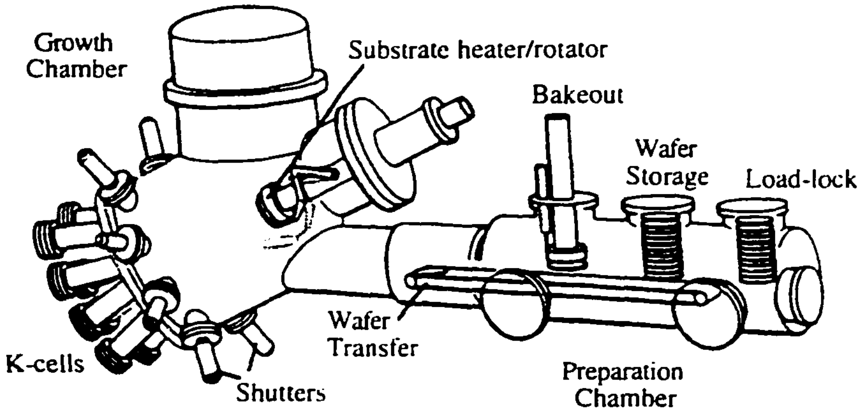

Figure 2.17 : Schematic of a typical semiconductor MBE system.[200] Note the long distance between the substrate and the sources.

The other major component in the main deposition chamber is the substrate holder/heater. There have been many types of heaters developed to meet the requirements for deposition of different materials. All of the designs stress temperature uniformity and reproducibility. The choice of material is also critical in order to avoid either excessive corrosion at the deposition temperature or outgassing. Thus, normally they are constructed of refractory metals such as Mo and Ta with pyrolytic BN ceramic for electrical insulation.[200] This is not the case for MBE of oxide materials, as will be discussed later. When the substrate holder is rotated during the deposition, the thickness and compositional uniformity of the film is improved. It is desirable for the rotation speed to be a harmonic of the monolayer deposition rate in order to ensure deposition uniformity.[200] A schematic of a typical rotating substrate heater/holder is shown in Fig. 2.18.

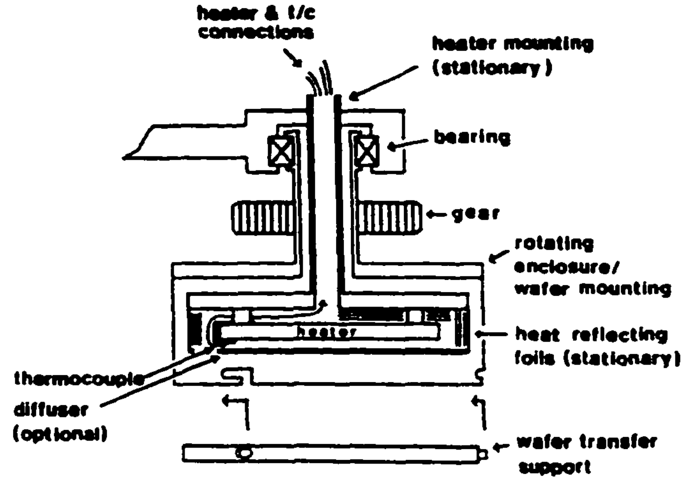

Figure 2.18 : Schematic of a typical substrate rotator/heater.[200]

2.4.1 MBE of Oxide Materials

Due to the layered crystal structure of YBCO, as well as many of the other superconducting oxides, MBE is an obvious method to study their deposition. However, precise composition control is extremely important in order to obtain the desired phase. The MBE technique described above was developed mainly for fixed stoichiometry semiconducting materials or alloys with a complete solid solution (i.e., III – V heterostructures). Using MBE to deposit multi-component oxide materials calls for some changes to the design of the system and its components.

Many oxides can be prepared in thin film form through other methods, including sputtering (rf, magnetron, ion beam), e-beam evaporation or pulsed laser deposition. These methods do hold some advantage over MBE. For example, for several of the alternative methods, only a single ceramic target of the desired composition is necessary for deposition. Thus, composition control is much more straightforward than for MBE. This is the main reason for the widespread use of PLD in high-T_c film growth. However, one drawback to PLD is the simultaneous deposition of micron sized particles, or "boulders", on the surface of the film. These macroparticles can severely affect the ability to form high quality heterojunctions, especially in terms of reproducibility. With sputtering methods, the energetic (100 – 1000 eV) bombarding particles can cause damage and intermixing at the interfaces.[202] While this can be avoided by using off-axis sputtering geometries, there is a tradeoff in terms of a decreased deposition rate. Compared to the alternative techniques, MBE provides advantages in terms of the ability to deposit metastable structures, layer-by-layer film growth and the ready use of powerful *in situ* diagnostic techniques. There are challenges in utilizing MBE to deposit oxides, however. These include: finding a strong enough oxidant to oxidize the incident species during deposition while maintaining the long mean free path (low pressure) necessary for MBE, using a low enough growth temperature to allow the formation of metastable phases and reduce the possibility of interdiffusion between epitaxial layers, and finally, controlling the stoichiometry (fluxes) of the individual species such that the desired complex phases are formed.[201,202]

2.4.2 Modification of Standard MBE for Oxide Deposition

As mentioned above, one of the difficulties in using MBE to grow YBCO was to find a powerful oxidizing agent that could provide sufficient oxygen to form $YBCO_{6-6.1}$ during deposition at ≈ 700 °C while still maintaining the long (≥ 20 cm) mean free paths of the depositing species. Fig. 2.19 shows the mean free path of several species as a function of O_2 pressure;[202] it is clear that a mean free path greater than 20 cm mandates a maximum pressure of 10^{-4} Torr. Unfortunately, according to Fig. 2.4, at this pressure, the $YBa_2Cu_3O_{6-6.1}$ phase is no longer thermodynamically stable at 700 °C. For this phase to be thermodynamically stable at 10^{-4} Torr, the growth temperature must be ≈ 550 – 600 °C. However, at this temperature, the kinetic barriers are too high to form high quality YBCO.[202,203] Thus, the use of molecular oxygen (O_2) is precluded in this case and a more reactive oxidant must be utilized.

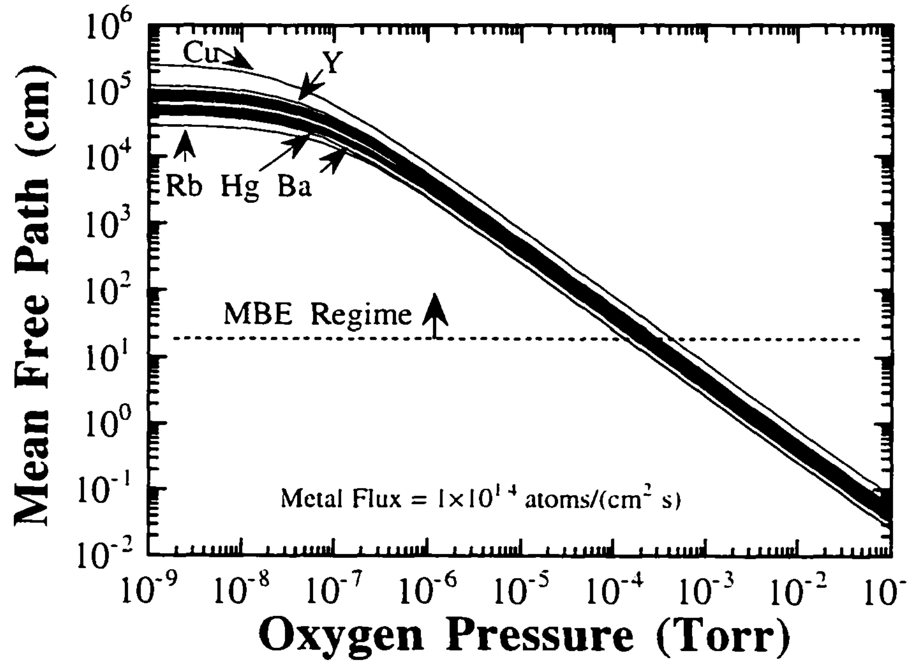

Figure 2.19 : The mean free path of atomic fluxes of the constituent species of high-T_c superconductors as a function of oxygen pressure. From Schlom *et al.*[202]

There are two primary methods used to produce a more reactive oxidizing agent. The first is to generate the species inside the growth chamber using a plasma source. The second is to generate the oxidizer outside of the system and then introduce it into the chamber through a valve system. The idea of using a plasma source to generate the oxidizing species is not conducive to the MBE environment. Typically, there needs to be a high pressure of molecular oxygen along with the desired oxidant in the plasma. This, in turn, decreases the mean free paths below the limit for MBE. Therefore, the second method is used. For this, the best oxidants have been shown to be NO_2 and ozone

(O_3).[201,204] Both can be formed as relatively pure beams and both are very reactive oxidants. For these species, the typical growth pressures at the substrate are from 10^{-5} to 10^{-7} Torr, which is well within the limits for MBE.[201,204] In addition, the temperatures needed to grow at these pressures are within the region shown in Fig. 2.4 for *in situ* film deposition.

Of the two choices, ozone is the most commonly used agent. The methods and equipment used to generate ozone are well established.[202] The output from a commercial ozone generator is purified via a distillation process and subsequently delivered to the growth chamber. In order to avoid decomposition of the ozone due to high temperature, a water cooled stainless steel nozzle is used to distribute the oxidant to the substrate region.[204,205]

As a result of the extreme oxidizing environment necessary to deposit YBCO using MBE, the traditional choices of materials utilized for system components must be reevaluated. Some of these components include crucibles, filaments and substrate heater/holder materials. For MBE of GaAs type structures, the most common material for high temperature parts is molybdenum. For oxide MBE, the combination of ozone pressure and high growth temperatures causes MoO_3 to volatilize, thus contaminating the depositing film.[202] As a replacement, materials such as stainless steel (Haynes®, Inconel®, etc.) or platinum must be used. This, in combination with confining the oxidant to the substrate region, reduces the possibility of degradation of the MBE components.

In comparison to the MBE growth of semiconductors, composition control for oxide MBE is critical. This is especially true for multi-component, metastable phases (i.e., $Bi_2Sr_2CaCu_2O_8$ or $YBa_2Cu_3O_7$). As mentioned earlier in this chapter, slight variations in material stoichiometry can result in drastic differences in the final structural and electrical properties. There are several methods which can be used to measure incident fluxes, such as ion gauges, atomic absorption spectroscopy (AA), mass spectrometry and quartz crystal microbalances. However, hot filament techniques (i.e., ion gauges) are not suitable due to the extreme oxidizing environment in oxide MBE. Other methods, for example AA and mass spectrometry, require rigorous *ex situ* calibrations to effectively measure fluxes. However, once calibrated they offer better than ± 1% composition control.[201,202] Quartz crystal microbalances offer the capability of absolute *in situ* flux measurements. Their operation is based on measuring the amount of material deposited over a given time by monitoring the vibrational frequency shift of the quartz as a function of mass loading.[206] A combination of methods is often used to obtain the highest precision, typically a quartz microbalance along with quadrupole mass spectrometry or AA yields the best results.[201,207]

Chapter 3

EXPERIMENTAL PROCEDURE

3.1 Film Deposition

The majority of the films studied in this work were deposited by molecular beam epitaxy (MBE). Specifics of the deposition parameters for individual films will be given in the following chapters. This section will provide an overview of the general experimental methods used for MBE, as well as a description of the *in situ* characterization capabilities of the system.

The MBE is an EPI model 930 (Minneapolis, MN). A diagram of the MBE is given in Figure 3.1. There are eight effusion cells available for deposition of a wide variety of materials. Of primary importance for this work are the Y, Ba and Cu sources. The entire MBE system is controlled by the MicroCrystal® computer program (WeckTech, Pleasanton, CA). Via this program, the user controls the temperature of each source, the flux of each source, the shutters, the substrate temperature, the substrate rotation speed, the pressure gauges, etc. In addition, within MicroCrystal®, the user can write a deposition program to open and close shutters, set source fluxes, set source doses, etc. Thus, it is possible to write programs for various methods of deposition (i.e., layer-by-layer, co-deposition or block-by-block) by writing the commands in the proper order.

During film deposition, purified ozone was used as the oxidant. Output from a commercial ozone generator (Model G1-L, PCI Ozone Corp., West Caldwell, NJ) has been measured to be about a 10% O_3 and 90% O_2 mixture.[205] In order to extract the ozone out of this mixture, a still was constructed based on the work of Schlom *et al.*[202]

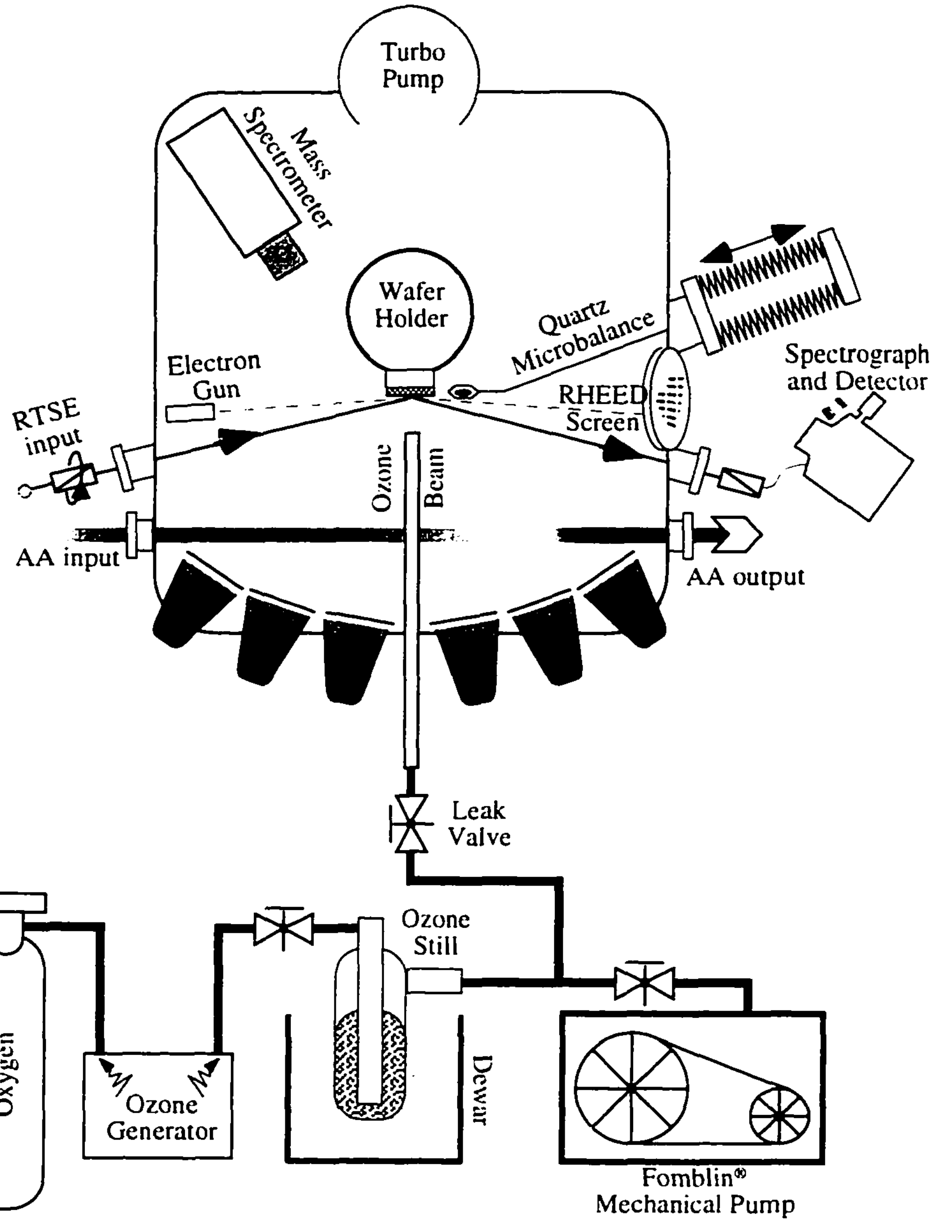

Figure 3.1 : A schematic of the MBE used for this work. AA = atomic absorption flux monitor.

The output from the ozone generator is fed into a glass still which is filled with silica gel. Dry nitrogen gas is flowed through a glass envelope that surrounds the still, and the entire assembly is placed into a dewar of liquid nitrogen. The combination of the liquid and gaseous nitrogen allows the temperature of the still to be controlled. If the temperature becomes too low, the ozone that is collected will liquefy, at which point it is extremely explosive. For this reason, the entire apparatus is kept in a gas cabinet. The ozone is adsorbed onto the silica gel surface as it flows through the still. As this happens, the gel turns a dark purple color. After 30 – 60 minutes of collection time, a vacuum is pulled on the still. The vapor pressure of the O_2 over the silica gel is higher than that of the O_3, thus after a few minutes the remaining gas is primarily ozone. During deposition, the ozone is leaked into the chamber through a needle valve until the desired pressure is obtained. The ozone is released through a nozzle (designed specifically for this MBE[205]) which is aimed directly at the substrate 8 cm away from the nozzle outlet. The actual purity of the ozone at the substrate position has been measured[208] and was found to be ≈ 80%. A portion of the ozone is broken down to O_2 as it travels from the still to the substrate.

One unique feature of this system is the method used for measuring the flux of each source material. Traditional MBE relies upon ion gauge flux measurements both prior and subsequent to each deposition in order to determine the flux of material. In this system, atomic absorption spectroscopy (AA) is used in tandem with quartz crystal microbalance (QCM) measurements in order to monitor each of the fluxes. The system used was developed by Intelligent Sensor Technologies (Mountain View, CA).[209] The basic principle of the measurement is that light from a hollow cathode lamp (made from the material that is being measured) will be absorbed as it passes through the flux beam. That absorption will be proportional to the flux. In order to use the AA system, it first must be calibrated with an absolute measurement of the flux. This is done with a set of QCM measurements. That is, first the source is set to a temperature and allowed to equilibrate. Then, the source shutter is opened and the amount of material deposited on the QCM is measured while the AA signal is measured. This is done for several temperatures where the flux is between 5×10^{13} atoms/cm^2•s and 5×10^{14} atoms/cm^2•s. In this way, a calibration curve of AA signal vs. flux can be constructed and stored in the computer for MicroCrystal® to access. Thus, when a specific dosage of atoms is called for in a deposition program, MicroCrystal® calculates the exact flux delivered based on the calibration table, and closes the shutter when the required dosage has been achieved.

In addition to the *in situ* flux monitoring capability, the MBE also has a reflection high-energy electron diffraction system (RHEED) for structural analysis during deposition (Staib Instrumente, Langenbach, Germany and k-Space, Ann Arbor, MI). A CCD camera is used to capture the RHEED image and send it to an analysis computer for immediate extraction of in-plane lattice constants, RHEED oscillations and for monitoring the formation of second phases. Fig. 3.2 shows a picture of the MBE system, indicating the location of the various *in situ* monitors, as well as the sources.

The general procedure for film deposition begins with cleaning the substrate. For experiments on Si, the substrate was cleaned in Micro® (an ammonia-based degreaser), rinsed with deionized water, rinsed with acetone, boiled in trichloroethylene (TCE), cleaned with the RCA etch[210] and spin dried. Some of the Si substrates were also HF-dipped, in order to remove the oxide overlayer. For experiments on $SrTiO_3$, the substrate was cleaned in Micro®, and then rinsed progressively with deionized water, acetone and isopropanol. In addition, a final etching step was used to obtain the desired surface termination. It has been shown[211] that by etching the $SrTiO_3$ substrate in an NH_4F-HF mixture, a smooth TiO_2-terminated surface can be achieved. Subsequent to the etching, the wafer was again spin dried. Next, the clean substrate was mounted on a wafer holder

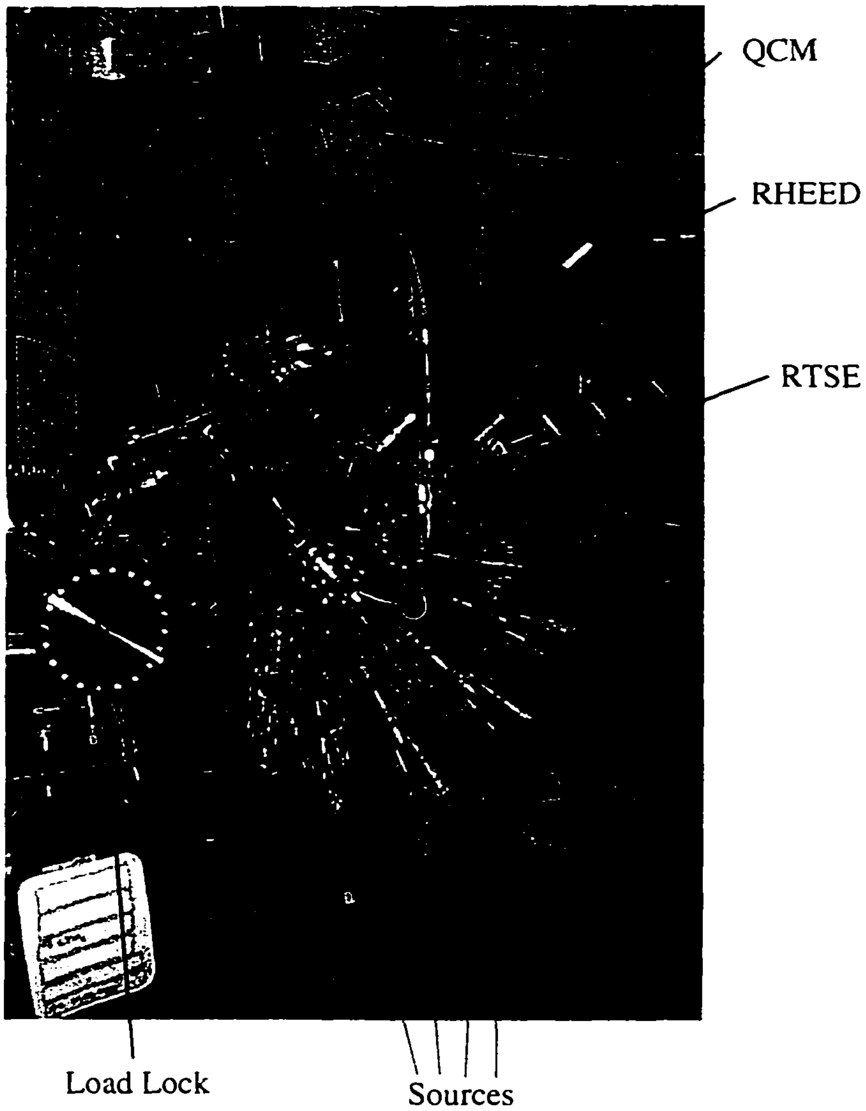

Figure 3.2 : A picture of the MBE system used for this work. The location of the various *in situ* monitors, as well as the sources, are indicated.

(puck) using silver paint. Some of the substrates were then baked on a hot plate for one hour. The puck was then loaded into the introduction chamber of the MBE and baked out at 100 °C for one hour. Upon cooling, the puck was loaded into the deposition chamber and mounted on the substrate manipulator. Ozone was collected, the sources were heated and the azimuthal angle of interest was found for *in situ* RHEED analysis. Finally, the deposition was completed.

Additional YBCO thin film samples were obtained from Duke University. These samples were prepared using 90° off-axis rf magnetron sputtering. The substrates were (001) oriented $SrTiO_3$. During deposition, the substrate temperature was 720 °C and the total pressure was typically 200 mTorr ($Ar/O_2 = 4:1$). More details are given elsewhere.[30,212]

3.2 Introduction to Spectroscopic Ellipsometry (SE)

Ellipsometry is a technique in which polarized light of a known wavelength is reflected off a sample and the relative changes in phase and amplitude of the parallel (p) and perpendicular (s) components of the light are measured. Those changes are characteristic of the depth profile of the dielectric function of the film. At a single wavelength, this does not yield enough information to completely characterize most thin film samples. Therefore, a spectroscopic technique is used where the polarization state of the reflected light is determined for many wavelengths between the near-ultraviolet and the near-infrared. This provides sufficient data for depth profiling to be performed.[104]

Each sample reflects light in a different manner according to its complex Fresnel p and s reflection coefficients (parallel and perpendicular to the plane of incidence, respectively). The electric field vector, E(t) of an incident light wave that is monochromatic and polarized at some angle, P, with respect to a reference laboratory frame can be described by:

$$E(t) = \left(E_x X + E_y Y\right) e^{(ikZ - i\omega t)} \qquad (3.1)$$

Where X and Y are unit vectors orthogonal to the propagation direction, Z, of the light. E_x and E_y are the components of the incident light in the plane of incidence and perpendicular to the plane of incidence, respectively. k is the wavevector of the light. ω is the frequency and t is the time. The light that is reflected from the sample surface can then be characterized by a similar equation:[213]

$$E(t) = \left(r_p E_x X + r_s E_y Y\right) e^{(ikZ - i\omega t)} \tag{3.2}$$

where r_p and r_s are the complex reflection coefficients parallel and perpendicular to the plane of incidence, respectively.

Spectroscopic ellipsometry permits measurement of the complex reflection coefficients at several wavelengths. By convention, the two ellipsometric angles (Δ and Ψ) are given by the complex ratio of the two reflection coefficients:

$$\rho \equiv \frac{r_p}{r_s} = \tan\Psi e^{i\Delta} \tag{3.3}$$

Since only ratios of measurable quantities are important in ellipsometry, accurate measurements of intensities are not needed. This is an advantage over other optical techniques, such as reflectance or transmission measurements. Each of the parameters in equation 3.3 is a function of the wavelength of the probing light, λ, the angle of incidence, θ, and the thickness, dielectric function and microstructure of the thin film sample. Once the ellipsometric angles have been determined for each incident wavelength, this information can be used along with a model of the depth profile of the thin film to determine the thickness and dielectric function of the sample. The simplest case is the two-phase model, shown in Figure 3.3. Here, the interface between the optically thick substrate with complex dielectric function $\tilde{\varepsilon}$ and the ambient (air) is sharp and the substrate is homogeneous. By substituting the Fresnel reflection coefficients into equation 3.3, the dielectric function at a particular wavelength can be expressed in terms of the complex reflectivity ratio, ρ, which is determined from the experimental values Δ and Ψ:[213]

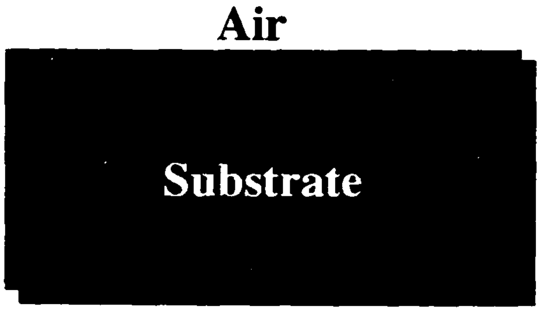

Figure 3.3 : Schematic of the two-phase model used for calculation of Δ and Ψ.

$$\tilde{\varepsilon} = \sin^2\theta\left(1 + \tan^2\theta\left(\frac{1-\rho}{1+\rho}\right)^2\right) \tag{3.4}$$

A complete description of the modeling procedure for more complex thin film structures will be given later.

The procedure for obtaining Δ and Ψ can be different, depending on what type of ellipsometer is used. For this work, two types of ellipsometers were used. The design and operation principles of each are different, and thus they will be described separately in the following sections, along with discussions of the principles of alignment and calibration for both types of instruments.

3.3 *Ex situ* Spectroscopic Ellipsometry

The configuration of the *ex situ* ellipsometer used in this study is shown in Fig. 3.4. It is a fixed polarizer-sample-rotating analyzer configuration (PSA_{rot}). The instrument is interfaced with a Gateway 2000 486/DX2 computer which maintains control over such operations as monitoring the photomultiplier tube (PMT) detector signal, determining the timing signals for taking data, converting light intensity as a function of analyzer angle to the ellipsometric angles Δ and Ψ, as well as other functions. An electronic feedback circuit is employed in the system in order to maintain a constant average signal level from the PMT at all energies of incident light. Therefore, comparisons of the ellipsometric spectra at different wavelengths are more reliable.[115] The light source is a 75 W broadband xenon lamp. This type of lamp provides a strong signal for the wavelength range used for this work (250 nm – 750 nm). The monochromator has a double Czerny-Turner configuration. Filters are used for

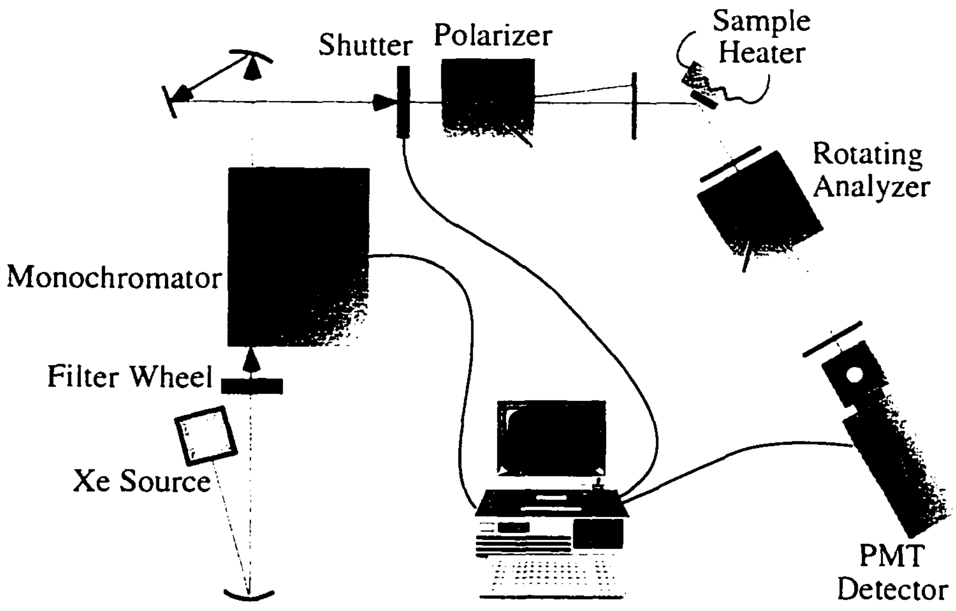

Figure 3.4 : A schematic of the *ex situ* SE used in this work.

wavelengths greater than 400 nm in order to eliminate higher orders of diffracted light from the monochromator. A filter with a cutoff wavelength of 380nm is inserted at 400 nm and a filter with a cutoff wavelength of 620 nm is inserted at 650 nm. The shutter is used to block the light beam in order to measure background spectra. This is done at each wavelength and the measured background intensity is subtracted from the raw data prior to calculation of Δ and Ψ. The polarizer and the analyzer are quartz rochon prisms. Finally, the sample holder has the capability of heating the sample up to 600 °C while taking ellipsometric data.[214] For these experiments, the sample is attached to a block heater with silver paint in order to improve the thermal contact.

The calculation of Δ and Ψ for this type of an ellipsometer can best be shown with the aid of Jones matrix representations. Using eq. 3.1 and 3.2, the ellipsometer in Fig. 3.4, with the sample, can be described by the following series of matrices (assuming an ideal system):

$$\begin{bmatrix} E_1 \\ E_2 \end{bmatrix}_{t,e} = \begin{bmatrix} 1 & 0 \\ 0 & 0 \end{bmatrix} \begin{bmatrix} \cos A & \sin A \\ -\sin A & \cos A \end{bmatrix} \begin{bmatrix} r_p & 0 \\ 0 & r_s \end{bmatrix} \begin{bmatrix} \cos P & -\sin P \\ \sin P & \cos P \end{bmatrix} \begin{bmatrix} 1 \\ 0 \end{bmatrix} E_o \tag{3.5}$$

Here, P and A are the angles that the polarizer and analyzer make with respect to the reference x-y frame of the laboratory. E_o is the electric field of the incident light. The common term, exp(ikZ-$i\omega$t), is left off for simplicity. This equation gives the electric field of the exiting light in the analyzer transmission-extinction (t,e) reference frame. It is straightforward to see that the exiting electric field components (E_1 and E_2) depend on the sample's complex Fresnel reflection coefficients. Thus, the coefficients can be determined, since all other quantities are either known or measured. Substituting eq. 3.3 into eq. 3.5, it is found that:

$$\begin{bmatrix} E_1 \\ E_2 \end{bmatrix}_{r,e} = \begin{bmatrix} 1 & 0 \\ 0 & 0 \end{bmatrix} \begin{bmatrix} \cos A & \sin A \\ -\sin A & \cos A \end{bmatrix} \begin{bmatrix} \rho & 0 \\ 0 & 1 \end{bmatrix} \begin{bmatrix} \cos P & -\sin P \\ \sin P & \cos P \end{bmatrix} \begin{bmatrix} 1 \\ 0 \end{bmatrix} E_o \qquad (3.6)$$

Since the irradiance of the exiting light is proportional to the square of its electric field, it can be shown that:[215]

$$I = \frac{1}{2}\left(1+\rho\rho^*\right)\left[1+\left(\frac{\rho\rho^*-1}{1+\rho\rho^*}\right)\cos 2A+\left(\frac{\rho+\rho^*}{1+\rho\rho^*}\right)\sin 2A\right] \qquad (3.7)$$

or,

$$I = I_o\left[1+\alpha\cos 2A+\beta\sin 2A\right] \qquad (3.8)$$

Where ρ^* is the complex conjugate of the reflectance ratio, and α and β are the normalized second order Fourier coefficients determined by analysis of the exiting light intensity as a function of analyzer angle. Once α and β are determined, the ellipsometric angles, Δ and Ψ, are calculated using eq. 3.3 and 3.7. The results are:[213]

$$\tan\Psi = \left[\frac{1+\alpha}{1-\alpha}\right]^{1/2}\tan P \qquad (3.9a)$$

$$\cos\Delta = \frac{\beta}{\sqrt{1-\alpha^2}} \qquad (3.9b)$$

Thus, the basic principle of the measurement is to obtain the intensity of the light as a function of the instantaneous analyzer angle and to subsequently Fourier analyze the signal. To do this, an optical encoder with two signal outputs is attached to the rotating analyzer. One of the signals outputs one pulse per revolution of the analyzer and the other outputs 90 pulses per revolution. Data are collected and digitized at each of the

90/revolution pulses. The 1/revolution pulse ensures that data collection always begins on the same 90/revolution pulse.

It is important to note that the above description assumed a system with perfect components and ideal samples. There are several calibrations that will be discussed which must be included in order to account for non-idealities in the system, as well as to determine the actual zero reference values of the polarizer and analyzer with respect to the plane of incidence.

3.3.1 *Ex situ* Ellipsometer Alignment and Calibration

There are three procedures used to align and calibrate the *ex situ* SE. They are: 1) the system alignment, 2) the residual calibration and 3) the eta calibration.

The system alignment is done after large system disruptions, such as replacing the light source, are completed. This calibration consists of removing the photomultiplier tube detector and putting a HeNe laser in its place. This allows for the tracing and centering of the light beam path throughout the system. This includes positioning of the polarizing optics, the mirrors, the monochromator and the light source. Once this is done, the detector is replaced and final adjustments can be made.

The residual calibration accounts for the difference between the azimuth of the polarizer, P, when it reads zero and the plane of incidence (set by the sample). There is a similar discrepancy with the analyzer that also must be accounted for. The zero of the analyzer is determined by the mounting of the rochon prism with respect to the 90/revolution pulse which starts the data collection (measured with respect to the plane of incidence). The procedure used was first developed by Aspnes.[216,217] The Jones matrix representation of the system given above can be generalized for this case. Including the difference in zero positions and the optical activity of the Rochon quartz polarizer and analyzer, the equation is:

$$\begin{bmatrix} E_1 \\ E_2 \end{bmatrix}_{r,e} = \begin{bmatrix} 1 & -i\gamma_A \\ 0 & 0 \end{bmatrix} \begin{bmatrix} \cos(A - A_S) & \sin(A - A_S) \\ -\sin(A - A_S) & \cos(A - A_S) \end{bmatrix} \begin{bmatrix} \rho & 0 \\ 0 & 1 \end{bmatrix} \begin{bmatrix} \cos(P - P_S) & -\sin(P - P_S) \\ \sin(P - P_S) & \cos(P - P_S) \end{bmatrix} \begin{bmatrix} 1 \\ i\gamma_P \end{bmatrix} E_o \tag{3.10}$$

where P_s and A_s are the calibrations for the exact zero positions and γ_A and γ_P are the optical activity coefficients of the analyzer and polarizer, respectively. All of these values are characteristic of the system, and therefore once they are determined, the calculation of the ellipsometric parameters can proceed as described above.

A perfectly absorbing material with linearly polarized light incident upon it will reflect linearly polarized light if the incident light is parallel or perpendicular to the plane of incidence (polarized at 0° or 90°). In addition, the light that is reflected is 100% modulated, or the minimum of the ac component amplitude is equal to the dc background.[217] However, if the incident light is not polarized precisely at 0° or 90°, the reflected light will have slight elliptical polarization and the modulation will be somewhat less than 100%. Thus, the point of 100% modulation is equal to P_s or $P_s+\pi/2$. However, the optical activity of the polarizer and analyzer must be considered, as well. The ellipticity imparted by these components causes the angle of 100% modulation to shift away from the zero position, P_s (A_s) to a position P_1 (A_1). It has been shown that the modulation level in the vicinity of P_s or $P_s+\pi/2$ depends quadratically on P.

Experimentally, this dependence is known as the residual function, R(P), and has the form:

$$R(P) = 1 - \left(\alpha^2 + \beta^2\right) \tag{3.11}$$

The minimum of this function is the position of maximum modulation, and therefore is equal to P_1 (or P_2 if $P \approx P_s + \pi/2$). This is determined by fitting the residual data to a quadratic function and calculating the minimum. P_s is then calculated from:[217]

$$P_s = P_1 - \left(\frac{\gamma_A \tan\Psi + \gamma_P \cos\Delta}{\sin\Delta}\right)\Bigg|_{P \equiv P_1} \tag{3.12a}$$

$$P_s = P_2 - \left(\frac{\gamma_A \cot\Psi + \gamma_P \cos\Delta}{\sin\Delta}\right)\Bigg|_{P \equiv P_s + \pi/2} \tag{3.12b}$$

Then, A_1 and A_2 are calculated. This is done by fitting the "phase function," $\Theta(P)$, to a line and evaluating it at P_1 and $P_2 + \pi/2$:[217]

$$\Theta(P) = A_1 = \frac{1}{2}\tan^{-1}\left(\frac{\beta}{\alpha}\right)\Bigg|_{P = P_1} \tag{3.13a}$$

$$\Theta(P) = A_2 = \frac{1}{2}\tan^{-1}\left(\frac{\beta}{\alpha}\right)\Bigg|_{P = P_2 + \pi/2} \tag{3.13b}$$

Finally, A_s is calculated from:

$$A_s = A_1 - \left(\frac{\gamma_P \cot\Psi + \gamma_A \cos\Delta}{\sin\Delta}\right) \tag{3.14a}$$

$$A_s = A_2 - \left(\frac{\gamma_P \tan\Psi + \gamma_A \cos\Delta}{\sin\Delta}\right) \tag{3.14b}$$

In the above equations, the optical activity of the polarizer and analyzer can, in principle, be found from:[217]

$$\gamma_A = \left[(A_1 - A_2)\cos\Delta - (P_1 - P_2)\cos 2\Psi\right]/D_1 \tag{3.15a}$$

$$\gamma_P = \left[(P_1 - P_2)\cos\Delta - (A_1 - A_2)\csc 2\Psi\right]/D_1 \tag{3.15b}$$

where

$$D_1 = 2\left(\cos^2\Delta - \csc^2 2\Psi\right) \tag{3.15c}$$

In practice, due to the relatively large scatter in the measured optical activity coefficients for the polarizer and analyzer, these values are fixed to the known values for quartz ($\gamma_i \approx 0.01 \times E(\mathrm{eV})$[218]). The calculated γ_A and γ_P are used as an additional check on the quality of the sample alignment and system alignment during calibration.

The procedure for this calibration is first, to align a highly absorbing gold sample in the system at a 70° angle of incidence. Δ and Ψ data are then collected on this sample at 500 nm. Next, the polarizer is stepped from about 5° - 10° below zero to 5° - 10° above zero, in steps of ≈0.1°. Residual function data are calculated for each point and then the entire curve is fitted to a quadratic equation. A similar procedure is then completed for values of the polarizer near 90°. The minima of the two residual functions correspond to P_1 and P_2, respectively. Once A_s and P_s are calculated for $P \approx 0°$ and $P \approx 90°$, the values are averaged to improve the accuracy.

Finally, the eta (η) calibration accounts for the fact that the α and β coefficients are obtained from the signal voltage at the input to the analog/digital converter, not the actual intensity. The ac component of the signal voltage is attenuated and phase-shifted relative to that of the actual intensity by the transfer characteristics of the signal processing circuit.[219] In addition, this attenuation is different as the voltage applied to the photomultiplier tube is changed. Chindaudom[220] demonstrated that η can be described as a linear function of the PMT voltage. The calibration is done by inserting a neutral density filter into the system, with the system in the straight through configuration (90° angle of incidence). The α and β coefficients are then calculated and used to find η by:

$$\eta = \frac{1}{\sqrt{\alpha^2 + \beta^2}} \tag{3.16}$$

Then, by rotating the neutral density filter, the intensity of the light incident on the PMT can be changed, hence changing the voltage applied to the PMT. η can then be calculated for various voltages and subsequently fit to a linear function with respect to the PMT voltage. During measurements, calculated η values are used to correct the experimental Δ and Ψ values. Equation 3.8 is modified to the following for the η correction:

$$I = I_o[1 + \eta\alpha\cos 2A + \eta\beta\sin 2A] \tag{3.17}$$

3.3.2 Obtaining *Ex situ* SE Data

Once all of the calibrations were completed, the sample was placed on a vacuum mount in the path of the beam (or mounted to the heater block for high temperature measurements). The angle of incidence was set, typically at 70° for absorbing materials and 80° for transparent materials. The sample was then aligned by rotating it around the x and y-directions and translating it in the z-direction. Alignment was completed by using a telescope, which looked into a mirror that diverted the light beam from the detector to the operator's eye. By focusing the telescope to different locations on the light beam, different images could be viewed. These views were centered in the image to align the sample. Final adjustments were made using an alignment program on the computer. Here, successive optical cycles were compared and adjustments to the alignment were made until differences between successive cycles were minimized. Differences on the order of ≤ 20 for each point and an average of ≤ 10 were desired for an acceptable alignment. Since the intensities were read by a 16 bit A/D converter, these differences were out of a maximum intensity reading of 65,536 (2^{16}).

Finally, the monochromator was set to 250 nm and the computer was programmed to take data at 5nm increments up to 750 nm. For each rotation of the analyzer the reflected light intensity was measured at 90 points. To minimize scatter in the data, 50 mechanical cycles were averaged at each wavelength. Also, at each wavelength the beam was blocked using the shutter and a background spectrum was obtained. This spectrum was then subtracted from the raw data prior to calculation of the ellipsometric angles. The computer then converted the corrected measured intensity data to the ellipsometric angles, Δ and Ψ, as a function of wavelength as described above. The entire measurement takes approximately 8 minutes.

3.3.3 *Ex situ* SE on Transparent Materials

The parameter Δ can be thought of as the difference between the phase shifts of the parallel and perpendicular components of the light upon reflection from a surface. For light reflected from a transparent material there will be a near zero phase shift, thus Δ

will be near 0° or 180°. De Nijs and van Silfhout[221] showed that in rotating analyzer ellipsometry (RAE), the experimental errors are proportional to 1/sinΔ. Thus, in measuring transparent materials using RAE, the errors can be significant. Chindaudom[220] overcame this problem by inserting an achromatic compensator into the RAE system, located after the polarizer and before the sample. In doing so, a phase retardation of ≈ 90° is imparted to the incident light so that it is nearly circularly polarized. There is still little change in Δ after reflection from the transparent material, however in this case Δ is near 90° and the error is significantly reduced.

The procedure used to measure transparent materials involved obtaining two sets of SE spectra. First, SE data were obtained without the sample and with the ellipsometer in the straight-through configuration (90° angle of incidence). This allowed the exact phase shift of the compensator to be measured as a function of wavelength.[220] Subsequently, data were obtained with the sample in place at an angle of incidence equal to 80°. Finally, Δ and Ψ for the sample were calculated from:[220]

$$\tan\Psi e^{i\Delta} = \frac{\tan\Psi_{cs} e^{i\Delta_{cs}}}{\tan\Psi_{c} e^{i\Delta_{c}}} \qquad (3.18)$$

where the subscript c refers to the straight-through measurement and cs refers to the measurement with the sample in place.

3.4 Real-Time Spectroscopic Ellipsometry (RTSE)

Ex situ ellipsometry has proven to be very useful throughout the past 25 years. Recently this technique has been modified for use as a real-time characterization method.

That is, instead of measuring spectra one wavelength at a time, the entire measurement can be completed in as little as 32 ms due to the adaptation of multichannel detectors to SE.[117,118,120,222] Thus, fully parallel operation has been achieved and is now being exploited for determination of the microstructure and optical properties of thin films while they are being deposited.[112,119]

The configuration of the real-time spectroscopic ellipsometer (RTSE) used in this work is shown in Figure 3.5. It is a rotating polarizer-sample-fixed analyzer ($P_{rot}SA$) configuration. This system was constructed specifically for an EPI 930 MBE system. Many of the components in this system are similar to those of the system described above, however they are positioned in different locations along the optical path. By placing the spectrograph (monochromator) after the optical elements (and before the detector), background light from the deposition chamber can be eliminated from affecting the measurement. There is background light in the chamber, but it is not focused onto the end of the optical fiber and thus does not affect the measurement. However, by placing the spectrograph in this location, the rotating element can no longer be the analyzer. This is due to the dependence of the spectrograph throughput on the polarization state of the incident light. Thus, the polarizer is made the rotating element and the analyzer is fixed. With a rotating polarizer instrument, inherent polarization of the light source can be a problem. This effect can be minimized by careful alignment of the lamp when it is installed. Table 3.1 is a listing of the individual components of the RTSE. Drawings for all of the custom designed components are given in Appendix A. Fig. 3.6 shows pictures of the input and output arms of the system, indicating various components described in the schematic of Fig. 3.5.

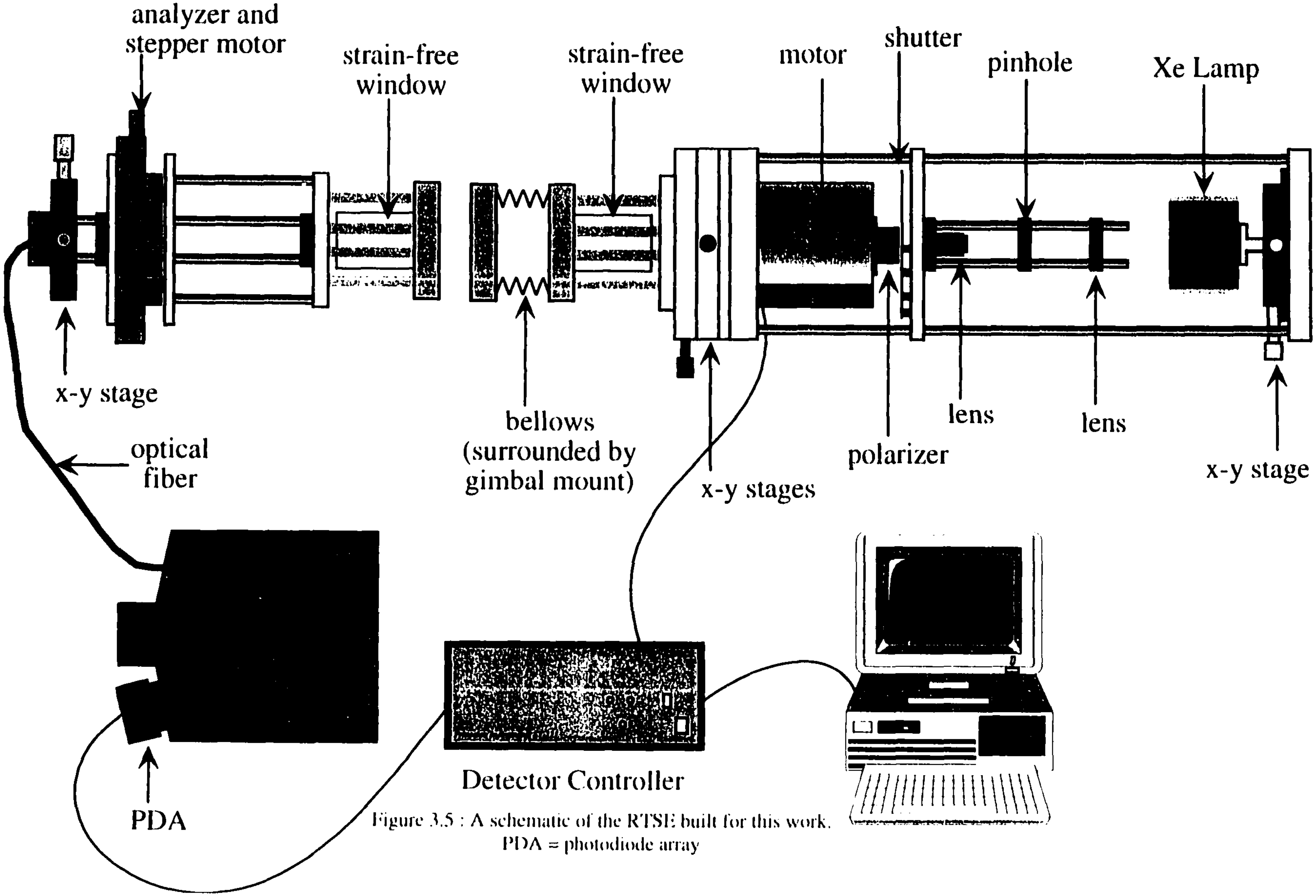

Figure 3.5 : A schematic of the RTSE built for this work. PDA = photodiode array

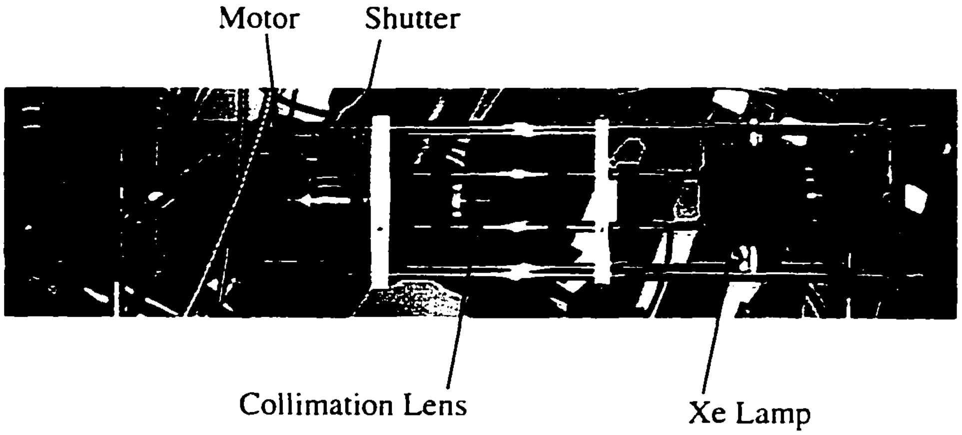

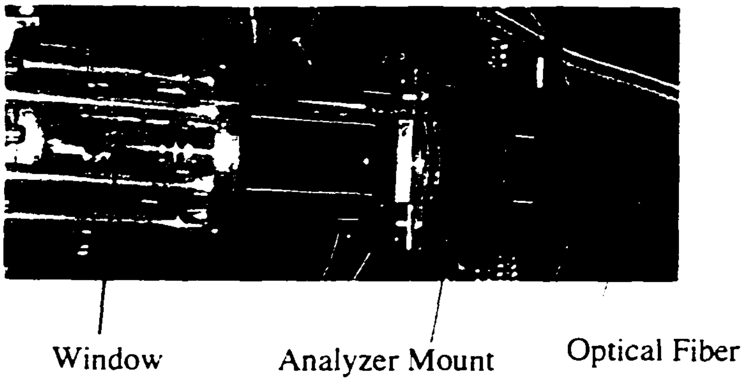

Figure 3.6 : Pictures of the input and output arms of the RTSE, indicating various components shown in Fig. 3.5.

Table 3.1: Components for the RTSE

[illegible]	[illegible]	[illegible]
Xe lamp	Hamamatsu Corp. • Bridgewater, NJ	Provides good output from 250 nm - 750 nm Model #'s E2419, C4262, C4251
Collimating lens	Optics for Research • Caldwell, NJ	UV achromat - #LMU-5X-U
Shutter	Vincent Associates • Rochester, NY	Maximum operating frequency = 40 Hz, model VS-25 with D122 controller
Polarizer and Analyzer	Zeta International Corp. • Mt. Prospect, IL	UV Glan-Taylor calcite with round mounting tube TY-EL-12
Motor	Airex Corp. • Dover, NH	Custom designed slotless motor with electronics and modified power supply
Strain-free windows	Bomco, Inc. • Gloucester, MA	2.75 in. flange mounted with proprietary seal[223] #B5935
Gimbal mount	MDC • Hayward, CA	Not shown in drawing, mates input arm to chamber (surrounds bellows) #676001
Analyzer mount	Oriel • Stratford, CT	Stepper motor controlled rotating mount- #13049, controller-#20025 resolution = 0.02°
Optical fibers	Fiberguide Industries • Stirling, NJ	600 μm core superguide MG- silica core, numerical aperture = 0.12±0.02 (≈f/4)
Spectrograph	SPEX • Edison, NJ	Model 270M, 0.27 meter, f/4 with dual exit ports, 1200 and 147 groove/mm gratings
Detector	Princeton Instruments • Trenton, NJ	PDA-1024 w/ ST-121 controller; 16 bit resolution, dynamic link libraries for interfacing
Control computer	Gateway 2000 • N. Sioux City, SD	200 MHz G6 Pentium
Optic mounts	Spindler & Hoyer • Milford, MA Newport • Irvine, CA Thorlabs • Newton, NJ Custom built • Eng. Shop Services, PSU	Purchased items include x-y stages, lens holders, pinholes, diaphragms Custom items were designed by the author and include all of the mounting plates, window modifications and polarizer and analyzer holders (see Appendix A)

White light with a spectral range from the near-UV to the near-IR is generated by the Xe arc lamp and focused onto a 1 mm pinhole. The light is then sent through a UV achromat and linearly polarized by the rotating polarizer. The polarizer and analyzer in this system are Glan-Taylor prisms, as opposed to the quartz rochon type used in the *ex situ* SE. The Glan-Taylor polarizer does not exhibit any optical activity effects. Thus, the optical activity coefficients, γ_A and γ_P, described in the previous section may be ignored.

After passing through the fixed analyzer, the beam is focused onto a 0.6 mm diameter optical fiber and subsequently mated to a f/4 spectrograph. Collimation optics were not required to match the f number of the fiber to that of the spectrograph because a ≈f/4 fiber was used. In addition, the fiber was directly coupled to the entrance slit with a x-y positioner. The spectrograph has two exit ports, one designed for a linear photodiode array (PDA) and one designed for a photomultiplier tube. At the exit port for the PDA, the spectrograph generates a flat focal plane (25mm wide) where the detector is placed. The detector is a 1024 element PDA and each element is 25 μm x 2.5 mm. Also, the detector has a saturation count level of 2^{16} and single-pixel and full-array read times of 5 μs and 5 ms, respectively.[224]

For a grating-based spectrograph, as opposed to a prism-based spectrograph, each pixel in an equally spaced linear array provides the same resolution in wavelength space. However, in photon energy space, this leads to a poorer resolution at high photon energies. The grating used for real-time studies in this work has 147 grooves/mm and is blazed at 300 nm. This results in a linear dispersion across the PDA of 23.6 nm/mm. Since each pixel is 25 μm across, a resolution of 0.59 nm/pixel is obtained when limited by pixel width. In terms of photon energy, this leads to a resolution of 0.001 eV at 1.5 eV, 0.004 eV at 3 eV and 0.009 eV at 4.5 eV. However, the width of the entrance slit also influences the resolution of the instrument. For a width of 0.15 mm, the resolution is 3.5 nm; for a width of 0.25 mm, the resolution decreases to 5.9 nm. Thus, in terms of photon energy, for a width of 0.25 mm (and 0.15 mm), the resolution is 0.011 eV (0.006 eV) at 1.5 eV, 0.042 eV (0.025 eV) at 3 eV and 0.094 eV (0.056 eV) at 4.5 eV.

Therefore, the resolution of the system is limited by the entrance slit width, which can be varied in steps of 2 μm. Slit widths of 0.15 – 0.25 mm were used here, depending on the sample. These values also dictate the number of adjacent pixels which should be averaged for the measurements (pixel grouping). For the case of a 0.15 mm slit width, since the resolution is limited to 3.5 nm and the pixels see 0.59 nm each, the pixels should be grouped by six.

Unlike a PMT, the PDA is an integrating detector. Therefore, the data acquisition speed of the instrument (determined by the rotational frequency of the polarizer) is directly limited by the time that it takes to read out the array. As will be discussed below, the array must be read out 10 times during one mechanical rotation of the polarizer. For the PDA used in this work, the minimum readout time is 5 ms. Thus, the maximum polarizer rotation frequency is:

$$f_{\max} = \frac{1}{2nt_r} \qquad (3.19)$$

Where $2n$ is the number of times the array must be read per polarizer rotation and t_r is the minimum readout time of the array. f_{max} for this system is 20 Hz. The motor used here can rotate at frequencies of 14.64 Hz, 15.51 Hz, 15.98 Hz and 16.49 Hz. As the rotational frequency approaches f_{max}, the exposure time of the PDA is correspondingly reduced and thus the signal-to-noise (S/N) ratio decreases.

For an integrating detector, a different approach is required to calculate α and β from the raw data. For this type of analysis, equation 3.8 is modified to:

$$I(P') = I_o\left[1 + \alpha'_k \cos 2P' + \beta'_k \sin 2P' + \alpha'_{4k} \cos 4P' + \beta'_{4k} \sin 4P'\right] \qquad (3.20)$$

Where α_4 and β_4 are the 4ω Fourier coefficients whose value give an indication of the non-ideality in the system (i.e. source polarization, window effects, etc.).[112] The subscript k refers to each pixel. For an integrating detector, the conventional Fourier analysis method cannot be applied to extract the normalized Fourier coefficients. Instead, Hadamard summation is used. For this case, the accumulated irradiance at the photodiode array over each of 5 equal time periods (or slices) during a single optical cycle of the polarizer is integrated. There are two optical cycles for every mechanical cycle of the polarizer; thus the array is read 10 times per revolution. The readout is triggered by an optical encoder on the rotating motor shaft. Again, there are two outputs from the encoder; a 1/revolution and a 10/revolution pulse. The 1/revolution pulse ensures that data collection always begins on the same 10/revolution pulse. These 5 integrals provide enough information to determine the four normalized Fourier coefficients, as well as Δ and Ψ.

The integrated intensity per slice, known as S_j, is given by:[121]

$$S_j = \int_{\frac{j-1}{5}\pi}^{\frac{j}{5}\pi} I(P')dP', \qquad j = 1,\ldots,5 \tag{3.21}$$

where $I(P')$ is given in equation 3.19. These integrals represent the counts collected over a π/5 rotation of the polarizer. However, they do not account for the fact that the position of the polarizer is changing as each pixel is read out. That is, the polarizer phase angle (P_s) varies linearly as a function of pixel number with a slope equal to the time it takes to read a pixel (δt) times the frequency of rotation (ω). The polarizer position at which pixel k starts its optical cycle is P_{sk}. Thus, the Fourier coefficients that are determined experimentally (α', β', α_4', β_4') have to be rotationally transformed by the correct polarizer phase angle (P_{sk}) prior to calculation of Δ and Ψ.

Therefore, after substituting equation 3.20 into equation 3.21 and integrating, the following equations are obtained in order to calculate the experimental Fourier coefficients from the raw data (S_j):[121]

$$\alpha' = 0.5344797 + \frac{1.195133(S_1 - S_2 - S_4 + S_5) - 2.672398(S_3)}{\pi I_o} \tag{3.22a}$$

$$\beta' = \frac{1.2566371(S_1 - S_5) - 2.0332815(S_2 - S_4)}{\pi I_o} \tag{3.22b}$$

$$\alpha_4' = \frac{0.8166123(S_1 + S_5) - 2.1379187(S_2 + S_4) + 2.6426128(S_3)}{\pi I_o} \tag{3.22c}$$

$$\beta_4' = \frac{2.5132741(S_1 - S_5) - 1.5532888(S_2 - S_4)}{\pi I_o} \tag{3.22d}$$

$$\pi I_o = S_1 + S_2 + S_3 + S_4 + S_5 \tag{3.22e}$$

Finally, the experimental Fourier coefficients were transformed according to:[121]

$$\begin{bmatrix} \alpha_k \\ \beta_k \end{bmatrix} = \begin{bmatrix} \cos 2P_{sk} & \sin 2P_{sk} \\ -\sin 2P_{sk} & \cos 2P_{sk} \end{bmatrix} \begin{bmatrix} \alpha_k' \\ \beta_k' \end{bmatrix} \tag{3.23a}$$

$$\begin{bmatrix} \alpha_{4k} \\ \beta_{4k} \end{bmatrix} = \begin{bmatrix} \cos 4P_{sk} & \sin 4P_{sk} \\ -\sin 4P_{sk} & \cos 4P_{sk} \end{bmatrix} \begin{bmatrix} \alpha_{4k}' \\ \beta_{4k}' \end{bmatrix} \tag{3.23b}$$

in order to correct for the polarizer rotation. Then, Δ and Ψ can be calculated as described in section 3.3.

A byproduct of this measurement is the ability to measure the reflectance of the depositing film. The dc component of the intensity is inherently measured as the summation of the intensities for the five slices of a given pixel. The measurement entails obtaining a reference spectrum from the substrate prior to growth for calculation of the Fresnel reflection coefficients of the substrate. From there, the reflectance of the growing film can be calculated.

3.4.1 RTSE Alignment and Calibration

The alignment of the RTSE components is extremely important in order to obtain reliable and reproducible data. Unfortunately, as opposed to other SE systems, there is no way to obtain a straight through (90° angle of incidence) configuration while the system is mounted onto the deposition chamber. Thus, a benchtop mount was constructed in order to align all of the components along the optical path and subsequently the ellipsometer was mounted to the chamber. First, a HeNe laser was placed in the lamp position for alignment of the analyzer and the polarizer. Each element was rotated and adjusted while observing the laser spot on a piece of paper located ≈3 m away. The prisms were adjusted until the wobbling of the spot during rotation was minimized. Next, the laser was removed and the lamp was inserted, along with the collimation optics. The lamp was aligned to follow the same optical path as the laser beam. Then, the optical fiber was connected to the coupler after the analyzer. The other end of the fiber was connected to the xy-stage mounted to the entrance slit of the spectrograph. At this point, the detector was attached to the spectrograph and the Xe spectra could be observed on the control computer using the WINSPEC program (shipped with the detector). The detector was aligned with the focal plane of the spectrograph by translation and rotation while observing the spectra until the signal was maximized and the spectral features became sharp. Finally, the xy-stages of the fiber coupler and the entrance slit were iteratively adjusted until the signal was maximized.

The strain-free windows were then attached to the deposition chamber. On the input side of the RTSE, a bellows was placed between the window and the flange. This allowed a gimbal mount to be placed around the bellows; thus the input arm was adjustable for sample alignment purposes. Last, the ellipsometer was mounted to the windows.

As was the case for *ex situ* SE, calibrations for the exact position of the polarizer and analyzer with respect to the plane of incidence (set by the sample) are critical. In addition to the residual calibration[217] described above, two other methods exist for calculation of A_s and P_{sk}. The first of these is the phase calibration method developed by De Nijs *et al.*[225] From inspection of equation 3.12, it can be seen that as $|\Delta|$ approaches 0° or 180°, the precision with which A_s (P_s in the case of PSA_{rot}) can be determined using the residual calibration decreases significantly. Thus, De Nijs proposed a procedure which is purported to be superior to the residual calibration when $|\Delta| < 30°$ and $|\Delta| > 150°$. The second method is known as the intensity calibration, and is based on the measurement of the dc component of the flux incident upon the detector (I_o). This method was developed by An,[120] and it has been shown that the Δ dependence exhibited by the other methods is absent for this calibration. Before discussion of these two methods, there is some additional information that must be introduced regarding the residual calibration and its application to the RTSE system.

Residual Calibration

The most significant difference in utilizing the residual calibration for RTSE is that the calibration is done spectroscopically. In this case, A_s and $P_s(k)$ are determined for each pixel (250 nm – 800 nm), thus statistical averaging can be used to improve the results. Also, as mentioned previously, the polarizer starting angle for each pixel is a function of the pixel number due to the rotation of the polarizer as the array is being read.

As described above, the procedure for the residual calibration involves measuring α and β at a range (typically ± 4°) of analyzer angles near $A_s(k)$ (where k is the pixel number). Then, $A_s(k)$ is calculated from the minimum in the parabolic function fit to R(A). Again, for this system there are no optical activity effects associated with the polarizing optics. The polarizer starting angle, $P_s(k)$, is found from the linear fit to the phase function ($\Theta(A,k)$ from eqs. 3.13) evaluated at $A = A_s(k)$. The value of A_s used in the calculation of Δ and Ψ is determined from:

$$A_s = \left(\frac{1}{N}\right)\sum_{k=1}^{N} A_s(k) \tag{3.24}$$

where N is the number of pixels. In practice, N can be limited such that uncertainty related to the value of Δ is minimized. For the case of Si at an 80° angle of incidence, pixels corresponding to 265 nm $\leq \lambda \leq$ 435 nm were used. Also, it is clear that $P_s(k)$ must be a linear function of the pixel number, k. This, then, was fit to the linear function:

$$P_s(k) = mk + P_o \tag{3.25}$$

where the slope is equal to the change in polarizer angle in the time that it takes to read a single pixel. For this system, the value is 0.026° at 14.64 Hz. This measurement was used to check the stability of the motor and the quality of the calibration from run to run.

Phase Calibration

The phase calibration involves measurement of the phase function (eqs. 3.13) in two different zones: near A = 0 and $\pi/2$. By measuring in two zones, the phase difference function can be obtained:[225]

$$\Phi(A,k) = \Theta(A - A_s,k) - \Theta(A - A_s + {}^{\pi}\!/_{2},k) \tag{3.26}$$

This can be approximated by:

$$\Phi(A,k) = (2\cos 2\Psi \cos\Delta)(A - A_s) \qquad |A - A_s| << 1 \tag{3.27}$$

where A_s is the A-axis intercept of the linear fit to this function for each pixel. $P_s(k)$ is determined in the same manner as in the residual calibration, with evaluation of the phase function at A_s. Inspection of equation 3.26 indicates that this calibration method will fail as $|\Delta|$ approaches $\pi/2$ or $|\Psi|$ approaches $\pi/4$. Thus, it is complementary to the residual calibration and the two methods may be combined for different spectral regions when calibrating for a sample which may have $0° < \Delta < 180°$ across the wavelength range.

Intensity Calibration

It can be shown[120] that the dc component of the incident light on the detector (I_o) is a symmetric function of the analyzer angle, A, about A_s. Using this, $I_o(A,k)$ for a range of analyzer angles around A_s (typically ± 4°) can be fit to a simple parabolic function of the form:

$$I_o(A,k) = a(A - A_s)^2 + b \qquad |A - A_s| << 1 \tag{3.28}$$

A_s is found by calculating the minimum of the fit. $P_s(k)$ is then determined by evaluating the phase function at $A = A_s$, as with the other methods. From equation 3.28, it is clear that this type of calibration does not contain the Δ dependence exhibited by the residual and phase calibrations. In addition, detector non-idealities (discussed below) do not influence this method. Generally, the intensity calibration was used for this work.

3.4.2 RTSE Detector Calibration

This section details the potential sources of error as a result of using the multichannel detection system. These sources of error include image persistence and detector nonlinearity. Detailed descriptions of the principles behind the calibrations to correct for these errors are given elsewhere.[116-118,120]

Image Persistence

The problem of image persistence is associated with the incomplete read-out of accumulated charge from individual pixels. This effect was characterized using a constant irradiance source. That is, the system was placed in the straight-through configuration with the polarization optics removed. Then, three successive spectra were obtained. The first spectrum was taken with the shutter open, the shutter was closed during the second exposure and kept closed for the entire last exposure.[117] The spectra were collected with the 147 groove/mm grating, an entrance slit width of 40 μm and an exposure time of 10 ms. Figure 3.7 shows the photon counts of the second and third spectra normalized to the first spectrum as a function of pixel group number. It can be

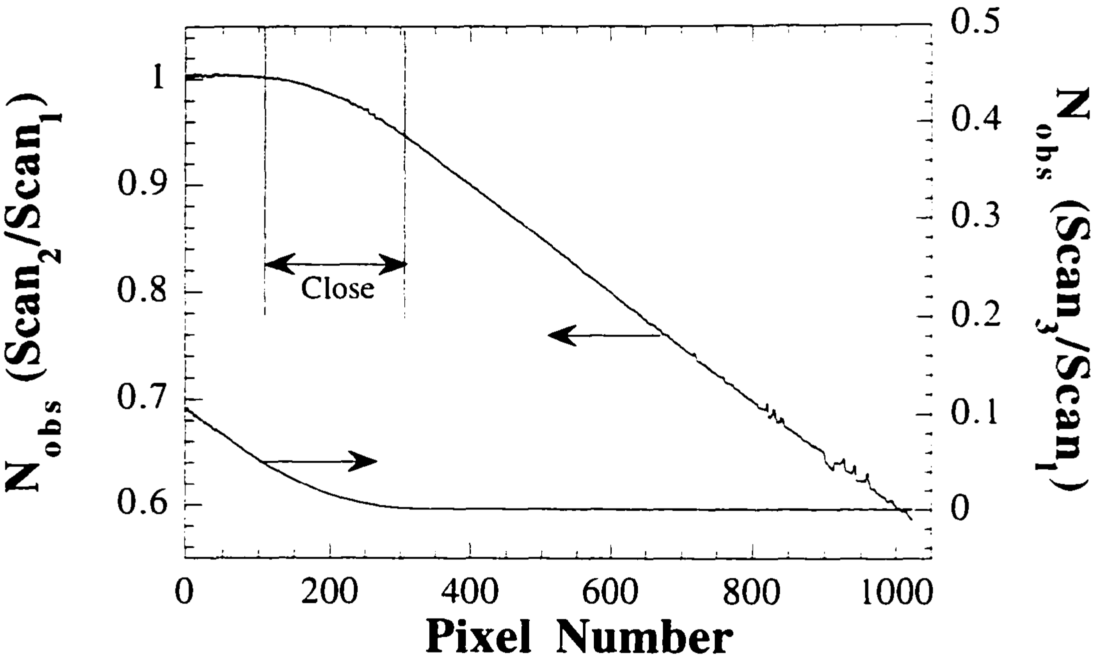

Figure 3.7 : Normalized photon counts for three successive exposures of the array. The shutter was closed during the second exposure and kept closed for the entire third exposure.

seen that the shutter was closed during the reading of pixel groups 100 – 300 of the second exposure. The linear behavior exhibited after the closing of the shutter, up to pixel number 300 of the third readout, indicates that for each successive pixel the shutter was closed for a linearly increasing fraction of the exposure time. For an ideal detector, the plateau at the end of the third exposure should read zero counts. However, this is not the case and these residual counts must be corrected for.

The image persistence level is plotted in Fig. 3.8, where the counts obtained on the plateau region for the third exposure are plotted against the counts obtained on the same pixels during the previous readout. A linear relationship is observed and by fitting the data, a correction factor of 0.09% is obtained. The correction takes the form of:[120]

$$S_{jk,c} = S_{jk,r} + \mathrm{C}_{\mathrm{IP}}\left(S_{jk,r}\right) - \mathrm{C}_{\mathrm{IP}}(S_{(j-1)k,r} \qquad (3.29)$$

Where $S_{jk,r}$ is the raw counts on pixel number k during slice j, $S_{jk,c}$ is the corrected data and C_{IP} is the correction factor determined from the curve fit shown in Fig. 3.8. The second term represents the counts that are not read out during the readout and the third term represents the counts which remain from the previous array readout. The level of image persistence shown by this system is significantly improved over previous RTSE systems.[120,121]

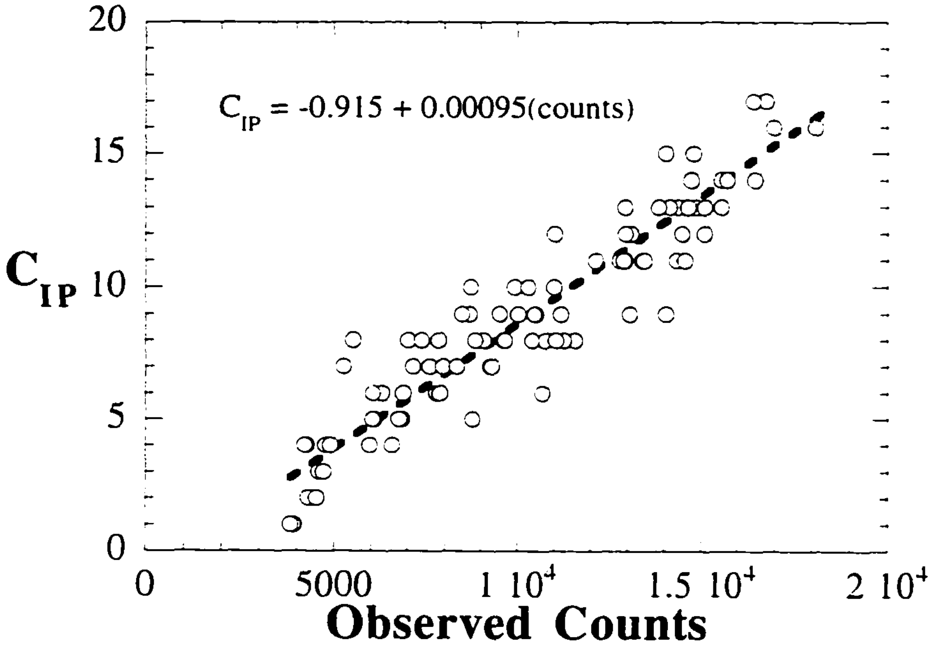

Figure 3.8 : Plot of image persistence level observed during the third exposure vs. counts observed on the second exposure. The curve fit gives the correction factor for the raw data.

Detector Nonlinearity

The nonlinear response of the detector was characterized with the system again in the straight-through position. The readout of the detector was set such that 50 exposures were taken successively with each exposure time increased by 5 ms over the previous readout (the exposure was set using the internal clock of the detector controller). The slit width and diaphragm were set such that the detector was not saturated for any of the pixels at the longest exposure time (55 ms). All of the spectra were corrected for background contributions by measuring at the same exposure times with the shutter blocking the beam. The results for the detector are shown in Fig. 3.9. It is clear that, as expected, the number of photon counts, N_{obs}, is a linear function of exposure time and is dependent on pixel number.

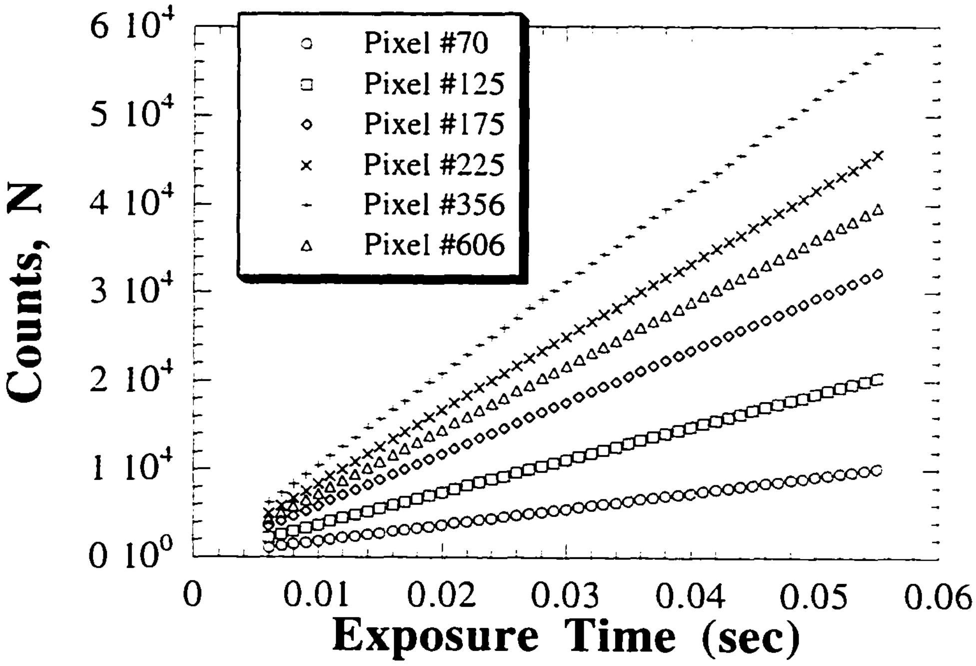

Figure 3.9 : Observed counts plotted against exposure time for 6 pixels across the photodiode array.

To increase the sensitivity to deviations from linear behavior, the data of Fig. 3.9 can be replotted as observed count rate vs. observed counts. These data are shown in Fig. 3.10 for the same six pixels. For a linear detector, the count rate should be independent of the total observed count for a given pixel.[120] From this figure, it is clear that the behavior of this detector is linear, and is significantly improved over previous RTSE systems. Thus, the correction for nonlinearity is not used in this system.

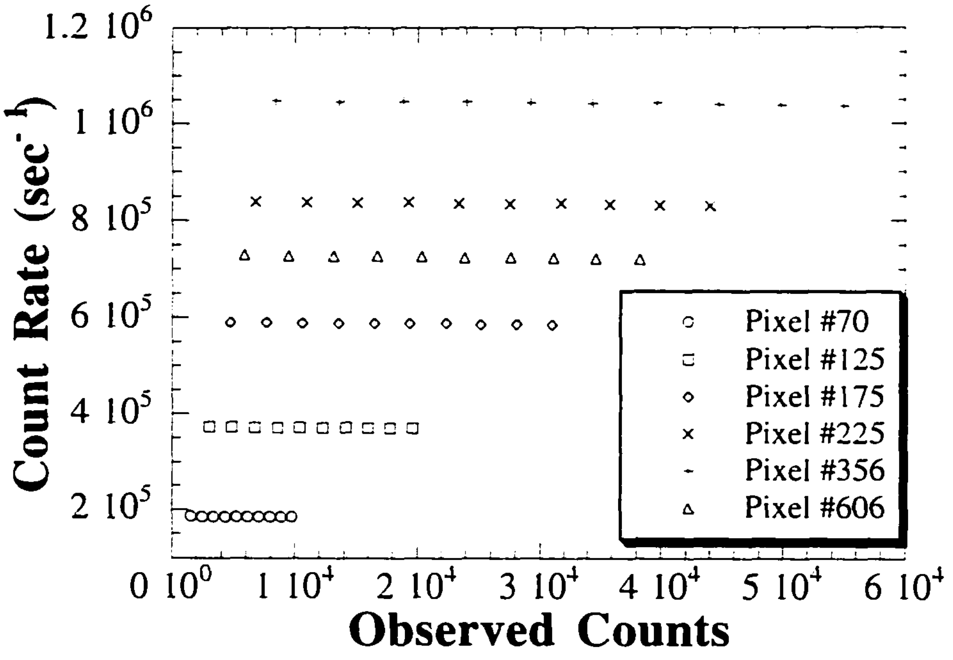

Figure 3.10 : Observed count rate plotted against total counts for 6 pixels.

A measure of the overall quality of the alignment of the optical components, as well as the calibrations for the detector nonidealities can be exhibited through plotting the residual function for the system in the straight-through configuration. This is shown in Fig. 3.11. It can be seen that the residual is within ±0.001 throughout the majority of the wavelength range, indicating excellent system alignment and detector calibration. Previous RTSE systems showed similar values, however calibrations for both nonlinearity and image persistence were necessary.

3.4.3 Obtaining RTSE Data

Once the ellipsometer was attached to the MBE and the detector was well characterized, real-time data collection could begin. First, the puck (with the substrate attached by silver paint) was loaded into the deposition chamber and mounted to the

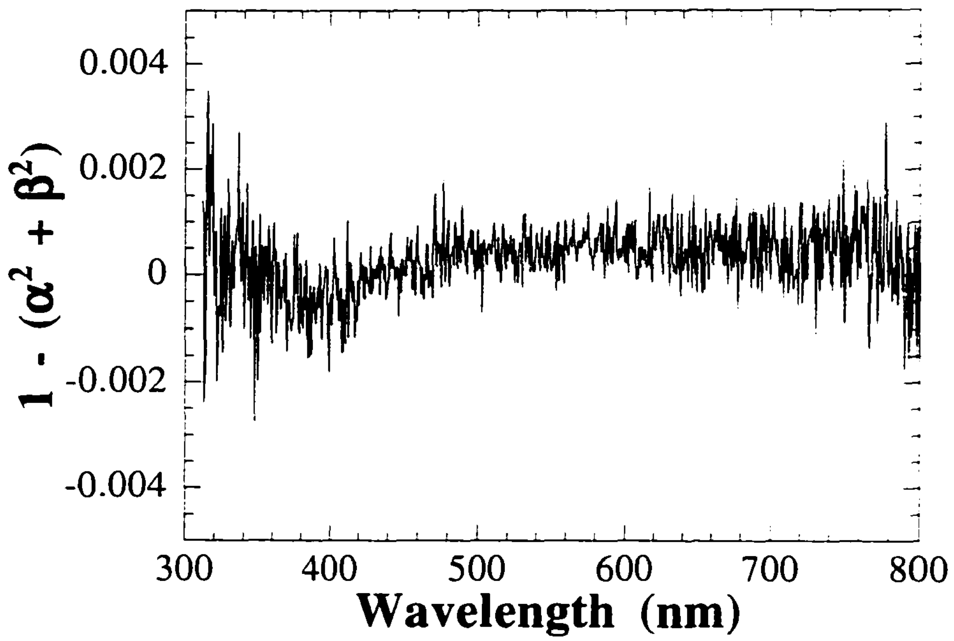

Figure 3.11 : Plot of the residual function for the RTSE in the straight-through configuration.

substrate rotator. Next, the azimuth of interest for RHEED observation was found. This set the position of the sample (and the plane of incidence) for the deposition. Then, the output arm of the ellipsometer was removed and a HeNe laser was put in its place such that the beam reflected off the sample and back along the input arm. This allowed for the input arm to be properly positioned with respect to the plane of incidence, which is set by the output arm and the sample. A sliding pinhole was placed on the arm and the arm was adjusted until the laser beam remained stationary on the pinhole as the pinhole was translated along the rails. Finally, the output arm was replaced and the system was calibrated prior to the onset of deposition.

Calibration of A_s and P_{sk} was completed via one of the methods described above (typically the intensity method). Subsequently, film deposition was initiated while real-time SE data were collected. The instructions for the RTSE software are given in Appendix B.

3.5 SE Data Modeling

Once the ellipsometric data were obtained, they were computer modeled. For unknown materials, the dielectric function, thickness, microstructure and optical properties can be determined. For known materials, the thickness and microstructure can be found. For materials with a well-characterized dielectric function vs. temperature response (i.e. Si), the temperature of the surface can be extracted. This analysis was done using programs developed by the spectroscopic ellipsometry group at the Materials Research Laboratory.[226] Details of the various modeling programs will be given as needed throughout the following chapters.

The basic premise of these programs is to model the film as a number of discrete layers (including the substrate as long as the film is optically thin), each with a specific thickness, density and wavelength dependent complex refractive index. Then, values of the ellipsometric parameters are calculated and compared to the experimental data using an unbiased estimator of error, σ, where:

$$\sigma = \frac{1}{N-P-1}\left[\sum_{i=1}^{N}\left(\cos\Delta'_{\text{exp}} - \cos\Delta'_{\text{cal}}\right)^2 + \left(\tan\Psi'_{\text{exp}} - \tan\Psi'_{\text{cal}}\right)^2\right]^{1/2} \tag{3.30}$$

Here, N is the number of data points taken (2 for each pixel) and P is the number of unknown variables in the model. A grid search of points is completed to find the point in parameter space with the minimum error function. The program then iterates around that point and a linear regression analysis is used to obtain the lowest error function for this geometry. The linear regression analysis also allows for the calculation of 90% confidence limits and an approximate Jacobian for the system. This shows any correlation between parameters. For modeling data from transparent materials, the error function is calculated using Δ and Ψ, not $\cos\Delta$ and $\tan\Psi$. This type of weighting function has been shown to be the most appropriate for analysis of transparent samples where the values of Δ are low.[220] It should be noted that for modeling of YBCO films, the optical anisotropy of the material was accounted for. This was done using code based on that developed by Parikh *et al.*[227] following the formalism of Yeh.[228,229]

The criteria for choosing the best fit were: 1) a good fit to the experimental data, 2) a low σ value (different for different samples), 3) a physically realistic model, 4) low correlation between parameters and 5) reasonable values for the 90% confidence limits.

3.6 Other Film Characterization

Several other characterization techniques were used for this work. For surface analysis, scanning tunneling microscopy (STM) and atomic force microscopy (AFM) were used (done at Los Alamos National Laboratory). Images were collected with a Digital Instruments, Inc. Nanoscope IIIa using a Multimode probe in tapping mode. That is, the cantilever is oscillating during data collection (typically at 300 kHz). In addition to these, optical micrographs taken with a Nomarski optical microscope were used to identify the presence of surface precipitates. For structural analysis, 4-circle x-ray diffraction (XRD) was used (done at Penn State). For compositional analysis, Rutherford backscattering spectroscopy (RBS) was used (done at the University of Arizona).

Chapter 4

REFERENCE DIELECTRIC FUNCTION DATA FOR COMMON YBCO SUBSTRATE MATERIALS

4.1 Introduction

Since the development and subsequent advancements in methods used to deposit high quality epitaxial thin films of YBCO, there has been a significant interest in the substrates used for these films. As described previously, there is a wide selection of substrates available that provide the necessary lattice match and chemical compatibility for deposition of YBCO films. However, there is little information regarding the optical properties of these materials. For SE to be useful as a characterization method for YBCO films on these substrates, it is necessary to have reference dielectric function data (ε_1 + $i\varepsilon_2$) for the individual materials in the sample of interest. As already mentioned, data for YBCO in the energy range of interest has been determined;[6] however data for common YBCO substrate materials is not as widespread.

Here, reference dielectric function data for five common YBCO substrate materials and one common reaction layer material were determined using *ex situ* SE. The substrates were: $LaAlO_3$ (LAO), $NdGaO_3$ (NGO), $(LaAlO_3)_{0.3}$-$(Sr_2AlTaO_6)_{0.7}$ (LSAT) supplied by Applied Technology Enterprises, Irmo, SC; $LaSrGaO_4$ (LSGO) from A. Dabkowski and H.A. Dabkowska, McMaster University; and 9.5 mol% Y_2O_3-ZrO_2 (YSZ) from Commercial Crystal Labs, Inc., Naples, FL. The reaction layer material was

$BaZrO_3$ (BZO) from Chang-Beom Eom, Duke University. It is known to form during deposition of YBCO on YSZ.[46-48]

4.2 Calculation of the Dielectric Functions

SE data were obtained as described in the previous chapter for transparent materials. That is, an achromatic compensator was inserted into the PSA_{rot} *ex situ* ellipsometer setup (see Fig. 3.4). The compensator is based on the design of King and Downs [230] and is made of vitreous silica with a coating of MgF_2. This is a three reflection quarter wave system that can produce an approximate 90° phase shift of the incident light over a wide wavelength range. Experimental data for the samples were corrected for the actual incident polarization state as described previously.[220]

Once the ellipsometric spectra were determined, the computer modeling program described in the previous chapter was used to develop a depth profile of the sample and to determine the optical properties of each material. In most cases, the sample was modeled as a layer of surface roughness on top of an infinite layer of bulk substrate material. A schematic of this geometry is shown in Fig. 4.1. The reference data for the $BaZrO_3$ were obtained from a thin film sample of $BaZrO_3$ deposited on YSZ. In this case, the model consisted of a layer of $BaZrO_3$ surface roughness on a layer of dense $BaZrO_3$ on the YSZ substrate. The surface roughness was modeled as a mixture of air and the material of interest using the Bruggeman effective medium approximation.[213,231] The refractive index as a function of wavelength ($n(\lambda)$) was modeled as a Sellmeier oscillator function, given by:

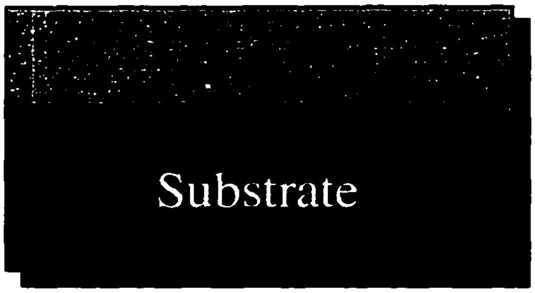

Figure 4.1 : Schematic of the model used to fit the SE data for YBCO substrates.

$$n^2 = 1.0 + \left[\frac{A\lambda^2}{\left(\lambda^2 - \lambda_o^2\right)}\right] \tag{4.1}$$

where n is the index of refraction, λ is the wavelength in nm and A and λ_o are the variables in the model which are related to the optical properties of the transparent material. For samples which exhibited absorption at higher energies, the data set was truncated so that the undamped Sellmeier oscillator would be a valid description of the data (no optical absorption in the material). The only additional variable in the model was the thickness of the surface roughness layer. The volume fraction of air in the surface layer was fixed to 50% for all of the models because the roughness layer thickness on these polished substrates is very low. Letting the volume fraction vary resulted in excessive correlation between variables.[220] For modeling of transparent materials, the weighting function used in the calculation of the unbiased estimator of the error (σ) was Δ and Ψ, rather than $\cos\Delta$ and $\tan\Psi$ as described previously. This weighting function has been shown to be the most appropriate for analysis of transparent samples where the values of Δ are low.[232]

With the depth profile and the Sellmeier constants of the material determined, it was possible to calculate the dielectric function ($\varepsilon_1 + i\varepsilon_2$) for the modeled wavelength range. When the data set was truncated, the higher energy dielectric function values were calculated using direct inversion of the ellipsometric data. It is important to emphasize here that these data were obtained while taking into account the surface roughness. In other methods where this inhomogeneity is not accounted for, the calculated data are subject to appreciable error. Specifically, anomalous values for the refractive index and the extinction coefficient can be obtained.[220]

The accuracy of the dielectric function data obtained by this method was checked by calculating data for a $SrTiO_3$ (from Commercial Crystal Labs, Inc., Naples, FL) substrate and comparing it to published data obtained by the angle of minimum deviation method.[233] Fig. 4.2 shows the excellent agreement between the two sets of data. The

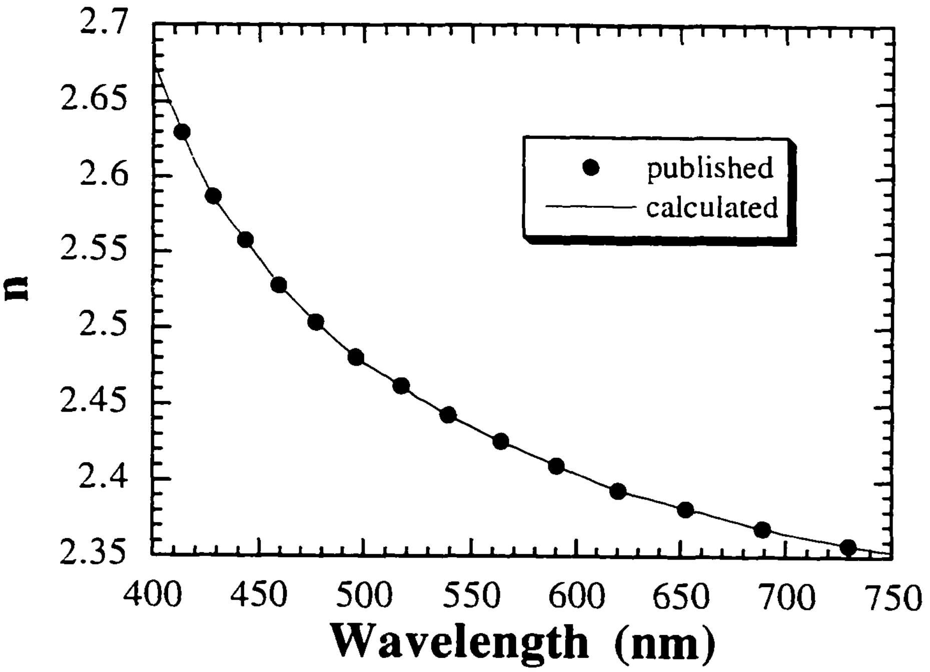

Figure 4.2 : Comparison of published dielectric function data to SE determined data for $SrTiO_3$.

values agree throughout this range to ± 0.001. Values below 400 nm cannot be directly compared because the available published data is obtained from measurements that do not account for the surface roughness.

Figure 4.3 shows the experimental and calculated Δ and Ψ spectra for YSZ. The difference between the two spectra is on the order of the accuracy of the instrument (± 0.01° for Ψ and ± 0.03° for Δ). The thickness of the surface roughness layer was determined to be 36 Å ± 0.2 Å. Figure 4.4 shows a similar plot of the measured and calculated ellipsometric parameters for $BaZrO_3$. Again, it is clear that the fit is very good. For this material, the data could only be modeled as a Sellmeier oscillator over the range of 400 nm – 750 nm. At shorter wavelengths, the $BaZrO_3$ begins to absorb the incident light. Thus, the assumption of a classical Sellmeier oscillator begins to break down. For the lower wavelength range, the experimental data were directly inverted (with the microstructure fixed to the values obtained from the model of the longer wavelength data) to obtain the complex dielectric function. The BZO film was found to be 1000 Å thick, including a 150 Å rough layer with 23% air.

Figures 4.5 – 4.8 show the Δ and Ψ fits for $LaAlO_3$, $NdGaO_3$, $(LaAlO_3)_{0.3}$-$(Sr_2AlTaO_6)_{0.7}$ and $LaSrGaO_4$. The quality of these fits is shown again by the excellent agreement between the measured and calculated spectra. The scatter in the data that is exhibited at longer wavelengths is due to the very low intensity of the reflected light. Table 4.1 lists the results of the SE modeling for each substrate material. The constants A and λ_0 from equation 4.1 are given along with the thicknesses of the surface roughness layer and the values of σ (all were on the order of the accuracy of the data). The value of

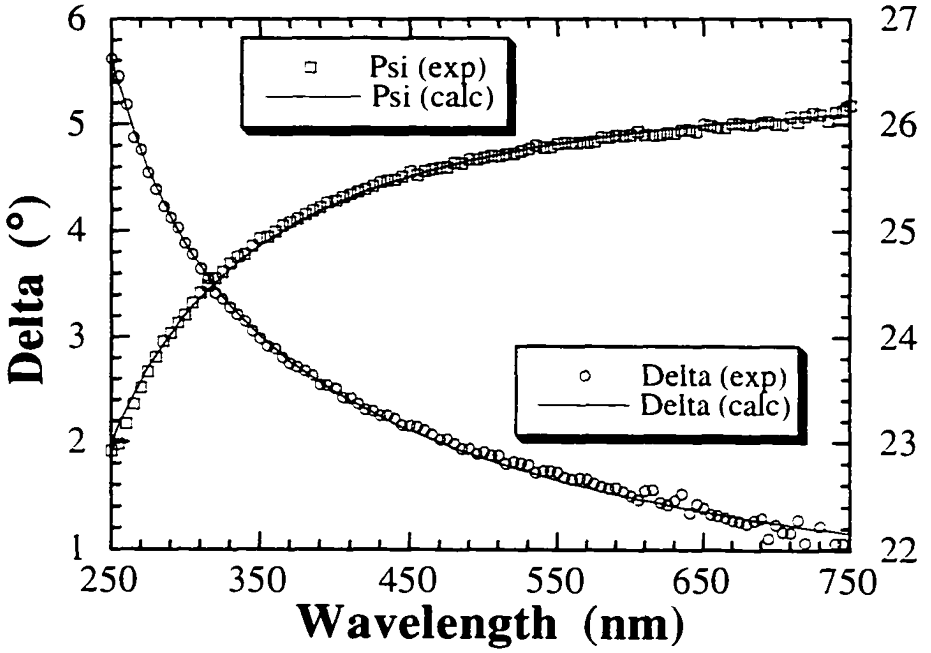

Figure 4.3 : Experimental and calculated Δ and Ψ data for 9.5 mol% Y_2O_3-ZrO_2.

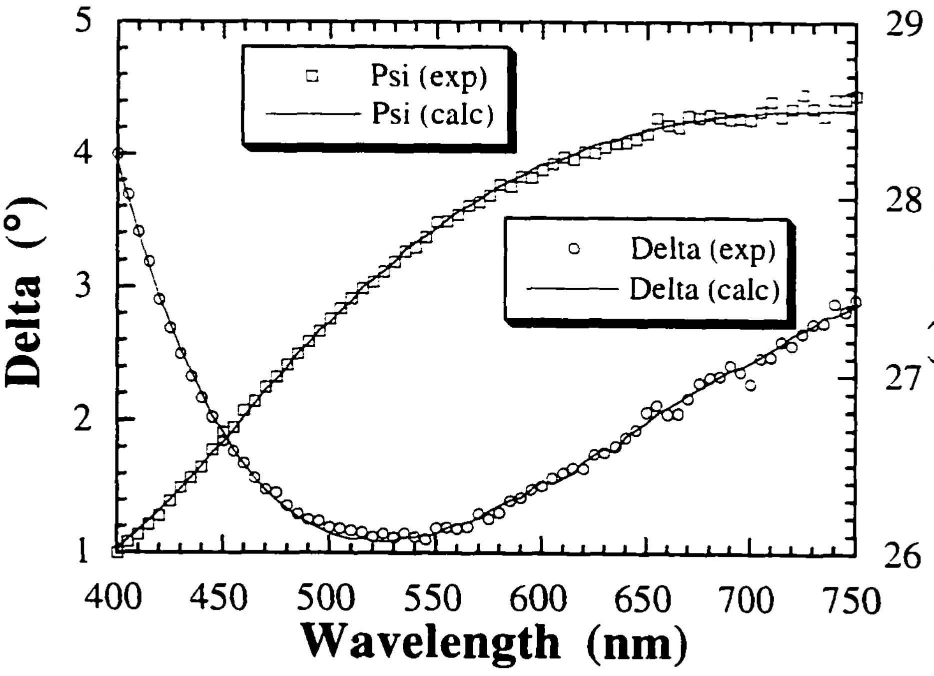

Figure 4.4 : Experimental and calculated Δ and Ψ data for a 1000 Å thick $BaZrO_3$ film on YSZ.

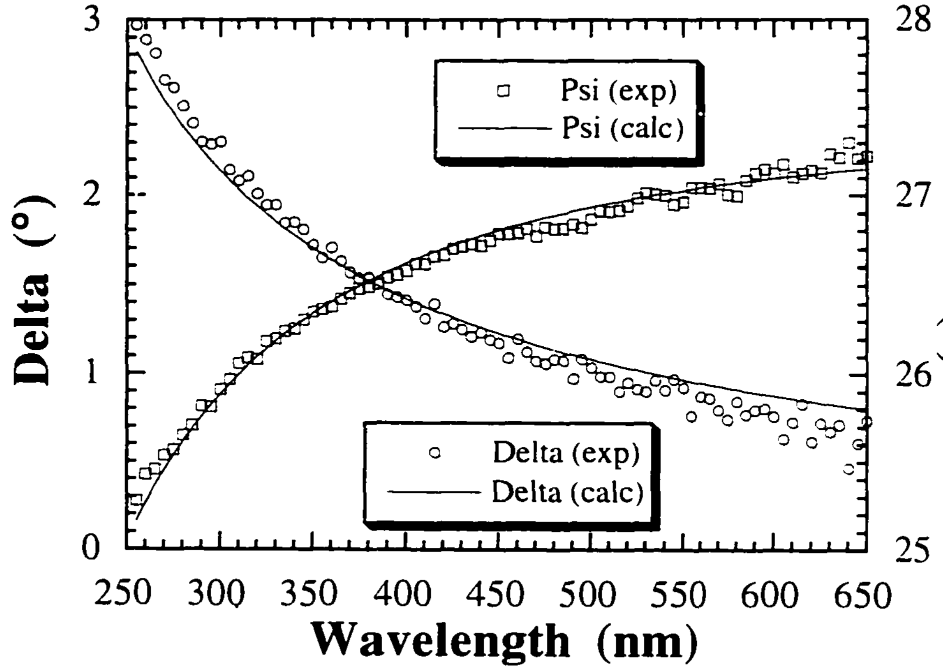

Figure 4.5 : Experimental and calculated Δ and Ψ data for $LaAlO_3$.

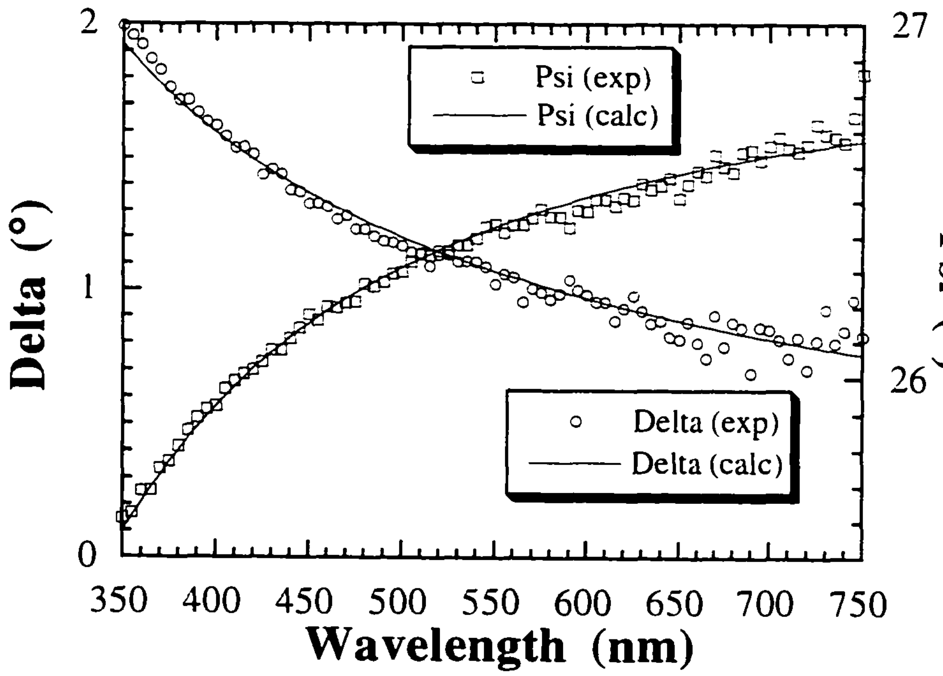

Figure 4.6 : Experimental and calculated Δ and Ψ data for $NdGaO_3$.

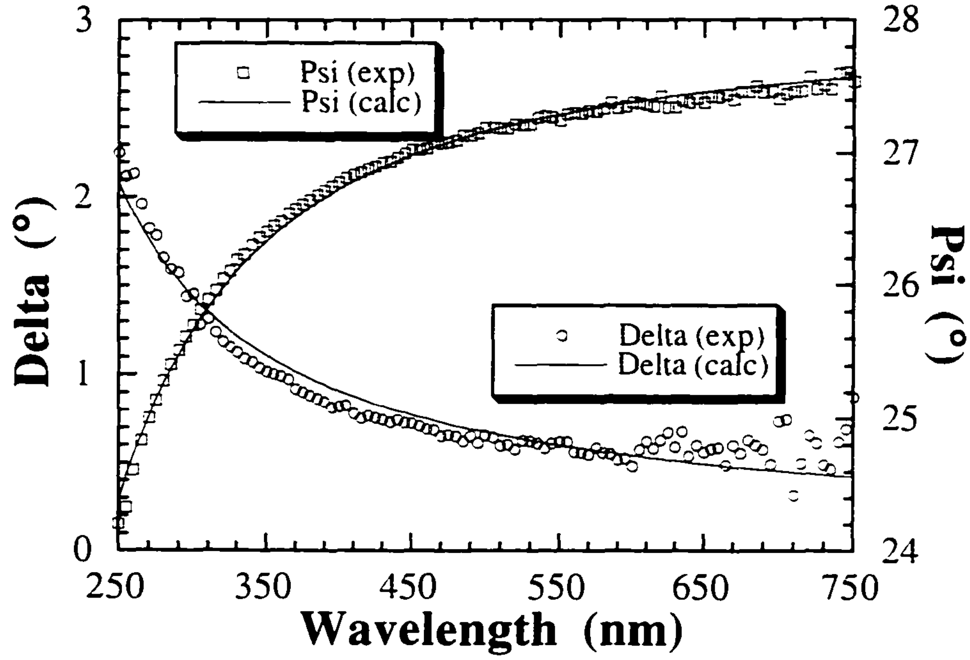

Figure 4.7 : Experimental and calculated Δ and Ψ data for $(LaAlO_3)_{0.3}$-$(Sr_2AlTaO_6)_{0.7}$.

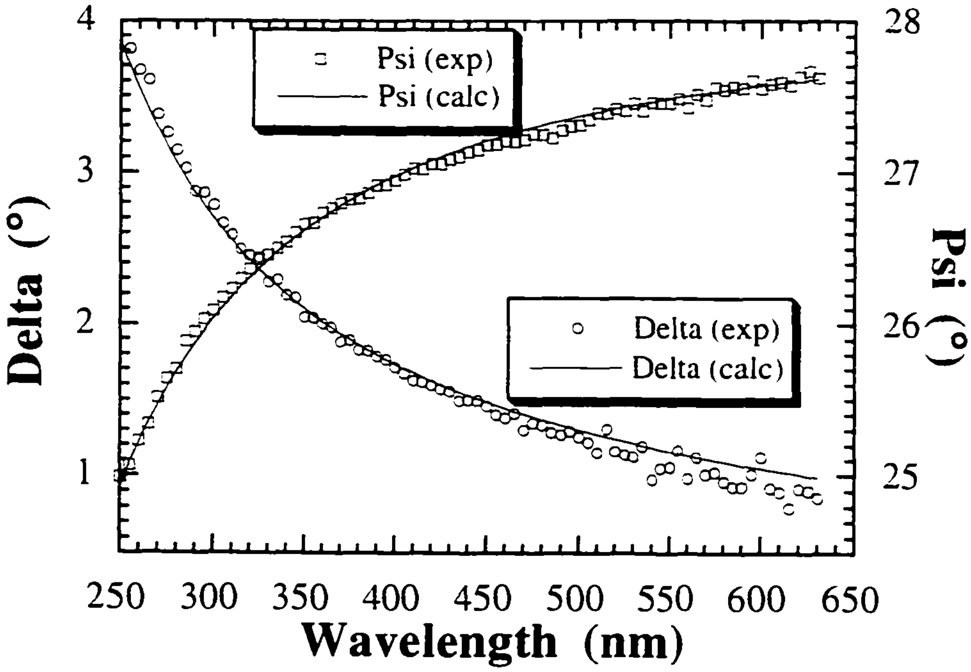

Figure 4.8 : Experimental and calculated Δ and Ψ data for $LaSrGaO_4$.

Table 4.1 : Values for the constants of the Sellmeier oscillator determined from modeling

Material	**A**	**λ_o (nm)**	**Surface Roughness (Å)**	**σ**
$LaAlO_3$	3.09 ± 0.01	125.5 ± 2.2	25 ± 0.4	0.12°
$BaZrO_3$	3.04 ± 0.01	159 ± 6	150 ± 5	0.06°
$NdGaO_3$	3.26 ± 0.01	140.2 ± 1.3	25 ± 0.3	0.11°
YSZ	3.50 ± 0.01	143.9 ± 0.8	36 ± 0.2	0.07°
LSAT	2.92 ± 0.01	144.9 ± 1.2	16 ± 0.3	0.08°
LSGO	2.88 ± 0.01	140.6 ± 1.4	33 ± 0.4	0.10°

λ_o is related to the natural frequency of the oscillator and A governs the magnitude of the refractive index over this particular wavelength range.

Finally, Fig. 4.9(a) is a plot of the real part of the dielectric function (ε_1) for all of the materials. Each curve was calculated using equation 4.1 and the Sellmeier constants determined from the SE data. The relationships between A and λ_o and the shape of the curve can be clearly visualized with this plot. As A increases, the height of the curve follows. As λ_o increases, the dispersion in the curve is more marked at shorter wavelengths (the onset of absorption shifts to higher wavelengths). Fig. 4.9(b) shows the imaginary part of the dielectric function for $BaZrO_3$ and $NdGaO_3$. These results were obtained as described above (from direct inversion of the ellipsometric data). These data are given only at higher energies, where the Sellmeier oscillator was no longer a valid description of the data.

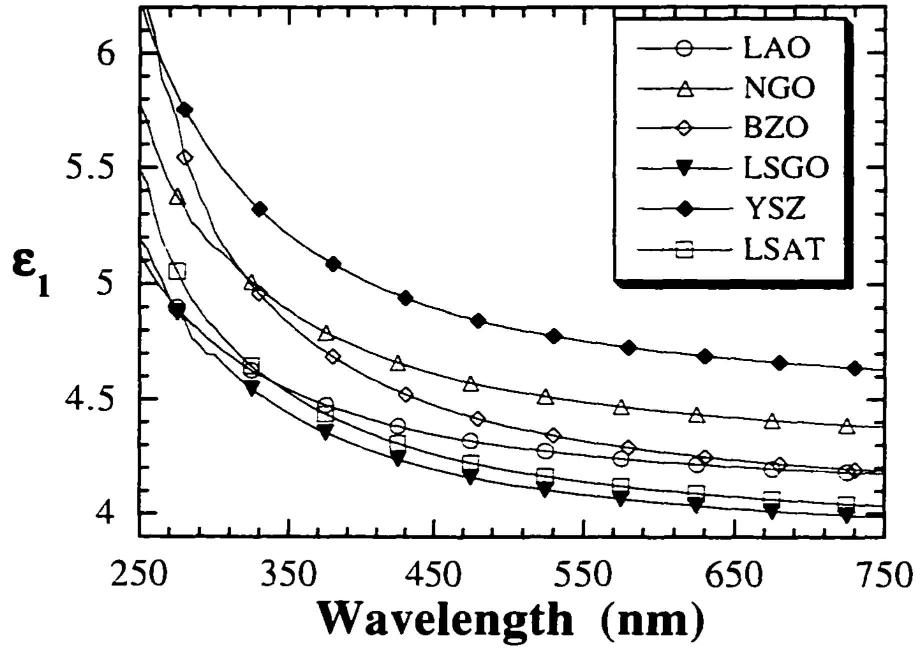

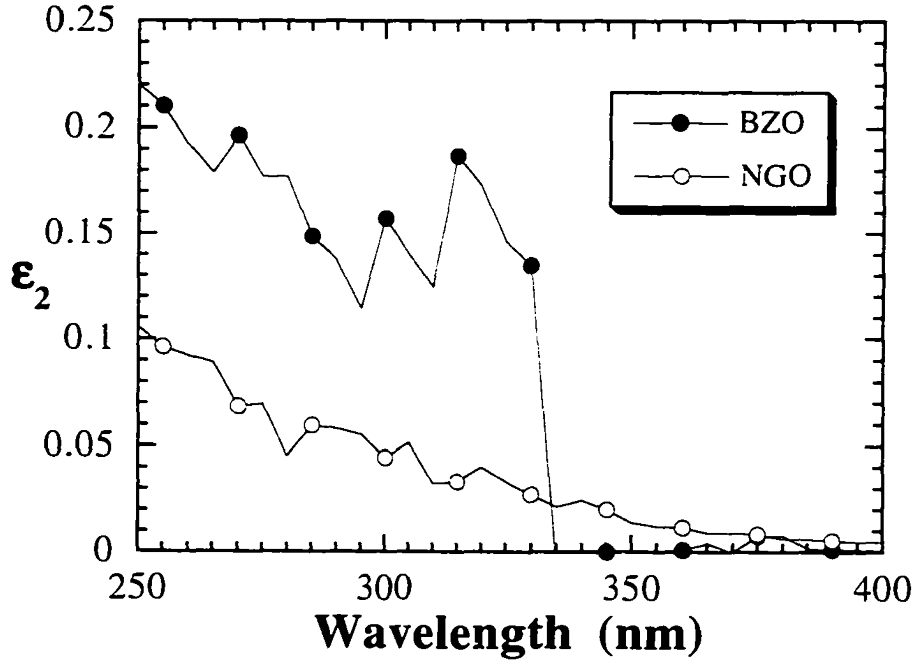

Figure 4.9 : Plot of the (a) real part and (b) imaginary part of the dielectric function for five YBCO substrate materials and $BaZrO_3$ as determined by SE.

Chapter 5

THE SENSITIVITY OF SPECTROSCOPIC ELLIPSOMETRY TO OXYGEN CONTENT IN YBCO THIN FILMS

5.1 Introduction

As described previously, the sensitivity of SE to the oxygen content in YBCO thin films has been exhibited by many researchers.[6,109,141,143,152,157] This sensitivity is a result of the strong dependence of the dielectric function of YBCO on the oxygen content (δ). This dependence can be seen in Fig. 2.11 as determined by Kircher *et al.*[6] As δ increases from 0 to 1, strong features which are characteristic of the non-superconducting tetragonal phase develop in the dielectric spectra, particularly near 4.1 eV (302 nm). The sensitivity of SE to any surface layer of oxygen-deficient YBCO on top of fully-oxygenated YBCO is directly related to the refractive index contrast between that surface layer and the rest of the film. The limits of this sensitivity in the case of graded oxygen contents have not been reported previously. Thus, this chapter describes the resolution of SE with respect to graded oxygen profiles in YBCO films. Emphasis is placed on structures relevant to superconducting Josephson junction devices.

As described in Chapter 2, for proper SNS junction device operation, clean and smooth interfaces between the N and S layers are critical. In addition, the superconductor must be fully oxygenated all the way to the interface with the normal layer. Even a very thin oxygen deficient layer at the S/N interfaces increases the effective thickness of the N layer, thus dramatically reducing the Josephson current. The ability to detect interfacial oxygen stoichiometry (on the length scale of the YBCO unit cell) for a buried YBCO film should significantly facilitate device processing, and thus improve resulting device performance and reliability.

The ability to detect oxygen content at this level exceeds the resolution limits for characterization tools such as secondary ion mass spectrometry (SIMS),[234] Rutherford backscattering spectrometry (RBS)[235] and Auger electron spectrometry (AES).[236] There is recent work, however, that suggests SE is capable of non-destructively depth profiling interfaces with graded compositions while maintaining a resolution far superior to SIMS, providing the dielectric function contrast is sufficiently high.[112] For example, SE was used to measure the graded concentration profile of C in amorphous–$Si_{1-x}C_x$:H thin films. The SE-determined full-width-at half-maximum of the diffusion profile was 36 Å, as compared to 103 Å measured by SIMS (broadened due to the knock-in effect). SE has also been shown to be useful for characterization and control of composition in $Al_xGa_{1-x}As$ quantum well structures.[237,238] In that case, it was shown that the composition could be controlled to within 0.02 in x by comparing SE determined profiles to SIMS data.

5.2 Simulation Procedure

The modeling program described in Chapter 3 was modified to include a concentration gradient in the sample. The code was based on the work of Koh where the sensitivity limits of SE for the characterization of optical coatings were derived.[239] The gradient was treated using a complementary error function to describe a diffusion profile. That is,

$$c(x) = c_s\left[1 - \mathrm{erf}\left(\frac{x}{2\sqrt{Dt}}\right)\right] \tag{5.1}$$

where c is the concentration at a given distance x from the surface of the film, c_s is the concentration of oxygen at the surface, D is the average diffusion coefficient and t is the time. The adjustable parameters for the model were taken to be c_s and Dt. A staircase function was used to approximate the concentration profile, as shown in Fig. 5.1. That is, the continuously varying concentration gradient was treated as a set of discrete layers, each of uniform composition. The dielectric function for each layer was calculated by averaging the two nearest reference spectra from Kircher *et al.*[6] For example, the dielectric function for $YBCO_{6.78}$ was calculated by a weighted average between $YBCO_{6.85}$ and $YBCO_{6.72}$ such that the resulting value was for the desired composition. To eliminate artifacts associated with spurious interference fringes, the graded region was subdivided

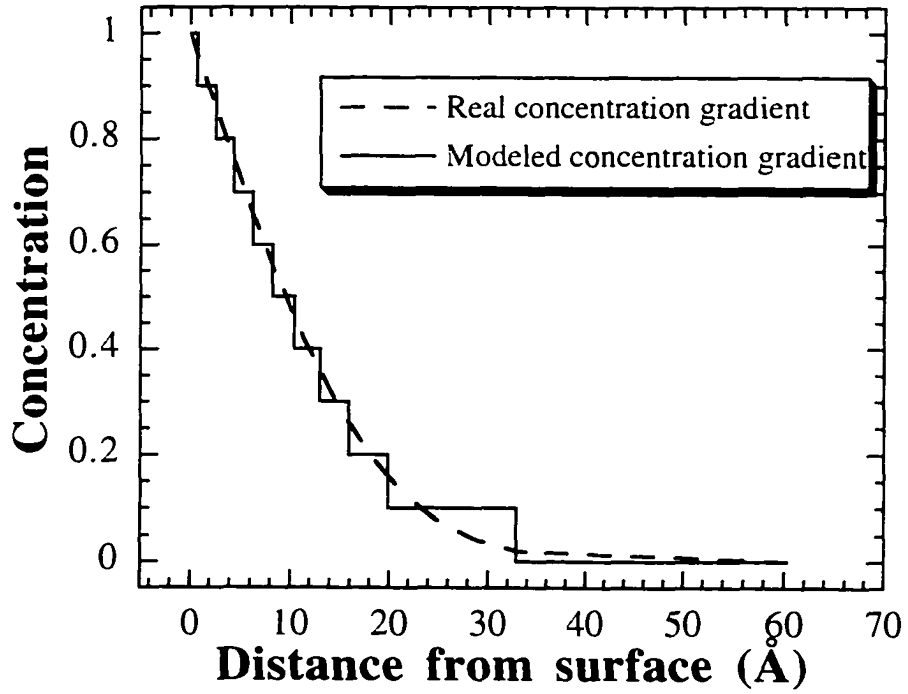

Figure 5.1 : Schematic of the staircase model used to approximate the concentration gradient in YBCO films. 50 layers were used for the calculations in this work.

into 50 layers. In the region where the concentration changes rapidly, there are more, thinner layers. Where the concentration changes slowly, the layers are thicker.

The modified modeling program was used to generate Δ and Ψ spectra for YBCO films with varying oxygen concentration profiles at a fixed angle of incidence of 70°. This allowed for the direct comparison of films with different diffusion depths of oxygen and/or different surface concentrations of oxygen. Thus, the sensitivity of SE with respect to these values could be determined by calculating the differences between spectra and comparing them to the experimental accuracy with which Δ and Ψ can be measured on a typical ellipsometer. Two different scenarios were considered: *a*-axis and *c*-axis oriented films on $SrTiO_3$. For each case, the sensitivities to changes in the diffusion depth or the surface oxygen concentration were calculated. Also, similar calculations were made for YBCO films buried under a 4 nm layer of metallic $SrRuO_3$ to model a S-N junction. Figure 5.2 shows the geometry which was used to generate the spectra in this work. Either c_s or the diffused depth (Dt) was changed, with the overall film thickness remaining the same. Calculations for a buried YBCO layer had the same geometry as in the figure, only with the layer of $SrRuO_3$ on top.

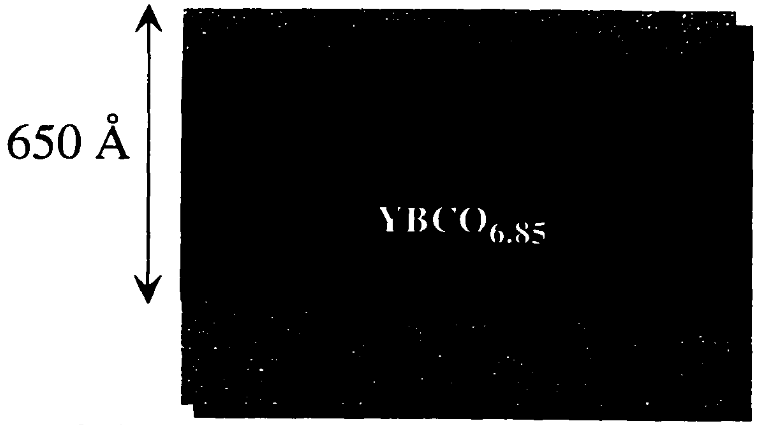

Figure 5.2 : Geometry used to calculate ellipsometric spectra of YBCO thin films with varying diffusion depths and/or surface oxygen concentrations of oxygen.

5.3 *c*-axis Oriented Films

The results will begin with a discussion of *c*-axis oriented YBCO films on $SrTiO_3$. Both exposed and buried layers will be reviewed in the following sections.

5.3.1 Sensitivity to Changes in the Diffusion Depth

The first set of calculations was used to determine the sensitivity of SE to changes in the diffused depth of the graded layer. For these generated spectra, the films were fixed at 650 Å thick with no surface roughness. The surface concentration (c_s) was fixed at $YBCO_{6.07}$ and the diffused depth was varied from 0 to 110 Å or 350 Å to 450 Å. The diffusion depth was defined as the point where the refractive index of the graded layer was within 0.001 of the non-diffused layer value ($YBCO_{6.85}$). For comparison, generated ellipsometric data for two types of films are shown in Fig. 5.3. One film has a graded oxygen content 20 Å thick ($YBCO_{6.07}$ to $YBCO_{6.85}$) while the other has a discrete 20 Å layer of $YBCO_{6.07}$ on the surface. It is clear that the effects of a graded layer cannot be modeled effectively by a discrete layer.

Fig. 5.4 shows the generated Δ and Ψ spectra for different diffused depths, as well as a fully oxidized $YBCO_{6.85}$ film of the same thickness. The effects of the reduced surface layer are clear, even for the thinnest depths. To clarify the effect of small changes to the depth of the graded layer, Fig. 5.5 shows plots of how Δ and Ψ change ($\delta\Delta$ and $\delta\Psi$) when the reduced surface layer thickness starts at 10 Å and is subsequently increased by 10 Å, 20 Å, 30 Å, 50 Å and 100 Å. It has been shown that typical

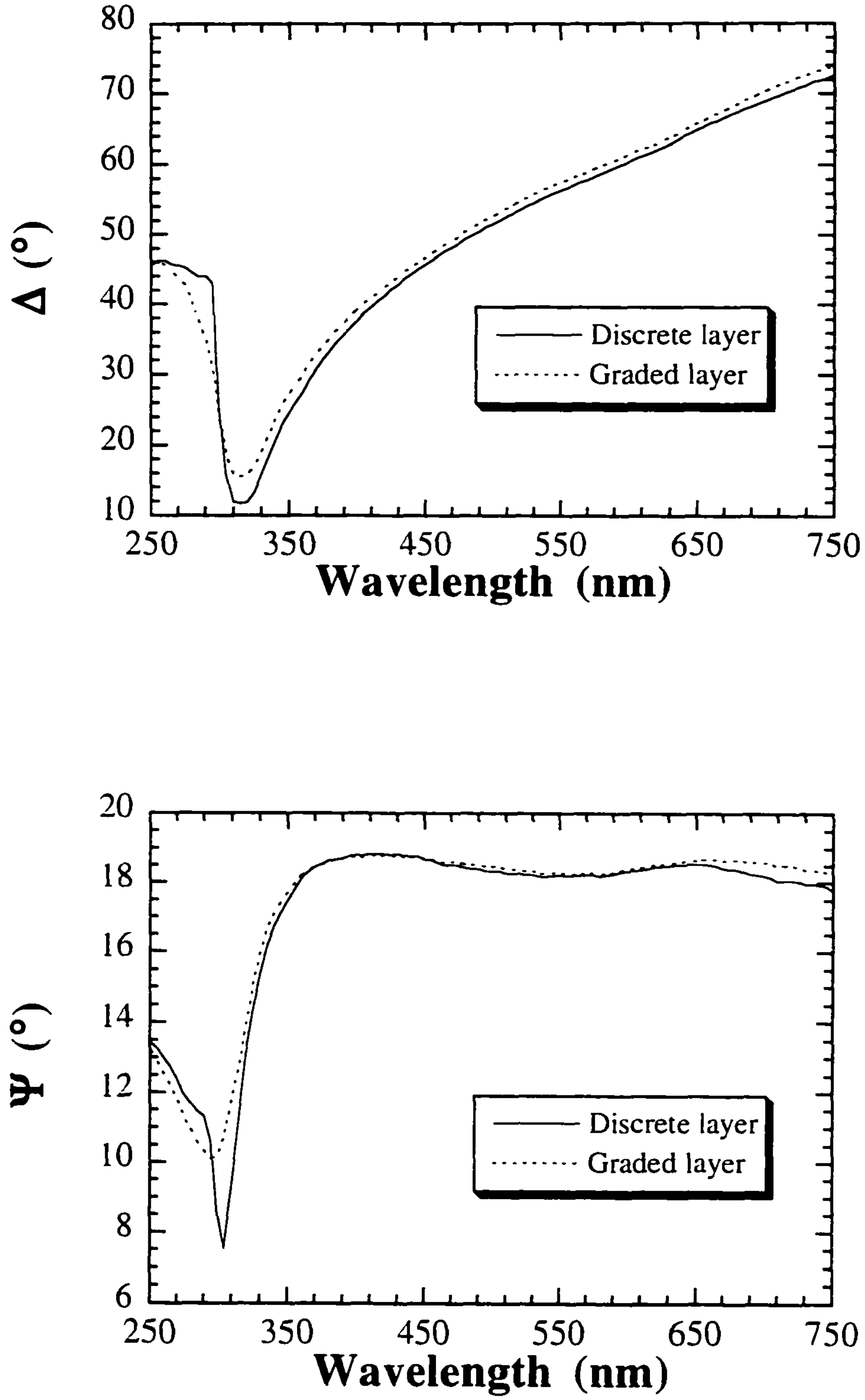

Figure 5.3 : A comparison of ellipsometric spectra for two 650 Å thick films, one with a 20 Å thick graded oxygen content layer with a surface oxygen concentration of $YBCO_{6.07}$ and one with a 20 Å thick discrete layer of $YBCO_{6.07}$ on the surface.

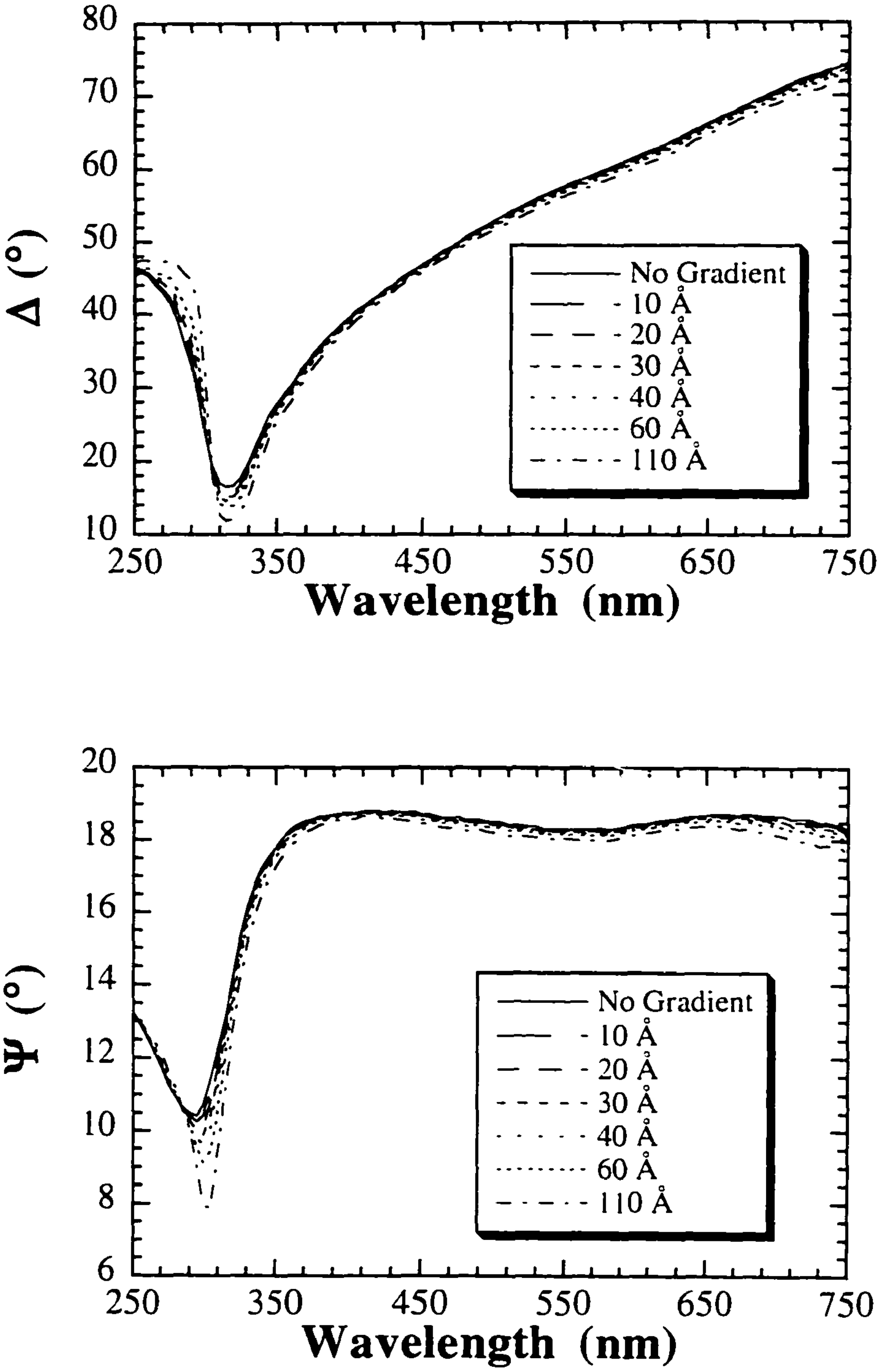

Figure 5.4 : Calculated Δ and Ψ spectra for a 650 Å thick, *c*-axis oriented YBCO$_{6.85}$ film with a c_s of YBCO$_{6.07}$. The diffusion depth was varied from 0 to 110 Å. The solid lines correspond to spectra for a fully oxidized film (no gradient).

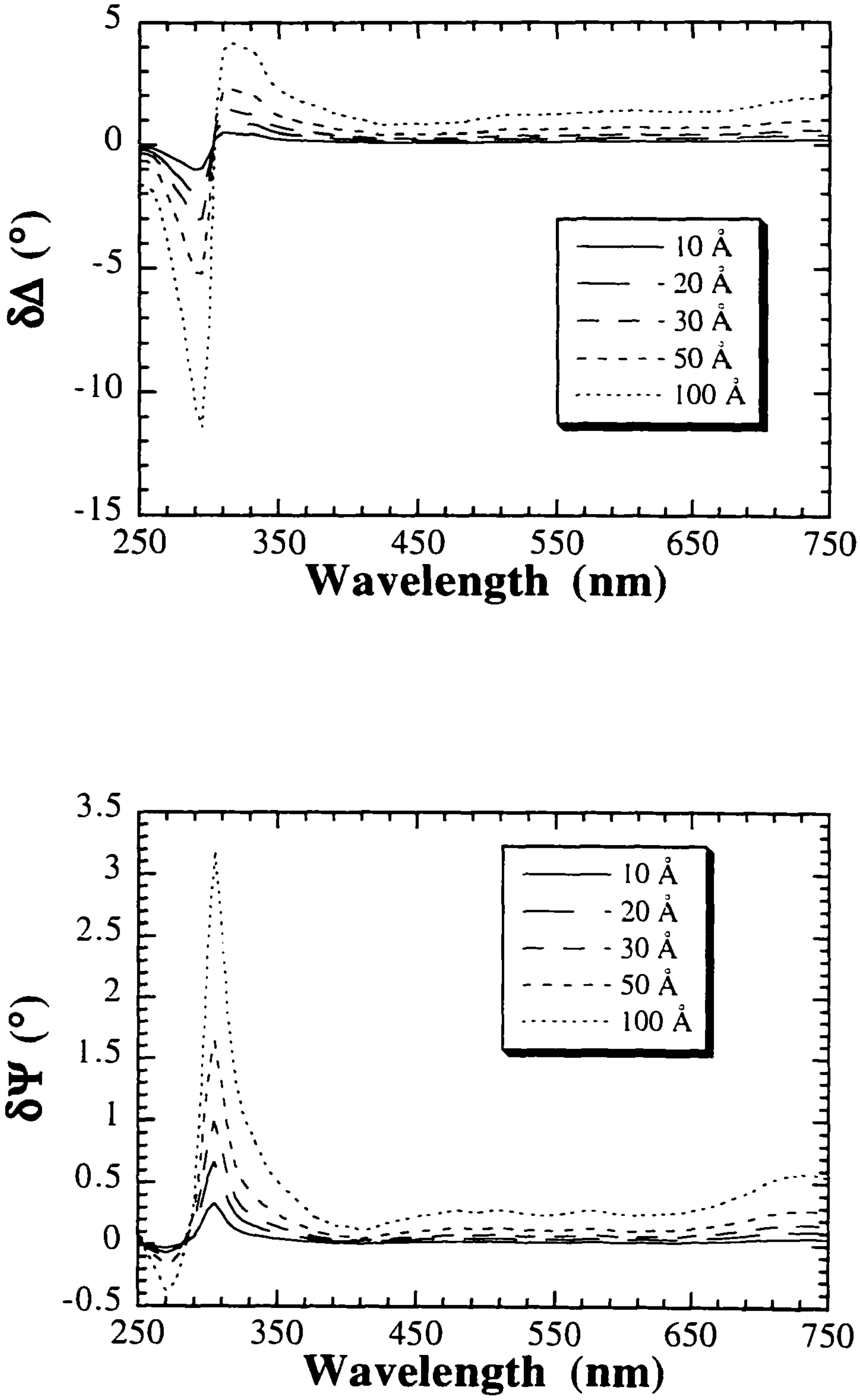

Figure 5.5 : Changes in Δ and Ψ resulting from changes in the diffused depth from 10 Å for a *c*–axis oriented YBCO film. c_s was fixed at $YBCO_{6.07}$. The legend describes the amount by which the diffusion depth was increased.

accuracies of SE measurements are 0.03° in Δ and 0.01° in Ψ.[220] Considering these values, it is clear that for a change in the diffused depth of only 10 Å the changes in the ellipsometric parameters are large enough to detect across the entire wavelength range, with particularly good sensitivity near 300 nm (≈ 4.1 eV). That is, SE is sensitive to the oxygen content within one unit cell of *c*-axis oriented YBCO, even when the oxygen profile is graded. To the author's knowledge, there is no other technique that can determine the oxygen content in YBCO thin films on that length scale. In order to determine if this sensitivity is maintained for the same changes to thicker reduced surface layers, similar calculations were done for films with an initial graded layer thickness of 350 Å. The results for this case are shown in Fig. 5.6. Here, unit cell sensitivity to graded oxygen content is still exhibited, only the sensitivity is more pronounced in Ψ across the entire wavelength range, rather than Δ. Δ is extremely sensitive at ≈ 4.1 eV, where it changes as much as 35° depending on the change to the reduced layer thickness; it is relatively insensitive across the rest of the wavelength range.

5.3.2 Sensitivity to Changes in the Surface Oxygen Concentration

The next set of generated spectra were used to determine the sensitivity of SE to different surface oxygen concentrations (c_s) for graded layers on top of $YBCO_{6.85}$. For these calculations, the film thickness was again fixed at 650 Å with no surface roughness and the diffused depth was fixed to 40 Å or 450 Å. Figure 5.7 shows the changes in Δ and Ψ for films with different surface concentrations with respect to a $YBCO_{6.85}$ film of

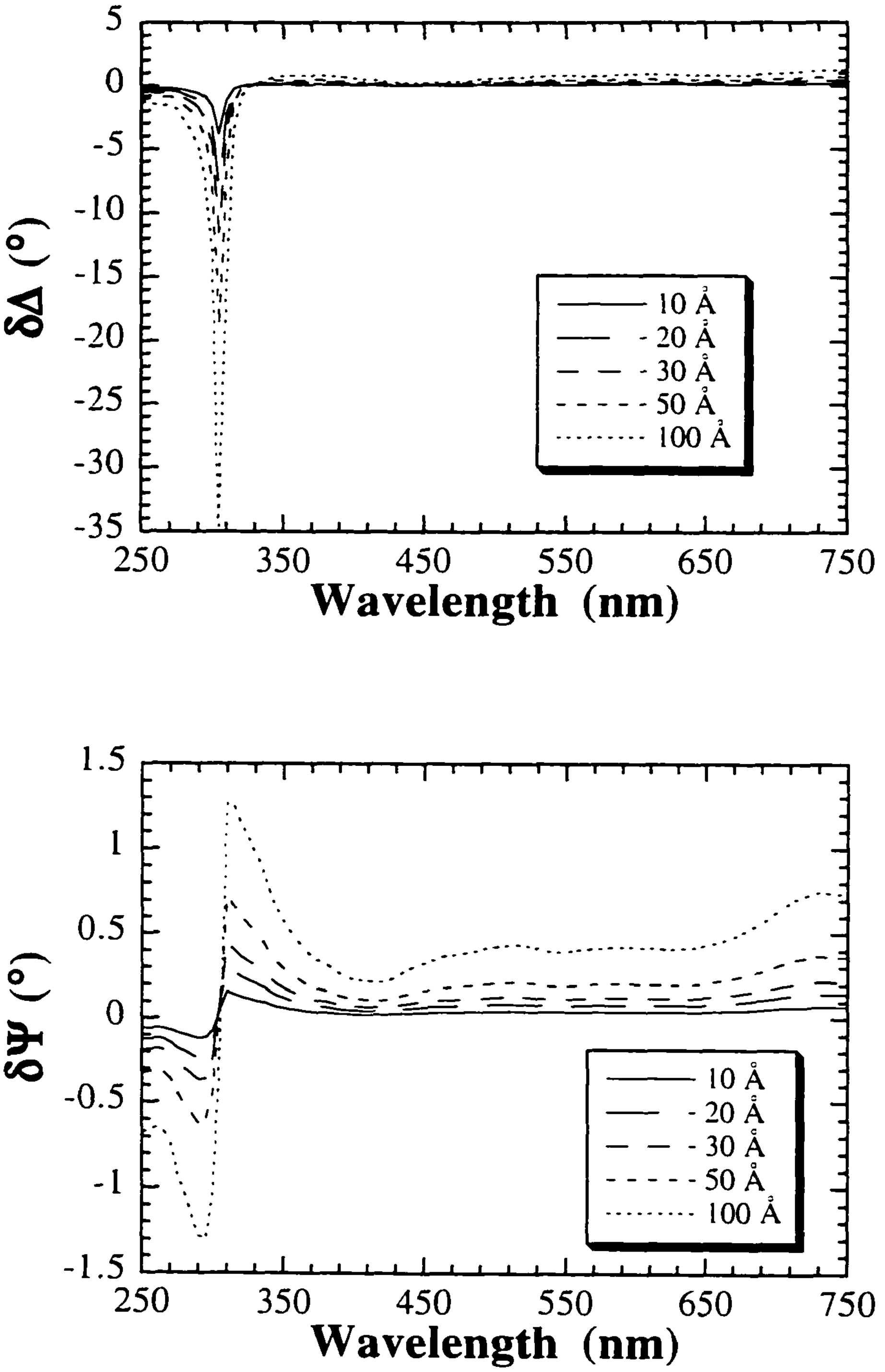

Figure 5.6 : Changes in Δ and Ψ resulting from changes in the diffused depth from 350 Å for a c-axis oriented YBCO film. c_s was fixed at $YBCO_{6.07}$. The legend describes the amount by which the diffusion depth was increased.

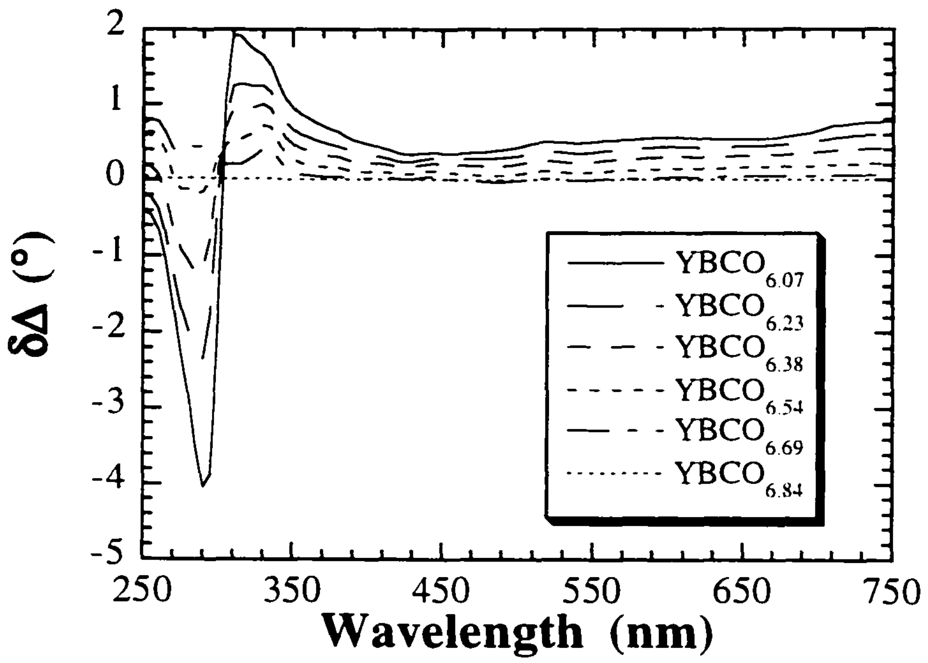

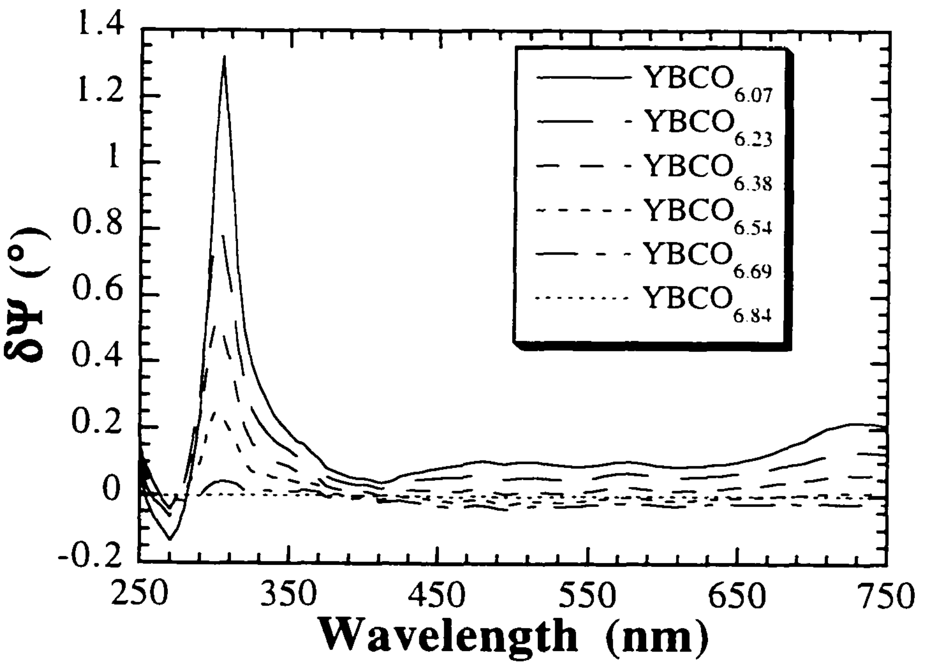

Figure 5.7 : Changes in Δ and Ψ for varying levels of surface oxygen concentration. The changes are with respect to a fully oxidized *c*-axis oriented $YBCO_{6.85}$ film of the same thickness. The diffused depth was fixed at 40 Å.

the same thickness. For these plots, it can be seen that even a 40 Å thick diffused layer that has a surface oxygen concentration of $YBCO_{6.69}$ can significantly affect the ellipsometric data, specifically at lower wavelengths.

The minimum detectable change in surface oxygen concentration (c_s) is also of significant interest. Since the majority of the film is $YBCO_{6.85}$, it is reasonable to expect that the sensitivity to small changes in c_s will be greater if c_s is further from $YBCO_{6.85}$ (i.e. for a heavily reduced surface). That is, the sensitivity will be higher for a larger dielectric function contrast between the surface and the rest of the film. Figure 5.8(a) shows the change in Δ when c_s starts at $YBCO_{6.772}$ ($\delta = 0.228$) and is subsequently changed to $YBCO_{6.764}$, $YBCO_{6.756}$, $YBCO_{6.749}$, $YBCO_{6.741}$, $YBCO_{6.733}$ and $YBCO_{6.694}$. Figure 5.8(b) shows similar calculations for when c_s starts at $YBCO_{6.148}$ ($\delta = 0.852$) and is changed to $YBCO_{6.156}$, $YBCO_{6.164}$, $YBCO_{6.171}$, $YBCO_{6.179}$, $YBCO_{6.187}$ and $YBCO_{6.226}$. From these plots, it is clear that for surface oxygen concentrations closer to $YBCO_{6.85}$ the sensitivity is lower, while for surface concentrations further from $YBCO_{6.85}$, the sensitivity is greater (a smaller change can be detected). Thus, for the lightly reduced surface, a change in δ of 0.023 (to $YBCO_{6.749}$) can be detected for wavelengths between 250 nm and 350 nm, while for a heavily reduced surface, a change in δ of 0.016 (to $YBCO_{6.164}$) can be detected over the same range. Again, to the author's knowledge there is no other technique that has the ability to detect such small changes in the surface oxygen content of YBCO thin films.

When the graded layer is set to 450 Å thick and the same calculations for changes in c_s are made, the sensitivities for both cases are increased. This is shown in Fig. 5.9 where it can be seen that a 0.016 change in δ is, in principle, detectable over the entire

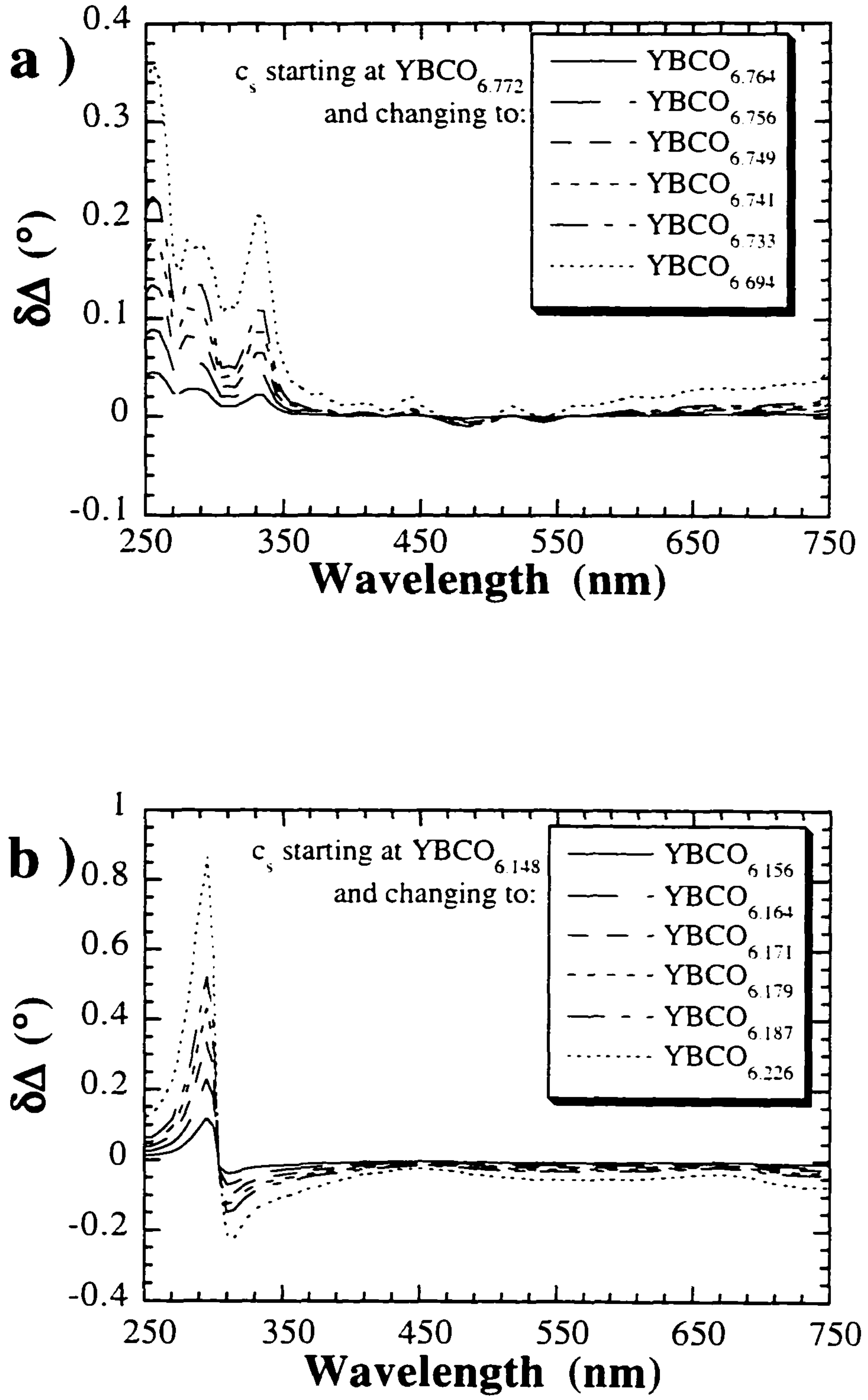

Figure 5.8 : Changes in Δ for (a) starting c_s of $YBCO_{6.772}$ and (b) starting c_s of $YBCO_{6.148}$ when c_s is changed by 0.008, 0.016, 0.023, 0.031, 0.039 and 0.078 (in δ) for a c-axis oriented YBCO film with the diffused depth fixed to 40 Å.

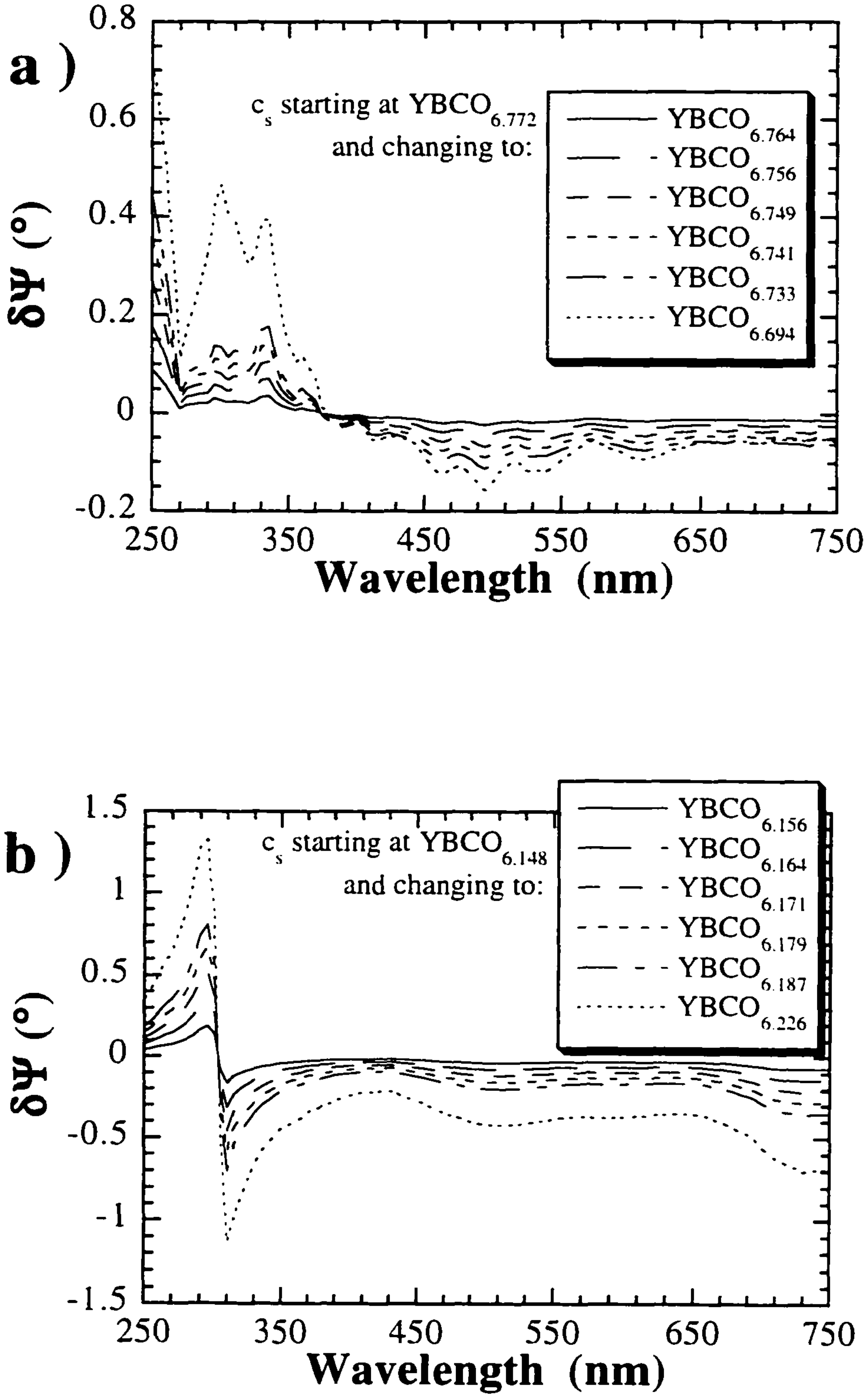

Figure 5.9 : Changes in Δ for (a) starting c_s of YBCO$_{6.772}$ and (b) starting c_s of YBCO$_{6.148}$ when c_s is changed by 0.008, 0.016, 0.023, 0.031, 0.039 and 0.078 (in δ) for a *c*-axis oriented YBCO film with the diffused depth fixed to 450 Å.

wavelength range for heavily reduced surface layers, and for wavelengths from 250 nm to 350 nm and greater than 450 nm for graded layers with compositions closer to that of the rest of the film. Note that in Fig. 5.9, $\delta\Psi$ is plotted because the sensitivities are more pronounced in Ψ for these calculations

5.3.3 Sensitivity Limits when the YBCO Layer is Buried Under a 4 nm Normal Metal Layer

In the above discussion, it was demonstrated that SE is clearly very sensitive to variations in the oxygen content in YBCO thin films when the graded layer is at the surface. However, in devices based on Josephson junction technology there is always some type of an interlayer (normal metal or insulator) adjacent to the superconducting film. As described previously, for proximity-effect junctions it is critical that the underlying YBCO film be fully oxygenated all the way to the interface with the normal metal. Even a small oxygen deficiency at the interface will result in a region of poor superconducting properties (depressed critical temperature, critical current, etc.) and thus effectively increase the N layer thickness. As a result, the device operation is significantly degraded and, at some point, it ceases to act as a true proximity-effect junction.[4]

In order to understand how the presence of an N layer affects the sensitivity of SE to oxygen content gradations in YBCO, ellipsometric data were generated for the same conditions as described in the previous sections, with the exception that a 4 nm thick layer of metallic $SrRuO_3$ was added as an overlayer on the surface. $SrRuO_3$ was chosen due to the availability of accurate optical reference data.[240] Figure 5.10 shows $\delta\Delta$ and $\delta\Psi$ for changes of 10 Å, 20 Å, 30 Å, 50 Å and 100 Å in the YBCO graded oxygen content layer depth (with respect to a starting graded layer thickness of 10 Å). Again, this diffusion depth is defined as the distance from the S/N interface at which the refractive index of the graded layer was within 0.001 of the non-diffused layer value ($YBCO_{6.85}$). In Δ, the changes are somewhat damped compared to the generated spectra without the $SrRuO_3$ layer, while in Ψ the changes are slightly enhanced. However, changes on the order of one unit cell of YBCO are still readily detectable throughout the entire wavelength range. That is, oxygen deficiency at the interface in a SN junction can be seen using SE. When the thickness of the graded layer starts at 350 Å and the same changes are introduced, sensitivity on the order of one unit cell is still shown over the entire wavelength range. However, as with the exposed case, the sensitivity is exhibited more so in Ψ over the whole wavelength range, rather than Δ. In Δ, the peak sensitivity is shown at ≈ 4.1 eV.

Next, the interfacial oxygen concentration (c_s) was varied for a YBCO film underneath a 4 nm layer of $SrRuO_3$. Figure 5.11 shows $\delta\Delta$ for when c_s starts at $YBCO_{6.772}$ or $YBCO_{6.148}$ and is changed by 0.008, 0.016, 0.023, 0.031, 0.039 and 0.078 in δ. Here again, the changes in Δ are slightly diminished relative to the case where the YBCO film is not buried. The minimum detection limit of a change in c_s is increased for samples with a more heavily reduced surface to 0.031 (to $YBCO_{6.179}$) over the wavelength range 250 nm – 350 nm. For calculations with the starting surface oxygen concentration closer

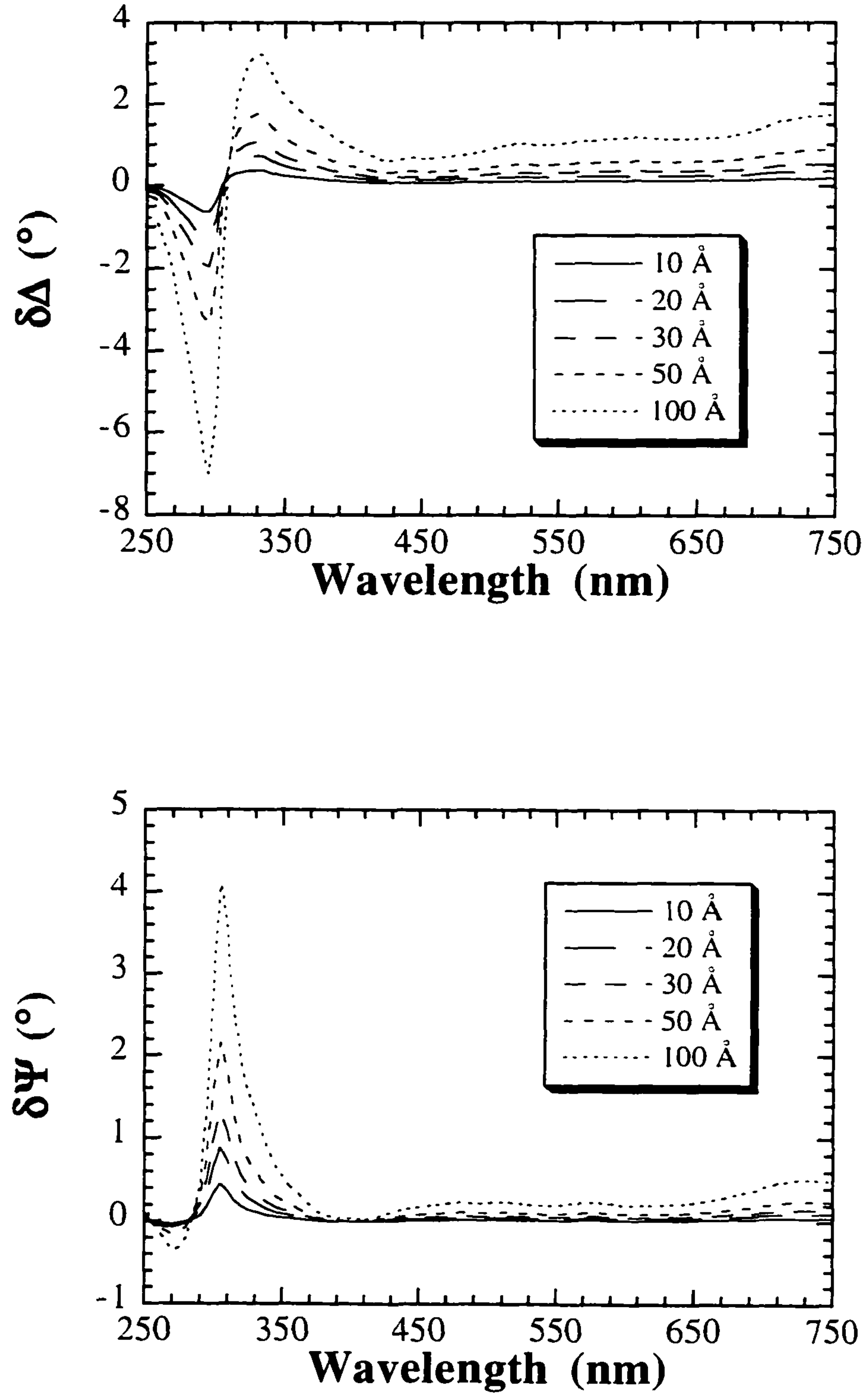

Figure 5.10 : Changes in Δ and Ψ resulting from changes in the diffused depth from 10 Å when the *c*-axis oriented diffused layer is buried beneath a 4 nm layer of metallic $SrRuO_3$. The legend describes the amount by which the diffusion depth was increased. *c*, was fixed to $YBCO_{6.07}$.

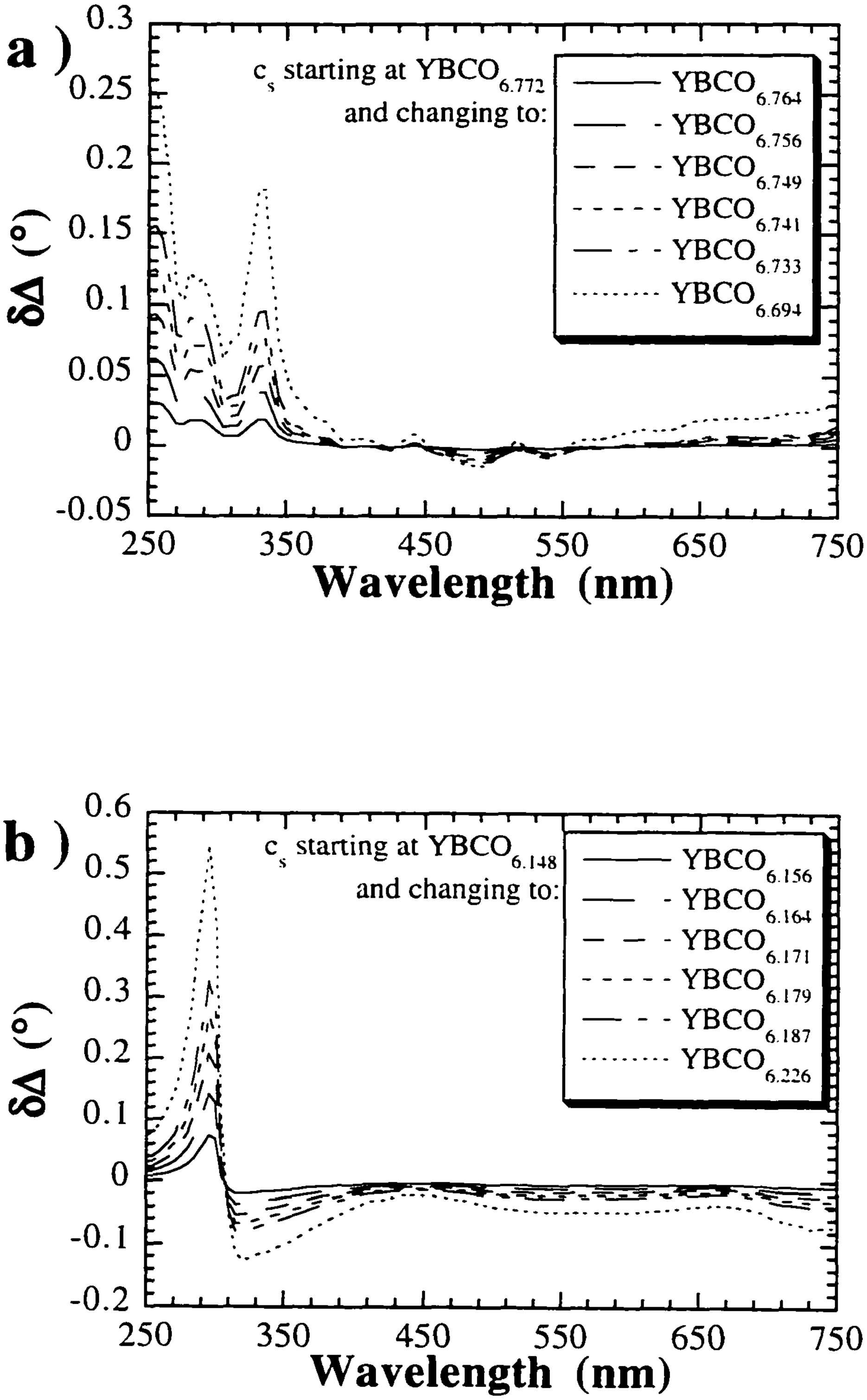

Figure 5.11 : Changes in Δ for (a) starting c_s of $YBCO_{6.772}$ and (b) starting c_s of $YBCO_{6.148}$ when c_s is changed by 0.008, 0.016, 0.023, 0.031, 0.039 and 0.078 (in δ) for a *c*-axis oriented YBCO film with a graded surface oxygen content buried under a 4 nm layer of metallic $SrRuO_3$. The diffused depth was fixed to 40 Å.

to the rest of the film ($YBCO_{6.85}$), a 0.039 change in δ (to $YBCO_{6.733}$) can be detected between 250 nm and 340 nm. When the graded layer thickness of the buried YBCO film is 450 Å, the sensitivities for both cases are improved. Minimum changes in c_v on the order of 0.016 can be detected for wavelengths greater than 430 nm. Once again, the sensitivities are more pronounced in the changes in Ψ for the thicker graded layer.

5.4 *a*-axis Oriented Films

a-axis oriented YBCO thin films are of significant technological interest for use in sandwich type Josephson junction applications because of the longer superconducting coherence length along the *a*/*b*-direction with respect to the *c*-direction.[212] Thus, as in the above discussion, ellipsometric spectra were generated for *a*-axis oriented films 650 Å thick with and without a 4 nm overlayer of metallic $SrRuO_3$. For these simulations, the YBCO film was assumed to be twinned in-plane, with equal amounts of *c*-axis and *b*-axis oriented regions parallel to a given substrate edge for 100 edge-oriented $SrTiO_3$. In addition, the edge of the substrate was set to be parallel to the plane of incidence. For this particular case, the reference in-plane optical data for YBCO is simply an average of the *a*/*b*- and *c*-axes dielectric functions.

5.4.1 Sensitivity to Changes in the Diffusion Depth

Figure 5.12(a) shows the changes in Δ when a reduced surface layer initially 10 Å thick is increased in thickness by 10 Å, 20 Å, 30 Å, 50 Å and 100 Å for an *a*-axis

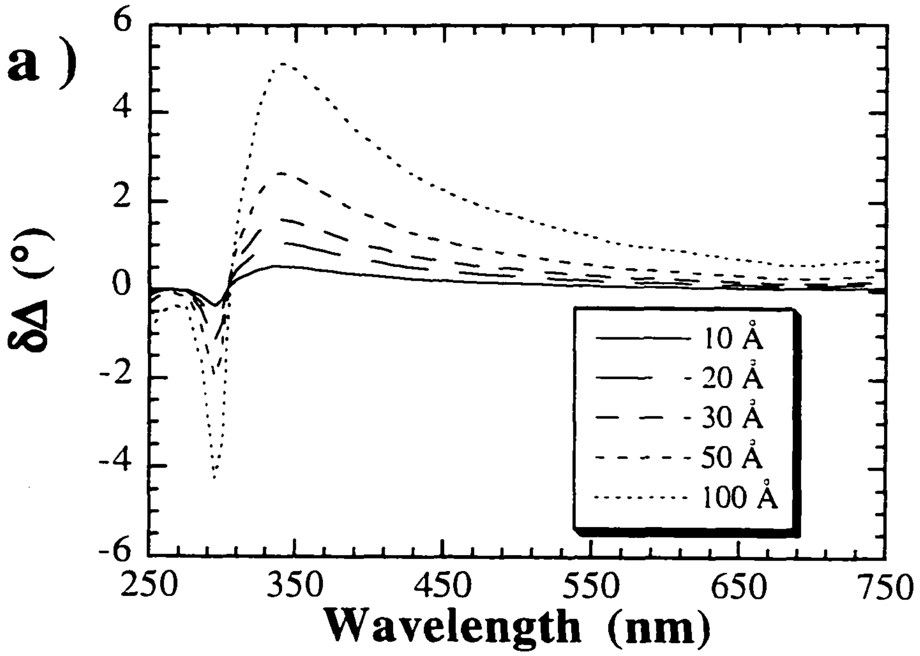

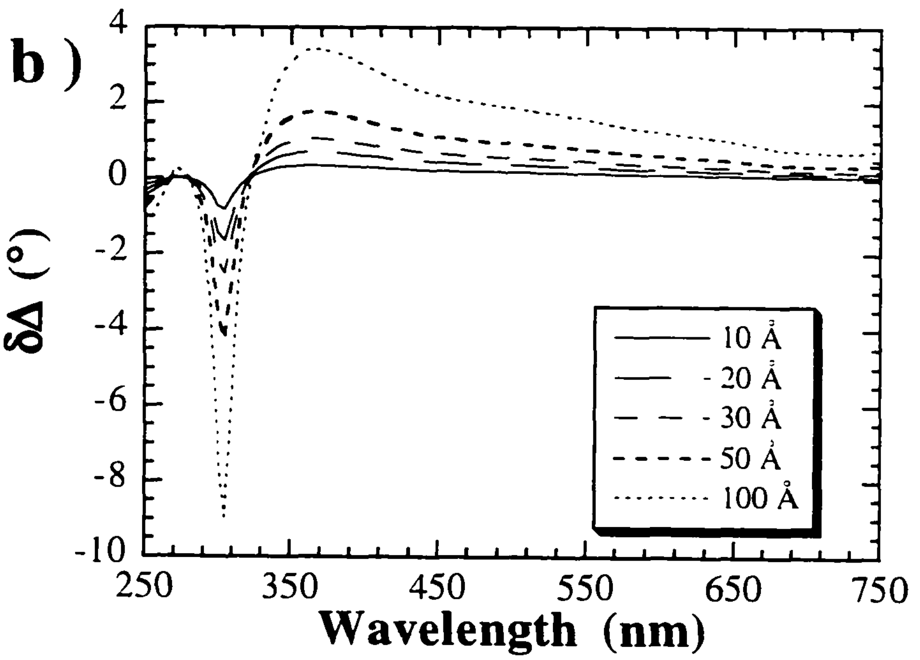

Figure 5.12 : Changes in Δ resulting from changes in the diffused depth from (a) 10 Å and (b) 350 Å for an *a*-axis oriented YBCO film. The legends describe the amount by which the diffusion depth was changed.

oriented YBCO film. As was the case for *c*-axis oriented films, the $\delta\Delta$ values for thickness differences as little as 10 Å are large enough to be detected for wavelengths greater than 310 nm. The changes in Ψ also indicate the ability to detect this level of oxygen deficiency, only over a reduced wavelength range. In Fig. 5.12(b), the results are given for when the reduced surface layer starts at 350 Å thick and the same changes are introduced. It can be seen that detection of a 10 Å difference is still possible over a wide wavelength range (>350 nm) in $\delta\Delta$ for this case. In contrast to *c*-axis oriented films, the sensitivity is more pronounced in Δ, rather than Ψ, for the thicker graded layer calculations.

5.4.2 Sensitivity to Changes in the Surface Oxygen Concentration

The next set of generated spectra were used to determine the sensitivity of SE to different surface concentrations of oxygen (c_s) for graded layers on top of *a*-axis oriented $YBCO_{6.85}$. Figure 5.13(a) shows $\delta\Delta$ for a YBCO surface when c_s starts at $YBCO_{6.772}$ ($\delta = 0.228$) and is subsequently changed to $YBCO_{6.764}$, $YBCO_{6.756}$, $YBCO_{6.749}$, $YBCO_{6.741}$, $YBCO_{6.733}$ and $YBCO_{6.694}$. Figure 5.13(b) shows similar calculations for when c_s starts at $YBCO_{6.148}$ ($\delta = 0.852$) and is changed to $YBCO_{6.156}$, $YBCO_{6.164}$, $YBCO_{6.171}$, $YBCO_{6.179}$, $YBCO_{6.187}$ and $YBCO_{6.226}$. In both cases the diffused depth was fixed at 40 Å. As before, the SE data are more sensitive to small changes in the surface oxygen concentration when the surface is heavily reduced (the dielectric function contrast is high). For this case, the minimum detectable change over a wide wavelength range (275 nm – 450 nm) in the

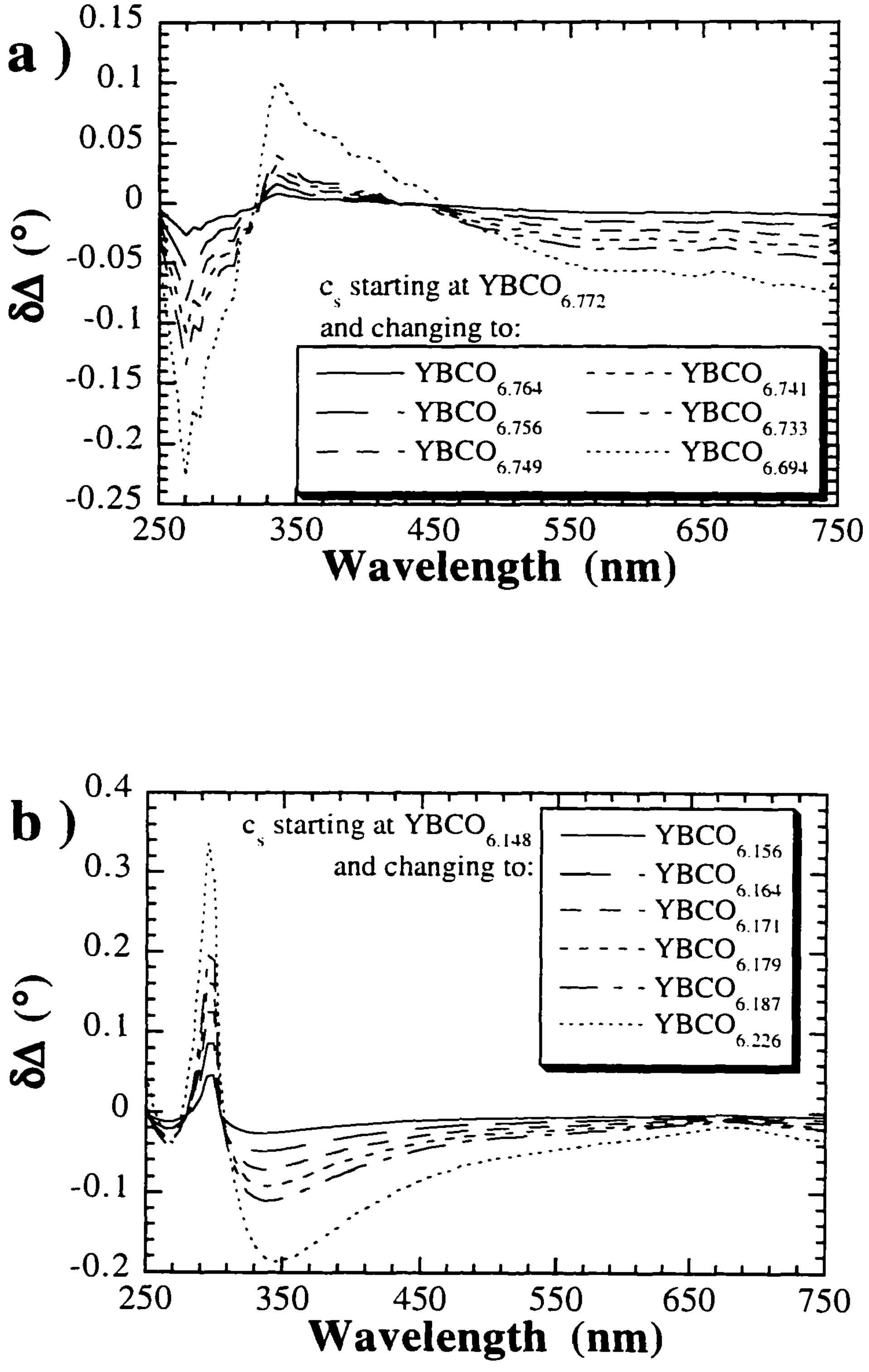

Figure 5.13 : Changes in Δ for (a) starting c_s of YBCO$_{6.772}$ and (b) starting c_s of YBCO$_{6.148}$ when c_s is changed by 0.008, 0.016, 0.023, 0.031, 0.039 and 0.078 for an *a*-axis oriented film with a graded surface oxygen content. The diffused depth was fixed to 40 Å.

surface oxygen concentration is 0.023 (in δ). For values of c_s which are closer to $YBCO_{6.85}$, the sensitivity is lower; with a minimum detection limit of 0.078 (in δ) over a reasonable wavelength range. When the diffused depth is set to 450 Å and the same calculations are made, the overall sensitivities to small changes in c_s were improved. For heavily reduced surfaces, the minimum detection limit for a change in δ was 0.008 and for lightly reduced surfaces, the limit was 0.016.

5.4.3 Sensitivity Limits when the YBCO Layer is Buried Under a 4 nm Normal Metal Layer

In order to understand how the presence of a N layer affects the sensitivity of SE to oxygen content gradations in *a*-axis oriented YBCO, ellipsometric data were generated for the same conditions as described above, with the exception that a 4 nm thick layer of metallic $SrRuO_3$ was added as an overlayer on the surface. Figure 5.14(a) shows δΔ for changes in the YBCO graded oxygen content layer depth (with respect to a starting graded layer thickness of 10 Å). It is clear that a 10 Å change in the diffused depth can be seen even under a 4 nm layer of $SrRuO_3$ for wavelengths greater than 310 nm. Figure 5.14(b) shows the results for when the initial thickness of the reduced surface layer is 350 Å and the same changes are introduced. Changes on the order of 10 Å can still be detected here, as well. Also, in contrast to *c*-axis oriented films, these changes are more pronounced in Δ, rather than Ψ.

Finally, Fig. 5.15 shows the results for varying the surface concentration of an *a*-axis YBCO film buried under 4 nm of $SrRuO_3$. As before, Fig. 5.15 shows δΔ for

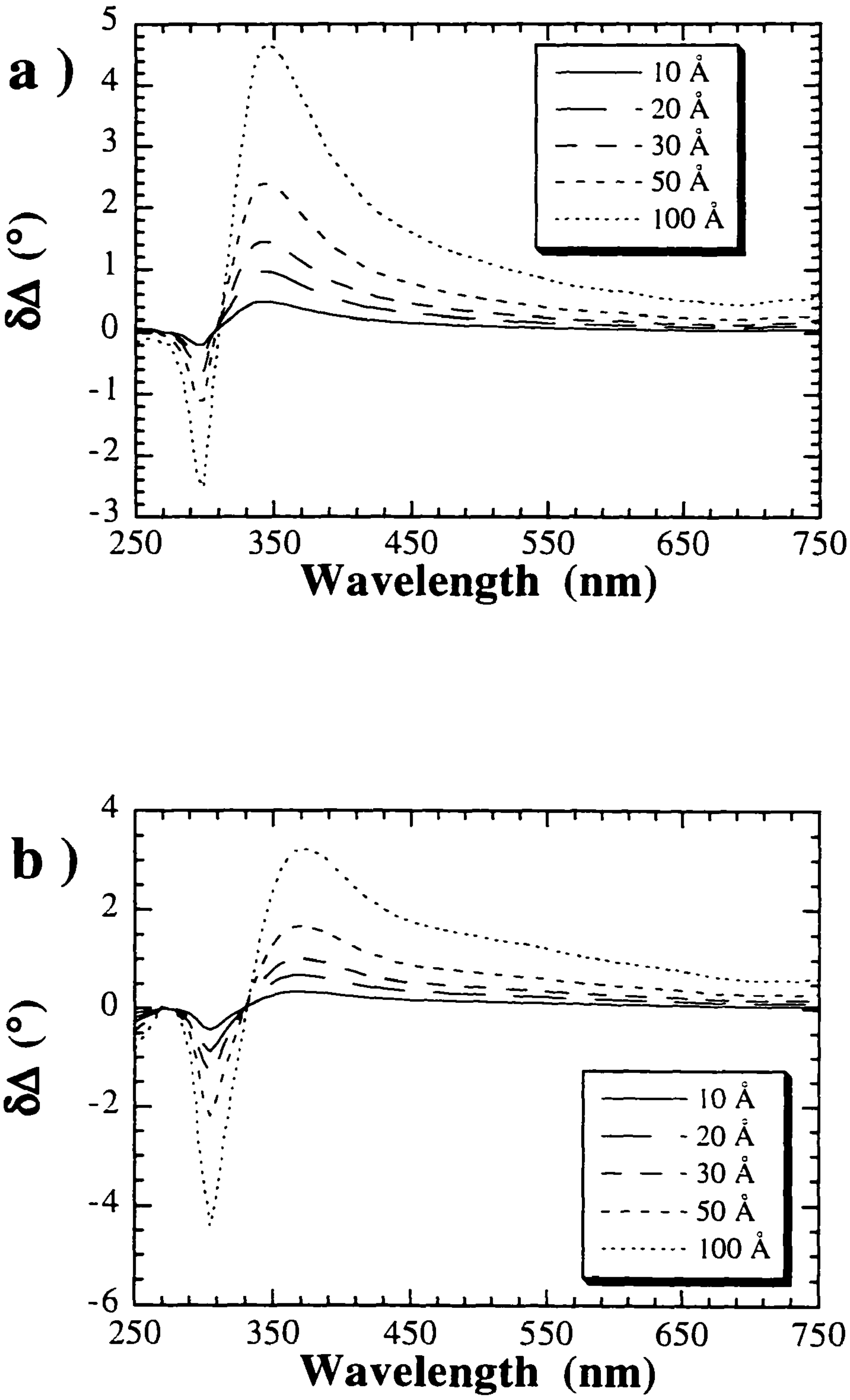

Figure 5.14 : Changes in Δ resulting from changes in the diffused depth from (a) 10 Å and (b) 350 Å for an *a*-axis oriented YBCO film buried under 4 nm of metallic $SrRuO_3$. The legends describe the amount by which the diffusion depth was increased.

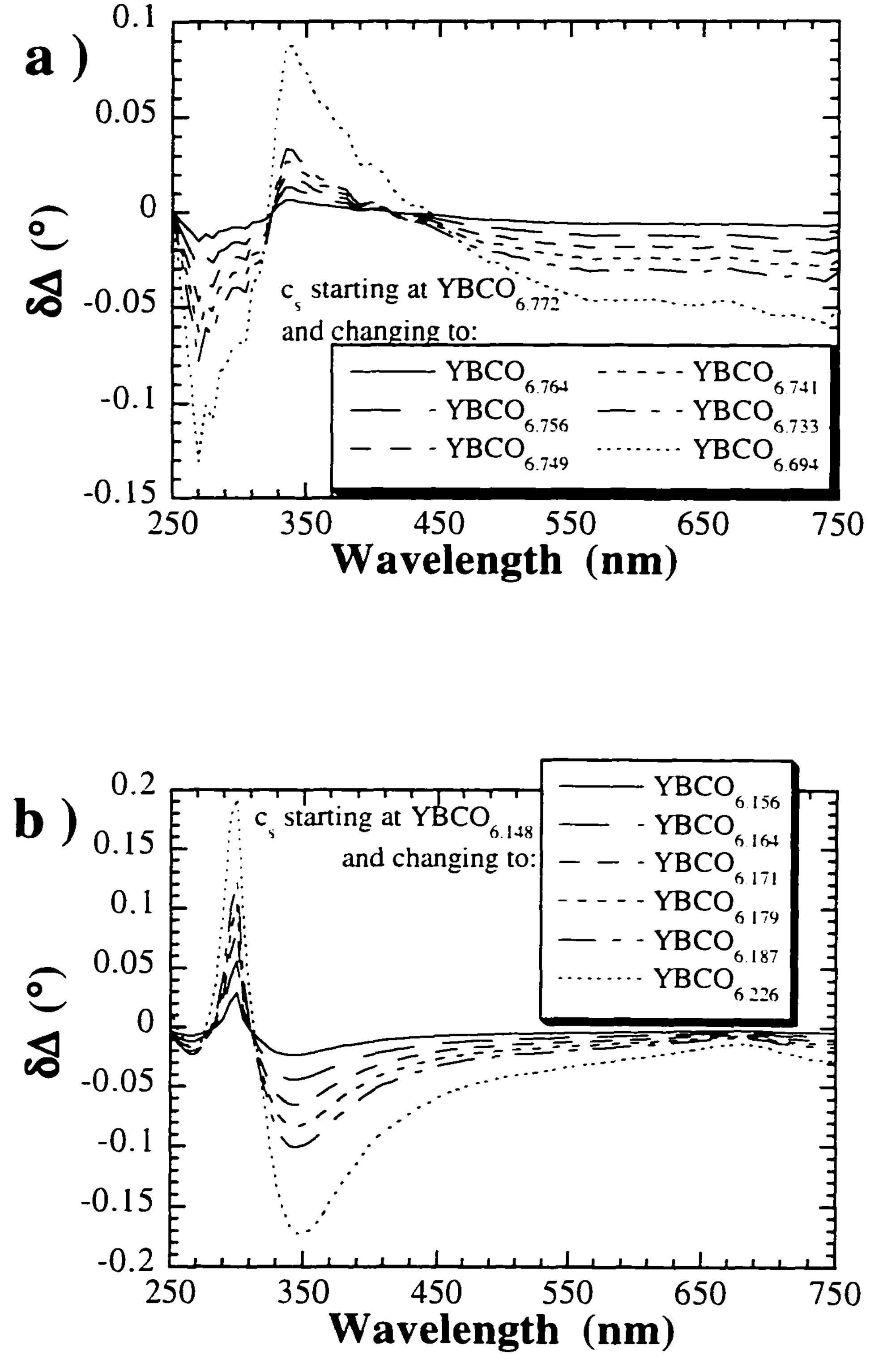

Figure 5.15 : Changes in Δ for (a) starting c_s of YBCO$_{6.772}$ and (b) starting c_s of YBCO$_{6.148}$ when c_s is changed by 0.008, 0.016, 0.023, 0.031, 0.039 and 0.078 (in δ) for a *a*-axis oriented YBCO film with a graded surface oxygen content buried under a 4 nm layer of metallic SrRuO$_3$.

when c_s starts at $YBCO_{6.772}$ or $YBCO_{6.148}$ and is subsequently changed by 0.008, 0.016, 0.023, 0.031, 0.039 and 0.078. The limit of detection for wavelengths between 275 nm – 450 nm is 0.031 (in δ) for heavily reduced interfaces and 0.078 (in δ) for c_s values closer to that of the non-graded layer (lightly reduced interfaces). In similar calculations where the diffused depth was fixed to 450 Å, the overall sensitivities to small changes in the surface oxygen content were improved. Minimum detection limits on the order of 0.008 (in δ) were calculated for heavily reduced interfaces and 0.016 for lightly reduced interfaces.

It is important to restate that these calculations were done for ideal YBCO thin films with no surface roughness at an angle of incidence of 70°. With roughness present, these sensitivities would be degraded somewhat. This is likely because the large refractive index contrast between YBCO and air may overwhelm comparatively subtle changes in the YBCO surface oxygen concentration (i.e. the sensitivity would be decreased especially for lightly reduced surfaces). However, for deposition of a uniform, pinhole-free interlayer on the order of 4 nm thick, the underlying YBCO surface must be smooth; thus, these calculated sensitivities are relevant for potential Josephson junction device applications.

These results show that, as expected, the sensitivities of SE are higher when there is a high dielectric function contrast between the surface (or interface for a buried layer) and the rest of the film. As the graded layer becomes thicker, in general the sensitivities for *c*-axis oriented films are more strongly exhibited in Ψ, rather than Δ. For *a*-axis films, the opposite is true; the sensitivities are more strongly exhibited in Δ. Thus, based on these data. for graded layer thicknesses up to 450 Å the accuracy of measuring changes to that thickness is not a strong function of the total graded layer thickness. This is in contrast to the case of graded composition profiles in all-dielectric systems.[241] A summary of the results of the sensitivity limits determined in this chapter are given in tables 5.1 and 5.2.

Table 5.1 : Summary of the sensitivity limits of SE to changes in the diffused depth. For thin layers. the sensitivities are with respect to a starting graded layer thickness of 10 Å. For thick layers. the sensitivities are with respect to a starting graded layer thickness of 350 Å.

Sensitivity to Changes in the Diffused Depth

		Detectable Change (Å)	Wavelength Range (nm)
Thin *c*-axis graded layers	Exposed	10 Å	250 – 750
	Buried	10 Å	250 – 750
Thick *c*-axis graded layers	Exposed	10 Å	250 – 750
	Buried	10 Å	250 – 750
Thin *a*-axis graded layers	Exposed	10 Å	310 – 750
	Buried	10 Å	310 – 750
Thick *a*-axis graded layers	Exposed	10 Å	350 – 750
	Buried	10 Å	350 – 750

Table 5.2 : Summary of the sensitivity limits of SE to changes in the surface oxygen concentration. For thin layers, the diffused depth was fixed to 40 Å. For thick layers, the diffused depth was fixed to 450 Å. Sensitivities are given for both heavily and lightly reduced surface layers. The detectable change given is the minimum change in δ that can be detected.

Sensitivity to Changes in c_s

		Heavily Reduced Surface		**Lightly Reduced Surface**	
		Detectable Change	Wavelength Range (nm)	Detectable Change	Wavelength Range (nm)
Thin *c*-axis graded layers	Exposed	2%	250 - 350	3%	250 – 350
	Buried	4%	250 - 350	5%	250 – 340
Thick *c*-axis graded layers	Exposed	2%	250 – 750	2%	250 - 350, 450 - 750
	Buried	2%	430 – 750	2%	430 – 750
Thin *a*-axis graded layers	Exposed	3%	275 – 450	10%	250 – 310, 500 – 750
	Buried	4%	275 – 450	10%	250 – 310, 500 – 750
Thick *a*-axis graded layers	Exposed	1%	290 – 750	2%	390 - 750
	Buried	1%	300 – 750	2%	400 - 750

Chapter 6

RTSE AS A CHARACTERIZATION TOOL FOR MBE

As described in chapter 3, a real-time spectroscopic ellipsometer (RTSE) was constructed and adapted for use on an existing molecular beam epitaxy (MBE) deposition system. The RTSE was designed as a complementary tool to the other existing *in situ* deposition monitors on the MBE, including atomic absorption flux monitoring (AA), quartz crystal flux monitoring (QCM) and reflection high energy electron diffraction (RHEED). This was the first time that RTSE has been applied to the deposition of oxide films by MBE, thus this chapter describes how it was used, its limitations and how it complements the other *in situ* techniques.

6.1 MBE Substrate Temperature Calibration

Because of the arrangement of the substrate heater/rotator in the MBE system, it is not possible to directly attach a thermocouple to the sample (or sample holder) in order to measure the substrate temperature during deposition. The substrate thermocouple is located behind the wafer holder (puck) and near the quartz lamp heater. Thus, it does not give an accurate assessment of the substrate temperature. Typically, an infrared pyrometer (Minolta/Land Cyclops 152) is used to measure the temperature of the substrate. However, most pyrometers obtain the temperature from an absolute irradiance measurement. Thus, complications can arise due to the optical losses that may occur upon transmission through the access window. In addition, errors may be generated due to the assumption of a given emissivity for the surface being measured. Therefore, a more accurate method of measuring temperature in the MBE is desired.

SE has been used to extract the substrate temperature in other deposition systems.[242] These measurements rely upon the fact that the optical properties of Si have been investigated extensively. Specifically, the behavior of the dielectric spectra as a function of temperature is known.[243] The well-defined structures observed in the dielectric spectra can be analyzed in terms of standard analytic line shapes. The 3.375 eV feature in the Si dielectric function has been found to decrease linearly (in energy position) with increasing temperature for 80 °C $\leq T \leq$ 550 °C according to the equation:[243]

$$E(\text{eV}) = 3.375 - 4.07 \times 10^{-4}[T(^\circ\text{C})] \tag{6.1}$$

Here, as in previous work, it is assumed that the linear behavior extends to higher temperatures as well.[242,243] Thus, using this relationship, and extraction of the position of the transition energy from ellipsometric data, the temperature of the substrate can be determined. An additional advantage to this method is that the penetration depth of the light in Si at this energy position is only 220 Å.[242] Therefore, the SE-determined temperature is a true surface temperature.

The key to this type of temperature calibration is to extract the true dielectric function of the Si sample being analyzed, so that the exact position of the critical point can be determined. That is, the transparent overlayer of SiO_2 must be accounted for. To do this, ellipsometric data are collected on the sample at the base thermocouple temperature (typically ≈ 40-50 °C by the thermocouple). Using the modeling program described in chapter 3, these data are fit to obtain the angle of incidence of the measurement, as well as the thickness of any oxide overlayer on the sample. For the samples used here, oxide thicknesses on the order of 20 Å to 30 Å were typically observed. Using these values, the true dielectric function of the underlying Si can be obtained by mathematically inverting the ellipsometric data while accounting for the geometry of the sample (i.e. accounting for the overlayer).

Subsequently, to determine the temperature of the substrate, a critical point analysis is used for the structure at 3.375 eV. This involves taking second derivatives of the extracted Si dielectric function with respect to photon energy, and fitting the data for both the real and imaginary parts using an excitonic line shape:[243]

$$\frac{d^2\varepsilon}{dE^2} = 2A\left[\exp(i\Phi)\right]\left[\left(E - E_c + i\Gamma\right)^{-3}\right] \qquad (6.2)$$

Where A is the critical point amplitude, E_c is the critical point energy, Γ is the critical point broadening parameter and Φ is the critical point phase.

Typical experimental results for the critical point analysis are shown in Fig. 6.1. Both the experimental data and the fits are given, as well as the fitted parameters of the excitonic line shape analysis. For the plots here, the MBE thermocouple temperature was set to 200 °C. From the SE analysis, the temperature was determined to be 249 °C ± 11 °C. The pyrometer was not able to give a measurement at this low temperature. Fig 6.2 shows a complete temperature calibration for the MBE, including pyrometer measurements, where available. The pyrometer measurements were taken from two access windows to the MBE. One window was facing the substrate at a 45° angle, and the pyrometer was focused directly onto the substrate surface. The other window is at normal incidence to the substrate, however it was not possible to directly

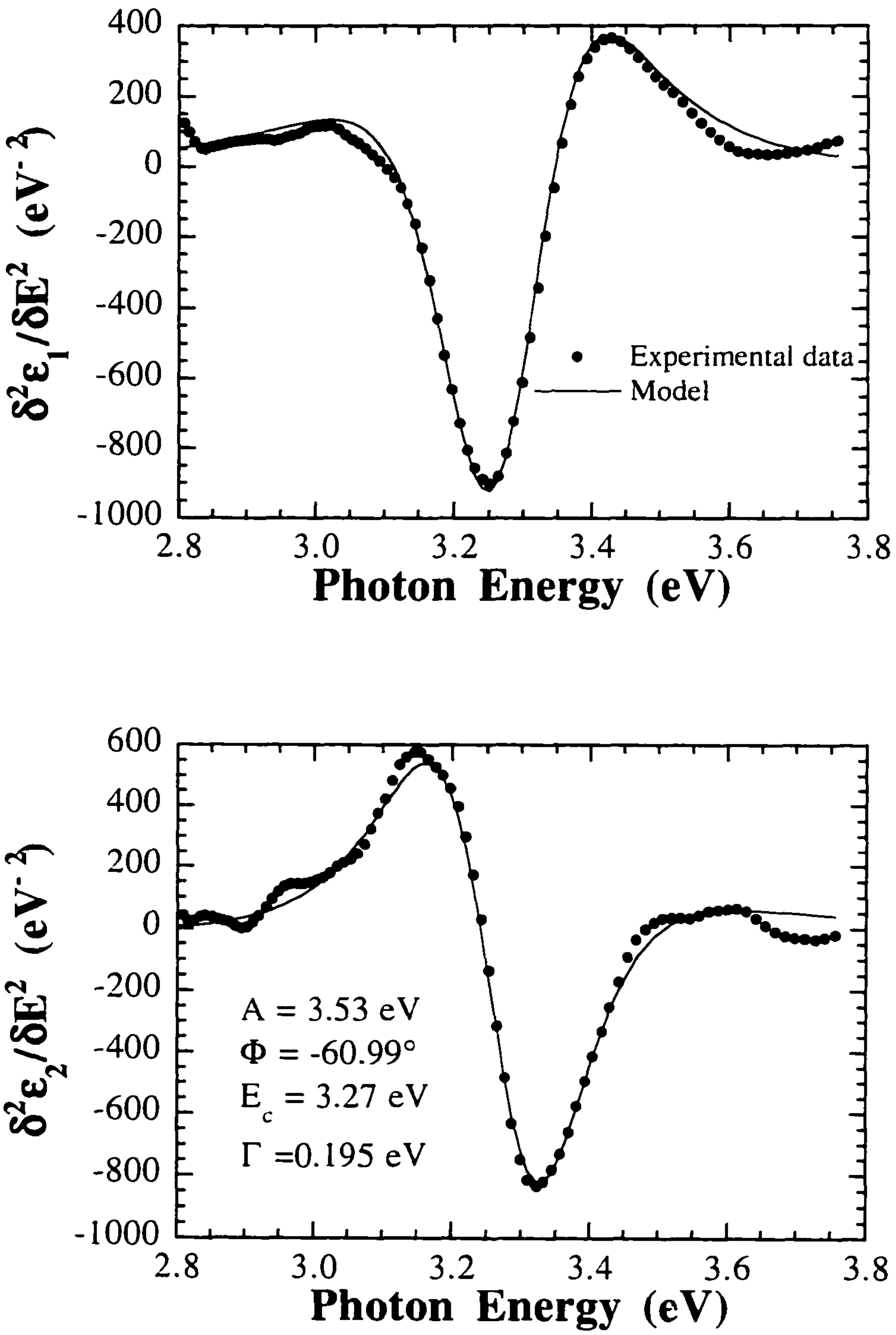

Figure 6.1 : Excitonic line shape fits to the Si dielectric function extracted from ellipsometric data in the MBE. The thermocouple temperature was 200 °C and the SE determined temperature was 249 ± 11 °C.

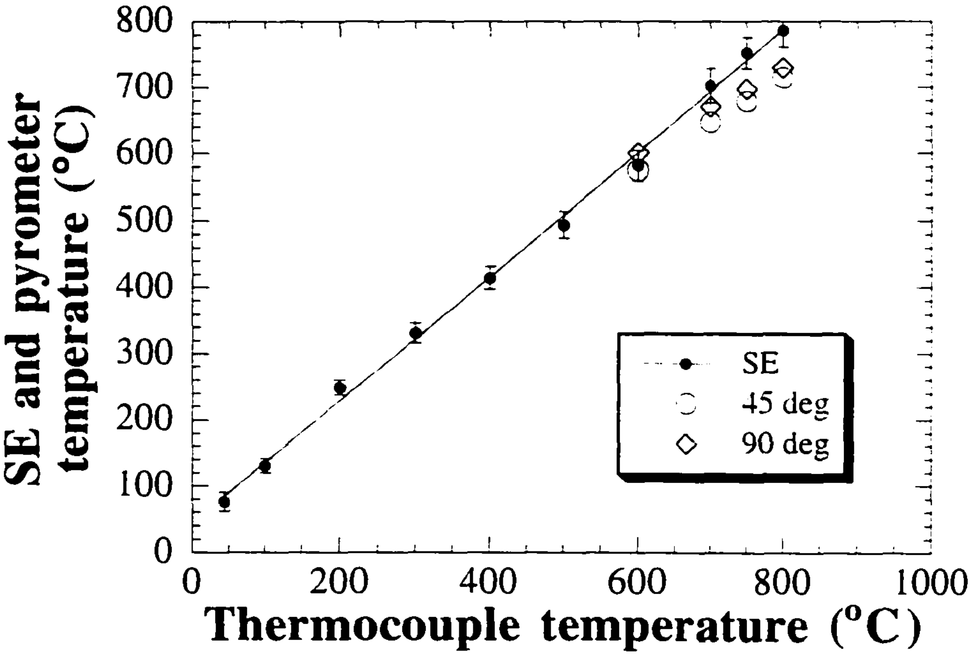

Figure 6.2 : A complete temperature calibration for the MBE.

focus the pyrometer onto the substrate surface since the ozone nozzle blocked the view. Therefore, these measurements were taken from the wafer holder "puck" (always from the same area on the puck). Measurements from different areas of the puck were seen to be different by as much as 50 °C. In measuring the temperature by SE, this variability is eliminated (the measurement is much less operator dependent). It was found that the Si substrate surface temperature could be linearly related to the MBE thermocouple temperature by:

$$SE\ temperature(^{\circ}\mathrm{C}) = 42.7 + 0.93(thermocouple\ temperature(^{\circ}\mathrm{C})) \tag{6.3}$$

As mentioned, the pyrometer measurements are affected by the assumption of an emissivity of the surface that is being measured. This can be a significant factor when obtaining measurements on different wafer holders that may be coated with material from previous depositions. Thus, for these measurements, the wafer holder was thoroughly scraped clean prior to mounting the Si sample. In addition, it is critical that the temperature calibration be completed whenever the MBE chamber is opened to atmosphere. During an opening the position of the thermocouple can change, resulting in a drastic change in the SE temperature calibration.

6.2 Oxide Deposition on Silicon

Since SE is sensitive both to the thickness and the dielectric function of the material depositing on the substrate, it can provide a quantitative value for the incorporation of the incoming flux into the growing film. Then, by comparing the *in situ* atomic absorption (AA) flux measurements to the SE determined thickness as a function of time, the sticking coefficient of various species can be determined. This comparison can be augmented by measuring the flux before and after the deposition using a quartz crystal monitor (QCM), as well.

This was done for the deposition of Y_2O_3 on (100) and (111) oriented Si. The Si substrates were prepared as described in chapter 3 using the RCA etch.[210] The ozone background pressure during the deposition was 1×10^{-6} Torr and the substrate temperature (determined by SE) was 720 °C – 740 °C. The Y flux was typically set to between 5 and 7×10^{13} atoms/cm^2•s. The method used to deposit Y_2O_3 on Si is based on the work of Goettler *et al.*[244] and McKee *et al.*[245,246] Initially, enough flux for 3 monolayers of Y is introduced to the substrate surface in vacuum. This causes a RHEED pattern to appear; the pattern indicates the formation of ordered Y_2O_3 at the substrate surface. At this point, the main shutter is closed and ozone is introduced into the chamber. When the ozone pressure is stabilized to 1 × 10^{-6} Torr, the main shutter (which blocks the substrate from exposure to all of the sources and the ozone nozzle) and the Y shutter are opened simultaneously and deposition proceeds until the desired thickness is achieved.

Fig. 6.3(a) shows a final RHEED pattern subsequent to deposition on (111) Si. It is indicative of (111) oriented Y_2O_3, and confirms that the growth is epitaxial. Fig. 6.3(b) gives similar data for deposition of (110)-Y_2O_3 on (100) Si. The spottiness of this RHEED pattern is most probably due to outgrowths of (110)-oriented Y_2O_3. The breadth of the spots is indicative of very small (in height and lateral extent) outgrowths.

Fig. 6.4(a) shows the Θ-2Θ x-ray measurement of the (111)-oriented film. The absence of second phases in the x-ray pattern in conjunction with the streaks in the RHEED pattern suggest that the surface is smooth. Fig. 6.4(b) is a φ-scan of the $\bar{2}22$ Y_2O_3 peak, indicating the film is epitaxial. The smaller peaks in that figure arise from the shoulder of the Si $\bar{1}11$ peak. Fig. 6.5(a) shows x-ray measurements for the film deposited on (100) oriented Si. In this case, the film is > 95 % (110)-oriented Y_2O_3, with a small fraction of (111)-oriented Y_2O_3. Fig. 6.5(b) is a φ-scan of the 404 Y_2O_3 peak. This scan indicates that the film has 90° rotation twins. One of the twins has an epitaxial relationship with Si of: $(110)_{Y_2O_3} // (100)_{Si}$ and $[001]_{Y_2O_3} // [011]_{Si}$. The other is: $(110)_{Y_2O_3} // (100)_{Si}$ and $[001]_{Y_2O_3} // [01\bar{1}]_{Si}$.

Real-time SE data for the growth of the film shown in Figs. 6.3(b) and 6.5 is given in Fig. 6.6. Here, the Si ellipsometric spectra at the growth temperature can be

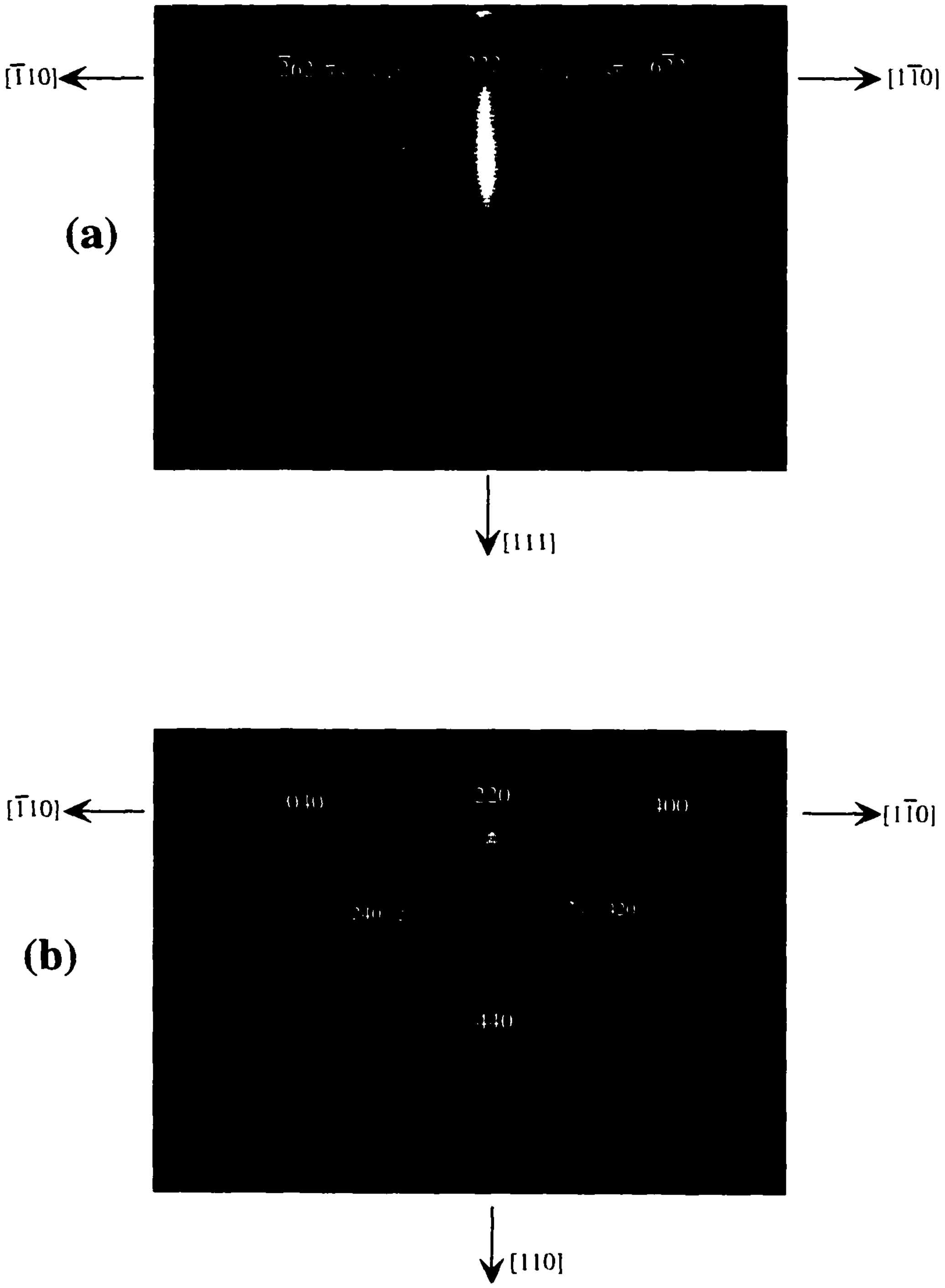

Figure 6.3 : (a) Final RHEED image of a (111)-oriented Y_2O_3 film on (111) Si. The image was taken along the $[11\bar{2}]$ azimuth. (b) Final RHEED image of a (110)-oriented Y_2O_3 film on (100) Si. The image was taken along the [001] azimuth.

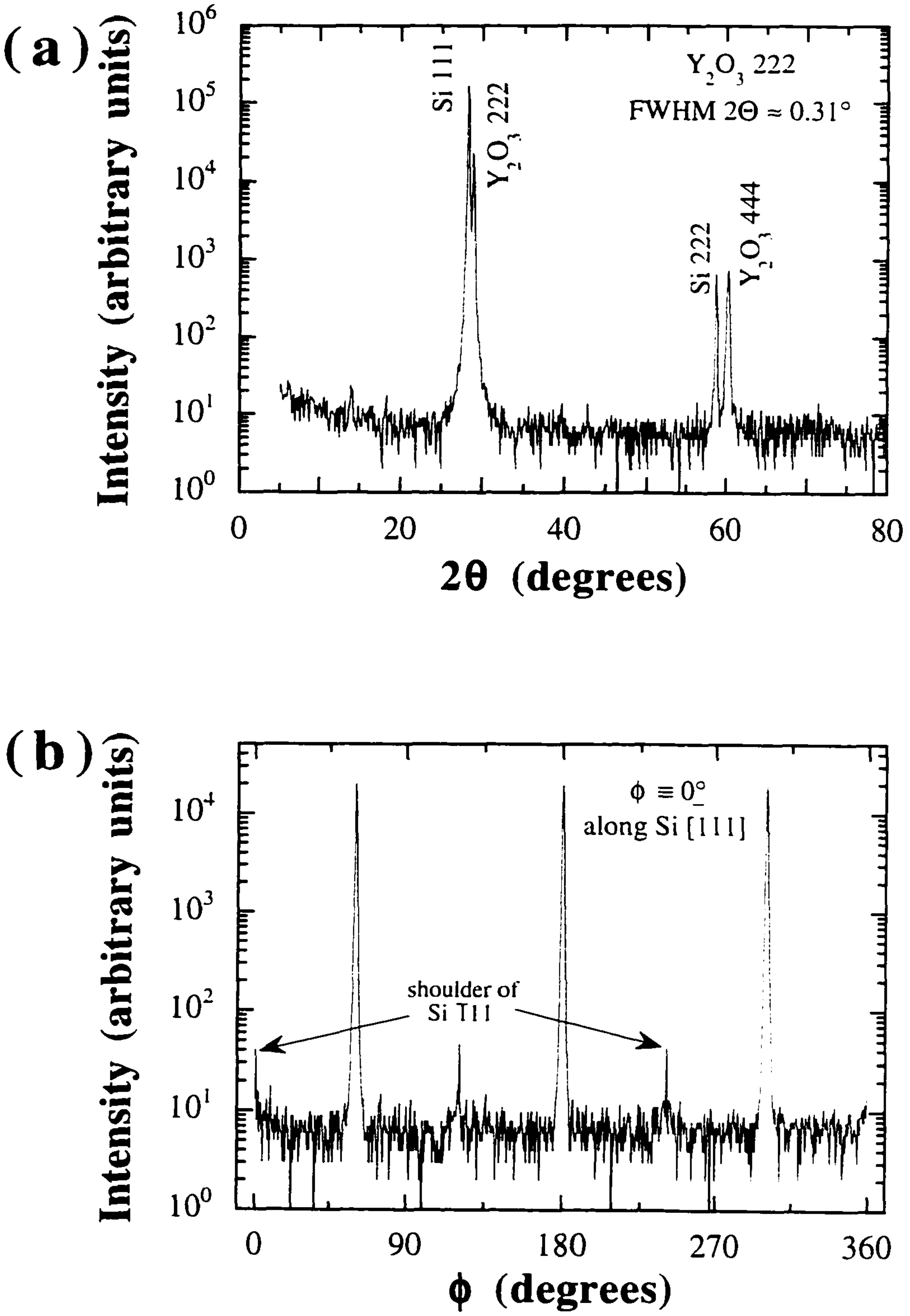

Figure 6.4 : (a) Θ-2Θ x-ray measurements for a (111)-oriented Y_2O_3 film on (111) Si. (b) a φ-scan of the Y_2O_3 $\bar{2}22$ peak.

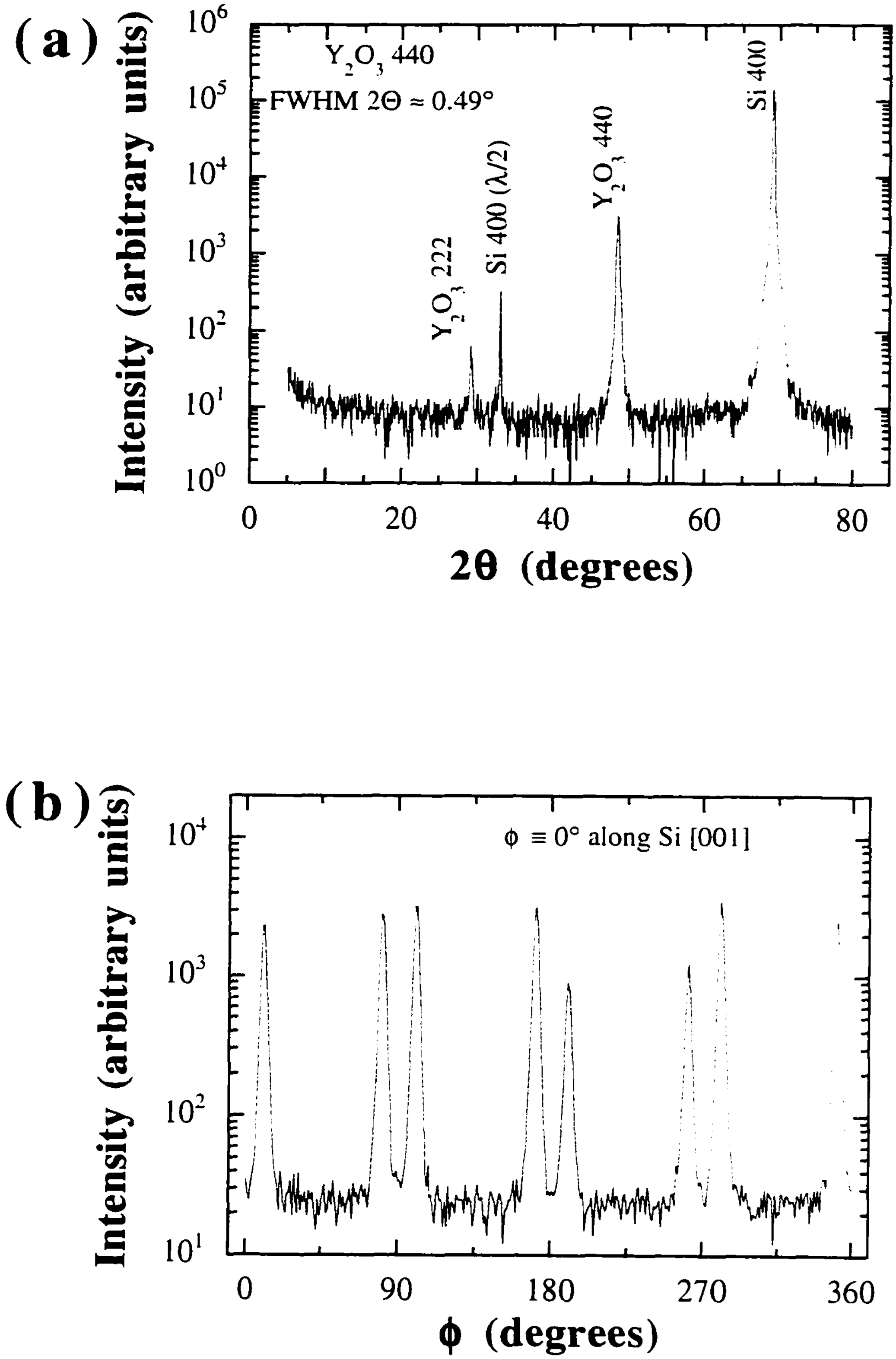

Figure 6.5 : (a) Θ-2Θ x-ray measurements for a (110)-oriented Y_2O_3 film on (100) Si. (b) a φ-scan of the Y_2O_3 404 peak.

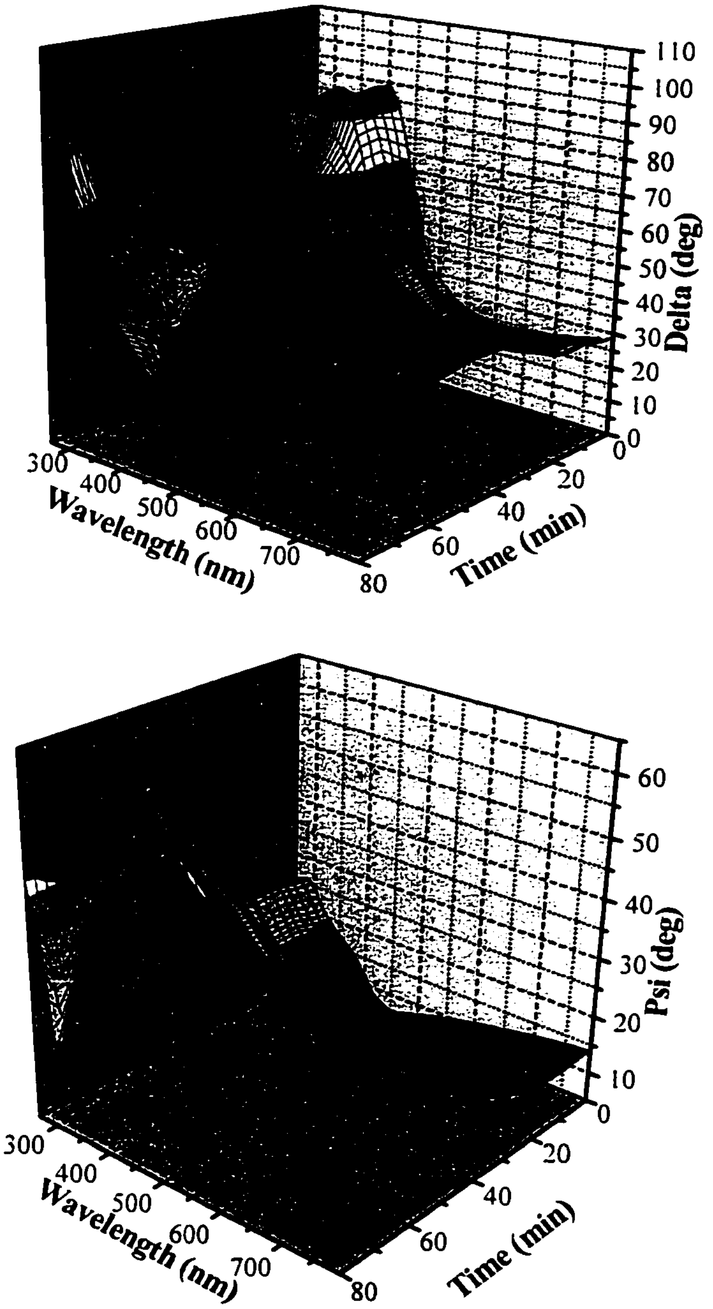

Figure 6.6 : RTSE data for (110) Y_2O_3 deposition on (100) Si.

seen prior to initiation of deposition. At the onset of growth, the peak heights in Δ (between 300 and 400 nm) decrease rapidly. Thus, it is clear that the magnitude of these peaks at a given temperature is very sensitive to the presence of an overlayer. During the deposition, the development of interference fringes can be seen in the data. This is due to the interference between reflections from the surface of the growing Y_2O_3 film and the interface between the Y_2O_3 and Si.

After deposition, the RTSE data were modeled at various points throughout the deposition sequence. In addition, after removal of the sample from the MBE, *ex situ* ellipsometric data were obtained to confirm the results of the RTSE analysis. The results of the *ex situ* modeling are given in Fig. 6.7. The fits are very good, with a final σ value of 0.048. Several geometries were attempted for the modeling; including those with an SiO_2 layer at the interface, or surface roughness or a low density layer at the interface. The best fit geometry for these data did not include any surface roughness or an interfacial layer. The film thickness was determined to be 1330 Å ± 3 Å. Modeling the final RTSE spectra at the growth temperature resulted in a film thickness of 1325 Å ± 11 Å. The evolution in thickness determined from modeling the RTSE spectra during deposition is given in Fig. 6.8. Again, the best fit models did not include any surface roughness. Based on these data, a deposition rate of 11.2 Å/minute was extracted. In addition, the fitted line has an intercept of ≈ 0 Å, as is expected.

In order to confirm the lack of surface roughness in the best fit geometries from the SE analysis, the sample was observed using atomic force microscopy (AFM). The results of this are shown in Fig. 6.9. Here, it can be seen that the surface structure

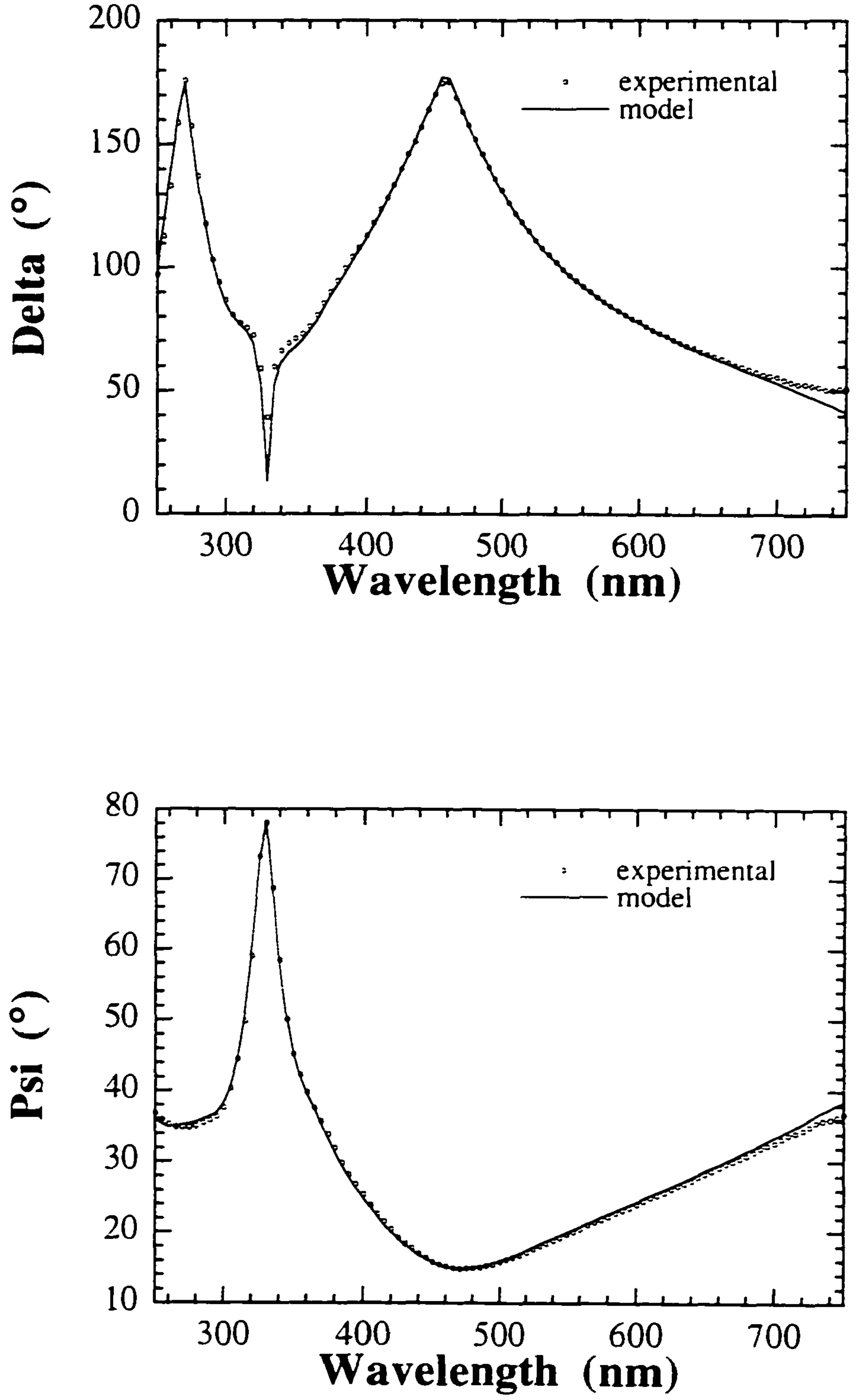

Figure 6.7 : *Ex situ* ellipsometric data and model for a (110)-oriented Y_2O_3 film on (100) Si.

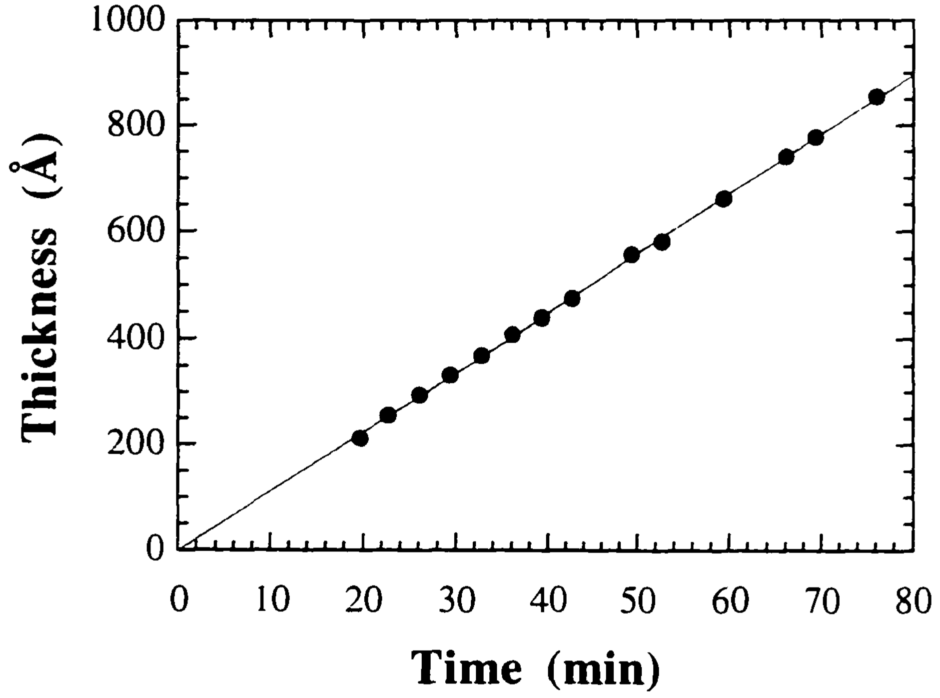

Figure 6.8 : Best fit film thicknesses determined from analysis of RTSE data taken during the deposition of (110) Y_2O_3 on (100) Si.

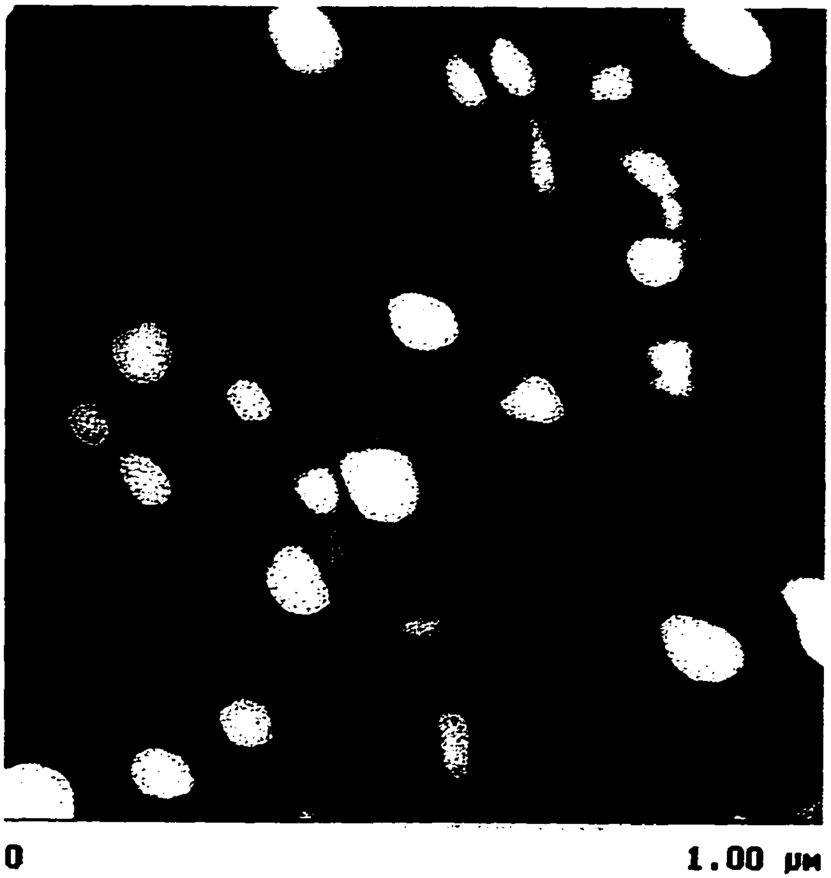

Figure 6.9 : AFM image of a (110) Y_2O_3 film deposited on (100) Si. The image is 1 µm x 1µm. The particles are 6 nm high and the RMS roughness of the underlying basket-weave structure is 6 Å.

consists of a very smooth, basket-weave structure with some larger particles on the surface. The larger particles are between 75 nm and 125 nm across, and ≈ 6 nm high. The dimension of these particles is near the point where the Bruggeman effective medium approximation begins to break down (when particle sizes are ≥ 0.2 times the wavelength of the probing light).[231,247] Thus, it is not surprising that they cannot be modeled effectively. The RMS roughness of the underlying basket-weave structure is 6 Å, confirming that the film is smooth. The inability to detect this very thin layer of roughness in the SE analysis was due to excessive correlation between variables when roughness was introduced.

Similar analysis was performed on the (111) oriented Y_2O_3 film deposited on (111) oriented Si. The results of the RTSE analysis as a function of time are given in Fig. 6.10. In this case, a growth rate of 13.7 Å/minute was extracted. The final thickness obtained by SE was 825 Å ± 11 Å, and again, surface roughness or an SiO_2 layer did not improve the fits significantly. A very smooth surface was also implied by the RHEED pattern. The results of AFM analysis on the film are given in Fig. 6.11. The RMS roughness value was 2.7 Å, confirming the RHEED and SE results. The final thickness obtained by measuring the flux by QCM before and after deposition was 850 Å ± 40 Å (assuming a 5% variability in the flux determined by the QCM[248]), showing good agreement.

One of the key goals of this thesis was to determine how RTSE could be used to complement existing *in situ* diagnostic tools. In particular, AA measurements describe the flux which is incident on the substrate, while SE is sensitive to the species which are

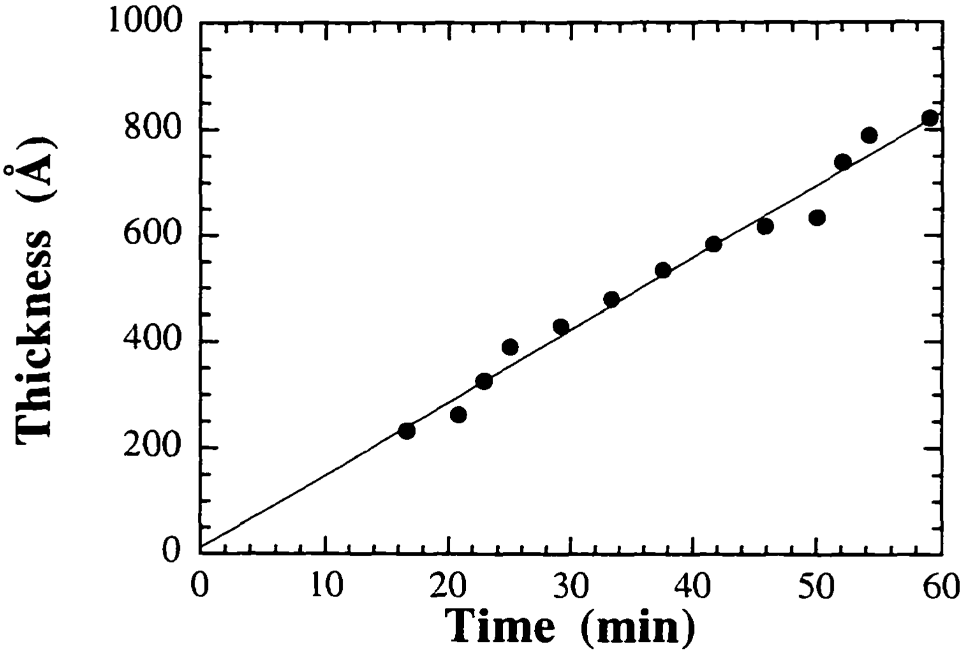

Figure 6.10 : Best fit film thickness determined from analysis of RTSE data taken during the deposition of (111) Y_2O_3 on (111) Si.

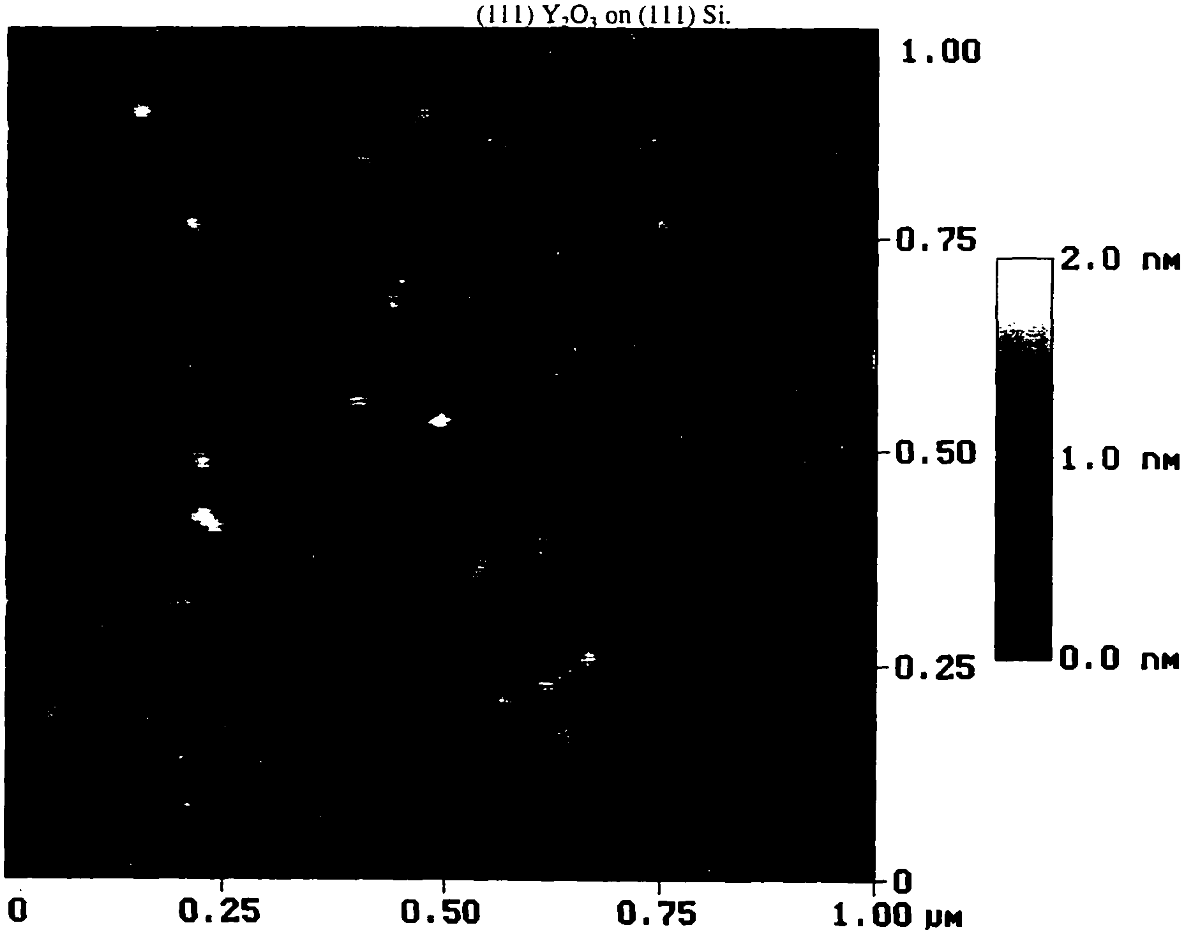

Figure 6.11 : AFM image of a (111) Y_2O_3 film on (111) Si.

incorporated into the film. Consequently, comparison of the two numbers enables the sticking coefficient to be calculated. This was done as follows for the (110) oriented Y_2O_3 film:

- Y flux (measured by AA) = 4.94×10^{13} atoms/cm^2•sec
- Shutter open (measured by MicroCrystal©) = 6,952 seconds
- Total Y dose = 3.4×10^{17} atoms/cm^2
- Thickness by AA = $\dfrac{3.4\times10^{17}\,\text{atoms}/\text{cm}^2}{7.1\times10^{14}\,\text{atoms}/\text{monolayer}}\left(\dfrac{10.6\ \text{Å}}{4\ \text{monolayers}}\right)$

$\approx$ **1280 Å ± 30 Å**

This is in comparison to the SE obtained film thickness of ≈ **1325 Å ± 11 Å**. Using the SE-determined deposition rate, and the time the shutter was open, a final film thickness of **1300 Å** is found. For a direct comparison, the same sample was sent for Rutherford backscattering spectroscopy analysis (RBS). Results from these measurements give an absolute quantification of the amount of Y and O in the thin film. For this sample, there was found to be $334 \pm 10 \times 10^{15}$ Y atoms/cm^2 and $500 \pm 28 \times 10^{15}$ O atoms/cm^2. Based on these values, and assuming a bulk density of 5.01 g/cm^3, a thickness of **1250 Å ± 30 Å** is obtained. Thus, the agreement between AA (calibrated with the QCM), RTSE and RBS is excellent. In addition, the agreement between SE (which is sensitive to the incorporation of flux in the film) and AA (which is a measure of the flux to the film surface) indicates that the sticking coefficient of Y in Y_2O_3 is $\approx 1.00 \pm 0.07$.

The ability of RTSE to measure the sticking coefficient holds some advantages over other methods. For instance, when the QCM is used to measure the sticking coefficient, the fact that the QCM is water cooled must be accounted for. For elements with appreciable re-evaporation rates (i.e. Pb and Bi), this is significant. That is, when the same element is deposited on a hot substrate, the sticking coefficient is likely to be less than that measured by the QCM (at a much lower temperature). For this case, RTSE can directly measure the amount of incorporated species on the hot substrate. In addition, in certain cases, there are changes in the deposition rates when two species are deposited together with respect to delivering them independently. Since RTSE gives both thickness and optical properties, it should be good for composition determination even in this case. Finally, some elements are not well suited to atomic absorption analysis (i.e. Ti and Al); the absorption values are much too low to quantify the flux. In this case, RTSE can be extremely helpful for flux calibration.

From the SE analysis subsequent to deposition, the optical properties of the sample were obtained at the deposition temperature, as well as room temperature. This was done using a Sellmeier oscillator (see chapter 4) to model the dispersion of the refractive index. In the models, no amount of absorption was detected, indicating the film is well oxidized. The values were compared to bulk values obtained by measurement of the Brewster angle in reflection and by interferometry.[249] This comparison is shown in Fig. 6.12, along with the high temperature data and values from evaporated Y_2O_3 films deposited by Feldman *et al.*[250] It should be noted that the values of Feldman *et al.* are very similar to other studies on Y_2O_3 thin films.[251-253] It can be seen that previous results on Y_2O_3 films show very low refractive index values compared to bulk. The authors attributed the lower values to second phase formation, changes in film stoichiometry, stress and observed extended lattice constants. The films from this work show values much closer to those of the bulk. The data for the MBE-deposited film at 730 °C show a shift in the onset of absorption to lower wavelengths and an increase in the magnitude of the refractive index.

From examination of Fig. 6.5, lattice constants of 10.63 Å ± 0.02 Å for the *a* and *b* axes and 10.59 Å ± 0.06 Å for the *c*-axis were determined (compared to 10.604 Å for the bulk material (JCPDS card #43-631)). This corresponds to a density of 4.99 ± 0.05 g/cm^3 (compared to 5.01 g/cm^3 for the bulk material). From a volume fraction analysis, it can be calculated that ≈ 0.5% air mixed with bulk Y_2O_3 is needed to bring the bulk density down to the value obtained for the film. Using Bruggeman effective medium averaging to generate refractive index values, it can be shown that mixing 1.5% air with the bulk refractive index curve brings it down to the observed film values. This lower density is believed to be the source of the lower refractive index values of the epitaxial films grown here.

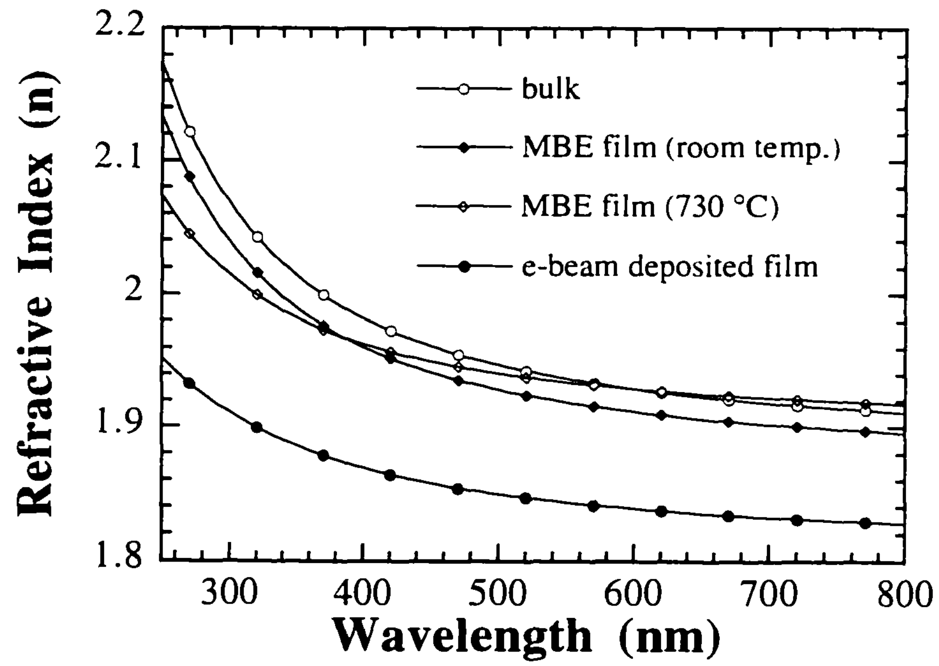

Figure 6.12 : Comparison of refractive index values for bulk Y_2O_3,[249] MBE deposited Y_2O_3 at room temperature and 730 °C, and evaporated Y_2O_3 from Feldman *et al.*[250]

Finally, observation of the growth of Y_2O_3 on Si by RTSE indicated a method for real-time extraction of the thickness and the growth rate. That is, these values can be rapidly determined during the growth, not by post-deposition modeling the RTSE data. From the real-time SE spectra shown in Fig. 6.6. A minimum in Δ can be seen in the last spectra at ≈ 500 nm. This minimum is an interference fringe and is directly related to the optical path length of the light through the depositing film. The movement of this minimum across the wavelength range is determined by the current thickness of the film. For the derived thickness to be accurate, the optical properties of the film must be previously known, and the morphology of the growing should be independent of time. For example, based on the deposition of (110) and (111) Y_2O_3, the optical properties of the films were determined, and the surfaces were found to be very smooth. Therefore, for future depositions, the relationship between the minimum in Δ and the thickness of the film can be used. Fig. 6.13 shows the linear behavior of the relationship between the

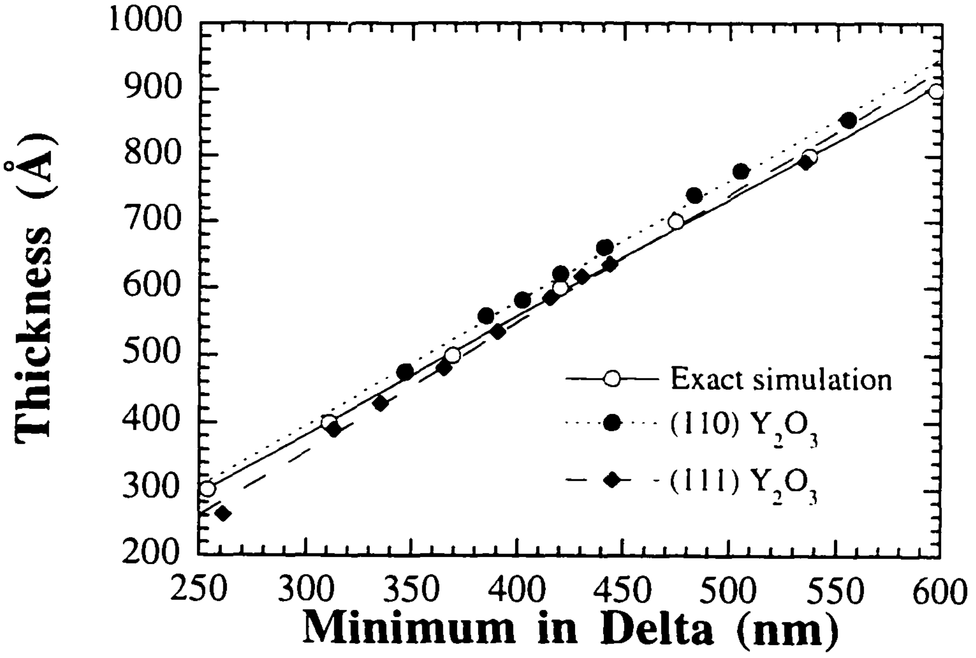

Figure 6.13 : Linear relationship between the thickness of the film and the position of the minimum in Δ.

thickness and the minimum in Δ. Also plotted is an exact simulation of the position of the fringe for a given thickness calculated from the optical properties of the (110)-oriented Y_2O_3 film.

RTSE has been shown to be useful for characterization of the growth of one of the constituent oxides of YBCO. It is necessary to do a similar analysis for the other constituent oxides, as well. This work does show, however, that RTSE can be successfully applied to the deposition of oxides by MBE. The RTSE complements AA, RHEED and QCM measurements in various ways. Extension of this technique to the deposition of YBCO should prove useful for understanding the growth mechanisms and surface roughness development of these films.

Chapter 7

OXYGEN DIFFUSION IN YBCO

As described in chapter 1, one of the major materials-related issues delaying the implementation of high-T_c Josephson junction technology is the ability to attain smooth YBCO films that are fully oxygenated all the way up to the interface with the interlayer material. Therefore, it is critical to understand the oxygen diffusion behavior in YBCO during, and subsequent to, thin film processing in various environments. This will assist in the development of reliable and reproducible Josephson junction-based devices.

This chapter describes the use of *ex situ* and real-time SE for observation and characterization of oxygen diffusion in YBCO films deposited by MBE and 90° off-axis sputtering. Microstructural and structural information on the films used in these experiments is also given, as factors like surface precipitates or misoriented material would be expected to affect the diffusion rates. This information is missing from previous studies of oxidation/reduction kinetics in YBCO by SE.

7.1 *Ex Situ* Single Wavelength Ellipsometry

The initial studies to observe oxygen diffusion in YBCO films were completed on the *ex situ* ellipsometer described in chapter 3. Due to the slower spectroscopic data collection (≈8 minutes for a full spectrum), only a single wavelength (302 nm) was monitored during the heating of a YBCO film. According to the studies on the sensitivity limits, this wavelength provides the best sensitivity to the oxygen content in the film. For the data reported here, MBE-deposited films on $SrTiO_3$ were used. The films were deposited at 720 °C (measured by pyrometry) in a background pressure of 2.4×10^{-5} Torr of an 80% O_3/20% O_2 mixture. Typical lattice constants of the films as determined by x-ray diffraction were $c = 11.72 \pm 0.03$ Å and $a = 3.85 \pm 0.04$ Å, indicating a δ value close to 0.*[23] The surface as measured by STM is shown in Fig. 7.1. The growth spirals discussed in chapter 2 are apparent. In addition, no surface precipitates were observed in the optical micrographs.

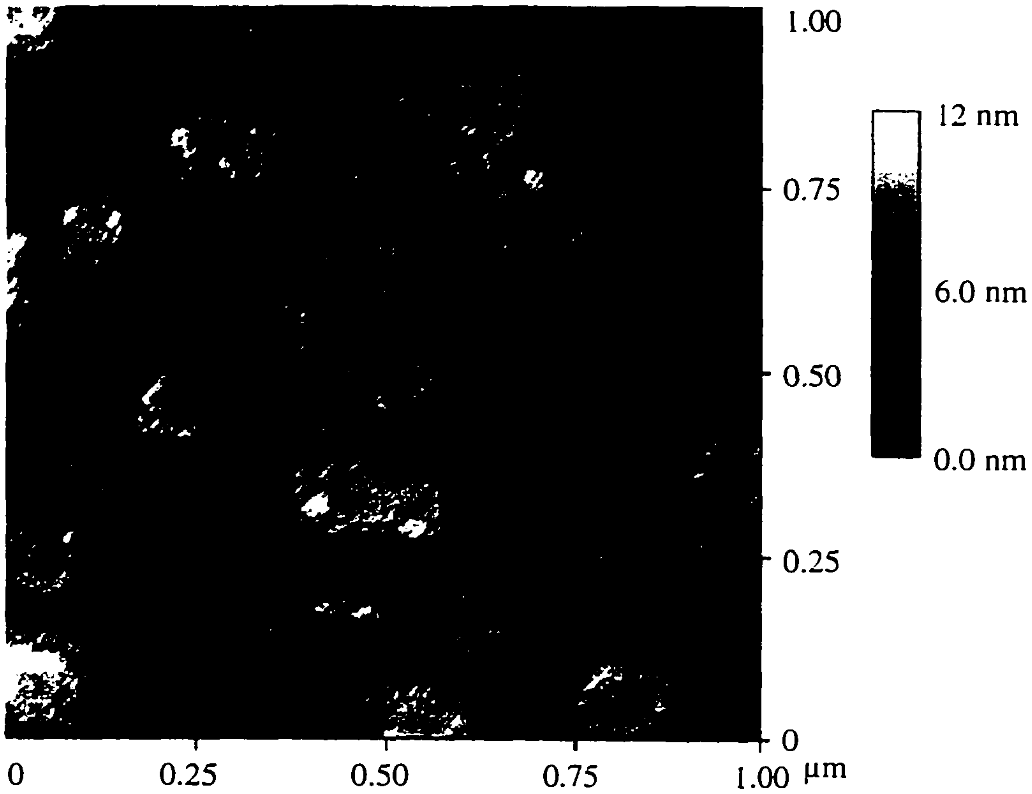

Figure 7.1 : An STM image of the MBE-deposited YBCO film on $SrTiO_3$ used for the *ex situ* single wavelength ellipsometry studies of oxygen diffusion.

The sample was heated under a flowing Ar atmosphere at 50 °C/minute up to 530 °C while single wavelength ellipsometric data at 302 nm were collected at a 70° angle of incidence. The results of this experiment are shown in Fig. 7.2. The most

---

[*] The relationship between δ and the c-axis length for bulk YBCO is not as accurate for thin films due to extended lattice constants arising from factors other than solely oxygen deficiency (e.g., thermal expansion mismatch, lattice mismatch, bombardment, etc.[254])

noticeable feature of this plot is the drastic change in Δ and Ψ beginning at 400 °C - 450 °C. Δ increases by 66° while Ψ drops 9° and then increases by 12°. The observed changes took place in ≈2 minutes. X-ray diffraction measurements subsequent to this processing showed an extension of the c-axis lattice constant to 11.86 ± 0.05 Å, indicating a δ value near 1. Thus, the dramatic changes seen in the ellipsometric spectra can be attributed to oxygen out-diffusion from the film. Again, the magnitude of the changes seen is not surprising given the strong dependence of the dielectric function on oxygen content at this wavelength. It should be noted that the overall quality of the x-ray results were degraded somewhat (i.e., increased FWHM, decreased peak intensity). This is most probably due to the fact that these experiments were conducted in an essentially open system. That is, atmospheric humidity was present which could accelerate

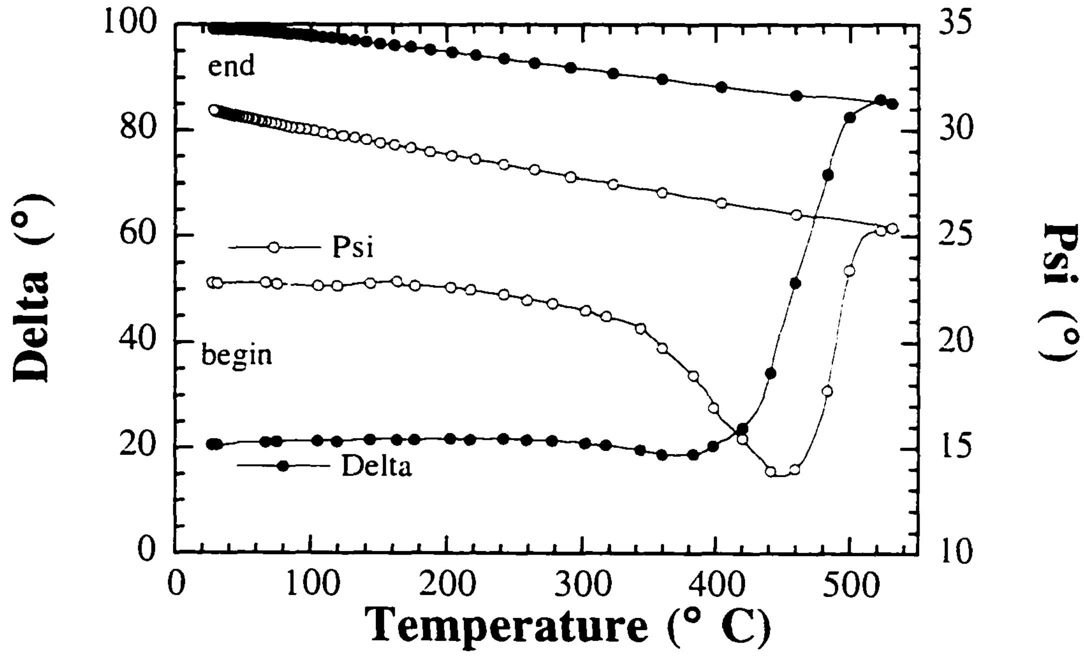

Figure 7.2 : Δ and Ψ for an initially fully oxygenated MBE-deposited YBCO film on $SrTiO_3$ upon heating in a flowing Ar atmosphere at 50 °C/minute up to 530 °C.

formation of surface contaminant layers during heating. The other noticeable feature of this graph is the significant difference between the temperature dependence of the ellipsometric parameters for oxygen-deficient and oxygen-rich YBCO. Between 30 °C and 400 °C, Δ changes from 20.8° to 20.4° (0.4°) for fully oxygenated YBCO and from 88.4° to 99.6° (11.2°) for oxygen-deficient YBCO.

In order to interpret data for oxygen in-diffusion into an initially oxygen-deficient film, the temperature dependence of the ellipsometric parameters must be accounted for. This is required to distinguish changes in the ellipsometric parameters due to oxidation of the film from those due to their temperature dependence. To measure the temperature dependence, an initially oxygen-deficient MBE-deposited film (on $SrTiO_3$) was heated to 500 °C under flowing Ar while ellipsometric data at 302 nm (4.1 eV) were collected. The flowing Ar prevented oxidation of the film, thus only the temperature dependence of $YBCO_6$ is observed. Fig. 7.3 shows Δ and Ψ during this heating run. It can be seen that the changes upon heating in Ar are completely reversible. In addition, a linear dependence is observed. The temperature coefficient of Δ is -3.2×10^{-2} °/° C and for Ψ, it is -1.1×10^{-2} °/° C over the plotted temperature range.

Following characterization of the temperature dependence, the same sample (still oxygen-deficient) was heated in an air atmosphere first up to 150 °C and cooled, and then up to 260 °C and cooled (both at 20 °C/minute). By heating in air, oxidation of the film should occur. The results are given in Fig. 7.4, where Ψ is plotted (normalized to the value at room temperature). The reversibility of the data up to 150 °C indicates that these

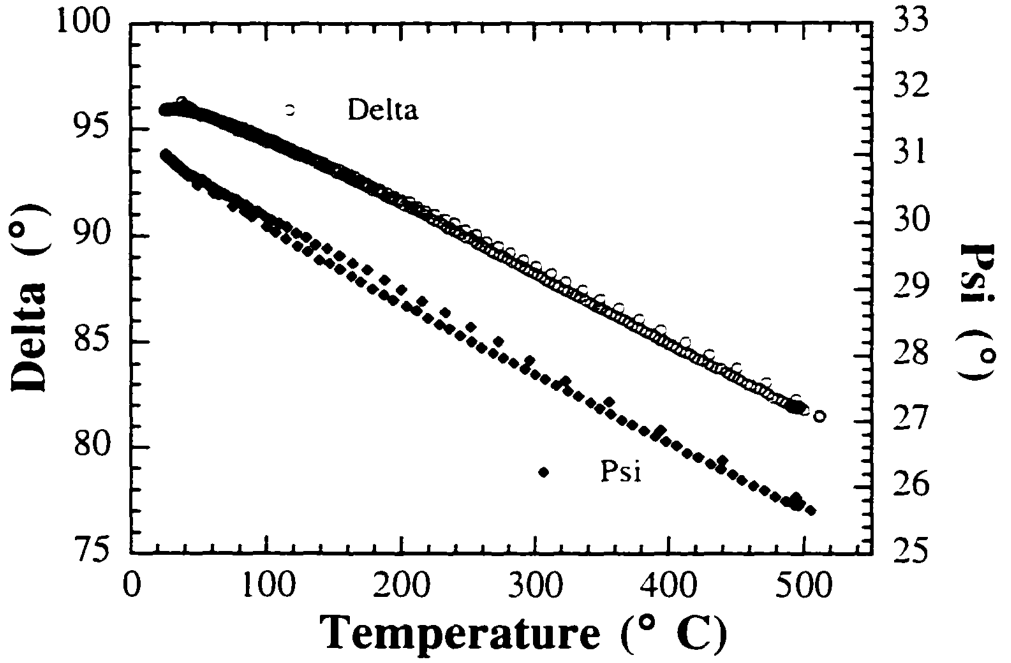

Figure 7.3 : Ellipsometric data at 302 nm for an initially oxygen-deficient MBE-deposited YBCO film heated up to 530 °C in flowing Ar. Note the reversibility of the data, indicating that it is due solely to the temperature dependence of the ellipsometric parameters (and not to changes in δ).

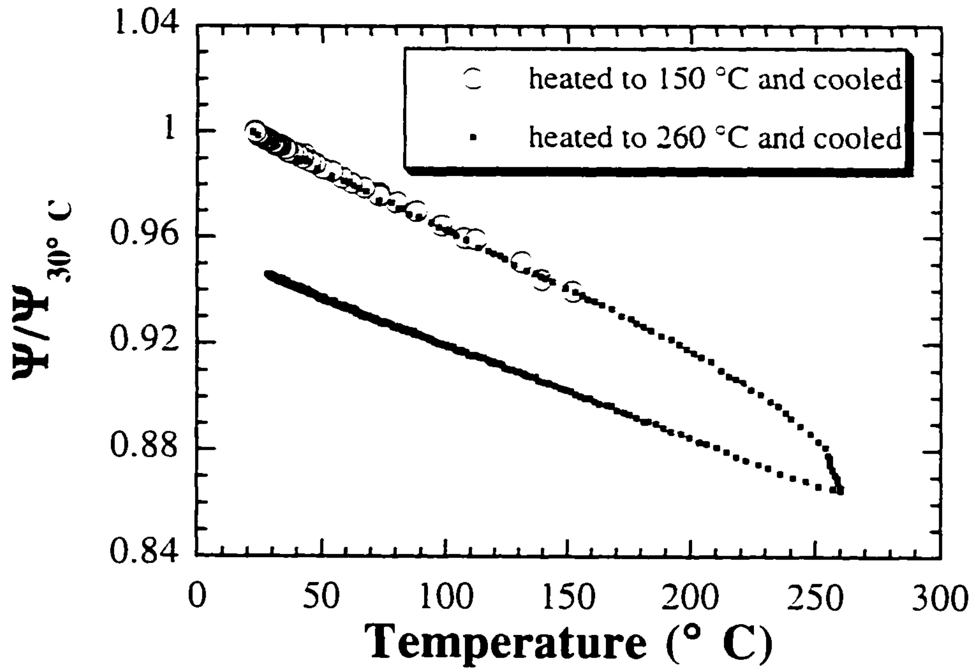

Figure 7.4 : Ψ (normalized to the room temperature value) for an initially oxygen-deficient MBE-deposited YBCO film heated to 150 °C and cooled, then heated to 260 °C and cooled. The irreversibility exhibited on cooling from 260 °C indicates the onset of oxidation in the film.

changes are due to the temperature dependence of the ellipsometric parameters. However, on heating to 260 °C, some irreversibility is exhibited. These additional changes in the ellipsometric parameters are associated with the onset of oxidation in the film. It is estimated that these changes correspond to oxidation of the top 15 - 20 Å of the film from a simple fit of the data assuming a fully oxidized surface on a fully reduced film.

The experiments described above can be extended in temperature up to the point where complete oxygenation of the film occurs. Data showing this are given in Fig. 7.5, where normalized Δ and Ψ (with respect to the values at room temperature) are shown for an MBE-deposited YBCO film on $SrTiO_3$ heated to 500 °C at 20 °C/minute in air. The temperature dependence of the ellipsometric parameters is also plotted for reference. Deviations from the temperature dependence begin to occur at approximately 250 °C, indicating the onset of oxidation. This temperature is similar to that seen in Fig. 7.4. The large changes saturate at $\approx$ 400 °C, indicating the completion of oxidation.

Upon completing similar measurements at slower heating rates (1 °C/minute and 10 °C/minute) the onset of oxidation was seen at progressively lower temperatures, as expected. For a slower heating rate, the time at a given temperature is longer, thus oxidation should be complete at a lower temperature. These experiments were also conducted on pulsed laser deposited and sputtered films. The behavior of the sputtered films was similar to that of the MBE films. The data for the PLD films, however, were affected by the high density of macroparticles present on the film surface.

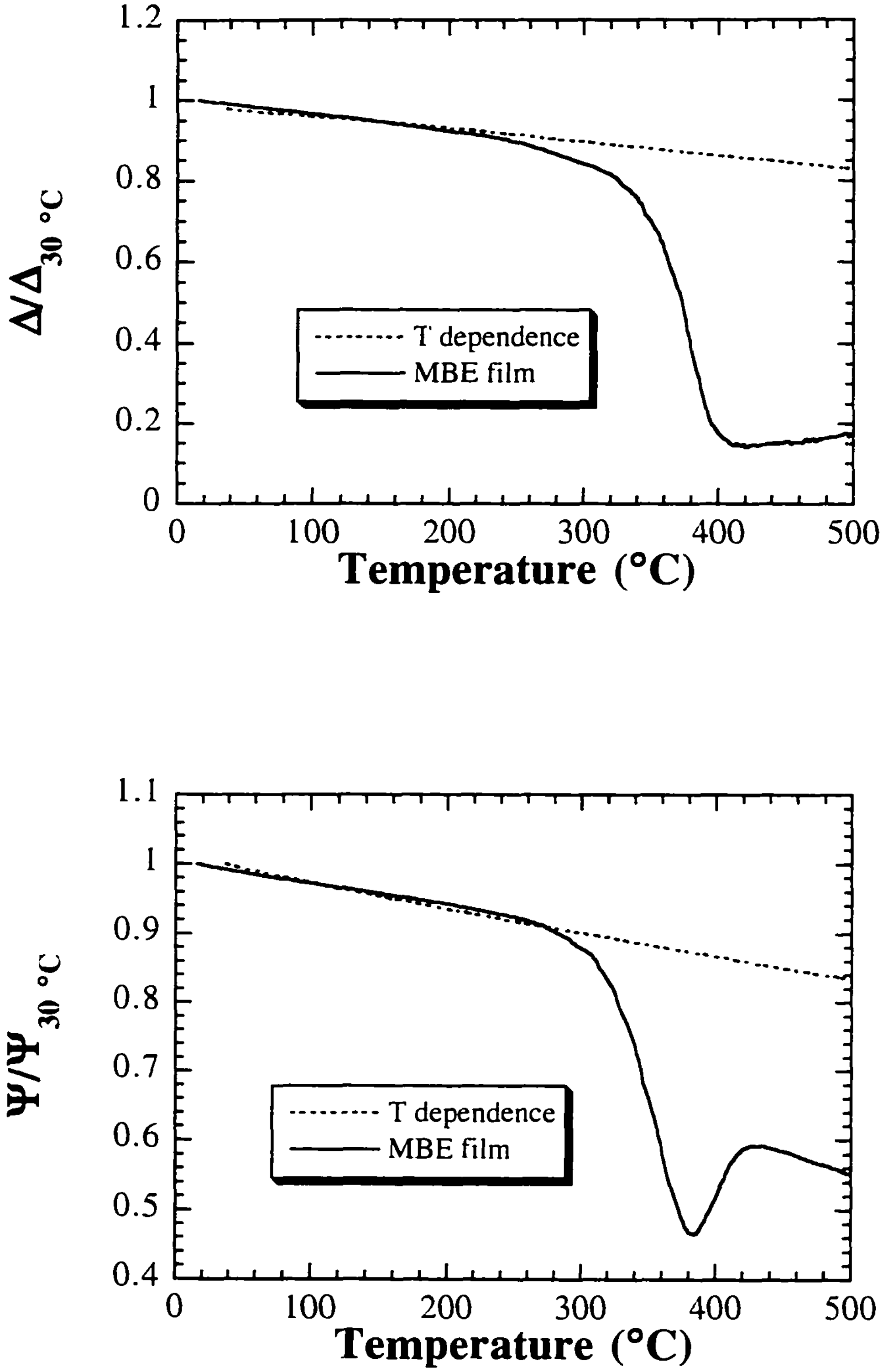

Figure 7.5 : Normalized ellipsometric parameters (with respect to room temperature values) for an initially oxygen-deficient MBE deposited YBCO film heated in air to 500 °C at 20 °C/minute. The temperature dependence from Fig. 7.3 is also plotted.

These experiments are instructive as to the general behavior of oxygen in and out-diffusion, however, completing them in an air atmosphere is not ideal. As described in chapter 2, YBCO can react with air to form a degraded surface layer, which could subsequently affect the diffusion behavior. It should be noted that after several temperature cyclings (> 3) the surface of a given film began to appear cloudy, indicating some amount of surface damage. In addition, x-ray measurements subsequent to heating in air showed decreased intensities and increased full-width-at-half-maximums. This was addressed by performing similar experiments in a vacuum chamber, where the ambient conditions could be controlled.

7.2 Real-Time Spectroscopic Ellipsometry

Using the RTSE described previously, oxygen diffusion experiments were conducted within the MBE chamber in a variety of atmospheric conditions. The following sections describe the results of these experiments and include the spectroscopic temperature dependence of the ellipsometric parameters, the diffusion of oxygen in molecular oxygen and ozone/molecular oxygen atmospheres and finally, the relative reactivity of ozone with respect to molecular oxygen.

7.2.1 The Spectroscopic Temperature Dependence of the Ellipsometric Parameters

A set of experiments was designed to monitor the spectroscopic temperature dependence of the ellipsometric parameters of $YBCO_6$ and $YBCO_7$ at an angle of incidence of 80° in the RTSE over a temperature range of 100 °C to 550 °C. The system used can collect a full spectrum of data in as little as 32 ms, thus the temperature dependence of the entire spectrum can be extracted while the film is heated. In addition to enabling experiments on samples with relatively pristine surfaces (degradation due to exposure to humidity at elevated temperatures is eliminated), the ambient conditions can be precisely controlled. Thus, a particular oxidation state can be maintained over a broader temperature interval. As shown above, Δ and Ψ at 302 nm are affected both by temperature and oxygen content, which makes interpretation of single wavelength real-time diffusion experiments difficult. Therefore, what is desired for a simple *in situ* monitoring system is a wavelength(s) that is (are) relatively insensitive to changes in temperature while maintaining sufficient sensitivity to the oxygen content in the film. Appropriate energy ranges for this can be identified from the RTSE data.

For these spectra, as well as for the rest of the following experiments, a 90° off-axis rf-magnetron sputtered YBCO film on $SrTiO_3$ was used. The sample was 650 Å thick and was found to have an RMS roughness of 20 Å by AFM. An AFM image of the sample surface is given in Fig. 7.6. The spiral features are generally not quite as clear in AFM images (as compared to STM images), however they can be seen. In addition, the sample displayed none of the surface precipitates discussed in chapter 2. From x-ray measurements, the *c*-axis lattice parameter was found to be 11.70 ± 0.01 Å, indicating a δ value close to 0. Since the sample was exposed to air, upon introduction to the chamber the sample was heated to 500 °C under flowing 80% ozone + 20% oxygen (distilled output from the ozone generator) and then cooled to room temperature in the same

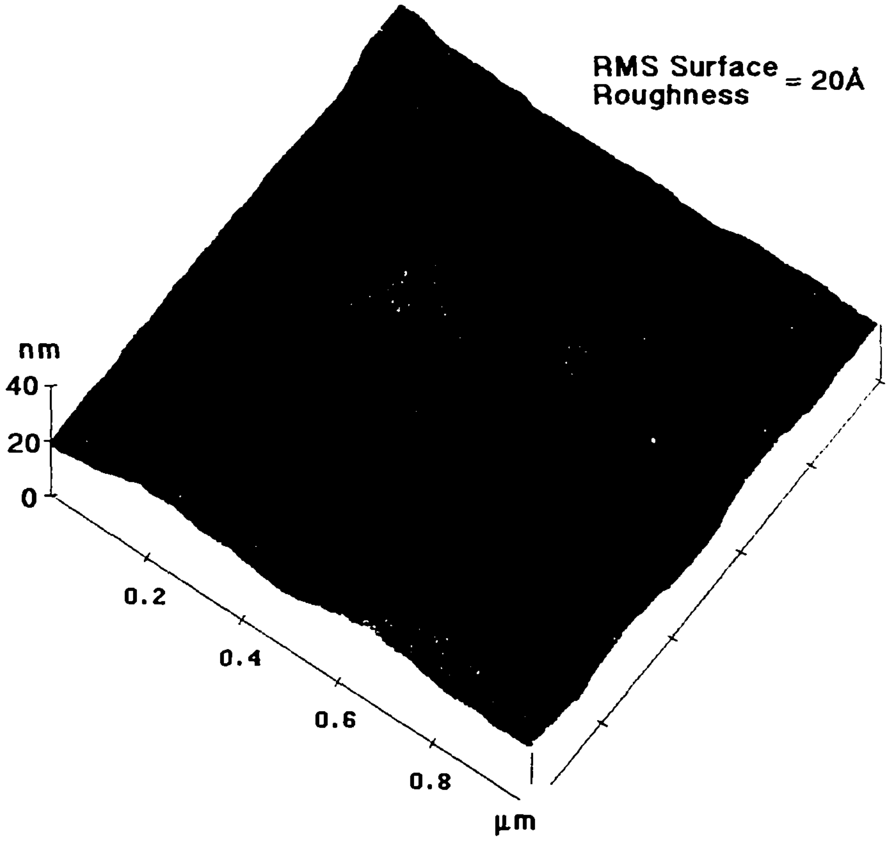

Figure 7.6 : AFM image of a sputter deposited YBCO film on $SrTiO_3$.

environment. This was done in order to attempt to minimize any surface layers that may have formed.

Subsequently, the film was heated in 2 × 10^{-5} Torr of a 10% ozone/90% oxygen mixture (output from the ozone generator) at 1 °C/second. The results of this experiment are shown in Fig. 7.7. For these data, 30 cycles of the polarizer were averaged. From these plots, it can be seen that the temperature dependence of a fully oxygenated YBCO film is not significant for measurements made at an 80° angle of incidence. This result corresponds well with the single wavelength data obtained previously at a 70° angle of incidence. Figs. 7.8 and 7.9 show isoenergetic (same wavelength) traces from the three

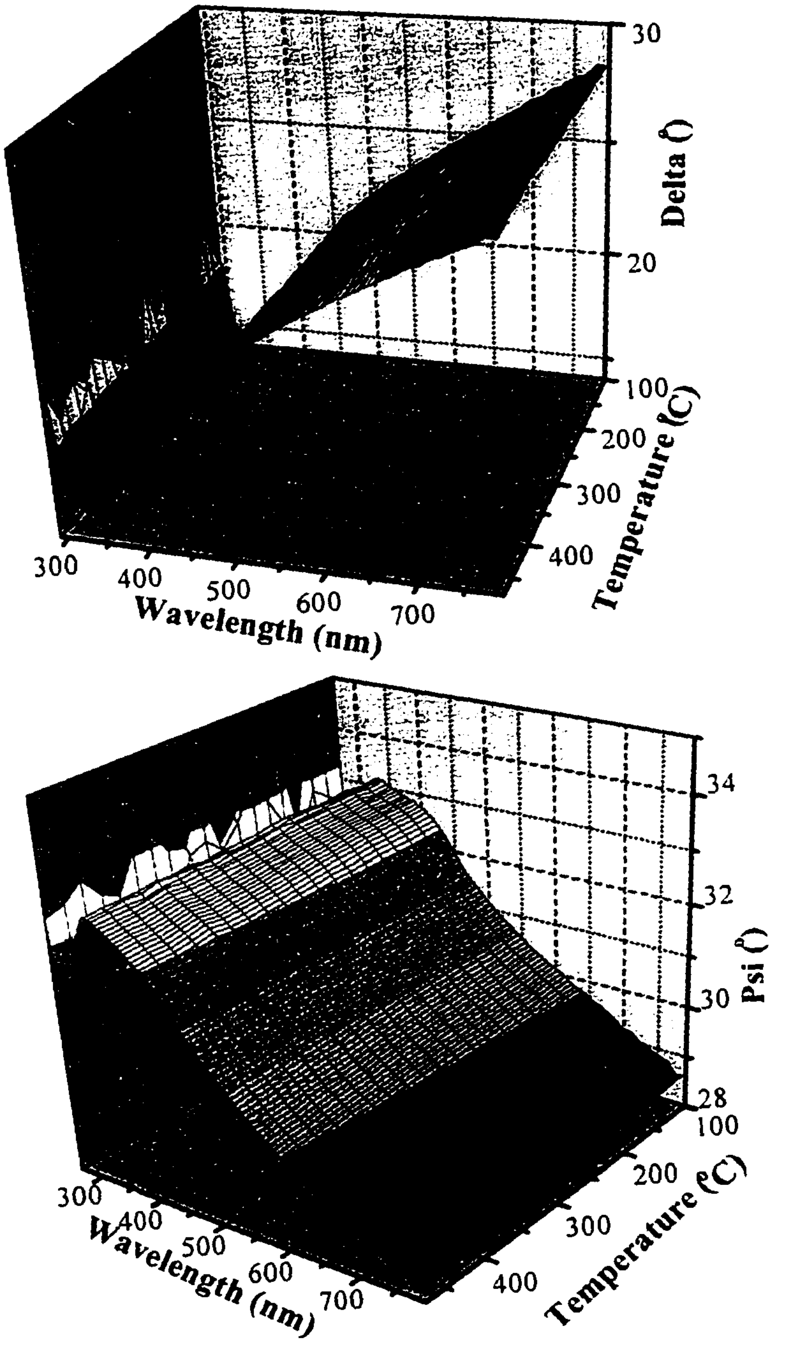

Figure 7.7 : Spectroscopic temperature dependence of YBCO$_7$.

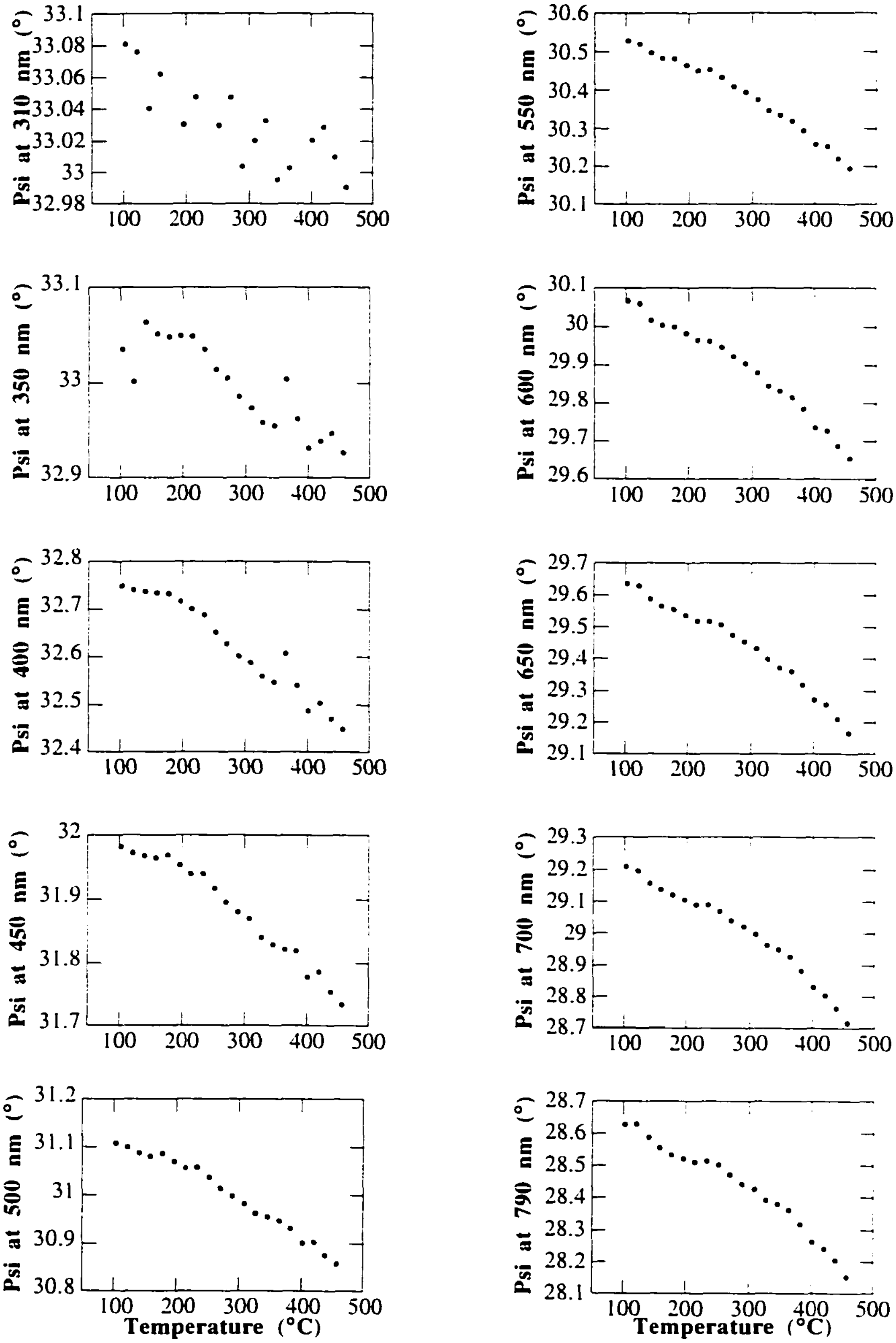

Figure 7.8 : Isoenergetic traces in Ψ for a fully oxygenated YBCO film on $SrTiO_3$ from Fig. 7.7

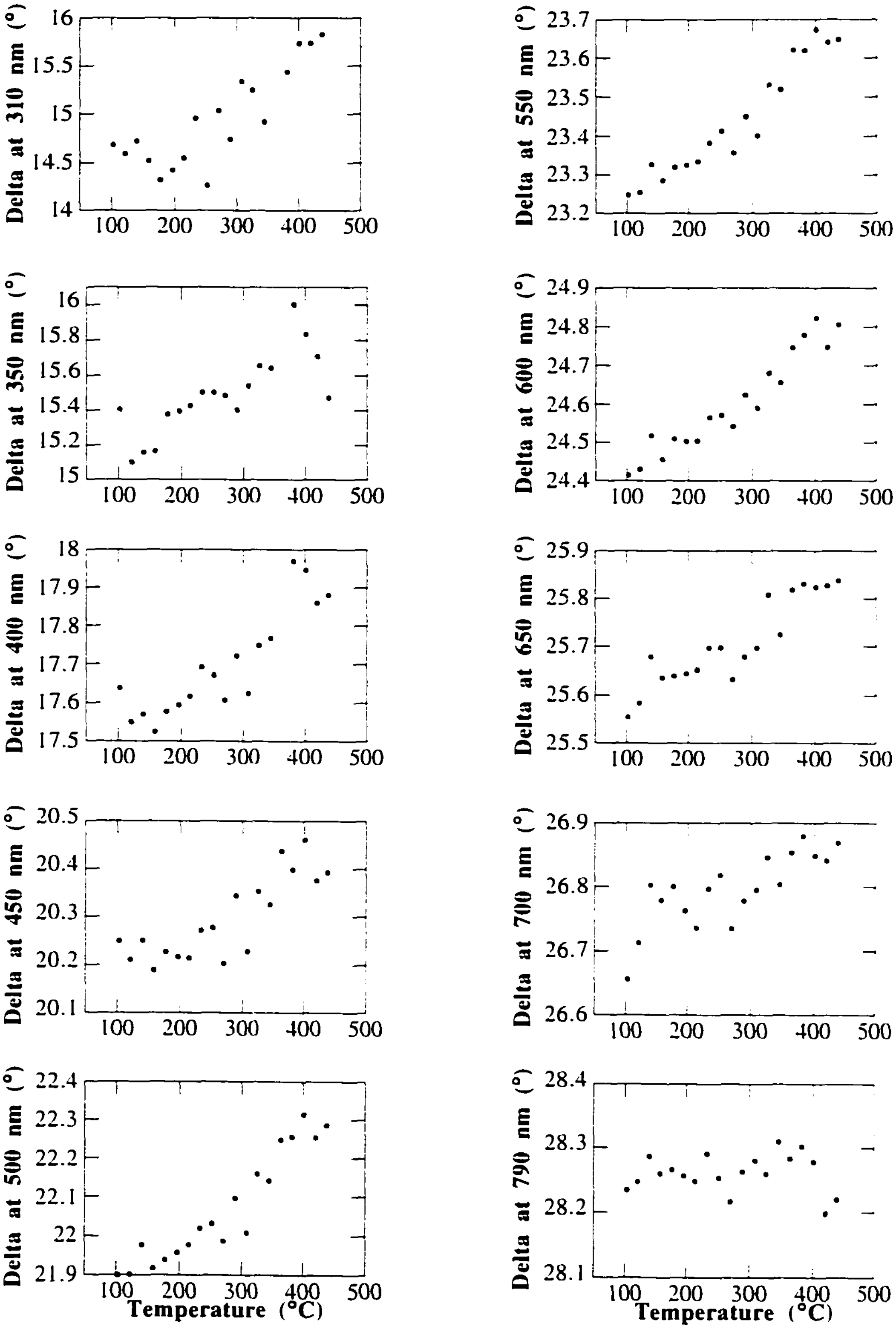

Figure 7.9 : Isoenergetic traces in Δ for a fully oxygenated YBCO film on $SrTiO_3$ from Fig. 7.7.

dimensional plots given in Fig. 7.7. For Ψ, the temperature coefficient is negative (Ψ decreases with increasing temperature). The changes are also small, with the maximum change over a 350 °C interval being ≈0.5° at 650, 700 and 790 nm and the minimum being ≈0.10° at 310 and 350 nm. For Δ, the data are slightly noisier than in Ψ. For the wavelengths shown, the temperature coefficient is positive up to 790 nm, where it levels off. Again, the changes between 100 °C and 450 °C are small; the largest being ≈1.2° at 310 nm and the smallest being <0.1° at 790 nm. Above 450 °C, the O_3/O_2 pressure was insufficient to maintain the oxygen content within the film, thus the changes were no longer due to the temperature dependence alone.

While the film was at 500 °C, the O_3/O_2 mixture was turned off, leaving the sample at the base chamber pressure of $\approx 1 \times 10^{-7}$ Torr. The film was then cooled, which resulted in an oxygen deficient film. Subsequently, the temperature dependence of the ellipsometric parameters for oxygen-deficient YBCO was measured. As before, the film was heated at 1 °C/second, only in vacuum. The spectroscopic measurement is shown in Fig. 7.10. From these plots, it can be seen that there are some regions which show significant temperature dependence while there are others where the temperature dependence is comparable to the data for fully-oxygenated YBCO. The single wavelength data at 302 nm exhibited a significant dependence. Isoenergetic traces are shown in Figs. 7.11 and 7.12. For Ψ, the temperature coefficient is positive for wavelengths greater than 500 nm and less than 350 nm. At 400 nm, the temperature coefficient is negative. The magnitude of the changes range from ≈0.05° at 350 nm and 450 nm to ≈2° at 790 nm. In Δ, again the data are noisier than in Ψ. The temperature

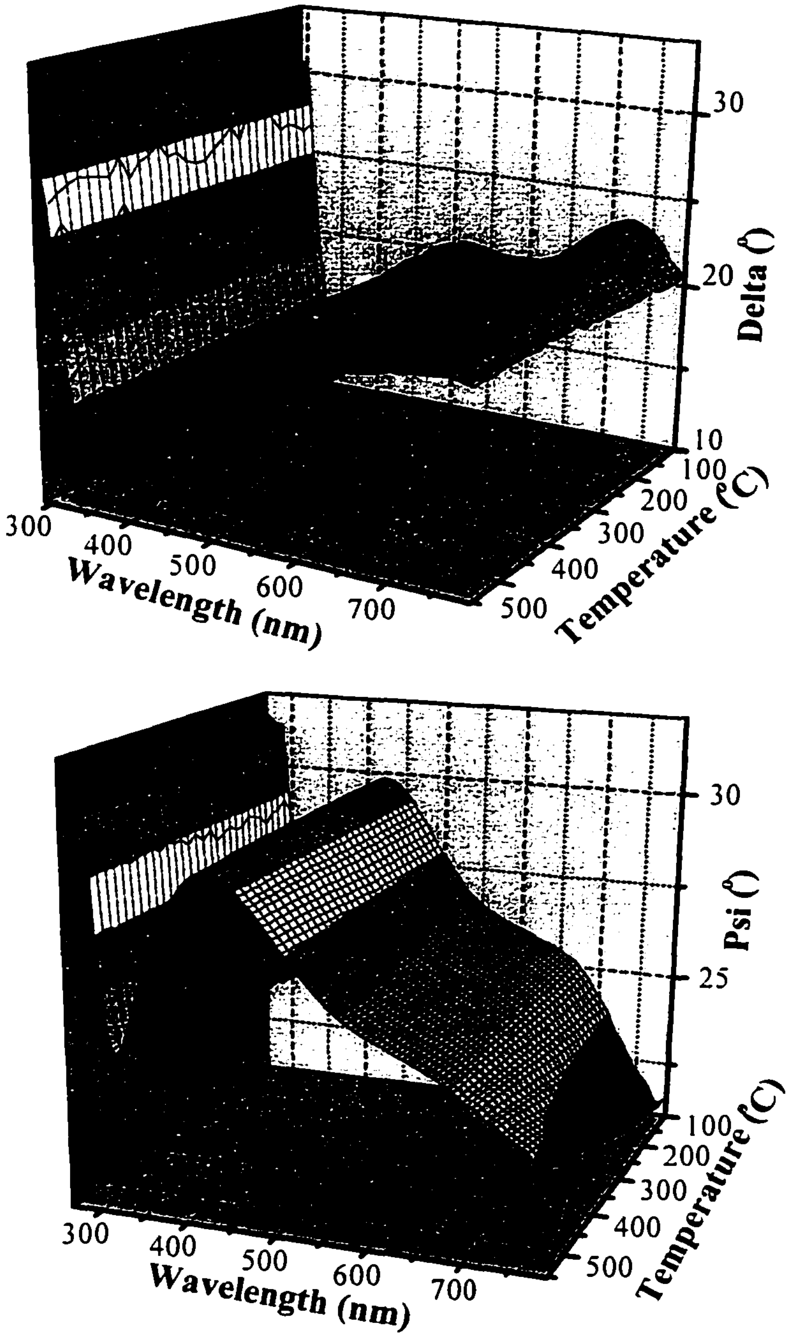

Figure 7.10 : The spectroscopic temperature dependence of oxygen-deficient YBCO.

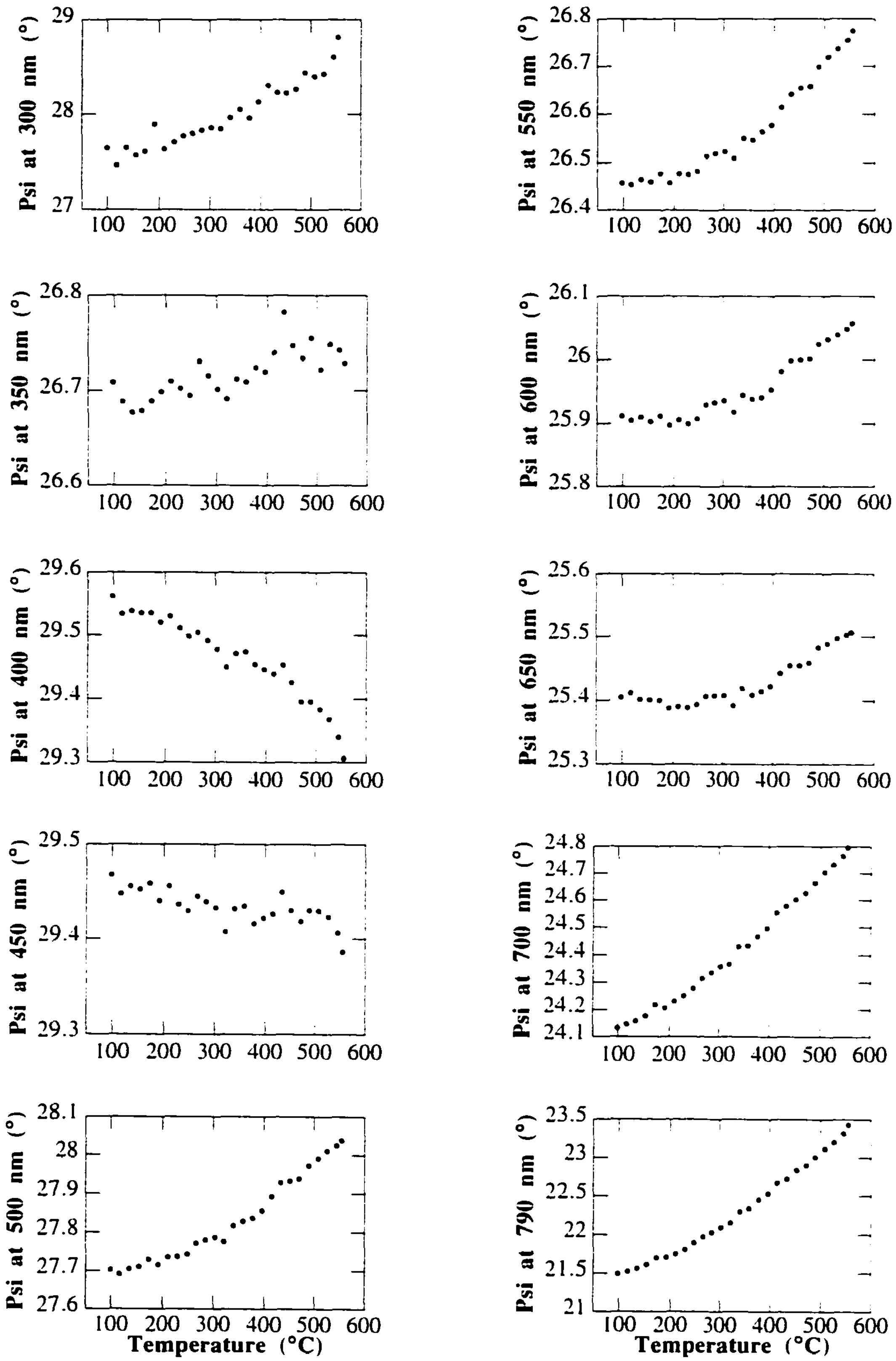

Figure 7.11 : Isoenergetic traces in Ψ for an oxygen-deficient YBCO film on SrTiO$_3$ from Fig. 7.10.

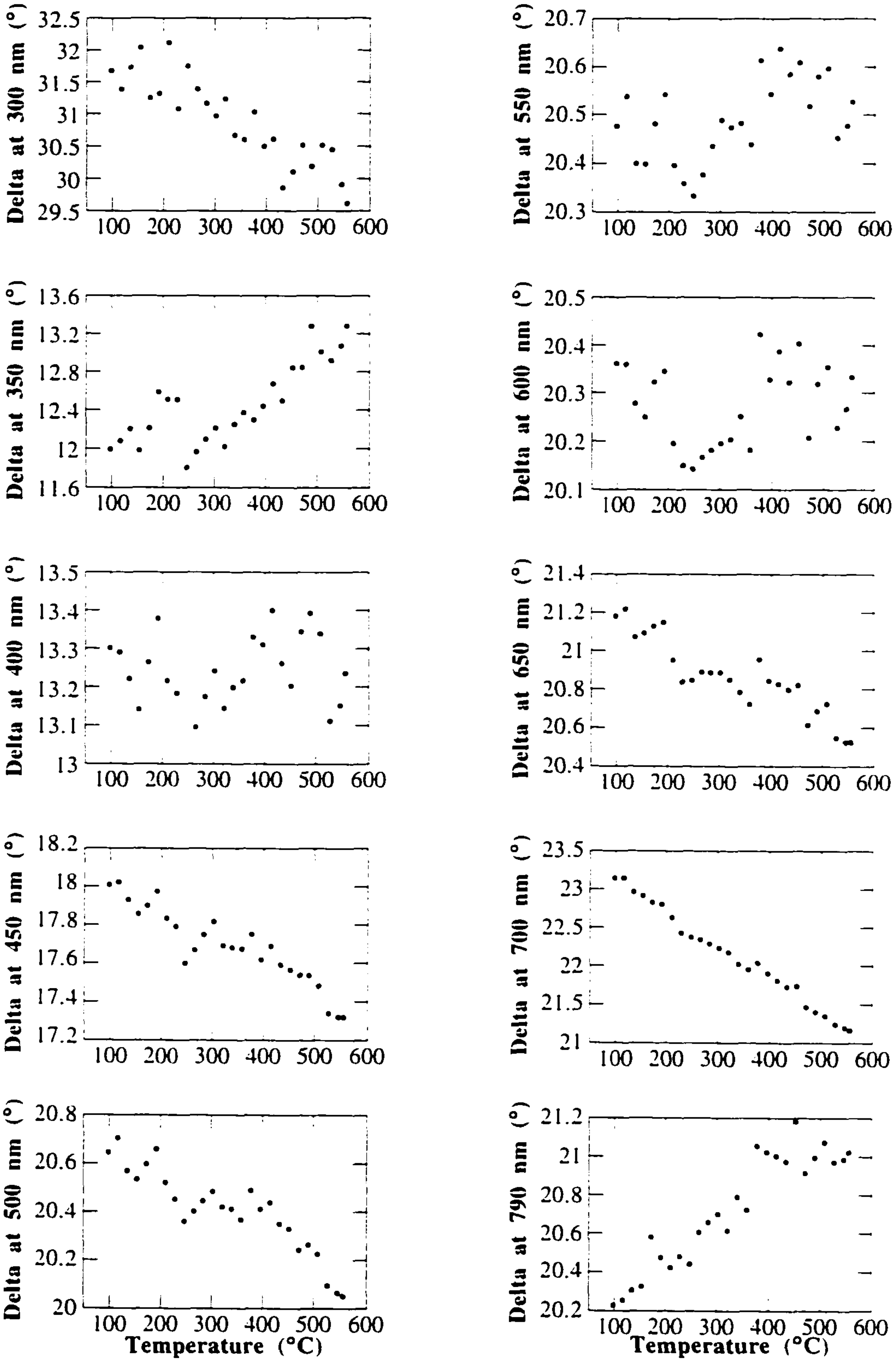

Figure 7.12 : Isoenergetic traces in Δ for an oxygen-deficient YBCO film on $SrTiO_3$ from Fig. 7.10

coefficient varies in the wavelength range plotted. Changes in Δ range from ≈0.3° at 400, 550 and 600 nm to ≈2.5° at 300 nm.

As mentioned above, a wavelength (or range of wavelengths) is desired where the ellipsometric parameters show more of a dependence on the oxygen content rather than the temperature. To investigate this, ellipsometric spectra were calculated for 6 films with different oxygen contents: $YBCO_{6.07}$, $YBCO_{6.10}$, $YBCO_{6.21}$, $YBCO_{6.36}$, $YBCO_{6.73}$ and $YBCO_{6.85}$. In order to generate the maximum changes, no oxygen gradient was assumed. That is, the entire film was assumed to have a constant stoichiometry. The geometry chosen was that of the film studied in the experiments and the angle of incidence was set to 80°. Values of Ψ and Δ as a function of oxygen content (δ) are shown in Figs. 7.13 and 7.14. Based on these data and the temperature dependence, in Ψ it appears that the best combination of minimal temperature dependence and maximum oxygen content dependence is at 350 nm and from 550 nm to 650 nm. Here, the changes due to oxygen content are 4°-6° while the temperature change causes a change between 0.05° and 0.5° for both $YBCO_6$ and $YBCO_7$. In Δ, the optimal wavelength(s) is somewhat more difficult to determine due to the scatter in the data. In general, it appears that the best combination can be found between 550 nm and 600 nm. Here, the changes due to the temperature dependence are ≈10% of those due to changes in oxygen content. It should be noted that the temperature dependence of the ellipsometric parameters was only investigated for $YBCO_6$ and $YBCO_7$. For compositions between, it was assumed that the temperature dependence was within the bounds set by the outer stoichiometries.

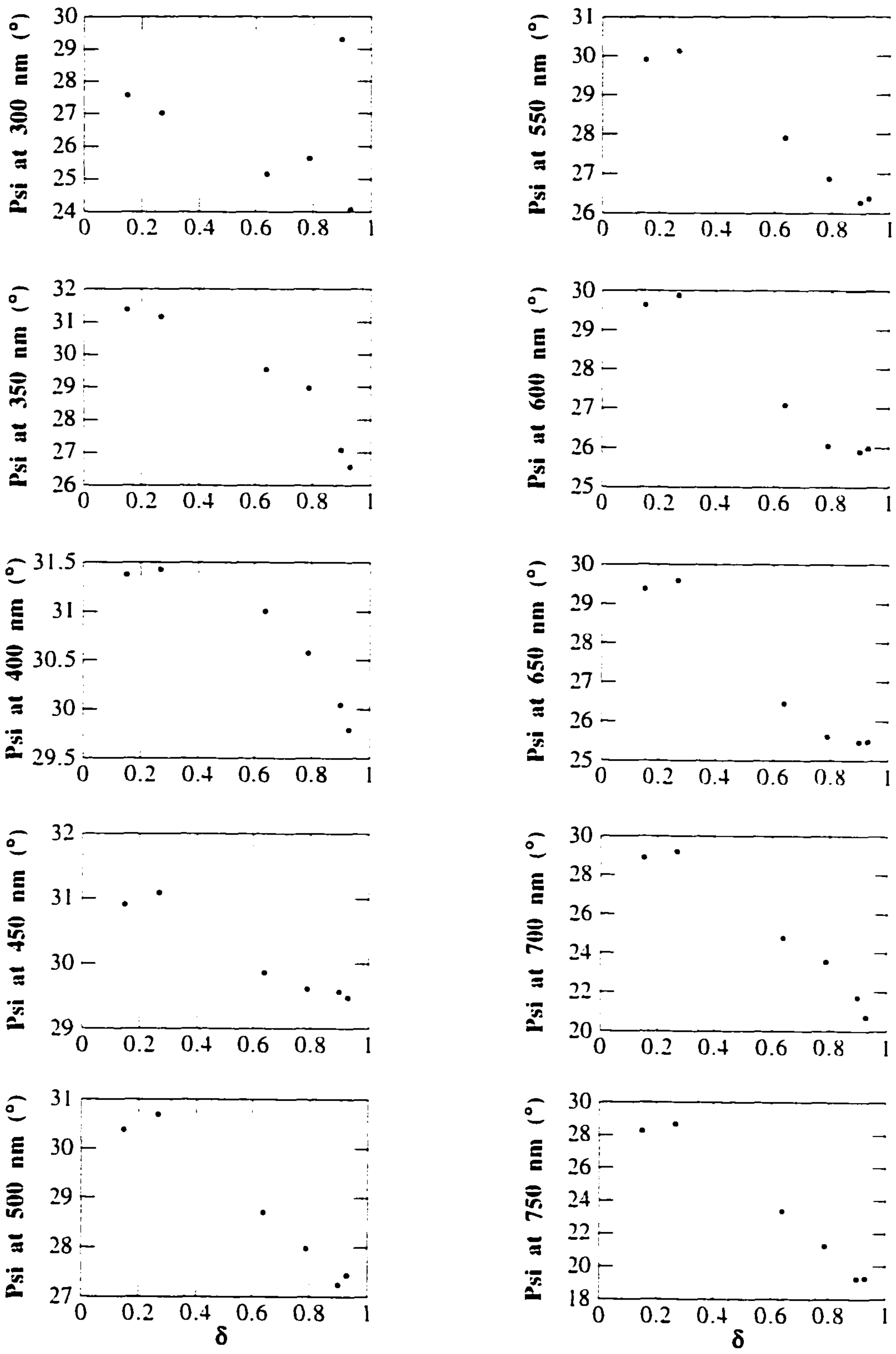

Figure 7.13 : Ψ at various wavelengths for films of varying oxygen content (δ) at an 80° angle of incidence.

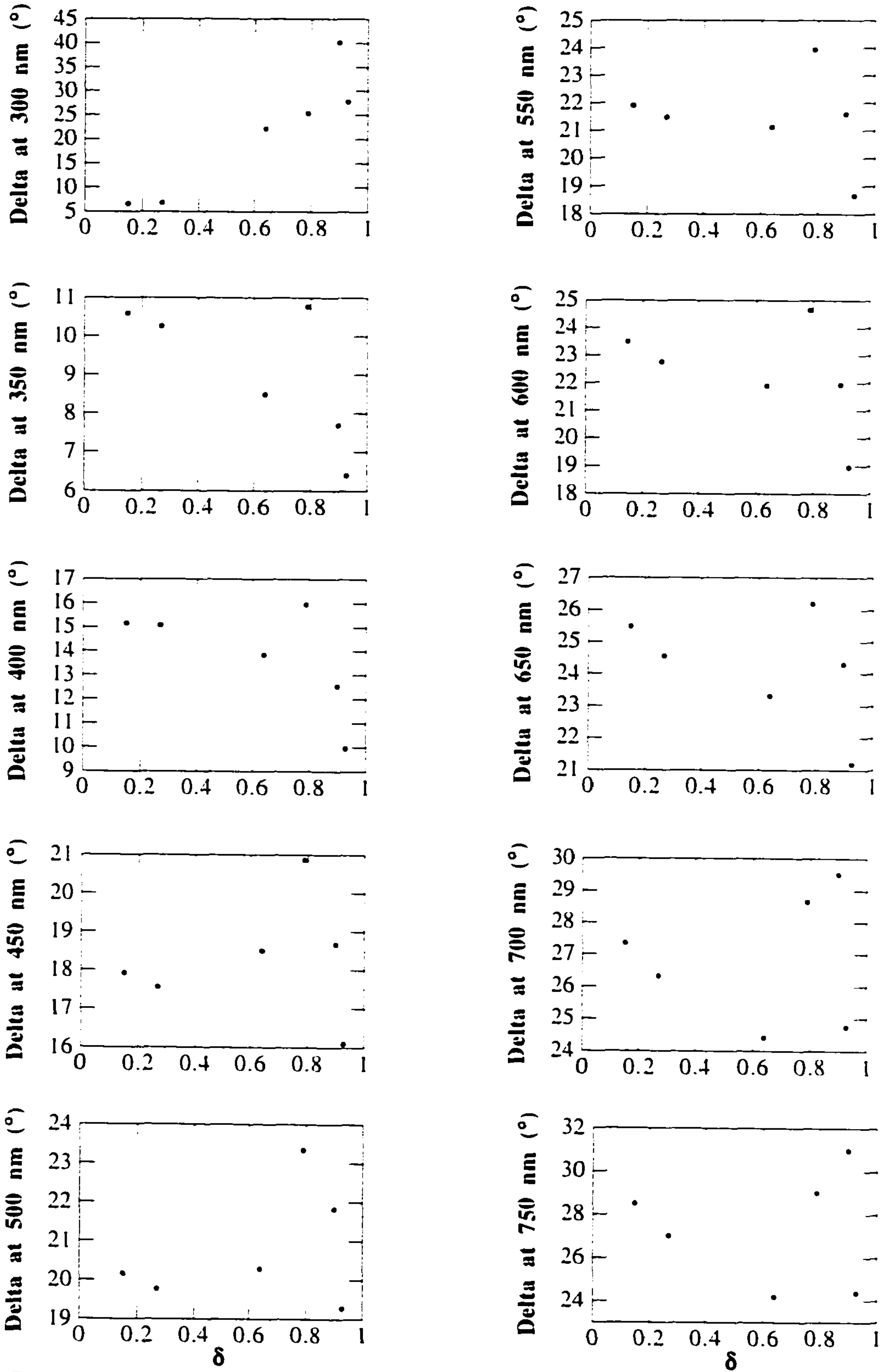

Figure 7.14 : Δ at various wavelengths for films of varying oxygen content (δ) at an 80° angle of incidence.

7.2.2 The Diffusion of Oxygen in Controlled Atmospheres

As mentioned in the discussion of the single wavelength ellipsometric data, a more complete analysis of the oxygen diffusion in YBCO would be facilitated by the ability to do similar experiments in a controlled atmosphere. This was done using the MBE chamber, along with three types of atmospheres; molecular oxygen, and two ozone/molecular oxygen mixtures (the unmodified and distilled outputs from the ozone generator). Again, the sample used was a 650 Å thick sputter deposited YBCO film on $SrTiO_3$.

Initially, the film was made oxygen-deficient as described above. The sample was then heated at 10 °C/minute up to 550 °C in 2×10^{-5} Torr of O_2. The results of this heating are shown in Fig. 7.15. From these plots, it can be seen that this atmosphere resulted in a depression of the peak intensity in Δ at 302 nm. This depression continued until ≈400 °C, at which point the peak began to increase. This initial depression indicates the onset of oxidation of the film. A similar effect can be seen in Ψ, where the amplitude of the dip at ≈300 nm begins to decrease, while the overall magnitudes of the spectra increase up to ≈400 °C. These changes are also indicative of oxidation. However, the relatively small magnitude of the observed changes suggests that the film is never fully oxidized. Otherwise, the behavior shown is similar to that caused by the temperature dependence of the ellipsometric parameters. In order to fully oxygenate the film, higher pressures must be used. Unfortunately, this could not be done due to limitations of the MBE. Therefore, an alternative oxidant had to be used to follow the oxygen in-diffusion behavior.

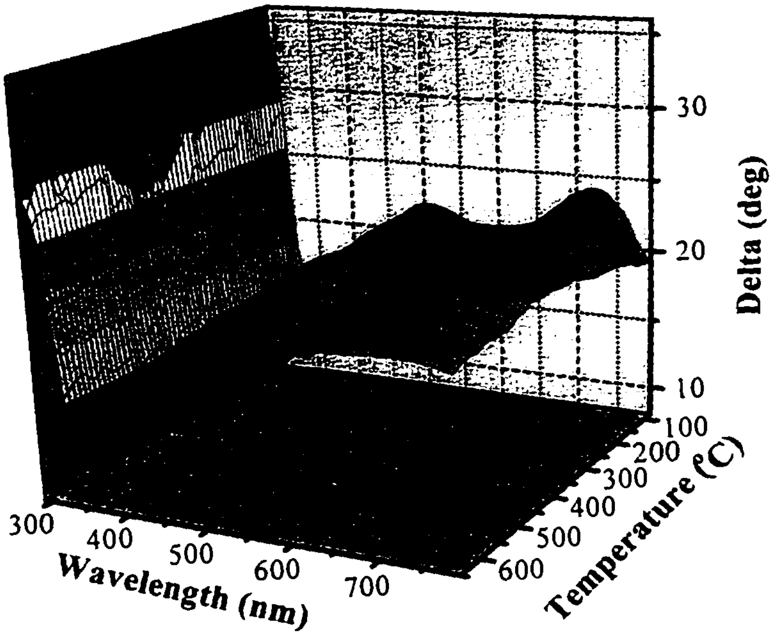

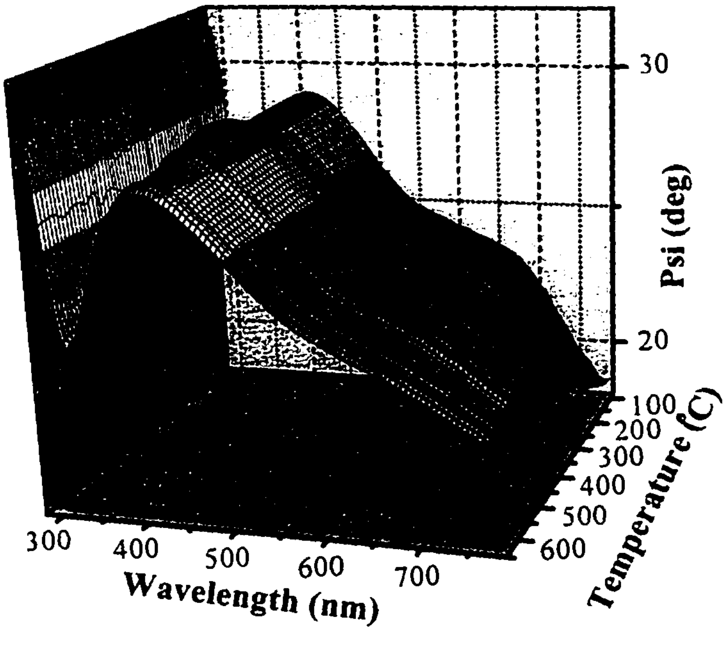

Figure 7.15 : Ellipsometric spectra of a sputter deposited YBCO film on $SrTiO_3$ heated at 10 °C/minute in 2×10^{-5} Torr of O_2.

It is well known that ozone is a more powerful oxidant than molecular oxygen. Therefore, the output from the ozone generator (10% O_3/90% O_2) was used as an atmosphere to conduct the same experiments. The initially oxygen-deficient sample was heated at 1, 3, 5, 10 and 15 °C/minute in 2×10^{-5} Torr O_3/O_2; the maximum temperature used was 550 °C. RTSE data were collected during these heating runs and are shown in Figs. 7.16-7.20. In each case, the data are indicative of oxidation of the film, with the onset of the reaction occurring at lower temperatures for lower heating rates. Changes begin to occur at temperatures as low as 100 °C which are of too great a magnitude to be caused by the temperature dependence of the ellipsometric parameters. Then, at higher temperatures, the oxidation slows and the temperature dependence dominates. This is shown through a comparison of the spectra at these higher temperatures and the temperature dependence plotted previously. The point at which the oxygenation ceases also decreases with decreasing heating rate. This effect is seen most clearly in the data for the 1 and 3 °C/minute heating rates. As the temperature is increased beyond the point of complete oxidation, reduction of the film begins to occur (see Fig. 7.18 – 7.20).

At faster heating rates, less time is available at a given temperature for diffusion, so full oxidation of the films is pushed to higher temperatures. In this work, the completion of oxidation was taken to correspond to the temperature at which the changes in the ellipsometric parameters slow to the temperature dependence of Δ and Ψ. Consequently, the activation energy of oxygen diffusion into a YBCO film in a 90% O_2/10% O_3 atmosphere can be determined by measuring the dependence of this temperature on heating rate.

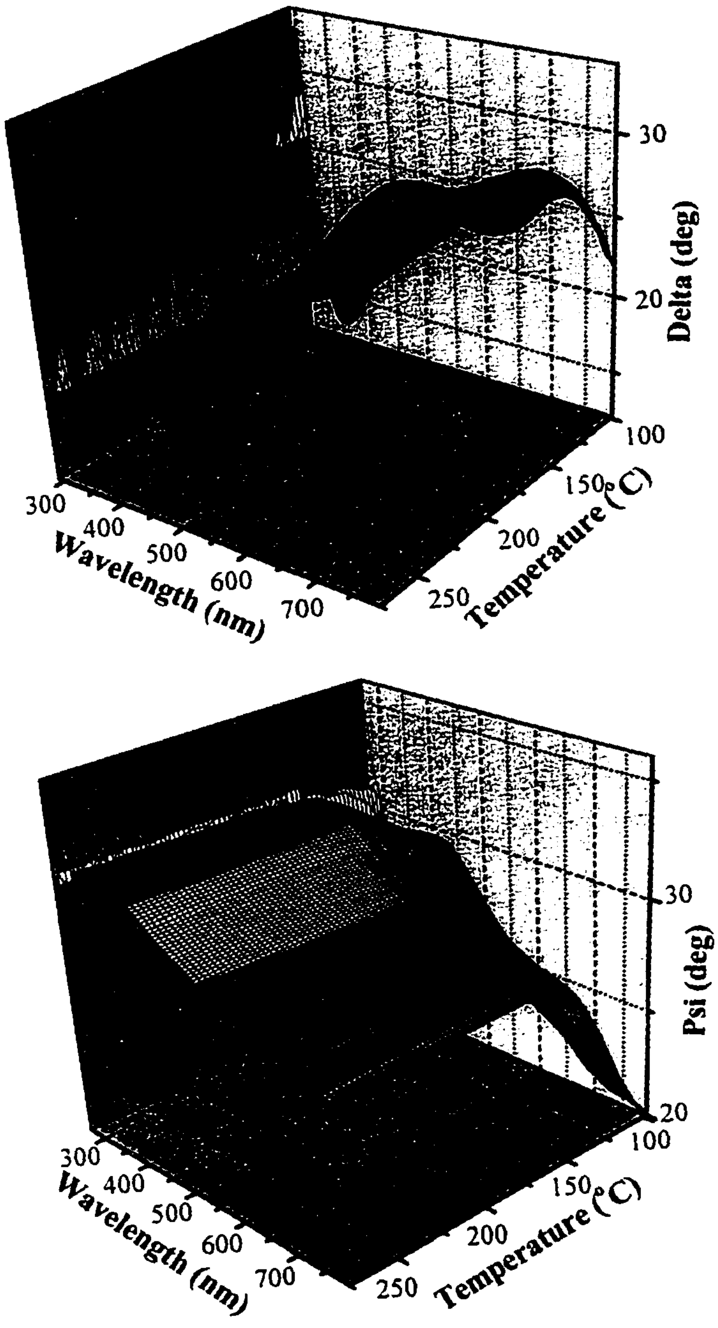

Figure 7.16 : Ellipsometric spectra of a sputter deposited YBCO film on $SrTiO_3$ heated at 1 °C/minute in 2×10^{-5} Torr of O_3/O_2.

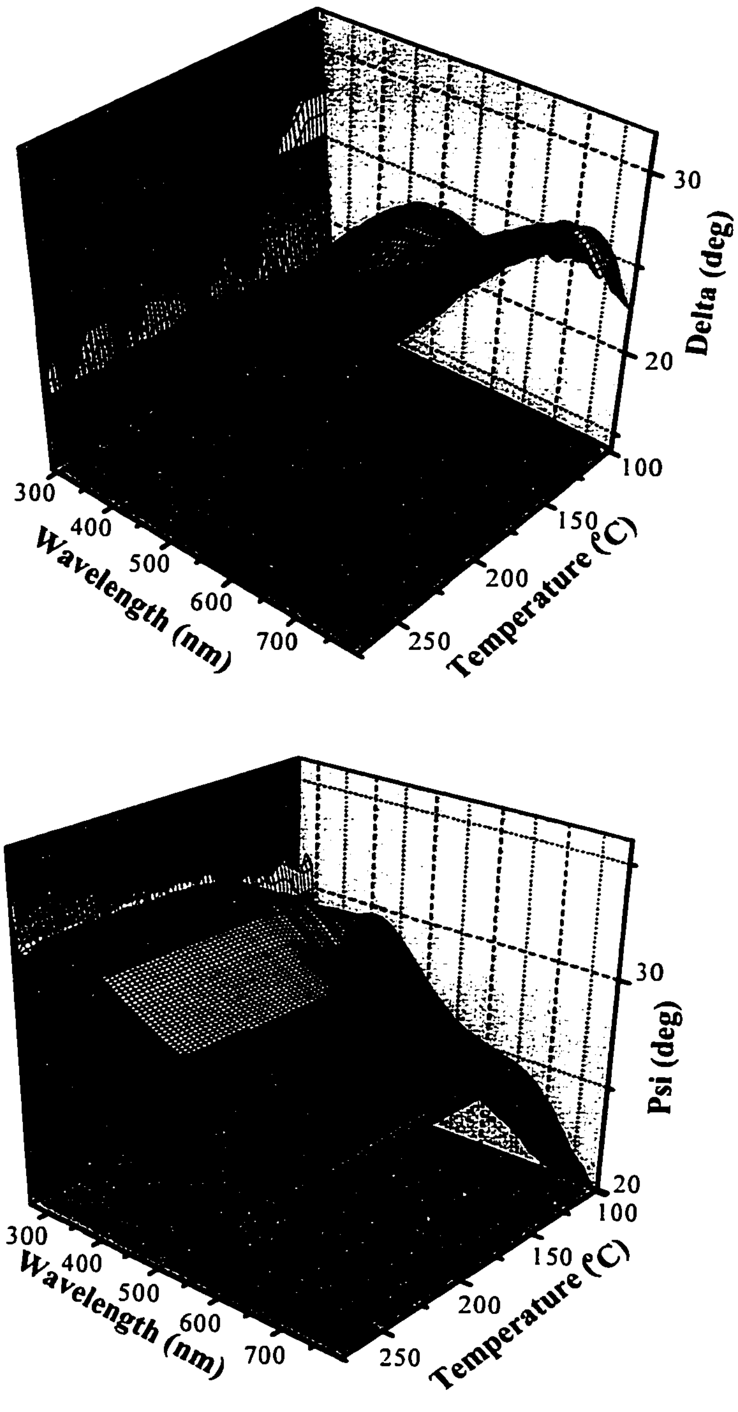

Figure 7.17 : Ellipsometric spectra of a sputter deposited YBCO film on $SrTiO_3$ heated at 3 °C/minute in 2×10^{-5} Torr of O_3/O_2.

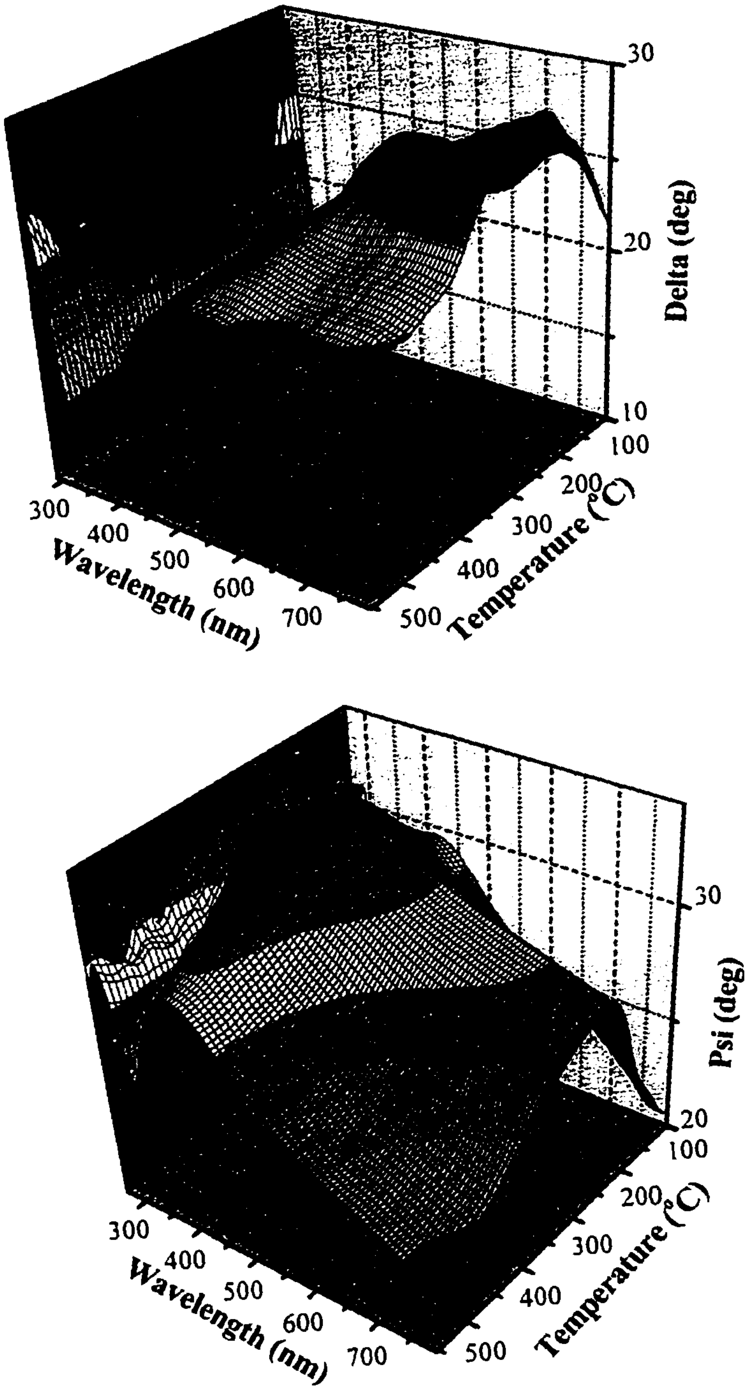

Figure 7.18 : Ellipsometric spectra of a sputter deposited YBCO film on $SrTiO_3$ heated at 5 °C/minute in 2×10^{-5} Torr of O_3/O_2.

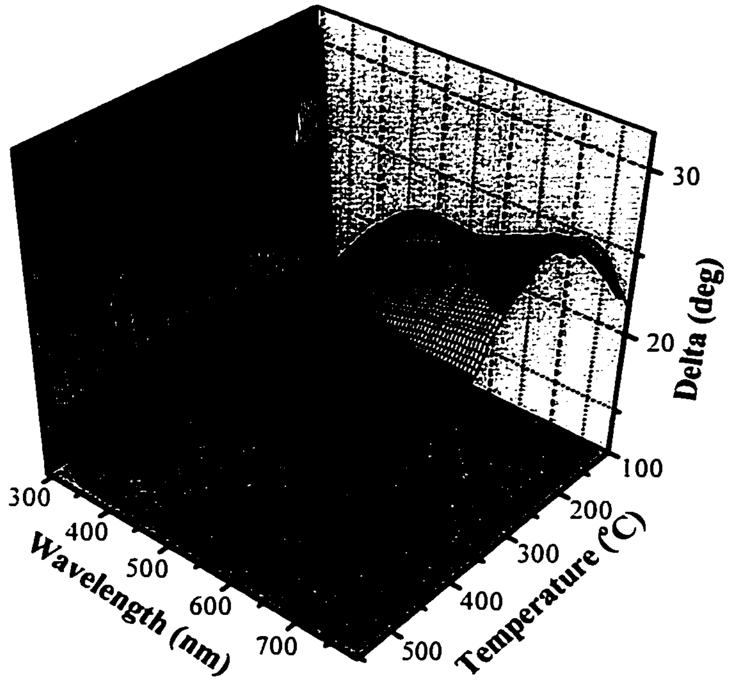

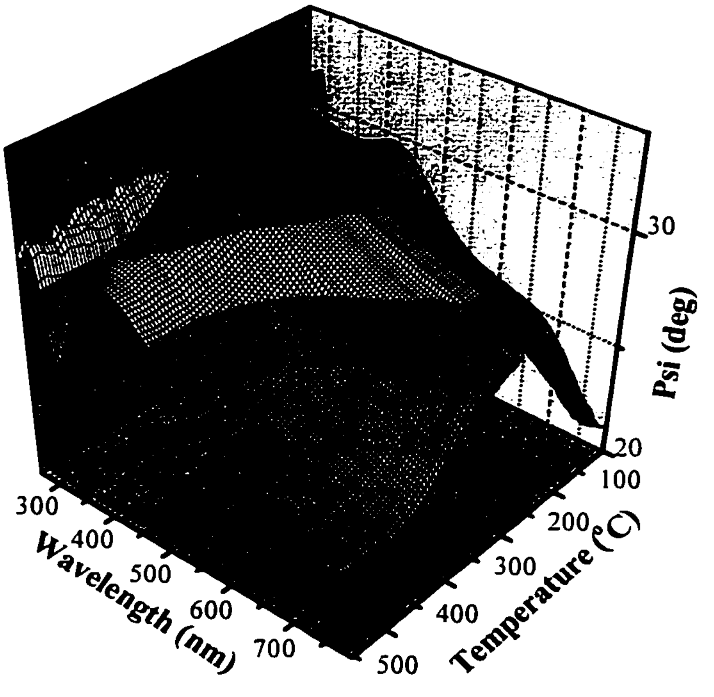

Figure 7.19 : Ellipsometric spectra of a sputter deposited YBCO film on $SrTiO_3$ heated at 10 °C/minute in 2×10^{-5} Torr of O_3/O_2.

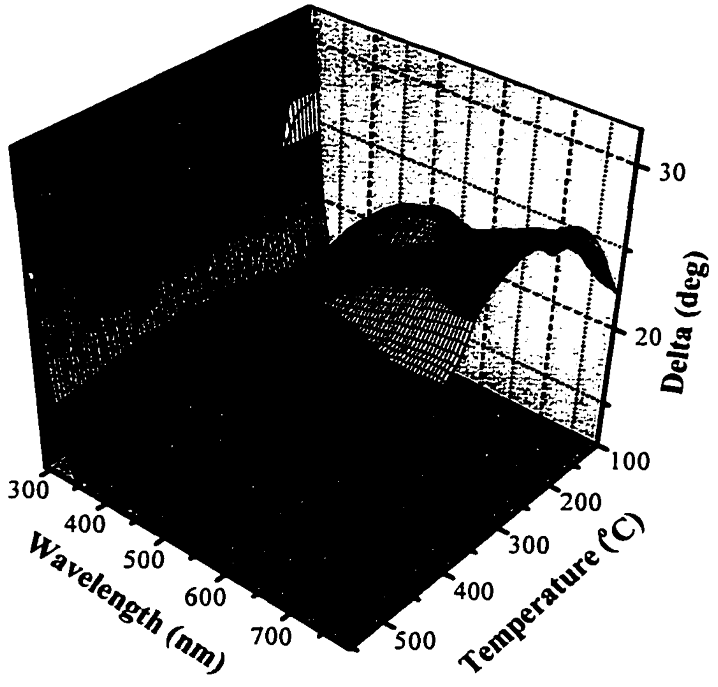

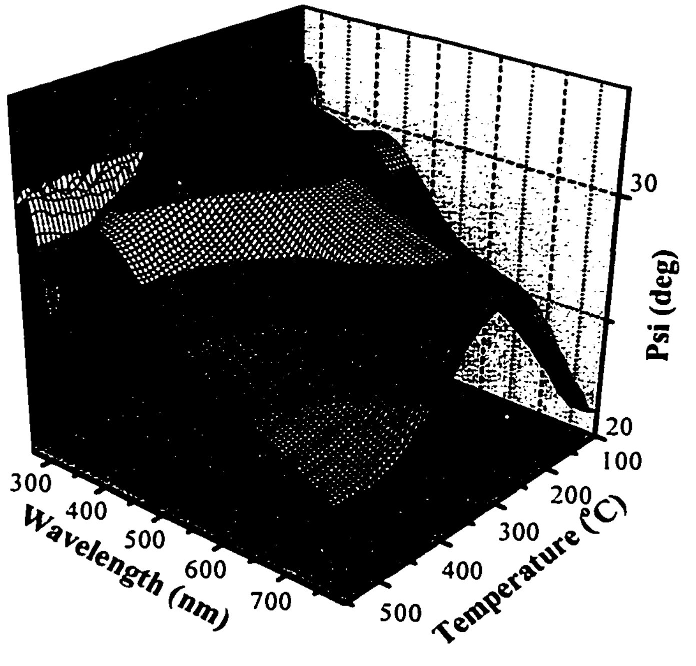

Figure 7.20 : Ellipsometric spectra of a sputter deposited YBCO film on $SrTiO_3$ heated at 15 °C/minute in 2×10^{-5} Torr of O_3/O_2.

To do this, the analysis of Tu *et al.*[177] for diffusion in ceramic YBCO is used. J is defined as the number of diffusing oxygen atoms per cm^2, N_v is the number of oxygen atoms in the CuO layer per cm^3 and δ is the fraction of missing oxygen atoms in the CuO layer (where $0 \leq \delta \leq 1$). If non-steady state diffusion is assumed, the total number of oxygen atoms diffused into the oxide per unit area over a time period, t_o is given by:

$$N_v\delta = \int_0^{t_o} -(\nabla \cdot J)dt \tag{7.1}$$

where:

$$J = -D\frac{\partial(N_v\delta)}{\partial x} \tag{7.2}$$

and:

$$D = D_o \exp\left(-E_a/_{kT}\right) \tag{7.3}$$

where D is the diffusivity in the film and E_a is the activation energy for diffusion into the film. Tu *et al.* changed the base from time to temperature and, assuming one-dimensional diffusion, obtained:

$$\delta = \int_{\mathrm{r.t.}}^{T_{\max}} D\left(\frac{\partial^2\delta}{\partial x^2}\right)\left(\frac{dt}{dT}\right)dT \tag{7.4}$$

where r.t. is room temperature and $T_{\max}$ is the temperature at which the changes in the ellipsometric spectra are no longer due to oxygenation of the film. At a constant heating rate, the solution of eq. 7.4 can be found from the thermal analysis of Kissinger[255] and Ozawa[256] to be:

$$\delta\left(\frac{dT}{dt}\right) = \left(D_o\frac{\partial^2\delta}{\partial x^2}\right)\left(\frac{kT_{\max}^2}{E_a}\right)\exp\left(-E_a/_{kT_{\max}}\right) \tag{7.5}$$

Two assumptions are made in solving for eq. 7.5. First, E_a is assumed to be constant and second, $\partial^2\delta/\partial x^2$ is assumed to be a slowly varying function of temperature. Tu justified the first assumption on the basis that a near-surface layer saturated with oxygen forms in the early stage of oxidation and this layer limits the in-diffusion of oxygen with a constant activation energy. Although this layer thickens with time, the oxygen concentration gradient does not vary much, so the second assumption is satisfied.

From eq. 7.5, E_a can be determined by plotting $\ln((dT/dt)/T^2_{max})$ versus $1/kT_{max}$, or, by plotting $\ln(dT/dt)$ versus $1/kT_{max}$, since T_{max} does not vary much as compared to the heating rate. First, T_{max} was determined from isoenergetic traces from each of the heating rates shown in Figs. 7.16-7.20. Two of these plots are shown in Fig. 7.21. To obtain T_{max}, best fit lines were drawn to the data before and after the changes due to oxidation ceased. The intersection of the lines was taken as T_{max}. This was done for several wavelengths from the ranges determined in the previous section. From the wavelengths used, the obtained temperatures varied less than 10 °C for each heating rate. Fig. 7.22 shows the two different approaches to calculating E_a. The lines are least-squares linear fits to the data. The good fit suggests that the assumptions made in the analysis are reasonable. The slopes give activation energies of 0.52 eV and 0.43 eV for oxygen diffusion in an O_2/O_3 atmosphere. For thin film *c*-axis oriented YBCO, Yamamoto *et al.*[193] calculated activation energies of 1.2 eV in molecular oxygen and 0.65 eV in atomic oxygen generated by an ECR plasma source. Thus, the values obtained here agree well with the value for an alternate activated oxygen species.

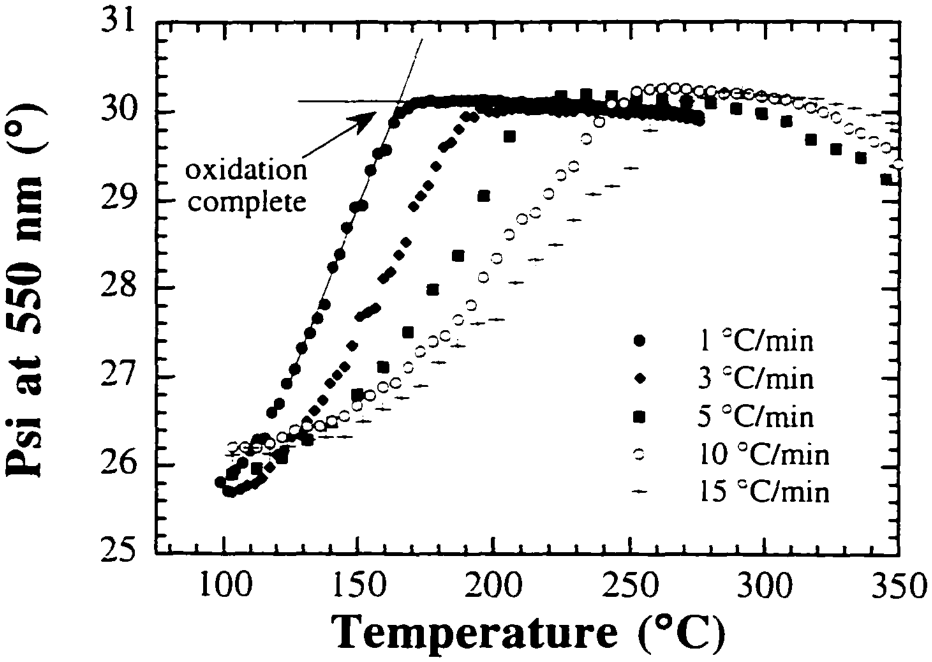

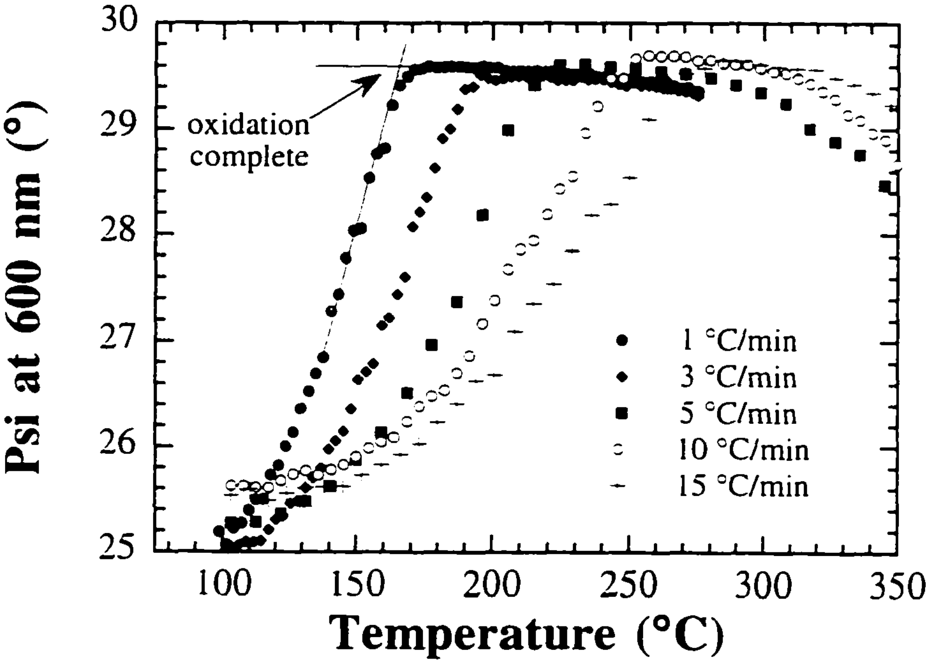

Figure 7.21 : Isoenergetic traces taken from Figs. 7.16 - 7.20. These plots were used to determine the point at which the changes in the ellipsometric parameters were no longer due to oxygenation of the film.

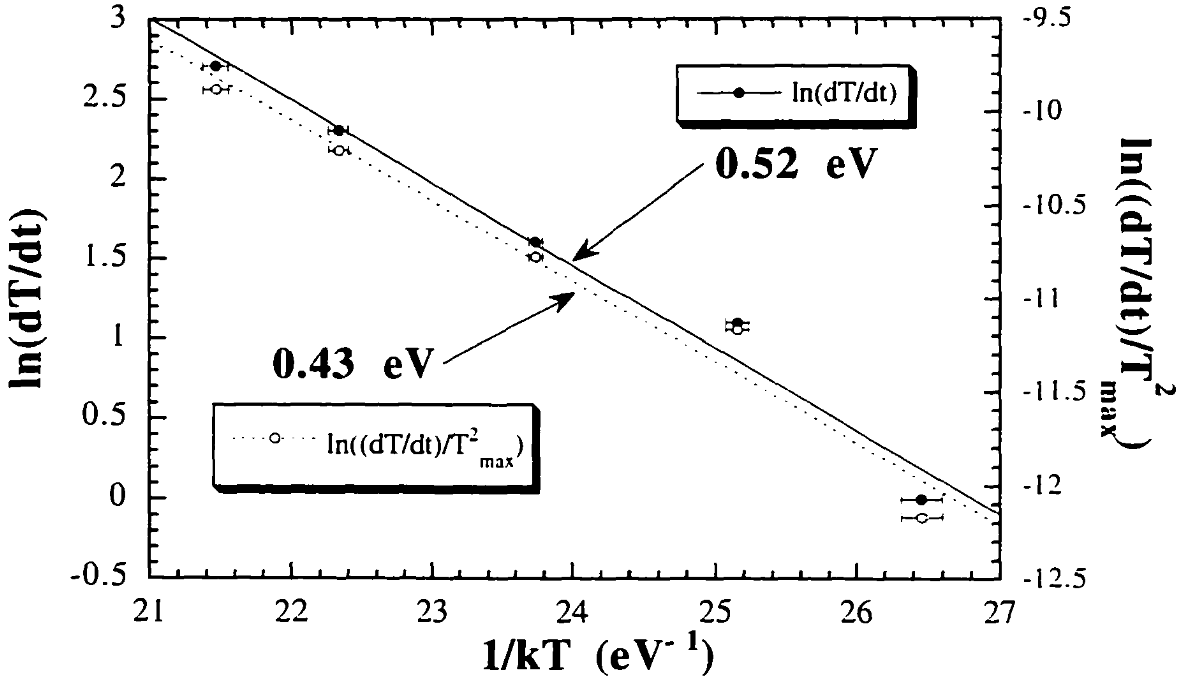

Figure 7.22 : Plots of ln(dT/dt) and ln((dT/dt)/T^2_{max}) versus $1/kT_{max}$ for five different heating rates. The slopes of the curve-fitted lines give the activation energy for diffusion of oxygen into YBCO in a 10% O_3/90% O_2 atmosphere.

Finally, the effects of an 80% O_3/20% O_2 atmosphere were examined (the distilled output from the ozone generator). Initially, the film was heated at 10 °C/minute in 2×10^{-5} Torr and the data were compared to those for the same heating rate in the ozone generator output atmosphere (10% O_3/90% O_2). Two isoenergetic traces are shown in Fig. 7.23 for the two different atmospheres. It can be seen that there is essentially no difference in the value of T_{max} for the two conditions. This indicates that at these low temperatures, the output from the ozone generator alone is sufficient to oxidize the film. However, at higher temperatures, the difference between the two atmospheres is marked. The purer ozone atmosphere prevents reduction in the film from occurring until higher temperatures. In general, the 80% ozone mixture delays the onset of reduction by 60 – 70 °C.

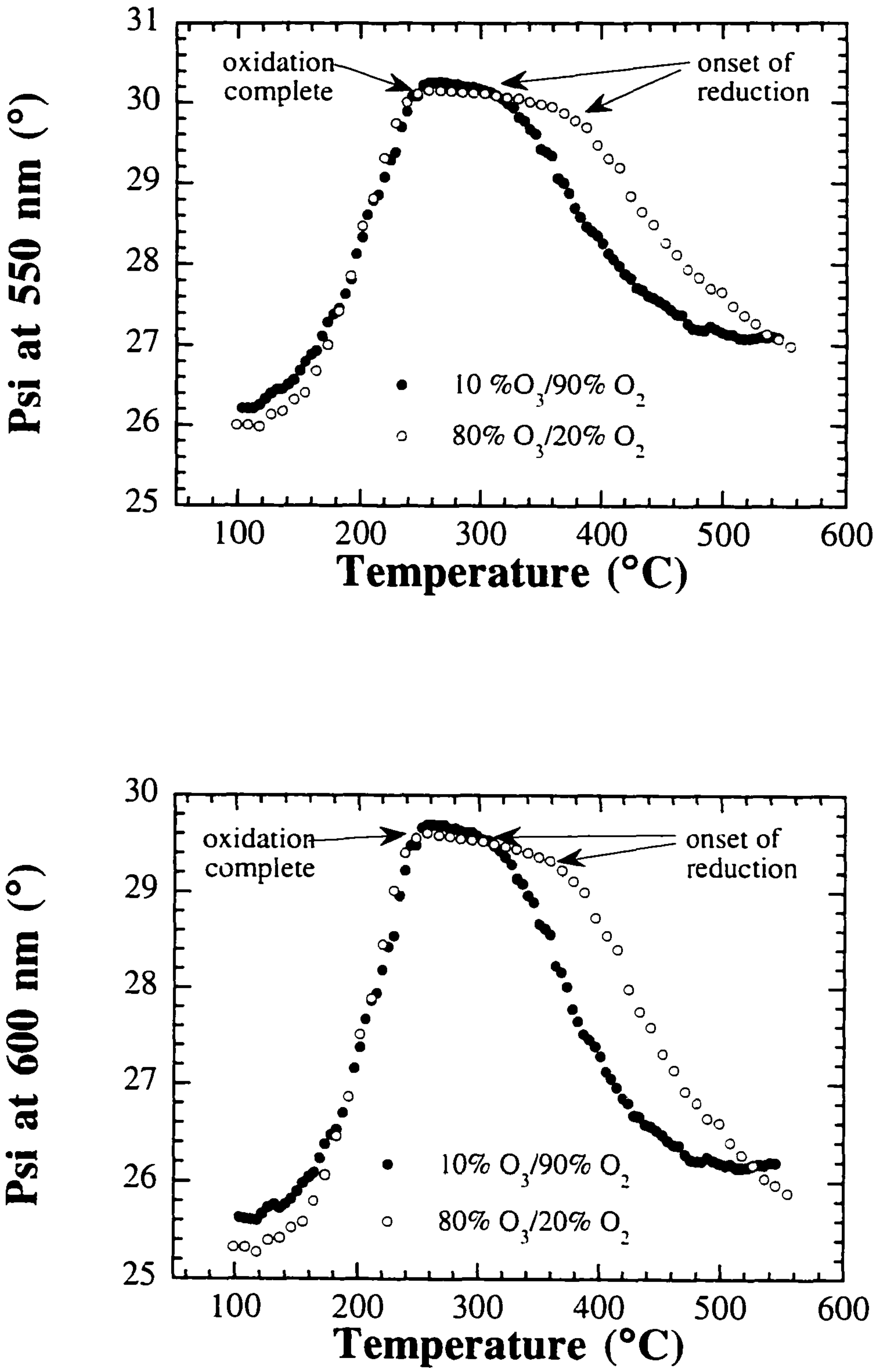

Figure 7.23 : Isoenergetic traces of a sputtered YBCO film heated at 10 °C/minute in 10% O$_3$/90% O$_2$ (output from the ozone generator) and 80% O$_3$/20% O$_2$ (distilled from the ozone generator).

As one final note in this section, it should be noted that during the complete transition from $YBCO_6$ to $YBCO_7$, there are no significant anomalies in the data. That is, there are no strong transitory features at intermediate oxygen contents. This indicates that the calculation of intermediate oxygen contents using the Bruggeman effective medium approximation (see chapter 5) are valid.

7.2.3 The Relative Reactivity of Ozone Compared to Molecular Oxygen

Based on the above results, it is possible to determine the relative reactivity of ozone at a given temperature compared to molecular oxygen at the same temperature. To do this, a sputter deposited YBCO film on $SrTiO_3$ was heated to 500 °C and held under various atmospheres. Initially, the sample was brought to equilibrium at 2×10^{-5} Torr of molecular oxygen. Subsequently, the ozone generator was turned on and the sample was allowed to equilibrate again. Then, the pressure was systematically decreased to 2×10^{-6} Torr, 5×10^{-7} Torr and 1×10^{-7} Torr. At each pressure, the sample was held for 10 minutes in order for the oxygen content to equilibrate. This was done by monitoring the RTSE spectra and waiting until the changes ceased.

Fig. 7.24 shows the Δ and Ψ spectra for each pressure and atmosphere. In the Δ spectra, the curves for the ozone atmosphere begin to approach that of the molecular oxygen atmosphere as the pressure is dropped, but they never coincide. The peak intensities at 302 nm in Δ do recover, however the rest of the spectrum in Δ do not match. A reduced wavelength range is plotted for Ψ, in order to magnify the most sensitive region with respect to oxygen content. It can be seen that at a pressure of 1×10^{-7} Torr of

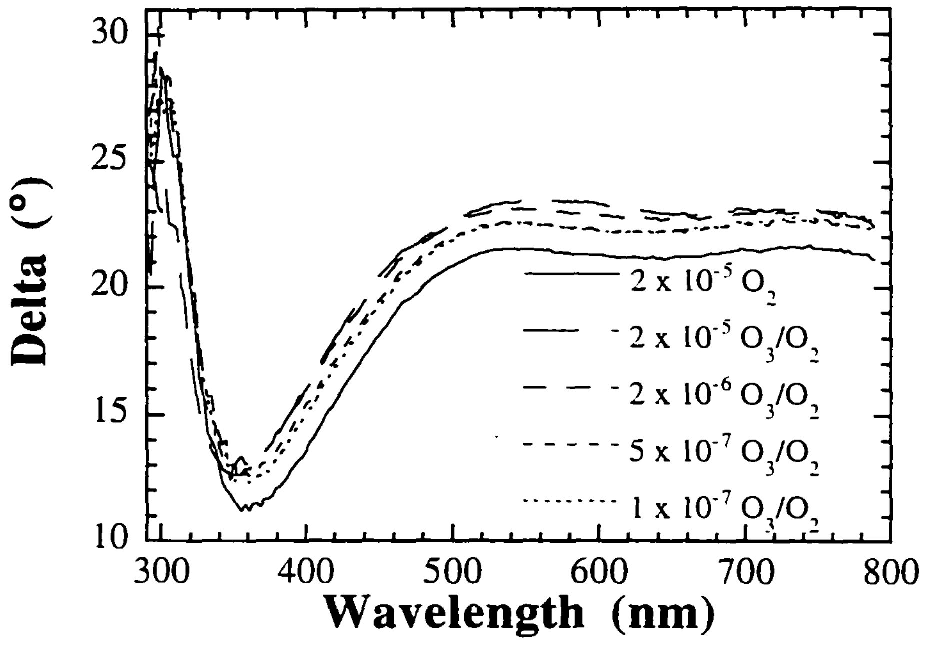

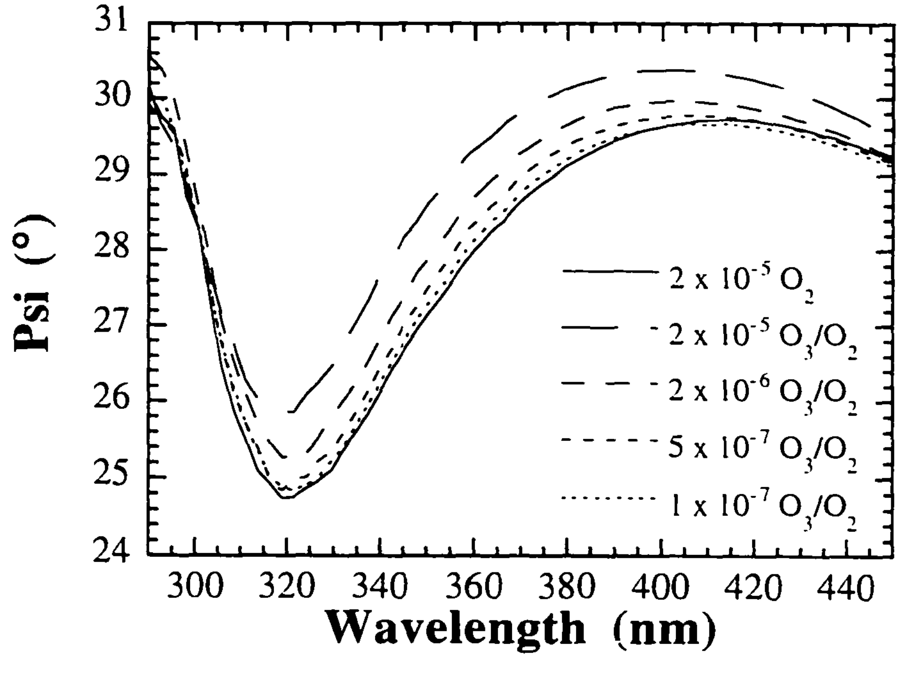

Figure 7.24 : Δ and Ψ spectra for a sputtered YBCO film in various pressures of molecular oxygen or 10% O_3/90% O_2 at 500 °C.

10 %O_3/90% O_2, the Ψ spectrum approaches that of molecular oxygen at 2 × 10^{-5} Torr. Based on these data, since there is only 10% ozone in the chamber, it can be concluded that ozone is at least 2000 times as reactive as molecular oxygen at 500 °C. Or, it can be said that the "effective" pressure of ozone is equivalent to at least 2000 times the pressure of molecular oxygen. This shows good agreement with Yamamoto *et al.*,[193] who determined the relative reactivity of atomic oxygen with respect to molecular oxygen to be 2000 times greater at 480 °C.

It is clear that RTSE has shown good sensitivity to the diffusion of oxygen in YBCO films. The advantage to having spectroscopic data over single wavelength data is clear from the analysis of the temperature dependence of the ellipsometric parameters. The ability to take spectroscopic measurements in real-time allows for the observation of several energy ranges where the sensitivity to the oxygen content is high (and the temperature dependence is minimal). The sensitivity of the RTSE to oxygen diffusion in YBCO could be improved even more by sacrificing the wider wavelength range for a very narrow range around 302 nm. This would be done by choosing a different diffraction grating for the spectrograph. Doing this would significantly enhance the throughput of the system in this energy range, and subsequently enhance the signal-to-noise ratio. In addition, by averaging more polarizer rotation cycles, the accuracy could be improved further at the expense of time resolution.

Chapter 8

CONCLUSIONS AND FUTURE WORK

8.1 Conclusions

Despite the promise of using high-T_c superconducting materials for Josephson junction based devices, there are significant materials and processing challenges that remain to be overcome. At this point, the key roadblocks to the implementation of this technology are: 1) excessive interfacial roughness between the YBCO and the normal metal interlayer, and 2) oxygen non-stoichiometry at the interface. Processing conditions which facilitate the fabrication of high quality high-T_c based Josephson junctions are currently unknown. Therefore, a characterization tool which can assist in the determination of these conditions would result in the development of a more reliable and reproducible Josephson junction technology.

In this thesis, *ex situ* and real-time spectroscopic ellipsometry were explored for use as a characterization tool for YBCO thin films. It was hoped that SE would prove to be a useful technique for developing a better understanding of the current obstacles to successful implementation of this material in Josephson junction based devices. SE is a non-destructive and non-invasive method which is capable of depth profiling samples with a resolution generally in the angstrom range. Most importantly, the sensitivity of SE is directly related to the dielectric function contrast in the film being studied. Thus, it is an ideal tool to observe the processing of YBCO films in real-time.

Since the development and subsequent advancements in methods used to deposit epitaxial thin films of YBCO, there has been a significant interest in the substrates used for these films. There is a wide selection of substrates available that provide the necessary lattice match and chemical compatibility for deposition of YBCO films. However, there is little information regarding the optical properties of these materials. For SE to be useful as a characterization method for YBCO films on these substrates, it is necessary to have reference dielectric function data ($\varepsilon_1 + i\varepsilon_2$) for the individual materials in the sample of interest.

Here, reference dielectric function data for five common YBCO substrate materials and one known reaction layer material were determined using *ex situ* SE. The substrates were: $LaAlO_3$ (LAO), $NdGaO_3$ (NGO), $(LaAlO_3)_{0.3}$-$(Sr_2AlTaO_6)_{0.7}$ (LSAT), $LaSrGaO_4$ (LSGO) and 9.5 mol% Y_2O_3-ZrO_2 (YSZ). The reaction layer material was $BaZrO_3$ (BZO). The dispersion of these materials was modeled using a Sellmeier oscillator. The oscillator parameters are summarized in Table 8.1.

Table 8.1 : Summary of Sellmeier oscillator modeling results for five common YBCO substrate materials and $BaZrO_3$.

Material	**A**	**λ_o (nm)**
$LaAlO_3$	3.09 ± 0.01	125.5 ± 2.2
$BaZrO_3$	3.04 ± 0.01	159 ± 6
$NdGaO_3$	3.26 ± 0.01	140.2 ± 1.3
YSZ	3.50 ± 0.01	143.9 ± 0.8
LSAT	2.92 ± 0.01	144.9 ± 1.2
LSGO	2.88 ± 0.01	140.6 ± 1.4

As described in chapter 2, the sensitivity of SE to the oxygen content in YBCO thin films has been exhibited by many researchers.[6,109,141,143,152,157] This sensitivity is a result of the strong dependence of the dielectric function of YBCO on the oxygen content (δ). As δ increases from 0 to 1, strong features which are characteristic of the non-superconducting tetragonal phase develop in the dielectric spectra, particularly near 4.1 eV (302 nm). The sensitivity of SE to any surface layer of oxygen-deficient YBCO on top of fully-oxygenated YBCO is directly related to the refractive index contrast between that surface layer and the rest of the film. The limits of this sensitivity in the case of graded oxygen contents were calculated for the first time using ellipsometric modeling code which was modified to include a concentration gradient of oxygen at the surface of the film.

It was shown for atomically smooth *c*-axis oriented films that SE is sensitive to the oxygen concentration to within one unit cell, even when the oxygen profile is graded (at an angle of incidence of 70°). In addition, the minimum detectable change of surface oxygen concentration (c_s) was determined to be between 0.016 and 0.023, depending on the starting value of c_s compared to the rest of the film. Subsequently, the sensitivity limits were determined for the case where the YBCO film is buried under a 4 nm thick normal metal layer of $SrRuO_3$. It was shown that for *c*-axis oriented films the sensitivities of SE were not changed significantly.

Similar calculations were made for *a*-axis oriented YBCO films. In this case, changes in the diffused depth of as little as 10 Å were shown to be detectable with and without the overlayer of $SrRuO_3$. When the surface oxygen concentration was changed without the overlayer, the minimum detectable change in c_s was found to be 0.023 - 0.078 depending on the starting c_s. With the $SrRuO_3$ in place, the sensitivity drops to 0.031 - 0.078.

A real-time spectroscopic ellipsometer (RTSE) was constructed and adapted for use on an existing molecular beam epitaxy (MBE) deposition system. The RTSE is of the rotating polarizer type and is a third-generation instrument. Controlling software was written using Microsoft's Visual C++ Developer Studio compiler along with National Instruments' LabWindows/CVI development system. The RTSE was designed as a complementary tool to the other existing *in situ* deposition monitors on the MBE, including atomic absorption flux monitoring (AA), quartz crystal monitor flux monitoring (QCM) and reflection high energy electron diffraction (RHEED). This was the first time that RTSE has been applied to the deposition of oxide thin films by MBE, thus it was important to determine how it could be used, its limitations and how it complemented the other *in situ* techniques.

Initially, the RTSE was used to calibrate the substrate temperature in the MBE. Typically, the temperature was measured using pyrometry. However, this method relies on an absolute irradiance measurement, thus complications can arise from optical losses and the necessary assumption of a given emissivity of the surface being measured. Critical point analysis was used to extract the exact position of the 3.375 eV feature in the Si dielectric function. This energy position was then related to the temperature using a known relationship.[243] A complete calibration curve was determined for a wide range of substrate thermocouple values. This calibration was subsequently used for the analysis of oxygen diffusion in YBCO thin films, as well as for the deposition of Y_2O_3 on Si.

Since SE is sensitive to the incorporation of the individual atomic species at the substrate, it can provide a quantitative comparison of how much of the incoming flux is incorporated into the depositing film. This was done by comparing the *in situ* AA flux measurements to the SE-determined thickness as a function of time. Y_2O_3 was deposited on both (100) and (111) oriented Si while collecting RTSE data. Excellent agreement was found between the SE and AA determined thicknesses for the deposition on (100) Si. In addition, Rutherford backscattering measurements (RBS) of the thickness also showed very good agreement. The sticking coefficient of Y in Y_2O_3 was found to be 1.00 ± 0.07. The deposition rate was also extracted from the SE measurements. The optical properties of the resulting film were modeled using a Sellmeier oscillator and compared to values for bulk material. The values for the film were slightly lower than those of the bulk, which was related to a slightly lower density for the film material.

As previously mentioned, one of the major materials-related issues regarding the implementation of Josephson junction technology is the ability to attain smooth YBCO films that are fully oxygenated all the way up to the interface with the interlayer material. Therefore, it is critical to understand the oxygen diffusion behavior in YBCO during, and subsequent to, thin film processing in various environments. This was done using single wavelength *ex situ* ellipsometry and real-time SE.

Initial experiments were conducted using the *ex situ* ellipsometer described in chapter 3. Due to the relatively slow data collection time, only a single wavelength could be monitored while the YBCO film was heated in air or in flowing Ar. Based on the YBCO dielectric function, as well as the calculations of the sensitivity limits of SE, 302 nm (4.1 eV) was chosen as the wavelength for monitoring oxygen diffusion. Substantial changes in the ellipsometric parameters were observed upon heating the film in flowing Ar due to reduction in the film. The temperature dependence of the ellipsometric parameters was also observed at 302 nm for $YBCO_6$ and $YBCO_7$. This dependence was much stronger for reduced YBCO. To explore this, an oxygen-deficient sample was heated under flowing Ar. The temperature coefficients for the ellipsometric parameters could be extracted and were found to be -3.2×10^{-2} °/° C for Δ and -1.1×10^{-2} °/° C for Ψ between 30 °C and 530 °C. Upon heating the same sample in air up to 150 °C and cooling, the ellipsometric parameters showed reversibility, indicating the changes were due to the temperature dependence. On heating to 260 °C and cooling, the data showed some irreversibility, indicating the onset of oxidation in the film. More quantitative analysis of the data was hindered by degradation of the sample after temperature cycling (as observed by x-ray measurements and optically), as well as to the lack of control over the local environment of the film on heating.

To eliminate these problems, the RTSE was used to observe the diffusion of oxygen in the MBE chamber under various controlled environments. First, the spectroscopic temperature dependence of the ellipsometric parameters were determined for both $YBCO_6$ and $YBCO_7$. It was determined that for Ψ, 350 nm and 550 to 650 nm provided the best combination of low temperature dependence and good sensitivity to the oxygen content. In Δ, it was somewhat more difficult to determine due to the noisier data, but in general wavelengths between 550 nm and 650 nm showed the best combination.

Next, oxygen in-diffusion studies were completed in three different atmospheres: 1) molecular oxygen (O_2), 2) output from the ozone generator (10% O_3/90% O_2) and 3) distilled output from the ozone generator (80% O_3/20% O_2). All experiments were conducted at 2×10^{-5} Torr. For molecular oxygen, it was found that the pressure was not high enough to induce complete oxidation of the film under the conditions used. The spectra indicated the onset of oxidation, however at 400 °C, reduction occurred. In 10% O_3/90% O_2, the kinetics were rapid enough to enable complete oxidation over a range of heating rates. Based on the analysis of oxygen diffusion in ceramic YBCO by Tu *et al.*[177] an activation energy for the diffusion of oxygen in an 10% O_3/90% O_2 atmosphere into thin film YBCO was determined. E_a was found to be between 0.43 eV and 0.53 eV depending on the analysis chosen. This value corresponds very well to the value of 0.65 eV obtained by Yamamoto *et al.*[193] for diffusion of oxygen in YBCO from an atomic oxygen environment. For the same experiments conducted in 80% O_3/20% O_2, it was found that the temperature at which oxidation ceased essentially remained the same as for the 10% O_3/90% O_2 atmosphere. This indicated that the output from the ozone generator is sufficient to oxidize YBCO at temperatures below 275 °C. However, the 80% O_3/20% O_2 environment delayed the onset of reduction to higher temperatures than for the 10% O_3/90% O_2 environment.

Finally, the reactivity of ozone as compared to molecular oxygen at 500 °C was determined for YBCO. By comparing ellipsometric spectra at 2×10^{-5} Torr of O_2, 2×10^{-5} Torr of O_3/O_2, 2×10^{-6} Torr of O_3/O_2, 5×10^{-7} Torr of O_3/O_2 and 1×10^{-7} Torr of O_3/O_2, it was possible to determine at what pressure of O_3/O_2 the spectra coincided with that in the pure oxygen atmosphere. It was found that the ozone is at least 2000 times as reactive as molecular oxygen alone at 500 °C.

8.2 Future Work

There are many avenues available pertaining to the application of RTSE to optimizing the deposition of YBCO films by MBE. As was discussed in chapter 2. one of the major roadblocks to the implementation of YBCO in Josephson junction devices is the ability to attain very smooth surfaces for subsequent deposition of the normal metal interlayer. RTSE is extremely sensitive to surface roughness and can be used to observe the development of film microstructure during deposition. The ability to do this for YBCO film growth would assist in the development of optimal processing conditions to obtain smooth YBCO surfaces.

To follow the initial stages of film growth, an achromatic compensator should be inserted into the RTSE setup. The substrates that are used for the deposition of YBCO (i.e., $SrTiO_3$) are transparent in the visible region, and thus Δ is near zero (where SE is inherently inaccurate). Use of a compensator ameliorates this problem by moving Δ data into a region where measurements are more accurate. The resulting system could be used to determine the manner in which roughness evolves during growth, which would facilitate optimization of the deposition conditions. In addition, the ability to characterize the initial growth stages could help to elucidate the mechanism of the formation of the screw dislocations leading to the development of the growth spirals.

A second area which would benefit from additional study is the dependence of the YBCO dielectric function on oxygen content. The data used here were for single crystals at six, widely spaced oxygen contents for $0 \leq \delta \leq 1$. In order to use the modeling code for diffusion gradients, dielectric function data for several more oxygen content values are desired. Reference data at intermediate δ values could be obtained by depositing YBCO films by MBE and incompletely oxidizing them. Ellipsometric spectra for these films would be used, in combination with STM measurements, to calculate the dielectric functions using a direct inversion method. After removal from the chamber, the oxygen content in the films could be measured using Raman spectroscopy.

The data analysis procedure of the RTSE includes the ability to measure the reflectance of a film while it is being deposited. Thus, three-parameter spectroscopy could be employed to garner additional information about the growth. Specifically, the reflectance would be very sensitive to the presence of surface precipitates. Thus, it should be possible to use the information gained from the reflectance measurements to determine at what point the precipitates form. This, along with RHEED measurements, would allow for tailoring of the deposition procedure to specifically avoid conditions conducive to precipitate formation. In addition, preliminary studies have indicated that the *ex situ* ellipsometric parameters are sensitive to off-stoichiometry in the film. The combination of SE and RHEED measurements presents a potentially very powerful *in situ* composition and microstructural monitor for the deposition of YBCO thin films by MBE.

In terms of the oxygen diffusion behavior in YBCO films, the in-diffusion studies completed in this work can be easily extended to different pressures of O_3/O_2. From this, the activation energy as a function of pressure could be obtained. Whether or not δ is a function of oxygen pressure is one of the discrepancies in the existing literature. For out-diffusion, experiments at constant temperature and varying pressure (similar to Tu's work) could be used to determine the activation energy. This would then be compared to that for in-diffusion. Additionally, the anisotropic ellipsometric modeling code (including the concentration gradient) could be used along with thin film reference dielectric function data to quantify the processes of oxidation and reduction. That is, the models would result in a thickness of a graded layer at the surface, thus the time dependence of the layer growth could be extracted.

Finally, it is important to note that the MBE is used to deposit a wide variety of materials, including dielectrics, ferroelectrics and superconductors. RTSE should be applicable to many of these material systems, as well. For instance, the ferroelectric material $PbTiO_3$ is well suited to observation by RTSE. This is due to the fact that the ordinary and extraordinary refractive indices depend strongly on the presence of the spontaneous polarization. It may be possible to observe the onset of this polarization during the deposition using RTSE, thus elucidating at what thickness the material becomes ferroelectric.

Appendix A

MECHANICAL DRAWINGS FOR THE RTSE

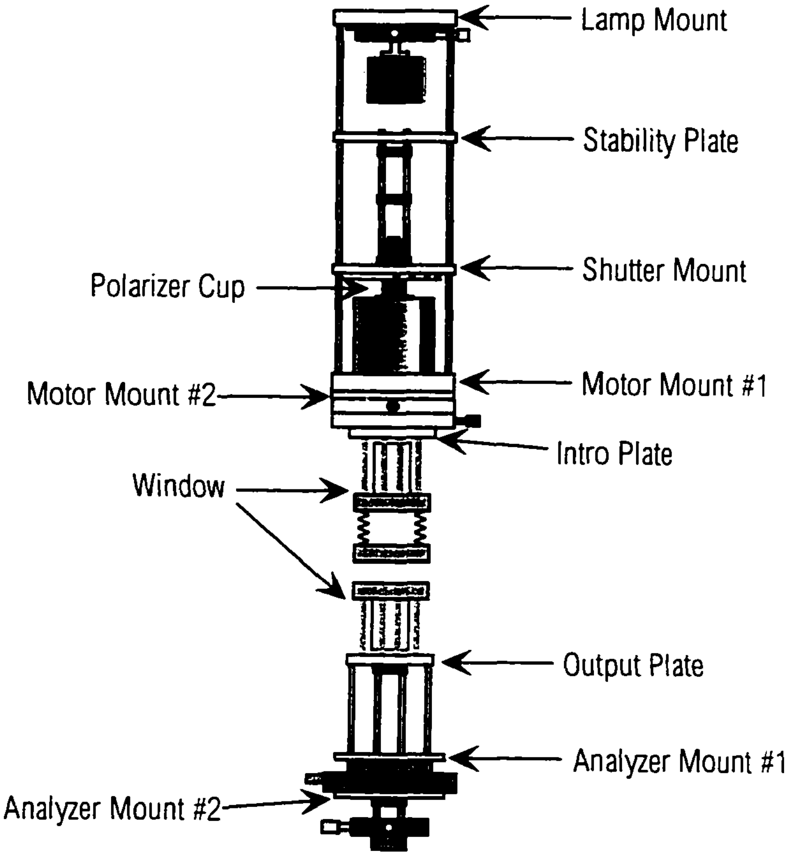

RTSE Diagram Indicating Custom Components

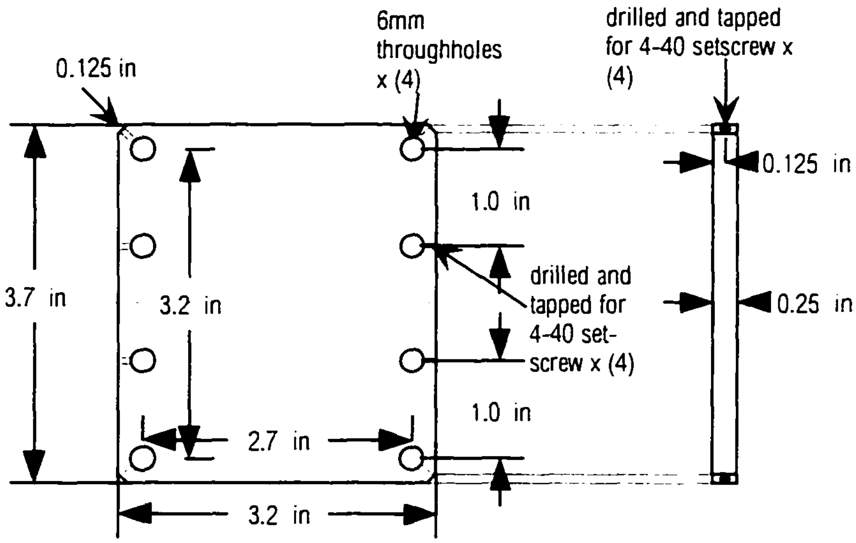

Lamp Mount

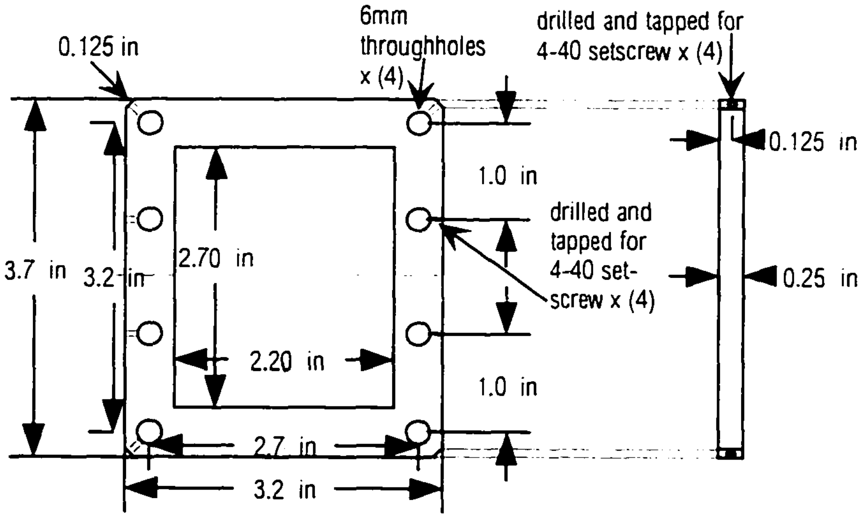

Stability Plate

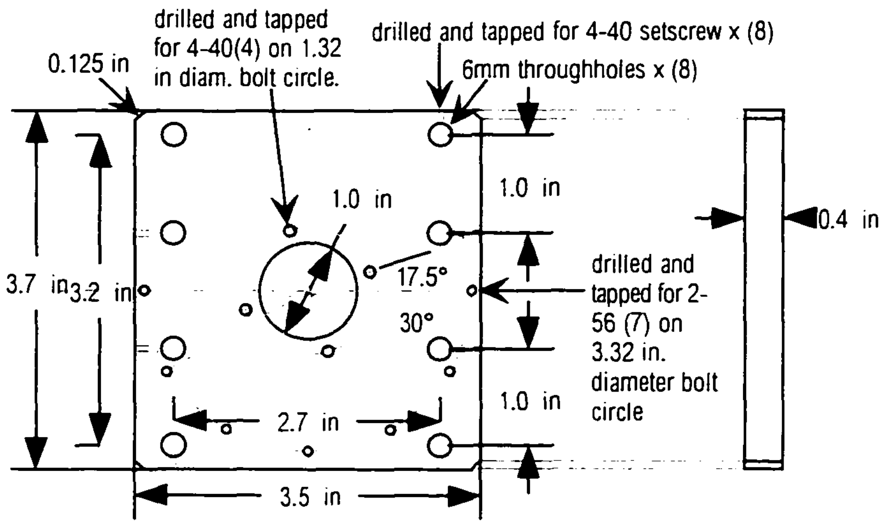

Shutter Mount

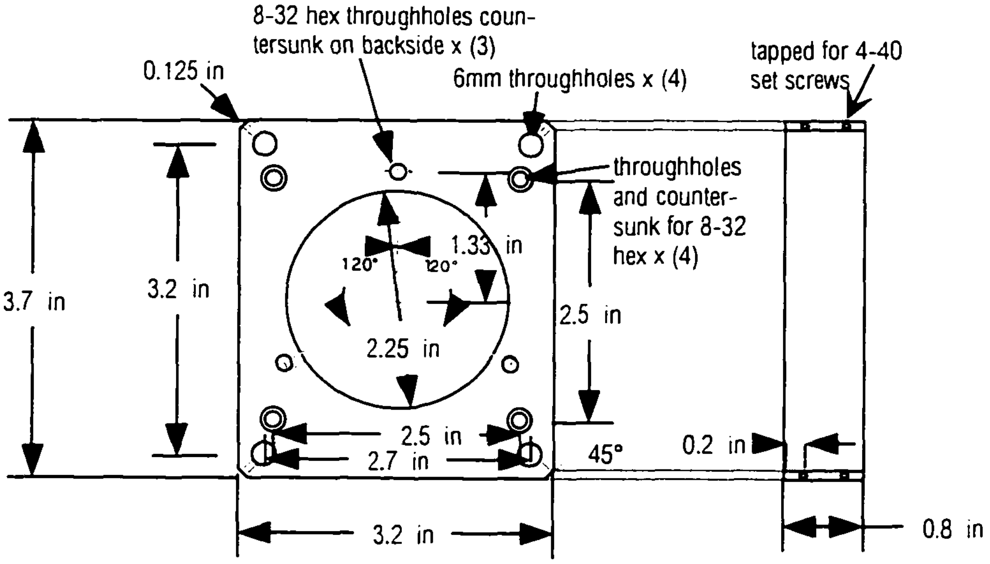

Motor Mount #1

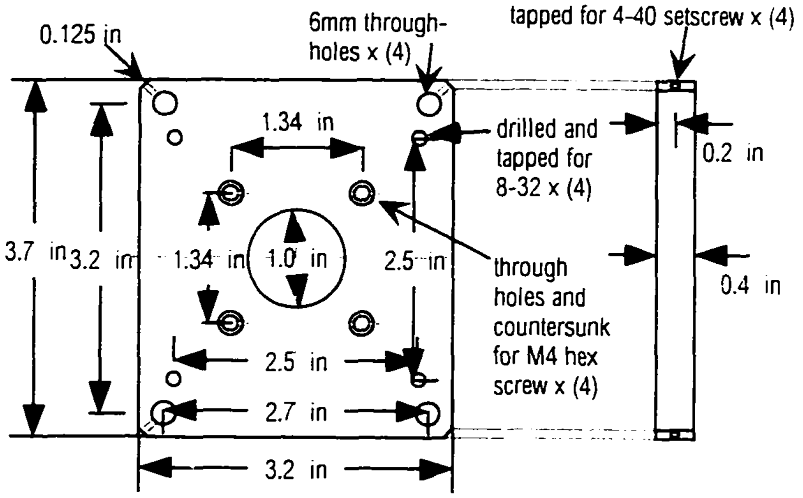

Motor Mount #2

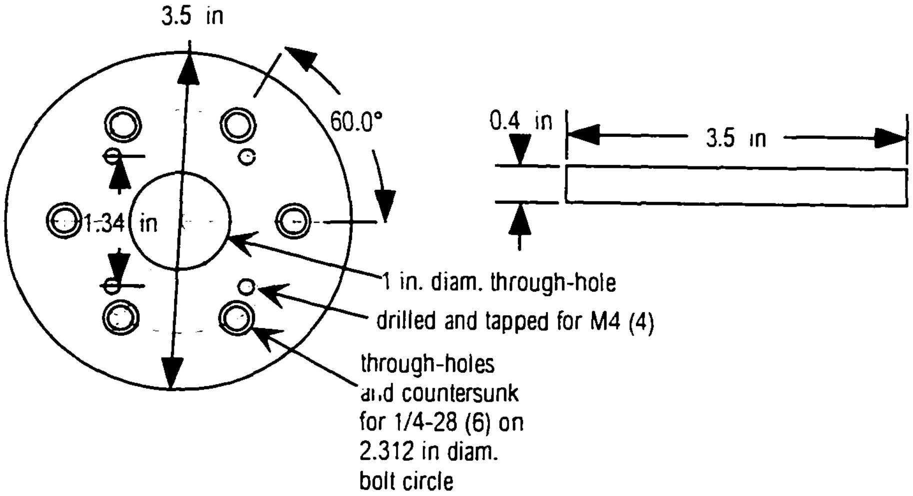

Intro Plate

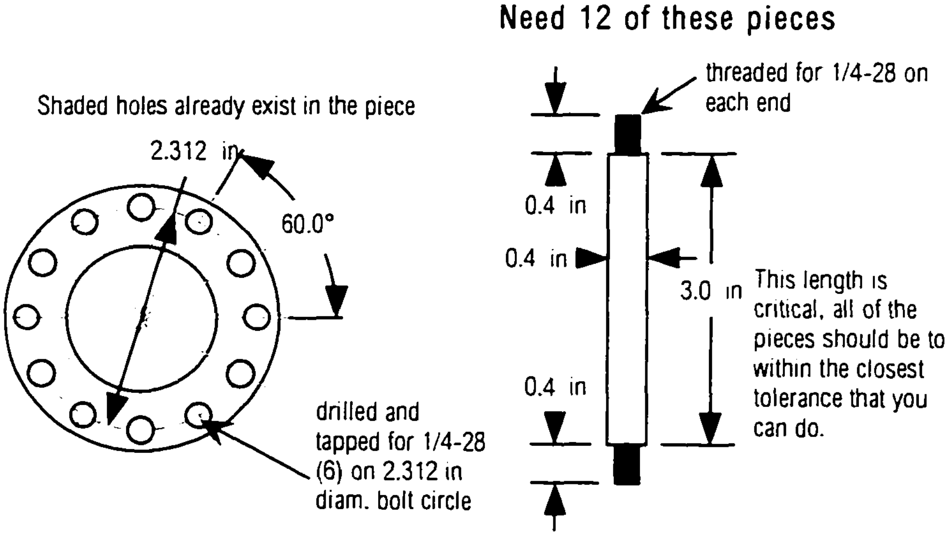

Bomco window modifications

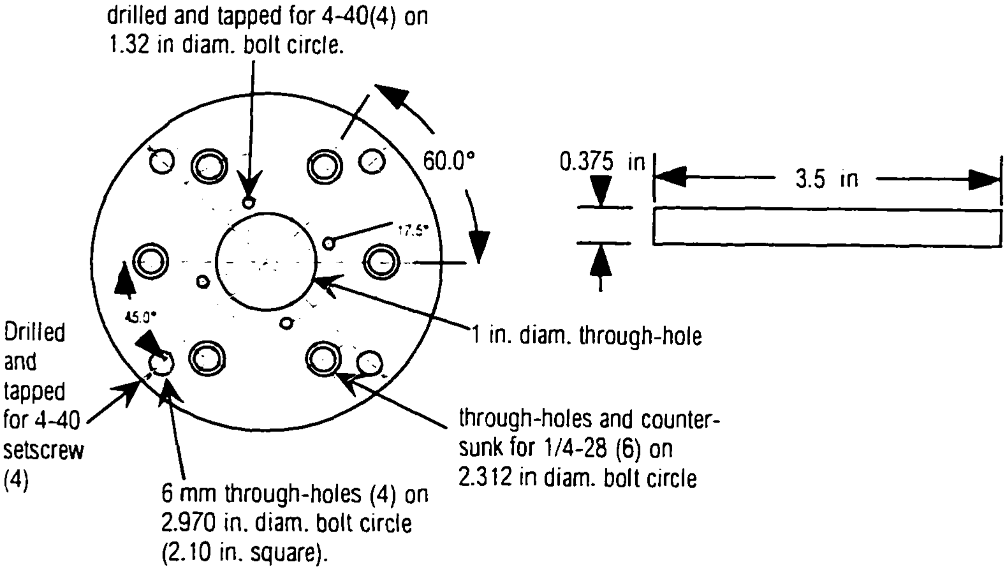

Output Plate

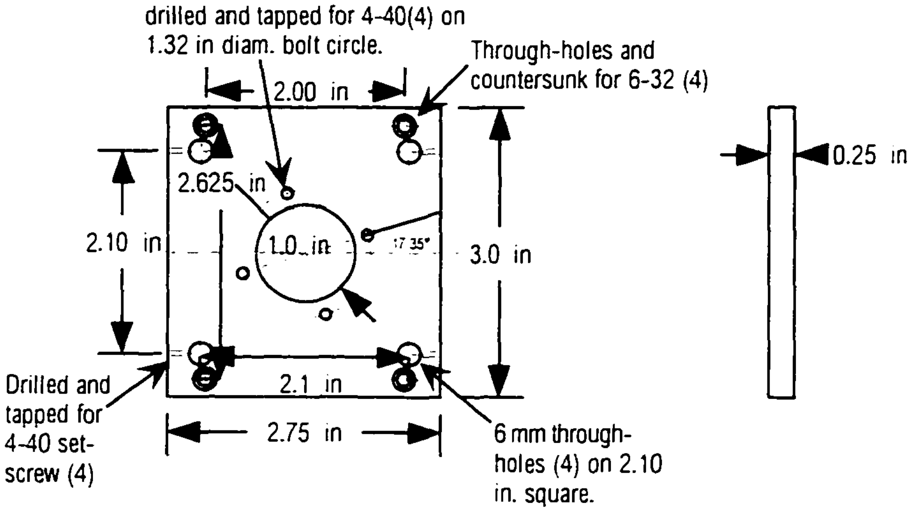

Analyzer mount #1

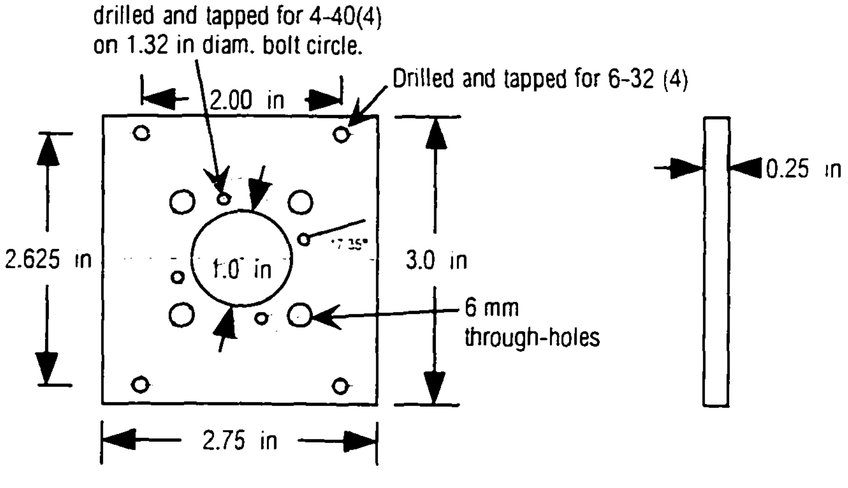

Analyzer mount #2

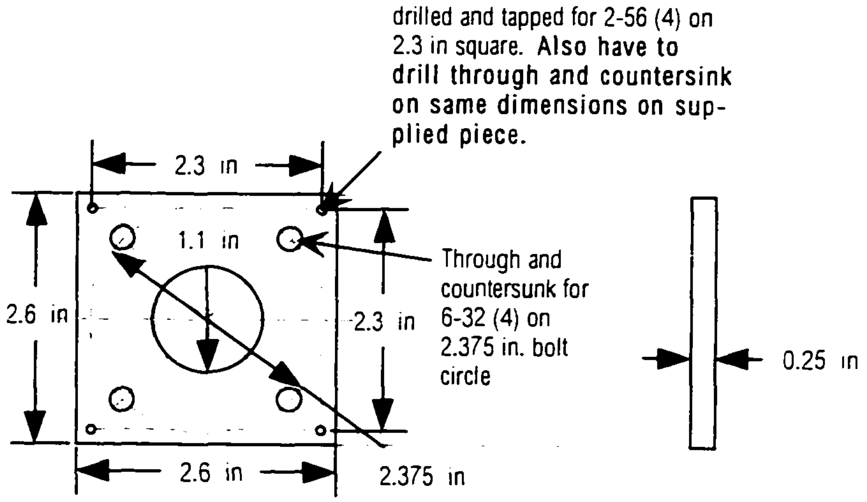
drilled and tapped for 2-56 (4) on 2.3 in square. Also have to drill through and countersink on same dimensions on supplied piece.

Through and countersunk for 6-32 (4) on 2.375 in. bolt circle

Spectrometer Mount

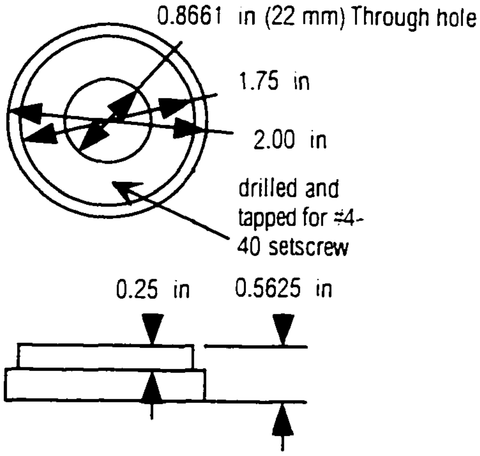
0.8661 in (22 mm) Through hole

drilled and tapped for #4-40 setscrew

Analyzer Cup

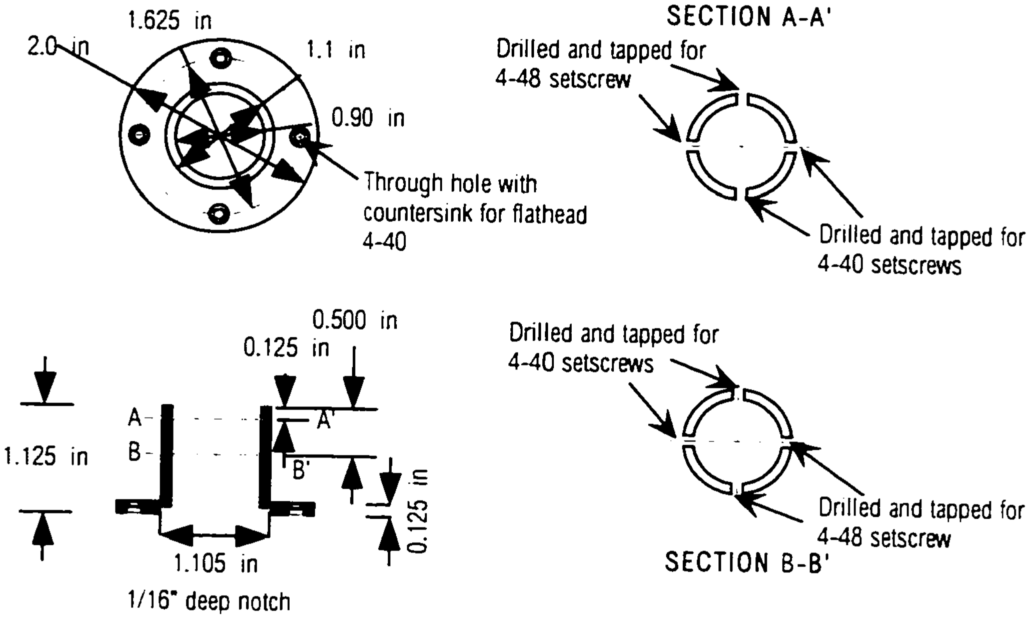

Polarizer Cup

Appendix B

SOFTWARE MANUAL OF RTSE FOR WINDOWS '95

B.1 Overview

RTSE for Windows '95 was developed by the author and is loosely based on original C code obtained from Dr. Robert Collins' ellipsometry group at the Materials Research Laboratory. The code was developed using two programs: the compiler was Microsoft's Visual C++/Developer's Studio® version 5.0 and the graphical user interface (GUI) was designed using National Instruments' LabWindows/CVI® version 4.0. This manual is not intended to be a guide for the use of the compiler or the GUI developer, thus the reader is referred to the appropriate sources for any questions regarding the operation of those programs. In addition, it is assumed that the reader is proficient in the C++ programming language and the principles of spectroscopic ellipsometry.

There are a number of files required to compile the software. These files can be classified into the following groups:

1) *.cpp	C++ source code files
2) *.h	Header files
3) *.uir	Graphical user interface files
4) *.obj, *.lib	Library files

The only files which the user should have to manually alter are those of types 1-3. Upon changing these files, it will be necessary to recompile the program for the changes to take effect. The source code for **RTSE for Windows '95** is given in Appendix C.

RTSE for Windows '95 has been specifically designed to run with the components for this particular ellipsometer. Calls specific to the Princeton Instruments (PI) ST121 detector controller are used throughout the code and cannot be used with any non-PI controller. Also, there are several locations in the code where the author has inserted menu items or subroutines to be used for the addition of a second detector. These will be noted throughout the manual.

B.2 Main Window Interface

Upon starting **RTSE for Windows '95**, the main window will appear. A schematic of the window is given in Fig. B.1. The individual components of the main window are as follows:

1) **Menu Bar** – To be described below. From here the user can access all of the functions of the main window buttons, as well as others.
2) **Psi vs. wavelength graph** – Graph which displays Ψ as a function of wavelength during data collection.
3) **Delta vs. wavelength graph** – Graph which displays Δ as a function of wavelength during data collection.
4) **Shutter control** – Manual switch used to open and close shutter after initialization.
5) **Analyzer position indicator** – Dial along with text display used to indicate current analyzer position.
6) **Calibrate button** – Button for access to the calibration dialog box.
7) **Number of spectra indicator** – Text box for indication of how many spectra have been collected during the user's experiment.
8) **Set data file button** – Button to set the rootfile name for the user's experimental data files.

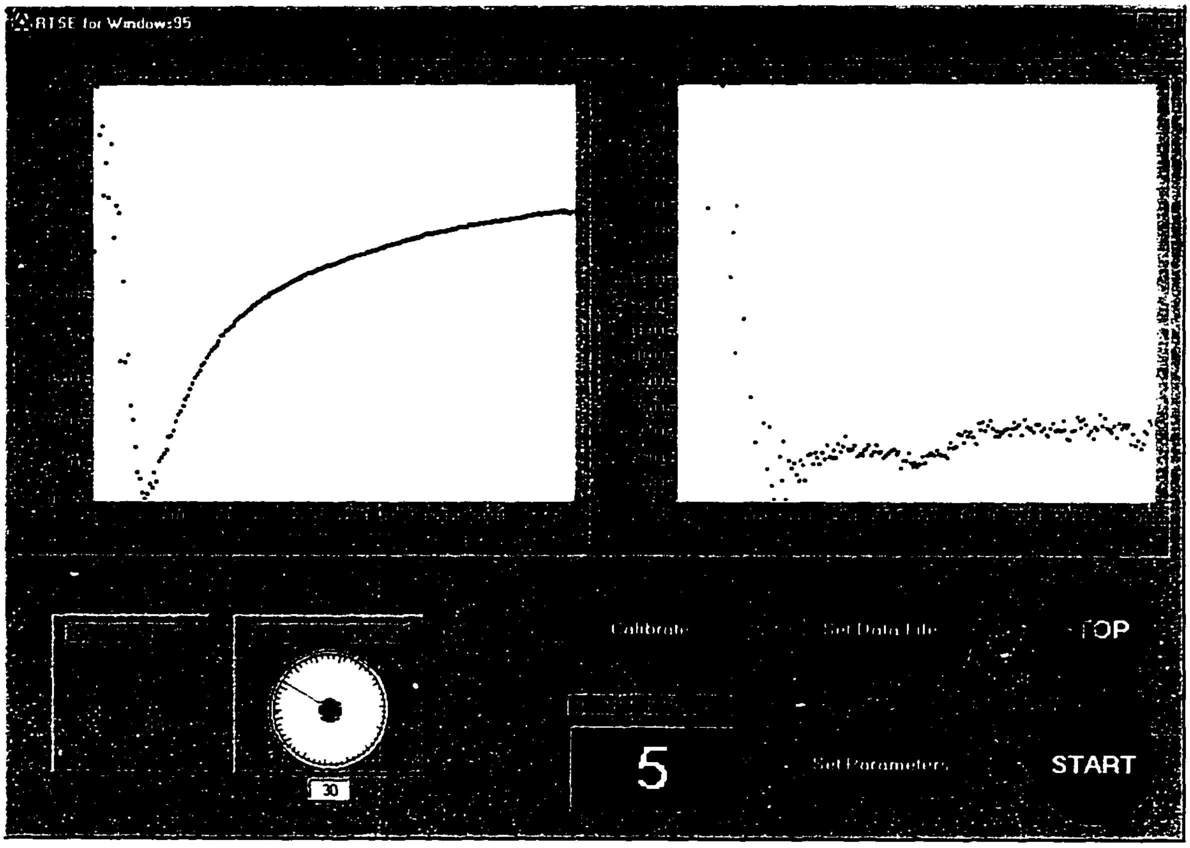

Figure B.1 : Main interface window of RTSE for Windows '95.

9) **Set parameters button** – Button to choose the settings for the user's experiment.
10) **Stop button** – Button to cease data collection.
11) **Start button** – Button to begin data collection.

B.3 Menu Commands

Within the main window of **RTSE for Windows '95**, there is a menu bar from which the user can access all of the functions located on the main window (as buttons), as well as others. The menus and submenus are listed here and shown in Fig. B.2:

File

1) **Open** – Used for access to data files. The selected file will open in Notepad.exe.

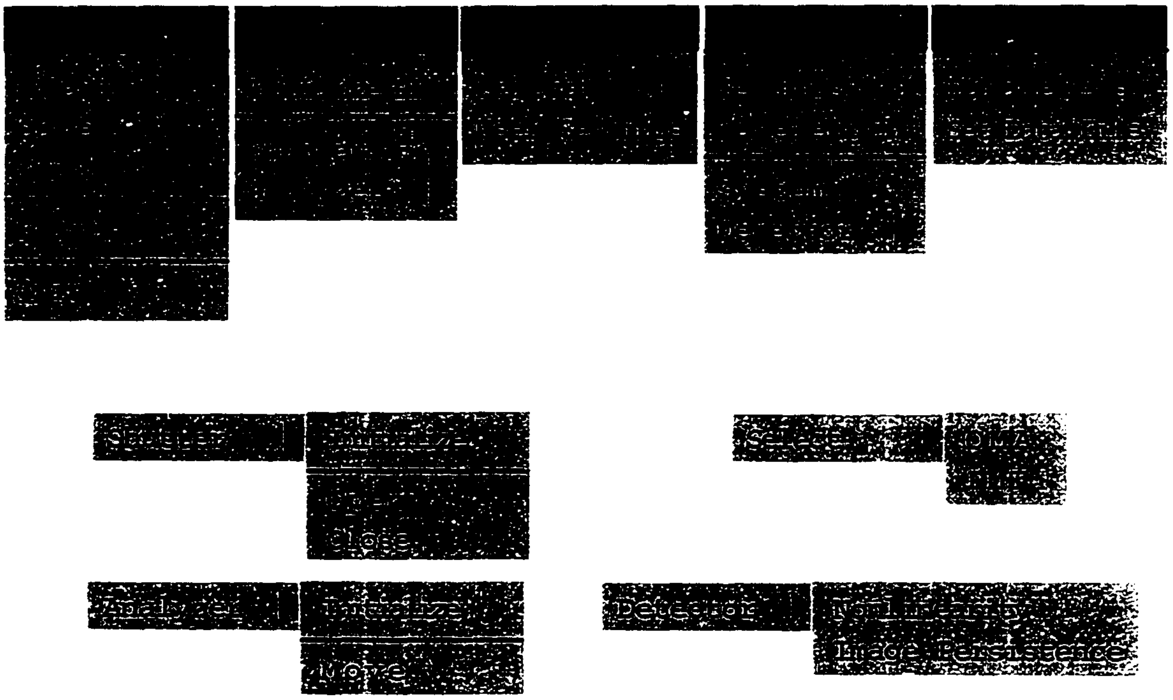

Figure B.2 : Menus and submenus of RTSE for Windows '95.

2) **Save** – Currently unused.

3) **Print** – Currently unused.

4) **Format Data** – This option is used to format a series of data sets with the same rootfile name. The data sets are read and separated into two (three if reflectance was measured) individual files. One file contains the delta values for each spectra and other contains psi. This allows for exporting the data into a 3-dimensional plotting program.

5) **Quit** – Terminates execution of the program.

Setup

1) **Initialize PI** – Initializes the detector controller. This must be the first command executed prior to use of the RTSE.

2) **Shutter** – This expands to a submenu which includes **Initialize**, **Open** and **Close**. The shutter must be initialized subsequent to PI initialization. The shutter is controlled from here, as well as from the switch on the main window.

3) **Analyzer** – This expands to a submenu which includes **Initialize** and **Move**. The analyzer must be initialized subsequent to PI initialization. Selecting move brings up a dialog box prompting the user for an angle to move to.

Detector

1) **Select** – This expands to a submenu which includes **OMA** and **PMT**. Currently the only available option is OMA.
2) **User Settings** – Currently unused.

Calibrate

1) **Settings** – Brings up a dialog box where P_s, P_{sk} and A_s are listed (or can be manually entered).
2) **Wavelength** – Brings up a dialog box where the user enters the slope and the intercept of the wavelength calibration.
3) **System** – Brings up a dialog box for the system calibration. Operates identically to the calibrate button on the main window.
4) **Detector** – This expands to a submenu which includes **Nonlinearity** and **Image Persistence**. Used for benchtop calibrations of the photodiode array.

Measure

1) **Parameters** – Brings up a dialog box for experimental settings. Operates identically to the Set Parameters button on the main window.
2) **Set Data File** – Operates identically to the Set Data File button.

B.4 Operation

Upon running RTSE for Windows '95, the user must first initialize the PI detector controller. All of the buttons and menu items will remain inactive until this is completed. Next, the shutter and analyzer must be initialized. Upon initialization of the analyzer, the user will be prompted to enter the current analyzer angle. This can be found on the analyzer or from the previous user.

The next step prior to data collection is to calibrate the system. This is initiated by selecting "**System**" from the calibrate menu or by pressing the "**Calibrate**" button on the main window. The dialog box that will appear is shown in Fig. B.3. Here, all of the settings for a system calibration can be accessed. The user must select the following:

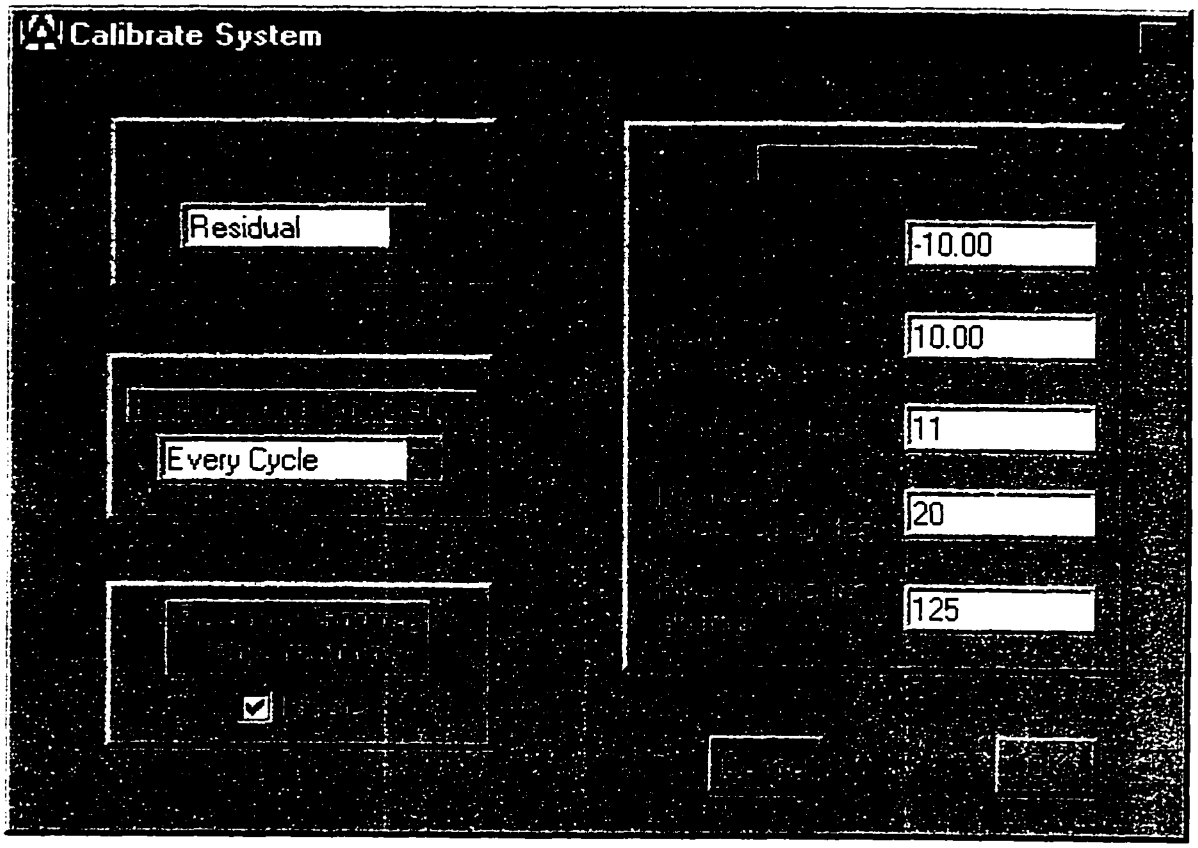

Residual

Every Cycle

☑

-10.00

10.00

11

20

125

Figure B.3 : System calibration window.

1) Type of calibration desired (Residual, Phase or Intensity).
2) Type of background correction (every measurement cycle or only once).
3) Currently the correction for residual source polarization is unused.
4) The starting (minimum) angle of the analyzer in degrees.
5) The ending (maximum) angle of the analyzer in degrees.
6) The number of steps to take between the starting and ending analyzer angles (typically 0.1° steps are necessary).
7) The number of polarizer cycles to average.

8) The pixel number used to plot the data in the calibration windows.

Once the settings have been entered, the user should click "OK" and the detector will be reinitialized and the calibration will begin. Three plot windows will immediately open. When the analyzer reaches the minimum angle, data for each step in the calibration will be plotted in the upper two windows. When the last data point is collected, the curve fits will be plotted on top of the data and the mean and standard deviation of A_s will be output along with P_s and P_{sk}. At this point, the user can decide whether or not the calibration is satisfactory. If not, just repeat the whole procedure.

Should something go wrong during data collection, i.e. the computer ceases to work and the user must reboot, it is not necessary to do a complete recalibration. By selecting "**Settings**" from the "**Calibration**" menu, a dialog box will open (see Fig. B.4). Here, the user can directly enter the values of A_s, P_s and P_{sk} from the previous calibration.

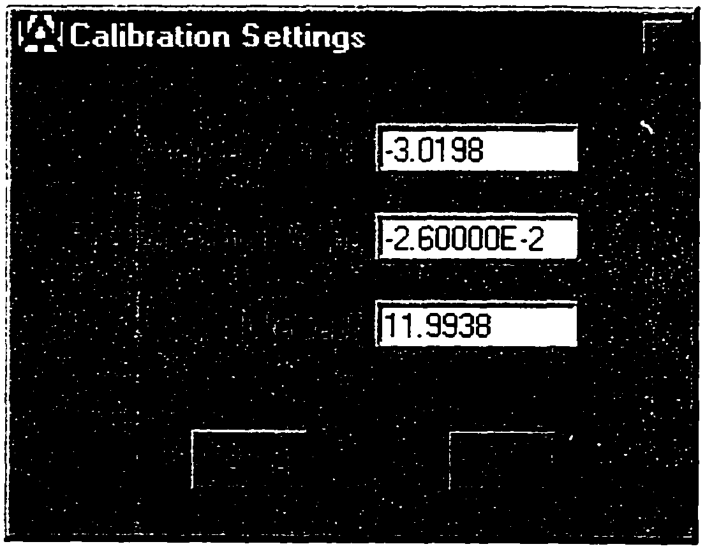

-3.0198

-2.60000E-2

11.9938

Figure B.4 : The system calibration settings dialog box.

Next, the user needs to input the slope and the intercept obtained from the wavelength calibration. That is, the dispersion across the PDA must be input to the program in order to calculate the wavelength from the pixel number. This is done by selecting "**Wavelength**" from the "**Calibration**" menu. The dialog box shown in Fig. B.5 will open for the user to enter these settings.

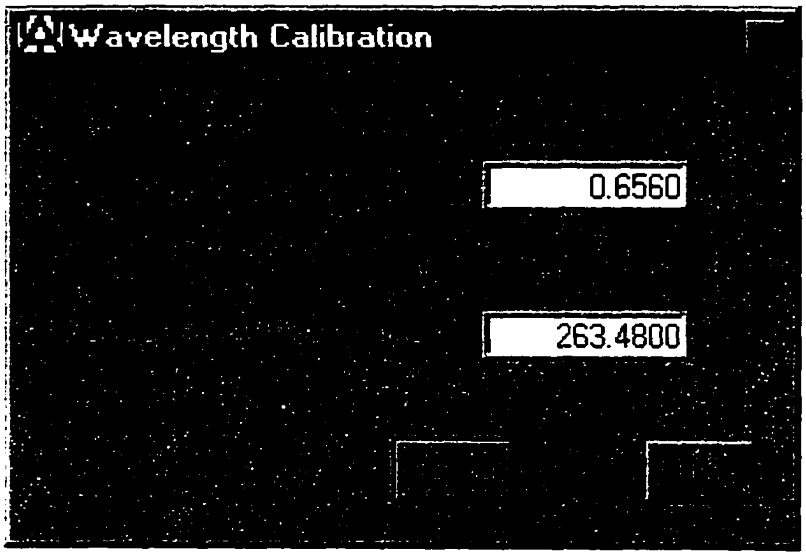

0.6560

263.4800

Figure B.5 : Wavelength calibration parameters dialog box.

Prior to the experiment, the user needs to select a rootfile for the data sets. The number of each spectrum and the extension .dat is appended to the rootfile for every data set. That is, if the user chose the rootfile "YBCO", the 14th spectra would be named YBCO14.dat, and stored in the directory chosen by the user. This parameter is set by choosing the "**Set Data File**" button on the main window, or under the same heading in the "**Measure**" menu. In addition to the *.dat files, a *.inf file is also generated. The experimental parameters are listed in this file, as well as space for the user to write additional notes regarding the experiment.

With the calibrations complete and the rootfile chosen, the user then needs to move the analyzer to the desired position for the experiment. This is done by choosing "**Move**" from the "**Analyzer**" submenu under "**Setup**". Upon selection, a dialog box will appear prompting the user to input the angle desired for the experiment. This dialog is shown in Fig. B.6.

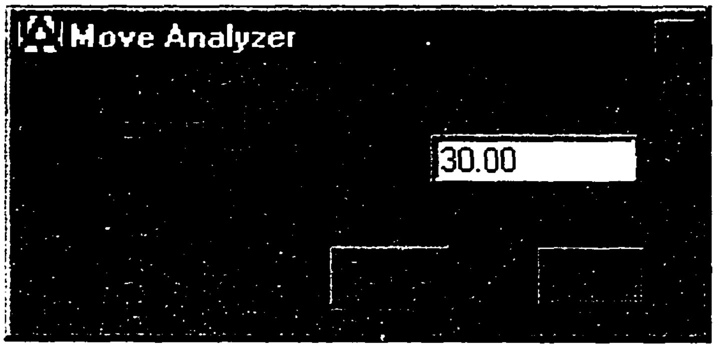

30.00

Figure B.6 : Move analyzer dialog box.

The last step prior to data collection is to set the experimental parameters. This is done by pressing the "**Set Parameters**" button or by selecting "**Parameters**" from the "**Measure**" menu. The dialog box that will appear is shown in Fig. B.7. The user must then select the following:

1) The repetition time for the experiment. That is the time between successive spectra measurements. If the repetition time is too short for the chosen number of averaged cycles, program execution will be halted and the user will be asked to use a longer repetition time. For this reason, it is recommended that the user do a "dry run" prior to actual data collection. This will ensure that the repetition time is long enough and data collection will not be halted during film deposition.
2) The number of mechanical cycles of the polarizer to average. This value will depend on how fast the user wishes to collect data. For each mechanical cycle there are two optical cycles.
3) The number of pixels to "group" by. This is not the same as grouping pixels in the hardware, as on previous RTSE systems. Here, it refers to averaging of adjacent pixels. The user can select 1, 2, 4 or 8 resulting in 800, 400, 200 or 100 data points.

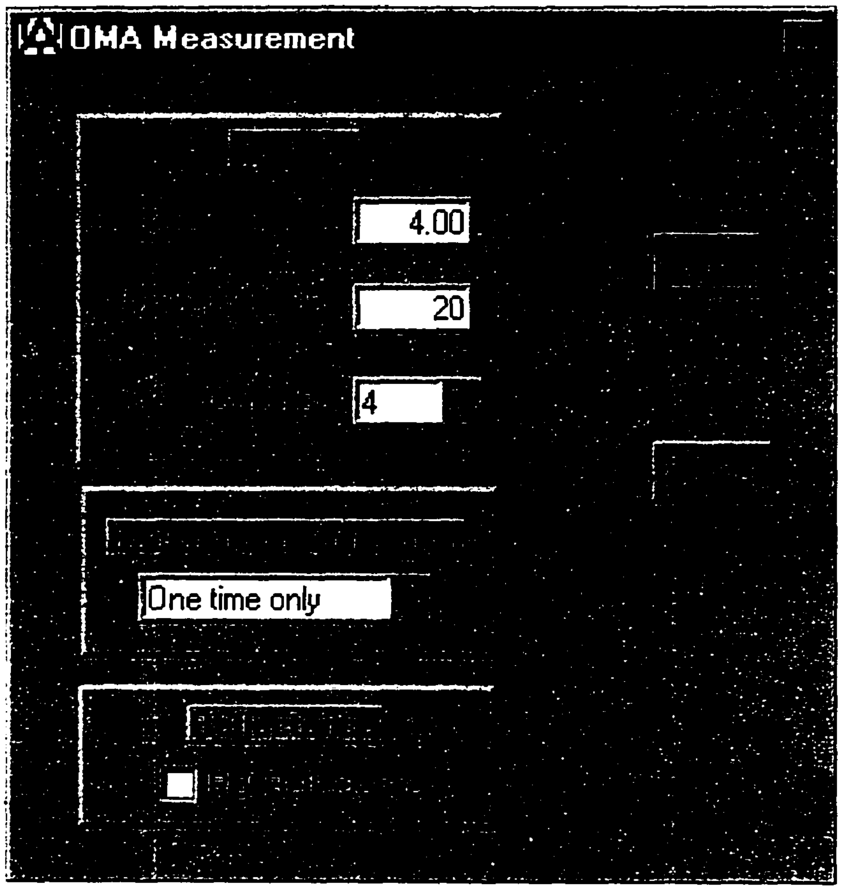

Figure B.7 : Dialog box for the experimental parameters.

4) The type of background correction. The user can choose to measure the background only once, at the beginning of the measurement, or prior to every spectrum. Choosing every cycle will, of course, add to the measurement time, thus the repetition time should be increased accordingly.
5) Whether or not the user chooses to measure reflectance for a particular experiment.

If the user chooses not to measure reflectance, data collection can begin. This is done by pressing the "**Start**" button on the main window. At this point, data collection will commence and continue until the user presses the "**Stop**" button on the main window. If the user does choose to measure reflectance, upon pressing "**Start**" a dialog box will appear asking the user if they would like to load a stored reference reflectance spectrum. This option is necessary if the user has interrupted data collection during a deposition and would like to restart using another rootfile name. That is, the reference spectrum taken on the substrate prior to deposition can still be used, even after growth has commenced. If there is no stored spectrum, the program will take a single spectrum and plot it on the screen. If the spectra are satisfactory the user will be prompted to save the reference reflectance spectrum for future use. At this point, data collection will commence and continue until the "**Stop**" button is pressed.

Finally, after data collection the user can format all of the data sets from a single rootfile for 3-dimensional plotting. This is done by selecting "**Format Data**" from the "**File**" menu. First, a file selection dialog box will appear. Here the user will enter the desired rootfile name. Next, the dialog box shown in Fig. B.8 will appear. The user is prompted to input the total number of data sets to format, as well as how many of those sets to skip. That is, if there are 100 data sets to format and the user wants to use every 5th set, there will be a total of 21 spectra formatted. The user must also input whether or not reflectance was measured. The program will put all of the delta and psi (and reflectance) values into individual files. This operation can be rather time consuming, depending on how many files are being formatted. A message will appear when the formatting is complete.

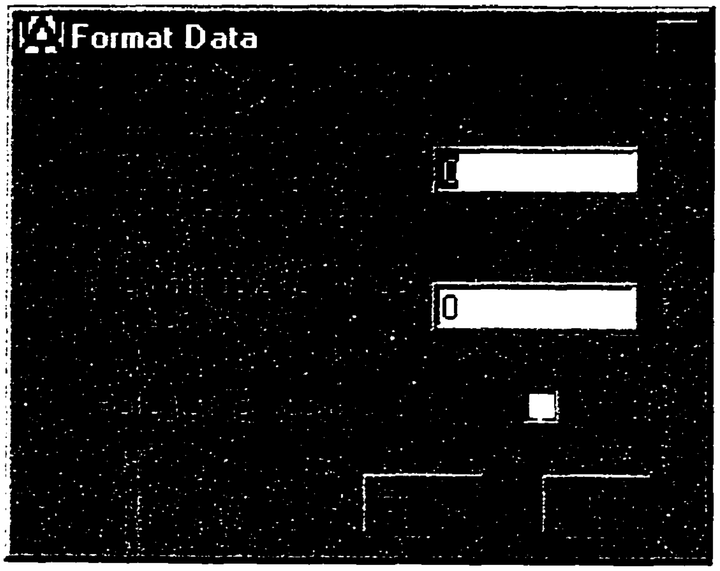

0

Figure B.8 : The format data dialog box.

Appendix C

SOFTWARE CODE FOR RTSE FOR WINDOWS '95

Appendix C is located in the pocket at the back of the thesis.

REFERENCES

[1] K.K. Likharev and V.K. Semenov, "RSFQ Logic/Memory Family: A new Josephson junction technology for sub-terahertz-clock-frequency digital systems," IEEE Transactions on Applied Superconductivity **1**, 3 (1991).

[2] K.K. Likharev, "Rapid single-flux-quantum logic," in *The New Superconducting Electronics*, edited by H. Weinstock and R.W. Ralston (Kluwer, Dordrecht, 1993), Vol. 251, pp. 423.

[3] J. Clarke, "SQUIDs: Theory and Practice," in *The New Superconducting Electronics*, edited by H. Weinstock and R.W. Ralston (Kluwer, Dordrecht, 1993).

[4] K.A. Delin and A.W. Kleinsasser, "Stationary properties of high critical temperature proximity effect Josephson junctions," Superconductor Science and Technology **9**, 227 (1996).

[5] M.K. Kelly, P. Barboux, J.-M. Tarascon and D.E. Aspnes, "Optical properties of copper-oxygen planes in superconducting oxides and related materials," Physical Review B **40** (10), 6797 (1989).

[6] J. Kircher, M.K. Kelly, S. Rashkeev, M. Alouani, D. Fuchs and M. Cardona, "Anisotropy and oxygen-stoichiometry dependence of the dielectric tensor of $YBa_2Cu_3O_{7-\delta}$ $(0 \leq \delta \leq 1)$," Physical Review B **44** (1), 217 (1991).

[7] M.K. Kelly, S.-W. Chan, K. Jenkin II, D.E. Aspnes, P. Barboux and J.-M. Tarascon, "Optical characterization of surface and interface oxygen content in $YBa_2Cu_3O_x$," Applied Physics Letters **53** (23), 2333 (1988).

[8] J.G. Bednorz and K.A. Müller, "Possible high T_c superconductivity in the Ba-La-Cu-O system," Zeitschrift für Physik **64**, 189 (1986).

[9] J.G. Bednorz, M. Takashige and K.A. Müller, "Susceptibility measurements support high-T_c superconductivity in the Ba-La-Cu-O system," Europhysics Letters **3**, 379 (1987).

[10] W.K. Wu, J.R. Ashburn, C.J. Torng, P.H. Hor, R.L. Meng, L. Gao, Z.J. Huang, Y.Q. Wang and C.W. Chu, "Superconductivity at 93 K in a new mixed-phase Y-Ba-Cu-O compound system at ambient pressure," Physical Review Letters **58** (9), 908 (1987).

[11] R. Beyers and T.M. Shaw, "The structure of $YBa_2Cu_3O_{7-\delta}$ and its derivatives," in *Solid State Physics* (Academic Press, 1989), Vol. 42, pp. 135.

[12] M.A. Beno, L. Soderholm, D.W. Capone II, D.G. Hinks, J.D. Jorgensen, J.D. Grace, I.K. Schuller, C.U. Segre and K. Zhang, "Structure of the single-phase high-temperature superconductor $YBa_2Cu_3O_{7-\delta}$," Applied Physics Letters **51** (1), 57 (1987).

[13] W.I.F. David, W.T.A. Harrison, J.M.F. Gunn, O. Moze, A.K. Soper, P. Day, J.D. Jorgensen, D.G. Hinks, M.A. Beno, L. Soderholm, D.W. Capone II, I.K. Schuller, C.U. Segre, K. Zhang and J.D. Grace, "Structure and crystal chemistry of the high-T_c superconductor $YBa_2Cu_3O_{7-x}$," Nature **327**, 310 (1987).

[14] A. Ourmazd, J.A. Rentschler, J.C.H. Spence, M. O'keeffe, R.J. Graham, D.W. Johnson Jr. and W.W. Rhodes, "Microstructure, oxygen ordering and planar defects in the high-T_c superconductor $YBa_2Cu_3O_{6.9}$," Nature **327**, 308 (1987).

[15] C. Kittel, *Introduction to Solid State Physics*, 7th ed. (Wiley, New York, 1996).

[16] J.W. Lynn, "Survey of Superconductivity," in *High Temperature Superconductivity*, edited by J.W. Lynn (Springer-Verlag, New York, 1990), pp. 1.

[17] T. Van Duzer and C.W. Turner, *Principles of Superconductive Devices and Circuits* (Elsevier, New York, 1981).

[18] R.J. Cava, B. Batlogg, C.H. Chen, E.A. Rietman, S.M. Zahurak and D. Werder, "Oxygen stoichiometry, superconductivity and normal-state properties of $YBa_2Cu_3O_{7-\delta}$," Nature **329**, 423 (1987).

[19] R.J. Cava, B. Batlogg, C.H. Chen, E.A. Rietman, S.M. Zahurak and D. Werder, "Single-phase 60-K bulk superconductor in annealed $Ba_2YCu_3O_{7-\delta}$ $(0.3<\delta<0.4)$ with correlated oxygen vacancies in the Cu-O chains," Physical Review B **36** (10), 5719 (1987).

[20] J.D. Jorgensen, M.A. Beno, D.G. Hinks, L. Soderholm, K.J. Volin, R.L. Hitterman, J.D. Grace, I.K. Schuller, C.U. Segre, K. Zhang and M.S. Kleefisch, "Oxygen ordering and the orthorhombic-to-tetragonal phase transition in $YBa_2Cu_3O_{7-x}$," Physical Review B **36** (7), 3608 (1987).

[21] R. Beyers, G. Lim, E.M. Engler, R.J. Savoy, T.M. Shaw, T.R. Dinger, W.J. Gallagher and R.L. Sandstrom, "Crystallography and microstructure of $Y_1Ba_2Cu_3O_{9-x}$, a perovskite-based superconducting oxide," Applied Physics Letters **50** (26), 1918 (1987).

[22] P. Strobel, J.J. Capponi, C. Chaillout, M. Marezio and J.L. Tholence, "Variations of stoichiometry and cell symmetry in $YBa_2Cu_3O_{7-x}$ with temperature and oxygen pressure," Nature **327**, 306 (1987).

[23] E.D. Specht, C.J. Sparks, A.G. Dhere, J. Brynestad, O.B. Cavin, D.M. Kroeger and H.A. Oye, "Effect of oxygen pressure on the orthorhombic-tetragonal transition in the high-temperature superconductor $YBa_2Cu_3O_x$," Physical Review B **37** (13), 7426 (1988).

[24] R. Feenstra, T.B. Lindemer, J.D. Budai and M.D. Galloway, "Effect of oxygen pressure on the synthesis of $YBa_2Cu_3O_{7-x}$ thin films by post-deposition annealing," Journal of Applied Physics **69** (9), 6569 (1991).

[25] J.D. Jorgensen, B.W. Veal, A.P. Paulikas, L.J. Nowicki, G.W. Crabtree, H. Claus and W.K. Kwok, "Structural properties of oxygen-deficient $YBa_2Cu_3O_{7-\delta}$," Physical Review B **41** (4), 1863 (1990).

[26] R. Beyers, B.T. Ahn and G. Gorman, "Oxygen ordering, phase separation and the 60 K and 90 K plateaus in $YBa_2Cu_3O_x$," Nature **340**, 619 (1989).

[27] See for example, *Science and Technology of Thin Films Superconductors I*, ed. R.D. McConnell and S.A. Wolf (Plenum, New York, 1988).

[28] See for example, *Science and Technology of Thin Film Superconductors II*, ed. R.D. McConnell and R. Noufi (Plenum, New York, 1990).

[29] R.M. Silver, J. Talvacchio and A.L. de Lozanne, "Sputter deposition of $YBa_2Cu_3O_{7-y}$ thin films," Applied Physics Letters **51** (25), 2149 (1987).

[30] C.B. Eom, J.Z. Sun, K. Yamamoto, A.F. Marshall, K.E. Luther, T.H. Geballe and S.S. Laderman, "*In situ* grown $YBa_2Cu_3O_{7-d}$ thin films from single-target magnetron sputtering," Applied Physics Letters **55** (6), 595 (1989).

[31] G. Koren, A. Gupta, E.A. Giess, A. Segmüller and R.B. Laibowitz, "Epitaxial films of $YBa_2Cu_3O_{7-\delta}$ on $NdGaO_3$, $LaGaO_3$, and $SrTiO_3$ substrates deposited by laser ablation," Applied Physics Letters **54** (11), 1054 (1989).

[32] K. Kamigaki, H. Terauchi, T. Terashima, Y. Bando, K. Iijima, K. Yamamoto and K. Hirata, "X-ray study on ultra-thin $YBa_2Cu_3O_{7-\delta}$ single crystal film in situ grown by an activated reactive evaporation method," Solid State Ionics **40/41**, 815 (1990).

[33] S. Takeno, S. Nakamura, M. Sagoi and T. Miura, "Defect structure study of $YBa_2Cu_3O_{7-x}$ epitaxial thin films on $SrTiO_3$ (100) and (110) substrates," Physica C **176**, 151 (1991).

[34] T. Haage, H.-U. Habermeier and J. Zegenhagen, "Periodic step structure of clean and $YBa_2Cu_3O_{7-\delta}$ covered vicinal $SrTiO_3$ (001) surfaces," Surface Science Letters **370** (1), L158 (1997).

[35] M. Bianconi, L. Correra, A. Lamagna, S. Nicoletti, R. Nipoti, M. Sánchez Balmaseda and M. Servidori, "Structural and electrical characterization of $YBa_2Cu_3O_{7-x}$ thin films grown on different substrates," High T_c Superconductor Thin Films, edited by L. Correra, 783 (1991).

[36] G. Lu, F. Phillipp, B. Leibold, A.A.C.S. Lourenco and H.-U. Habermeier, "Interface structure of YBCO thin films on different substrates," High Tc Superconductor Thin Films, edited by L. Correra, 689 (1991).

[37] T.-S. Gau, S.-L. Chang, H.-H. Hung, C.-H. Lee, T.-W. Huang, H.-B. Lu, S.-J. Yang and S.-E. Hsu, "Direct observation of the interface structure of thin $YBa_2Cu_3O_x$ film (<500 Å) deposited on $SrTiO_3$ (001) utilizing grazing incidence x-ray diffraction," Applied Physics Letters **65** (13), 1720 (1994).

[38] E.M.C.M. Reuvekamp, W.A.M. Aarnink, W.H. Minkjan, G.J. Gerritsma and H. Rogalla, "The effect of the substrate temperature on the growth of $YBa_2Cu_3O_{7-d}$ on $LaAlO_3$ using RF magnetron sputtering," High T_c Superconductor Thin Films, edited by L. Correra, 523 (1991).

[39] L.P. Guo, Y.J. Tian, J.Z. Liu, S.F. Xu, L. Li, Z.X. Zhao, Z.H. Chen, D.F. Cui, H.B. Lu, Y.L. Zhou and G.Z. Yang, "Microstructural features at the interface between laser ablated $YBa_2Cu_3O_7$ films and $LaAlO_3$ substrates," Applied Physics Letters **66** (24), 3356 (1995).

[40] S. Hontsu, J. Ishii, T. Kawai and S. Kawai, "$LaSrGaO_4$ substrate gives oriented crystalline $YBa_2Cu_3O_{7-y}$ films," Applied Physics Letters **59** (22), 2886 (1991).

[41] R. Feenstra, L.A. Boatner, J.D. Budai, D.K. Christen, M.D. Galloway and D.B. Poker, "Epitaxial superconducting thin films of $YBa_2Cu_3O_{7-x}$ on $KTaO_3$ single crystals," Applied Physics Letters **54** (11), 1063 (1989).

[42] K.A. Dean, D.B. Buchholz, L.D. Marks, R.P.H. Chang, B.V. Vuchic, K.L. Merkle, D.B. Studebaker and T.J. Marks, "$YBa_2Cu_3O_{7-\delta}$ on MgO films grown by pulsed organometallic beam epitaxy and a grain boundary junction application," Journal of Materials Research **10** (11), 2700 (1995).

[43] M. Aindow, D.J. Norris and T.T. Cheng, "Misfit dislocations in laser-ablated heteroepitaxial $YBa_2Cu_3O_{7-\delta}$ on MgO (001)," Philosophical Magazine Letters **74** (4), 267 (1996).

[44] O. Eibl, K. Hradil and H. Schmidt, "Interface analysis of epitaxial $YBa_2Cu_3O_7$ thin films deposited on sapphire (Al_2O_3) with YSZ buffer layers," Physica C **177**, 89 (1991).

[45] N.J. Wu, X.Y. Li, J. Li, H. Lin, H. Fredricksen, K. Xie, A. Mesarwi, A. Ignatiev and H.D. Shih, "Thin film deposition and interface characterization of YBCO on $LiNbO_3$ substrates," Journal of Materials Research **10** (12), 3009 (1995).

[46] J.A. Alarco, G. Brorsson, T. Claeson, Z.G. Ivanov, M. Löfgren and P.-A. Nilsson, "YBCO thin films on yttria stabilized zirconia and $LaAlO_3$-growth and properties," Physica C **185-189**, 2017 (1991).

[47] J.A. Alarco, G. Brorsson, H. Olin and E. Olsson, "Early stages of growth of $YBa_2Cu_3O_{7-\delta}$ high T_c superconducting films on (001) Y-ZrO_2 substrates," Journal of Applied Physics **75** (6), 3202 (1994).

[48] J.G. Wen, C. Traeholt, H.W. Zandbergen, K. Joosse, E.M.C.M. Reuvekamp and H. Rogalla, "A HREM study of the atomic structure and the growth mechanism at the $YBa_2Cu_3O_7$/YSZ interface," Physica C **218**, 29 (1993).

[49] D.G. Schlom, E.S. Hellman, E.H. Hartford, C.B. Eom, J.C. Clark and J. Mannhart, "Origin of the $\phi \approx \pm 9°$ peaks in $YBa_2Cu_3O_{7-\delta}$ films grown on cubic zirconia substrates," Journal of Materials Research **11** (6), 1336 (1996).

[50] J.M. Phillips, "Substrate selection for high-temperature superconducting thin films." Journal of Applied Physics **79** (4), 1829 (1996).

[51] K.-H. Hellwege, "Landolt-Börnstein: Numerical data and functional relationships in science and technology, New Series," in *Group III* (Springer-Verlag, Berlin, 1975), Vol. 7e, 134.

[52] R.H. Hammond and R. Bormann, "Correlation between the *in situ* growth conditions of YBCO thin films and the thermodynamic stability criteria," Physica C **162-164**, 703 (1989).

[53] D.G. Schlom, D. Anselmetti, J.G. Bednorz, R.F. Broom, A. Catana, T. Frey, C. Gerber, H.-J. Güntherodt, H.P. Lang and J. Mannhart, "Screw dislocation mediated growth of sputtered and laser-ablated $YBa_2Cu_3O_{7-\delta}$ films," Zeitschrift für Physik **86**, 163 (1992).

[54] M. Hawley, I.D. Raistrick, J.G. Beery and R.J. Houlton, "Growth mechanism of sputtered films of $YBa_2Cu_3O_7$ studied by scanning tunneling microscopy," Science **251**, 1587 (1991).

[55] C. Gerber, D. Anselmetti, J.G. Bednorz, J. Mannhart and D.G. Schlom, "Screw dislocations in high-T_c films," Nature **350**, 279 (1991).

[56] M. Yeadon, M. Aindow, F. Wellhöfer and J.S. Abell, "Topographical development and misfit relief in laser-ablated heteroepitaxial $YBa_2Cu_3O_{7-\delta}$ thin films," Journal of Crystal Growth **172** (1-2), 145 (1997).

[57] B. Dam, N.J. Koeman, J.G. Rector, B. Stäuble-Pumpin, U. Poppe and R. Griessen, "Growth and etching phenomena observed by STM/AFM on pulsed-laser deposited $YBa_2Cu_3O_{7-\delta}$ films," Physica C **261**, 1 (1996).

[58] B. Stäuble-Pümpin, V.C. Matiasevic, B. Ilge, J.E. Mooij, W.J.A.M. Peterse, P.M.L.O. Scholte, F. Tuinstra, H.J. Venvik, D.S. Wai, C. Traeholt, J.G. Wen and H.W. Zandbergen, "Growth mechanisms of coevaporated $SmBa_2Cu_3O_y$ thin films," Physical Review B **52** (1995).

[59] A. Catana, R.F. Broom, J.G. Bednorz, J. Mannhart and D.G. Schlom, "Identification of epitaxial Y_2O_3 inclusions in sputtered $YBa_2Cu_3O_7$ films: Impact on film growth," Applied Physics Letters **60** (8), 1016 (1992).

[60] M. Aindow and M. Yeadon, "The origins of growth spirals on laser-ablated $YBa_2Cu_3O_{7-\delta}$ thin films," Philosophical Magazine Letters **70** (1), 47 (1994).

[61] F. Baudenbacher, K. Hirata, P. Berberich, H. Kinder, W. Assmann and H.P. Lang, "Extremely smooth YBCO films on MgO with high critical current densities," Physica C **185-189**, 2177 (1991).

[62] J. Mannhart, D. Anselmetti, J.G. Bednorz, A. Catana, C. Gerber, K.A. Müller and D.G. Schlom, "Correlation between J_c and screw dislocation density in sputtered $YBa_2Cu_3O_{7-\delta}$ films," Zeitschrift für Physik B **86**, 177 (1992).

[63] J. Gao, B. Häuser and H. Rogalla, "High critical current density ultrathin $YBa_2Cu_3O_x$ films made by a modified rf-magnetron sputtering technique," Journal of Applied Physics **67** (5), 2512 (1990).

[64] P. Karen, O. Braaten and A. Kjekshus, "Chemical Phase Diagrams for the $YBa_2Cu_3O_7$ Family," Acta Chemica Scandinavica **46**, 805 (1992).

[65] B.T. Ahn, V.Y. Lee, R. Beyers, T.M. Gür and R.A. Huggins, "Quaternary phase relations near $YBa_2Cu_3O_{6+x}$ at 850 °C in reduced oxygen pressures," Physica C **167**, 529 (1990).

[66] C.C. Chang, X.D. Wu, R. Ramesh, X.X. Xi, T.S. Ravi, T. Venkatesan, D.M. Hwang, R.E. Muenchausen, S. Foltyn and N.S. Nogar, "Origin of surface roughness for *c*-axis oriented Y-Ba-Cu-O superconducting films," Applied Physics Letters **57** (17), 1814 (1990).

[67] J. Zhao, C.S. Chern, Y.Q. Li, P. Norris, B. Gallois, B. Kear, X.D. Wu and R.E. Münchausen, "Compositional effects on plasma-enhanced metalorganic chemical vapor deposition of $YBa_2Cu_3O_{7-x}$ thin films," Applied Physics Letters **58** (24), 2839 (1991).

[68] O. Eibl and B. Roas, "Microstructure of $YBa_2Cu_3O_{7-x}$ thin films deposited by laser evaporation," Journal of Materials Research **5** (11), 2620 (1990).

[69] J.P. Loquet, Y. Jaccard, C. Gerber and E. Mächler, "Origin of Cu-rich precipitate formation on superconducting films: A competition between nucleation, oxidation, and growth kinetics," Applied Physics Letters **63**, 1426 (1993).

[70] J.P. Gong, M. Kawasaki, K. Fujito, R. Tsuchiya, M. Yoshimoto and H. Koinuma, "Investigation of precipitate formation on laser-ablated $YBa_2Cu_3O_{7-\delta}$ thin films," Physical Review B **50** (5), 3280 (1994).

[71] A. Catana, J.G. Bednorz, C. Gerber, J. Mannhart and D.G. Schlom, "Surface outgrowths on sputtered $YBa_2Cu_3O_{7-x}$ films: A combined atomic-force microscopy and transmission electron microscopy study," Applied Physics Letters **63** (4), 553 (1993).

[72] A.F. Marshall, V. Matijasevic, P. Roesenthal, K. Shinohara, R.H. Hammond and M.R. Beasley, "Microstructure of Cu- and Y-rich $YBa_2Cu_3O_{7-x}$ thin films: Identification of the $CuYO_2$ phase," Applied Physics Letters **57** (11), 1158 (1990).

[73] M.F. Yan, R.L. Barns, H.M.O.B. Jr., P.K. Gallagher, R.C. Sherwood and S. Jin, "Water interaction with the superconducting $YBa_2Cu_3O_7$ phase," Applied Physics Letters **51** (7), 532 (1987).

[74] T.H. Büyüklimanli and J.H. Simmons, "Surface degradation of $YBa_2Cu_3O_{7-\delta}$ superconductors on exposure to air and humidity," Physical Review B **44** (2), 727 (1991).

[75] S.A. Alterovitz, R.M. Sieg, J.D. Warner, M.A. Stan and S. Vitta, "Ellipsometric study of $YBa_2Cu_3O_{7-x}$ laser ablated and co-evaporated films," Proceedings of the 2nd International Conference on Electronic Materials, edited by , 147 (1990).

[76] H. Behner, K. Rührnschopf, G. Wedler and W. Rauch, "Surface reactions and long time stability of YBCO thin films," Physica C **208**, 419 (1993).

[77] J.T. McDevitt, C.A. Mirkin, R.-K. Lo, K. Chen, J.-P. Zhou, F. Xu, S.G. Haupt, J. Zhao and D.C. Jurbergs, "Molecular level control over the surface and interfacial properties of high T_c superconductors," Chemistry of Materials (1996).

[78] B.D. Josephson, "Possible new effects in superconductive tunneling," Physics Letters **1**, 251 (1962).

[79] A. Barone and G. Paterno, *Physics and Applications of the Josephson Effect* (Wiley, New York, 1982).

[80] P.A. Rosenthal, E.N. Grossman, R.H. Ono and L.R. Vale, "High temperature superconductor-normal metal-superconductor Josephson junctions with high characteristic voltages," Applied Physics Letters **63** (14), 1984 (1993).

[81] J. Bardeen, L.N. Cooper and J.R. Schrieffer, "Theory of Superconductivity," Physical Review **108**, 1175 (1957).

[82] M.D. Strikovskiy and A. Engelhardt, "Ramp-type $YBa_2Cu_3O_{7-\delta}$ Josephson junctions with high characteristic voltage, fabricated by a new, completely *in situ*, growth technique," Applied Physics Letters **69** (19), 2918 (1996).

[83] R.H. Ono, J.A. Beall, M.W. Cromar, T.E. Harvey, M.E. Johansson, C.D. Reintsema and D.A. Rudman, "High-T_c superconductor-normal metal-superconductor Josephson microbridges with high-resistance normal metal links," Applied Physics Letters **59** (9), 1126 (1991).

[84] G.F. Virshup, M.E. Klausmeier-Brown, I. Bozovic and J.N. Eckstein, "Hysteretic, high T_c Josephson junctions using heterostructure trilayer films grown by molecular beam epitaxy," Applied Physics Letters **60** (18), 2288 (1992).

[85] M.E. Klausmeier-Brown, G.F. Virshup, I. Bozovic, J.N. Eckstein and K.S. Ralls, "Engineering of ultrathin barriers in high T_c, trilayer Josephson junctions," Applied Physics Letters **60** (22), 2806 (1992).

[86] K. Char, L. Antognazza and T.H. Geballe, "Study of interface resistances in epitaxial $YBa_2Cu_3O_{7-x}$/barrier/$YBa_2Cu_3O_{7-x}$ junctions," Applied Physics Letters **63** (17), 2420 (1993).

[87] A.W. Kleinsasser and K.A. Delin, "Demonstration of the proximity effect in $YBa_2Cu_3O_{7-\delta}$ edge junctions," Applied Physics Letters **66** (1), 102 (1995).

[88] B.D. Hunt, M.G. Forrester, J. Talvacchio, J.D. McCambridge and R.M. Young, "High-T_c superconductor/normal-metal/superconductor edge junctions and SQUIDs with integrated groundplanes," Applied Physics Letters **68** (26), 3805 (1996).

[89] M.S. DiIorio, S. Yoshizumi, K.-Y. Yang and M. Maung, "Practical high T_c Josephson junctions and dc SQUIDs operating above 85 K," Applied Physics Letters **58** (22), 2552 (1991).

[90] K. Char, M.S. Colclough, T.H. Geballe and K.E. Meyers, "High T_c superconductor-normal-superconductor Josephson junctions using $CaRuO_3$ as the metallic barrier," Applied Physics Letters **62** (2), 196 (1993).

[91] E. Olsson and K. Char, "Origin of nonuniform properties of $YBa_2Cu_3O_{7-\delta}$/$CaRuO_3$/$YBa_2Cu_3O_{7-\delta}$ Josephson edge junctions," Applied Physics Letters **64** (10), 1292 (1994).

[92] S. Rozeveld, K.L. Merkle and K. Char, "Interface microstructure and composition of a $YBa_2Cu_3O_{7-x}$/N/$YBa_2Cu_3O_{7-x}$ SNS edge junction with $CaRuO_3$ as the metallic barrier," Physica C **252**, 348 (1995).

[93] L. Antognazza, K. Char and T.H. Geballe, "Conductance-voltage characteristics of interfaces between $YBa_2Cu_3O_7$ and metallic oxides," Applied Physics Letters **68** (7), 1009 (1996).

[94] K. Char, "Crystal interface engineering in High T_c oxides," MRS Bulletin **19** (9), 51 (1994).

[95] Q.X. Jia, X.D. Wu, D. Reagor, S.R. Foltyn, C. Mombourquette, P. Tiwari, I.H. Campbell, R.J. Houlton and D.E. Peterson, "High-temperature superconductor Josephson junctions with a Pr-doped $Y_{1-x}Pr_xBa_2Cu_3O_{7-\delta}$ (x=0.1, 0.3, 0.5) as barriers," Applied Physics Letters **65** (22), 2866 (1994).

[96] Q.X. Jia, D. Reagor, H. Kung, M. Hawley, C. Mombourquette, S.R. Foltyn, X.D. Wu and D.E. Peterson, "High-temperature superconductor edge-geometry SNS junctions with engineered normal-metal layers," Superconductor Science and Technology **9**, 985 (1996).

[97] T. Umezawa, D.J. Lew, S.K. Streiffer and M.R. Beasley, "Josephson coupling in *a*-axis $YBa_2Cu_3O_{7-\delta}/Pr_{1-x}Y_xBa_2Cu_3O_{7-\delta}/YBa_2Cu_3O_{7-\delta}$ sandwich-type junctions," Applied Physics Letters **63** (23), 3221 (1993).

[98] C.T. Rogers, A. Inam, M.S. Hegde, B. Dutta, X.D. Wu and T. Venkatesan, "Fabrication of heteroepitaxial $YBa_2Cu_3O_{7-y}/PrBa_2Cu_3O_{7-z}/YBa_2Cu_3O_{7-y}$ Josephson devices grown by laser deposition," Applied Physics Letters **55** (19), 2032 (1989).

[99] J.B. Barner, C.T. Rogers, A. Inam, R. Ramesh and S. Bersey, "All *a*-axis oriented $YBa_2Cu_3O_{7-y}/PrBa_2Cu_3O_{7-z}/YBa_2Cu_3O_{7-y}$ Josephson devices operating at 80 K," Applied Physics Letters **59** (6), 742 (1991).

[100] T. Hashimoto, M. Sagoi, Y. Mizutani, J. Yoshida and K. Mizushima, "Josephson characteristics in *a*-axis oriented $YBa_2Cu_3O_{7-\delta}/PrBa_2Cu_3O_{7-\delta}/YBa_2Cu_3O_{7-\delta}$ junctions," Applied Physics Letters **60** (14), 1756 (1992).

[101] Q.X. Jia, X.D. Wu, D. Reagor, S.R. Foltyn, C. Mombourquette and D.E. Peterson, "Edge-geometry SNS dc SQUIDs using Ag-doped $YBa_2Cu_3O_{7-x}$ electrodes," Electronics Letters **32** (5), 499 (1996).

[102] R.M.A. Azzam and N.M. Bashara, *Ellipsometry and Polarized Light* (Elsevier, London, 1972).

[103] D.E. Aspnes and J.B. Theeten, "Optical properties of the interface between Si and its thermally grown oxide," Physical Review Letters **43**, 1046 (1979).

[104] P.J. McMarr, K. Vedam and J. Narayan, "Spectroscopic ellipsometry: A new tool for nondestructive depth profiling and characterization of interfaces," Journal of Applied Physics **59**, 694 (1986).

[105] K. Vedam, P.J. McMarr and J. Narayan, "Nondestructive depth profiling by spectroscopic ellipsometry," Applied Physics Letters **47**, 339 (1985).

[106] J. Narayan, S.Y. Kim, K. Vedam and R. Manukonda, "Formation and nondestructive characterization of ion implanted silicon-on-insulator layers," Applied Physics Letters **51**, 343 (1987).

[107] P. Chindaudom and K. Vedam, "Determination of the optical constants of inhomogeneous transparent LaF_3 thin films on transparent substrates by spectroscopic ellipsometry," Optics Letters **17**, 538 (1992).

[108] S. Trolier-McKinstry, P. Chindaudom, K. Vedam and B.V. Hiremath, "Characterization of optical thin films by spectroscopic ellipsometry," Journal of the American Ceramic Society **78** (9), 2412 (1995).

[109] B.J. Gibbons, S. Trolier-McKinstry, D.G. Schlom and C.B. Eom, "Oxide superconductor interfaces studied by spectroscopic ellipsometry," MRS Symposium Proceedings, Volume 401, 333 (1995).

[110] B.J. Gibbons and S. Trolier-McKinstry, "Dielectric functions of common YBCO substrate materials determined by spectroscopic ellipsometry," IEEE Transactions on Applied Superconductivity **7** (2), 2177 (1997).

[111] G. Zavala, J.H. Fendler and S. Trolier-McKinstry, "Characterization of PZT films by Scanning Force Microscopy (SFM)," MRS Symposium Proceedings, Volume 433 (1996).

[112] R.W. Collins, I. An, H. Fujiwara, J. Lee, Y. Lu, J. Koh and P.I. Rovira, "Advances in multichannel spectroscopic ellipsometry," Thin Solid Films **313-314**, 18 (1998).

[113] S. Trolier-McKinstry and J. Koh, "Composition profiling of graded dielectric function materials by spectroscopic ellipsometry," MRS Symposium Proceedings, Volume 411, edited by R.A. Gerhardt, S.R. Taylor, and E.J. Garboczi, 185 (1996).

[114] M. Fried, T. Lohner, W.A.M. Aarnink, L.J. Hanekamp and A. van Silfhout, "Nondestructive determination of damage depth profiles in ion-implanted semiconductors by spectroscopic ellipsometry using different optical models," Journal of Applied Physics **71**, 2835 (1992).

[115] R.W. Collins, "Automatic rotating element ellipsometers: Calibration, operation, and real-time applications," Review of Scientific Instruments **61** (8), 2029 (1990).

[116] N.V. Nguyen, B.S. Pudliner, I. An and R.W. Collins, "Error correction for calibration and data reduction in rotating-polarizer ellipsometry: applications to a novel multichannel ellipsometer," Journal of the Optical Society of America A **20** (1), 26 (1991).

[117] I. An and R.W. Collins, "Waveform analysis with optical multichannel detectors: Applications for rapid-scan spectroscopic ellipsometry," Review of Scientific Instruments **62** (8), 1904 (1991).

[118] I. An, Y.M. Li, H.V. Nguyen and R.W. Collins, "Spectroscopic ellipsometry on the millisecond time scale for real-time investigations of thin film and surface phenomena," Review of Scientific Instruments **63** (8), 3842 (1992).

[119] R.W. Collins, I. An, H.V. Nguyen and Y. Lu, "Real time spectroscopic ellipsometry for characterization of nucleation, growth, and optical functions of thin films," Thin Solid Films **233**, 244 (1993).

[120] I. An, "Development of real-time spectroscopic ellipsometry and its application to the growth and modification of amorphous silicon thin films," Ph.D. thesis, The Pennsylvania State University, 1992.

[121] B. Hong, "Development of Real-Time Spectroscopic Ellipsometry and its Application to the Growth of Diamond Thin Films by Microwave Plasma-Enhanced Chemical Vapor Deposition," Ph.D. thesis, The Pennsylvania State University, 1996.

[122] H.V. Nguyen, I. An and R.W. Collins, "Evolution of the optical functions of aluminum films during nucleation and growth determined by real-time spectroscopic ellipsometry," Physical Review Letters **68**, 994 (1992).

[123] H.V. Nguyen, I. An and R.W. Collins, "Evolution of the optical functions of aluminum films: A real-time spectroellipsometry study," Physical Review B **47**, 3947 (1993).

[124] H.V. Nguyen and R.W. Collins, "The optical functions of discontinuous aluminum films: Intraband and interband contributions to the particle resonance absorption," Journal of the Optical Society of America A **10**, 515 (1993).

[125] H.V. Nguyen and R.W. Collins, "Real-time spectroscopic ellipsometry studies of the nucleation, growth, and optical functions of thin films, Part II: Aluminum," in *Physics of Thin Films*, edited by K. Vedam (Academic, San Diego, 1994), Vol. 19, pp. 127.

[126] H.V. Nguyen and R.W. Collins, "Finite-size effects on the optical properties of Si nanocrystallites: A real-time spectroscopic ellipsometry study," Physical Review B **47**, 1911 (1993).

[127] H.V. Nguyen and R.W. Collins, "Analysis of critical points in semiconductor optical functions from *in situ* and real-time spectroscopic ellipsometry," Thin Solid Films **233**, 272 (1993).

[128] H.V. Nguyen, Y. Lu, S. Kim, M. Wakagi and R.W. Collins, "Optical properties of ultrathin crystalline and amorphous silicon films," Physical Review Letters **74**, 3880 (1995).

[129] I. An, H.V. Nguyen, N.V. Nguyen and R.W. Collins, "Microstructural evolution of ultrathin amorphous silicon films by real-time spectroscopic ellipsometry," Physical Review Letters **65**, 2274 (1990).

[130] Y.M. Li, I. An, H.V. Nguyen, C.R. Wronski and R.W. Collins, "Real-time spectroscopic ellipsometry determination of the evolution of amorphous semiconductor optical functions, bandgap, and microstructure," Journal of Non-Crystalline Solids **137 & 138**, 787 (1991).

[131] I. An, Y.M. Li, H.V. Nguyen, C.R. Wronski and R.W. Collins, "*In situ* determination of dielectric functions and optical gap of ultrathin a-Si:H by real-time spectroscopic ellipsometry," Applied Physics Letters **59**, 2543 (1991).

[132] Y.M. Li, I. An, H.V. Nguyen, C.R. Wronski and R.W. Collins, "Thin film coalescence in hydrogenated amorphous silicon probed by spectroscopic ellipsometry with millisecond resolution," Physical Review Letters **68**, 2814 (1992).

[133] R.W. Collins, I. An, H.V. Nguyen, Y.M. Li and Y. Lu, "Real-time spectroscopic ellipsometry studies of the nucleation, growth, and optical functions of thin films, Part I: Tetrahedrally-bonded materials," in *Physics of Thin Films*, edited by K. Vedam (Academic, San Diego, 1994), Vol. 19, pp. 49.

[134] B. Hong, M. Wakagi, W. Drawl, R. Messier and R.W. Collins, "Real-time spectroellipsometry study of the evolution of bonding in diamond thin films during nucleation and growth," Physical Review Letters **75**, 1122 (1995).

[135] G.N. Maracas, J.L. Edwards, K. Shiralagi, K.Y. Choi, R. Droopad, B. Johs and J.A. Woolam, "*In situ* spectroscopic ellipsometry in molecular beam epitaxy," Journal of Vacuum Science and Technology A **10** (4), 1832 (1992).

[136] G.N. Maracas, J.L. Edwards, D.S. Gerber and R. Droopad, "*In situ* spectroscopic ellipsometry in molecular beam epitaxy for photonic devices," Applied Surface Science **63**, 1 (1993).

[137] D.E. Aspnes, I. Kamiya, H. Tanaka, R. Bhat, L.T. Florez, J.P. Harbison, W.E. Quinn, M. Tamargo, S. Gregory, M.A.A. Pudensi, S.A. Schwarz, M.J.S.P. Brasil and R.E. Nahory, "Real-time optical diagnostics for measuring and controlling epitaxial growth," Thin Solid Films **225**, 26 (1993).

[138] D.E. Aspnes, "New developments in spectroellipsometry: the challenge of surfaces," Thin Solid Films **233**, 1 (1993).

[139] H.W. Dinges, H. Burkhard, R. Lösch, H. Nickel and W. Schlapp, "Spectroscopic ellipsometry: a useful tool to determine the refractive indices and interfaces of $In_{0.52}Al_{0.48}As$ and $In_{0.53}Al_xGa_{0.47-x}As$ on InP in the wavelength range from 280 to 1900 nm," Thin Solid Films **233**, 145 (1993).

[140] J. Rivory, S. Fisson, V. Van Nguyen, G. Vuye, Y. Wang, F. Abelés and K. Yu-Zhang, "Study of CaF_2 growth on Si, a-SiO_2 by *in situ* spectroscopic ellipsometry," Thin Solid Films **233**, 260 (1993).

[141] M.K. Kelly, P. Barboux, J.-M. Tarascon, D.E. Aspnes, W.A. Bonner and P.A. Morris, "Oxygen-deficiency-induced localized optical excitations in $YBa_2Cu_3O_x$," Physical Review B **38** (1), 870 (1988).

[142] I. Bozovic, K. Char, J.B. Yoo, A. Kapitulnik, M.R. Beasley, T.H. Geballe, Z.Z. Wang, S. Hagen, N.P. Ong, D.E. Aspnes and M.K. Kelly, "Optical Anisotropy of $YBa_2Cu_3O_{7-x}$," Physical Review B **38** (7), 5077 (1988).

[143] M. Garriga, J. Humlicek, M. Cardona and E. Schönherr, "Effects of oxygen deficiency on the optical spectra of $YBa_2Cu_3O_{7-x}$," Solid State Communications **66** (12), 1231 (1988).

[144] A. Bjorneklett, A. Borg and O. Hunderi, "Optical properties of superconducting Y-Ba-Cu-O," Physica A **157**, 164 (1989).

[145] M. Garriga, J. Humlícek, J. Barth, R.L. Johnson and M. Cardona, "Ellipsometric measurements of high-T_c compounds," Journal of the Optical Society of America B **6** (3), 470 (1989).

[146] J. Kircher, M. Alouani, M. Garriga, P. Murugaraj, J. Maier, C. Thomsen, M. Cardona, O.K. Anderson and O. Jepsen, "Anisotropy of the dielectric function in $YBa_2Cu_3O_6$," Physical Review B **40** (10), 7368 (1989).

[147] D.E. Aspnes and M.K. Kelly, "Optical properties of high-T_c superconductors," IEEE Journal of Quantum Electronics **25** (11), 2378 (1989).

[148] L.C. Sengupta, D. Huang, B. Roughani, J.L. Aubel, S. Sundaram and C.L. Chang, "Spectroscopic ellipsometry studies of $YBa_2Cu_3O_{7-\delta}$ deposited on $SrTiO_3$," Journal of Applied Physics **69** (12), 8272 (1991).

[149] H.-U. Habermeier, A.A.C.S. Lourenco, B. Friedl, J. Kircher and J. Köhler, "The growth of (110) Y-Ba-Cu-O thin films and their characterization by optical methods," Solid State Communications **77** (9), 683 (1991).

[150] A.L. Kotz, M.V. Klein, W.C. Lee, J. Giapintzakis, D.M. Ginsberg and B.W. Veal, "Anisotropy of the optical dielectric function in the *ab* plane for $YBa_2Cu_3O_{7-\delta}$," Physical Review B **45** (5), 2577 (1992).

[151] W.A.M. Aarnink, R.P.J. IJsselsteijn, J. Gao, A. van Silfhout and H. Rogalla, "Ellipsometric studies on c-axis oriented high-T_c superconducting $YBa_2Cu_3O_{7-x}$ thin films: thickness measurements and oxygen out-diffusion experiments," High T_c Superconductor Thin Films, edited by L. Correra, 49 (1992).

[152] W.A.M. Aarnink, R.P.J. IJsselsteijn, J. Gao, A. van Silfhout and H. Rogalla, "Oxygen transport in *c*-axis oriented high T_c superconducting $YBa_2Cu_3O_{7-\delta}$ thin films, studied *in situ* by ellipsometry," Physical Review B **45** (22), 13 (1992).

[153] G.-J. Babonas, R. Dagys, V. Kregzdé, G. Pukinskas, E. Belokoneva, L. Leonyuk and A. Vetkin, "Relationship between microstructure and optical properties in high T_c superconductors," Thin Solid Films **234**, 508 (1993).

[154] J. Kircher, S. Gopalan and M. Cardona, "Optical properties of the Y-Ba cuprates: mainly a band structure point of view," Thin Solid Films **234**, 522 (1993).

[155] L.V. Nomerovannaya, A.A. Makhnev and M.M. Kirillova, "Optical study of the doping effect of oxygen in $YBa_2Cu_3O_y$ and $Bi_2Sr_2CaCu_2O_{8+\delta}$ single crystals," Thin Solid Films **234**, 531 (1993).

[156] D.G. Walmsley, A. Sellai, P.G. McCafferty, P. Dawson, C.C. Smyth, T. Morrow and W.G. Graham, "Anisotropy of optical constants of YBCO," Journal of Superconductivity **7** (6), 943 (1994).

[157] M.E. Bijlsma, "An *in situ* ellipsometric study of high-T_c superconducting thin film growth," Ph.D. thesis, University of Twente, 1996.

[158] A. Michaelis, E.A. Irene, O. Auciello, A.R. Kraus and B. Veal, "A spectroscopic anisotropy ellipsometry study of $YBa_2Cu_3O_{7-x}$ superconductors," Thin Solid Films **313-314**, 362 (1998).

[159] G.J. Babonas, R. Dagys, L.I. Leonyuk, O. Hunderi and E. Wold, "Optical manifestation of structural features in layered-type HTSC cuprates," Superlattices and Microstructures **21** (Suppl. A), 11 (1997).

[160] P. Murugaraj, J. Maier and A. Rabenau, "Preparation of large crystals of Y-Ba-Cu-O superconductor," Solid State Communications **71** (3), 167 (1989).

[161] S. Tajima, H. Ishii, T. Nakahashi, T. Takagi, S. Uchida, M. Seki, S. Suga, Y. Hidaka, M. Suzuki, T. Murakami, K. Oka and H. Unoki, "Extensive study of the optical spectra for high-temperature superconducting oxides and their related materials from the infrared to the vacuum-ultraviolet energy region," Journal of the Optical Society of America B **6** (3), 475 (1989).

[162] T.-W. Nee, "Anisotropic optical properties of $YBa_2Cu_3O_7$," Journal of Applied Physics **12** (15), 6002 (1992).

[163] W. Markowitsch, W. Mayr, P. Schwab and X.Z. Wang, "Optical constants of YBaCuO from polarized reflectance measurements," Physica C **223**, 117 (1994).

[164] C.C. Homes, T. Timusk, D.A. Bonn, R. Liang and W.N. Hardy, "Optical properties along the *c*-axis of $YBa_2Cu_3O_{6+x}$, for x=0.50-0.95 Evolution of the pseudogap," Physica C **254**, 265 (1995).

[165] N. Kanda, M. Kawasaki, K. Nakano, T. Shiraishi, A. Takano and H. Koinuma, "*In situ* optical diagnosis of pulsed laser deposition and oxidation of $YBa_2Cu_3O_{7-\delta}$ thin films," Japanese Journal of Applied Physics **36** (4A), 2103 (1997).

[166] I. Bozovic, J.H. Kim, J.S. Harris, C.B. Eom, J. Phillips and J.T. Cheung, "Reflectance and Raman spectra of metallic oxides LaSrCoO and CaSrRuO: resemblance to superconducting cuprates," Physical Review Letters **73** (10), 1436 (1994).

[167] A. Bock, R. Kürsten, M. Brühl, N. Dieckmann and U. Merkt, "Desorption of oxygen from $YBa_2Cu_3O_{6+x}$ films studied with Raman spectroscopy," Physical Review B **54** (6), 4300 (1996).

[168] H. Chang, Q.Y. Chen and W.K. Chu, "Identification of chemical and structural impurities in $YBa_2Cu_3O_{7-\delta}$ films by Raman spectroscopy," Physica C (1996).

[169] K.N. Tu, S.I. Park and C.C. Tsuei, "Diffusion of oxygen in superconducting $YBa_2Cu_3O_{7-\delta}$ oxide upon annealing in helium and oxygen ambients," Applied Physics Letters **51** (25), 2158 (1987).

[170] K.N. Tu, C.C. Tsuei, S.I. Park and A. Levi, "Oxygen diffusion in superconducting $YBa_2Cu_3O_{7-\delta}$ oxides in ambient helium and oxygen," Physical Review B **38** (1), 772 (1988).

[171] B.A. Glowacki, R.J. Highmore, K.F. Peters, A.L. Greer and J.E. Evetts, "A calorimetric study of oxygen intercalation and desorption in bulk superconducting $Y_1Ba_2Cu_3O_{7-x}$," Superconductor Science and Technology **1**, 7 (1988).

[172] K.N. Tu, N.C. Yeh, S.I. Park and C.C. Tsuei, "Thermal recovery of oxygen-deficient superconducting $YBa_2Cu_3O_{7-\delta}$ oxides in ambient oxygen," Physical Review B **38** (7), 5118 (1988).

[173] V.A.M. Brabers, W.J.M. de Jonge, L.A. Bosch, C. v.d. Steen, A.M.W. de Groote, A.A. Verheyen and C.W.H.M. Vennix, "Annealing experiments on and high-temperature behaviour of the superconductor $YBa_2Cu_3O_x$," Materials Research Bulletin **23**, 197 (1988).

[174] N.C. Yeh, K.N. Tu, S.I. Park and C.C. Tsuei, "Effect of oxygen distribution on the resistivity in $YBa_2Cu_3O_{7-\delta}$ oxides $(0 \leq \delta \leq 0.8)$," Physical Review B **38** (10), 7087 (1988).

[175] D.J. Vischjager, P.J. Van der Put, J. Schram and J. Schoonman, "Oxygen diffusion in $YBa_2Cu_3O_{7-x}$: An impedance spectroscopy study," Solid State Ionics **27**, 199 (1988).

[176] Y. Ikuma and S. Akiyoshi, "Diffusion of oxygen in $YBa_2Cu_3O_{7-y}$," Journal of Applied Physics **64** (8), 3915 (1988).

[177] K.N. Tu, N.C. Yeh, S.I. Park and C.C. Tsuei, "Diffusion of oxygen in superconducting $YBa_2Cu_3O_{7-\delta}$ ceramic oxides," Physical Review B **39** (1), 304 (1989).

[178] S.J. Rothman, J.L. Routbort and J.E. Baker, "Tracer diffusion of oxygen in $YBa_2Cu_3O_{7-\delta}$," Physical Review B **40** (13), 8852 (1989).

[179] H.L. Tuller and E. Opila, "Defects and oxygen diffusion in high T_c superconductors," Solid State Ionics **40/41**, 790 (1990).

[180] J. Maier, P. Murugaraj and G. Pfundtner, "Defect chemistry and anisotropic transport in $YBa_2Cu_3O_{6...7}$," Solid State Ionics **40/41**, 802 (1990).

[181] J.L. Tallon and M.P. Staines, "Oxygen self-diffusion coefficient in the superconductor $YBa_2Cu_3O_{7-\delta}$ from internal friction measurements," Journal of Applied Physics **68** (8), 3998 (1990).

[182] Y. Scolnik, E. Sabatani and D. Cahen, "Chemical diffusion coefficient of oxygen in polycrystalline $YBa_2Cu_3O_{7-x}$ at room temperature," Physica C **174**, 273 (1991).

[183] T.B. Tang and W. Lo, "Oxygen diffusion in YBCO: an isothermal thermogravimetric study," Physica C **174**, 463 (1991).

[184] P. Schleger, W.N. Hardy and B.X. Yang, "Thermodynamics of oxygen in $YBa_2Cu_3O_x$ between 450 °C and 650 °C," Physica C **176**, 261 (1991).

[185] S.I. Bredikhin, G.A. Emel'chenko, V.S. Shechtman, A.A. Zhokhov, S. Carter, R.J. Chater, J.A. Kilner and B.C.H. Steele, "Anisotropy of oxygen self-diffusion in $YBa_2Cu_3O_{7-\delta}$ single crystals," Physica C **179**, 286 (1991).

[186] J.L. MacManus, D.J. Fray and J.E. Evetts, "Determination of different oxygen transport mechanisms and measurement of the oxygen ion conductivity of $YBa_2Cu_3O_{7-x}$," Physica C **190**, 511 (1992).

[187] C. Krauns and H.-U. Krebs, "Comparison of the oxygen diffusion in $Y_1Ba_2Cu_3O_Y$ bulk materials and thin films," Zeitschrift für Physik B **92**, 43 (1993).

[188] J.R. LaGraff and D.A. Payne, "Concentration-dependent oxygen diffusivity in $YBa_2Cu_3O_{6+x}$ I. Argon annealing studies," Physica C **212**, 470 (1993).

[189] K. Conder and C. Krüger, "Low temperature (<325 °C) chemical diffusion of oxygen in the orthorhombic $YBa_2Cu_3O_{6+x}$," Physica C **269**, 92 (1996).

[190] G. Sageev-Grader, P.K. Gallagher, J. Thomson and M. Gurvitch, "Rates of change in high temperature electrical resistivity and oxygen diffusion coefficient in $Ba_2YCu_3O_x$," Applied Physics A **45**, 179 (1988).

[191] A. Yoshida, H. Tamura, S. Morohashi and S. Hasuo, "Oxygen diffusion into oxygen-deficient $Ba_2YCu_3O_{7-x}$ films during plasma oxidation," Applied Physics Letters **53** (9), 811 (1988).

[192] Q.Y. Ying, H.S. Kim, D.T. Shaw and H.W. Kwok, Applied Physics Letters **55**, 1041 (1989).

[193] K. Yamamoto, B.M. Lairson, J.C. Bravman and T.H. Geballe, "Oxidation kinetics of $YBa_2Cu_3O_{7-x}$ thin films in the presence of atomic oxygen and molecular oxygen by *in-situ* resistivity measurements," Journal of Applied Physics **69** (10), 7189 (1991).

[194] S.H. Lee, S.C. Bae, J.K. Ku and H.J. Shin, "Oxygen diffusion in epitaxial $YBa_2Cu_3O_{7-x}$ thin films," Physical Review B **46** (14), 9142 (1992).

[195] Y. Li, J.A. Kilner, T.J. Tate, M.J. Lee, R.J. Chater, H. Fox, R.A. De Souza and P.G. Quincey, "Secondary-ion-mass-spectroscopy study of oxygen tracer diffusion in a *c*-axis-oriented $YBa_2Cu_3O_{7-\delta}$ film," Physical Review B **51** (13), 8498 (1995).

[196] Y.P. Li, J.R. Liu, W.K. Chu, J.A. Kilner and T.J. Tate, "Ion beam techniques applied to the study of oxygen diffusion in $YBa_2Cu_3O_{7-\delta}$ films" (1996).

[197] S.J. Rothman, J.L. Routbort, U. Welp and J.E. Baker, Physical Review B **44**, 2326 (1991).

[198] J.R. Arthur, "Interaction of Ga and As_2 molecular beams with GaAs surfaces," Journal of Applied Physics **39**, 4032 (1968).

[199] A.Y. Cho, "Epitaxy by periodic annealing," Surface Science **17**, 494 (1969).

[200] R.A. Kubiak, S.M. Newstead and P. Sullivan, "The technology and design of molecular beam epitaxy systems," in *Molecular Beam Epitaxy: Applications to Key Materials*, edited by R.F.C. Farrow (Noyes Publications, Park Ridge, NJ, 1995).

[201] J.N. Eckstein, I. Bozovic and G.F. Virshup, "Atomic layer-by-layer engineering of high-T_c materials and heterostructure devices," MRS Bulletin **19**, 44 (1994).

[202] D.G. Schlom and J.S. Harris Jr., "MBE growth of high T_c superconductors," in *Molecular Beam Epitaxy: Applications to Key Materials*, edited by R.F.C. Farrow (Noyes Publications, Park Ridge, NJ, 1995), pp. 505.

[203] E.S. Hellman and J. E.H. Hartford, "Synthesis of new oxide materials by molecular beam epitaxy: the Dy-Ba-Cu-O and Ba-K-Bi-O systems," Physica C **190**, 31 (1991).

[204] T. Shimizu, H. Nonaka, S. Hosokawa, S. Icimura and K. Arai, "Preparation of oxide superconducting films using NO_2 and O_3 gases," Physica C **185-189**, 2003 (1991).

[205] C. Kraisinger, "Design and evaluation of a nozzle for the efficient delivery of oxidizing gases during high vacuum deposition," M.S. thesis, The Pennsylvania State University, 1996.

[206] C. Lu, "Mass determination with piezoelectric quartz crystal resonators," Journal of Vacuum Science and Technology **12** (1), 578 (1975).

[207] H. Tabata and T. Kawai, "Atomic layer control of the growth of oxide superconductors using laser molecular beam epitaxy," Thin Solid Films **225**, 275 (1993).

[208] C.D. Theis and D.G. Schlom, "The reactivity of ozone incident onto the surface of perovskite thin films grown by MBE," Volume 97-39, edited by K. Spear, (1997).

[209] C. Lu and Y. Guan, "Improved method of nonintrusive deposition rate monitoring by atomic absorption spectroscopy for physical vapor deposition processes," Journal of Vacuum Science and Technology A **13** (3), 1797 (1995).

[210] W. Kern and D.A. Puotinen, "Cleaning solutions based on hydrogen peroxide for use in silicon semiconductor technology," RCA Review **31**, 187 (1970).

[211] M. Kawasaki, K. Takahashi, T. Maeda, R. Tsuchiya, M. Shinohara, O. Ishiyama, T. Yonezawa, M. Yoshimoto and H. Koinuma, "Atomic control of the $SrTiO_3$ crystal surface," Science **266**, 1540 (1994).

[212] C.B. Eom, A.F. Marshall, S.S. Laderman, R.D. Jacowitz and T.H. Geballe, "Epitaxial and Smooth Films of *a*-axis $YBa_2Cu_3O_7$," Science **249**, 1549 (1990).

[213] D.E. Aspnes, "Spectroscopic ellipsometry of solids," in *Optical Properties of Solids, New Developments*, edited by B.O. Seraphin (North-Holland Publishing Company, Amsterdam, NL, 1976), pp. 799.

[214] P. Aungkavattana, "Crystallization and microstructure development in sol-gel lead zirconate titanate thin films," Ph.D. thesis, The Pennsylvania State University, 1997.

[215] B.J. Gibbons, "A Spectroscopic Ellipsometric and Electrical Study of Processing Effects in Ferroelectric Thin Films," M.S. thesis, The Pennsylvania State University, 1995.

[216] D.E. Aspnes, "Measurement and correction of first-order errors in ellipsometry," Journal of the Optical Society of America **61** (8), 1077 (1971).

[217] D.E. Aspnes, "Effects of component optical activity in data reduction and calibration of rotating-analyzer ellipsometers," Journal of the Optical Society of America **64** (6), 812 (1974).

[218] J.F. Nye, *Physical Properties of Crystals* (Oxford University Press, Oxford, 1957).

[219] D.E. Aspnes and A.A. Studna, "High precision scanning ellipsometer," Applied Optics **14** (1), 220 (1975).

[220] P. Chindaudom, "Characterization of inhomogeneous transparent thin films on transparent substrates by spectroscopic ellipsometry," Ph.D. thesis, The Pennsylvania State University, 1991.

[221] J.M.M. De Nijs and A. van Silfhout, "Systematic and random errors in rotating-analyzer ellipsometry," Journal of the Optical Society of America A **5** (6), 773 (1988).

[222] I. An, H.V. Nguyen, A.R. Heyd and R.W. Collins, "Simultaneous real-time spectroscopic ellipsometry and reflectance for monitoring thin film preparation," Review of Scientific Instruments **65** (11), 3489 (1994).

[223] A.A. Studna, D.E. Aspnes, L.T. Florez, B.J. Wilkens, J.P. Harbison and R.E. Ryan, "Low-retardance fused-quartz window for real-time optical applications in ultrahigh vacuum," Journal of Vacuum Science and Technology A **7** (6) (1989).

[224] Princeton Instruments, "Manual for PDA-1024 detector," (1997).

[225] J.M.M. De Nijs, A.H.M. Holtslag, A. Hoeksta and A. Van Silfhout, "Calibration methods for rotating-analyzer ellipsometers," Journal of the Optical Society of America A **5** (6), 1466 (1988).

[226] R.W. Collins, K. Vedam, A. Heyd, P.J. McMarr, S. Trolier-McKinstry, P. Chindaudom, H. McKinstry, H. Fujiwara and B.J. Gibbons, Modeling programs for ellipsometric data (University Park, 1986-1998).

[227] A.N. Parikh and D.L. Allara, "Quantitative determination of molecular structure in multilayered thin films of biaxial and lower symmetry from photon spectroscopies. I. Reflection infrared vibrational spectroscopy," Journal of Chemical Physics **96** (2), 927 (1992).

[228] P. Yeh, "Electromagnetic propagation in birefringent layered media," Journal of the Optical Society of America **69** (5), 742 (1979).

[229] P. Yeh, "Optics of anisotropic layered media: A new 4x4 matrix algebra," Surface Science **96**, 41 (1980).

[230] R.J. King and M.J. Downs, "Ellipsometry applied to films on dielectric substrates," Surface Science **16**, 288 (1969).

[231] D.E. Aspnes, "Optical properties of thin films," Thin Solid Films **89**, 249 (1982).

[232] P. Chindaudom and K. Vedam, "Optical characterization of inhomogeneous transparent thin films on transparent substrates by spectroscopic ellipsometry," in *Physics of Thin Films* (Academic Press, 1994), p 205.

[233] F. Gervais, "Strontium Titanate ($SrTiO_3$)," in *Handbook of Optical Constants of Solids II*, edited by E.D. Palik (Academic Press, Boston, 1991), pp. 1035.

[234] C.G. Pantano, "Secondary Ion Mass Spectroscopy," in *Materials Characterization*, (ASM International, 1986), Vol. 10, pp. 610.

[235] W.K. Chu and G. Langouche, "Quantitative Rutherford backscattering from thin films," MRS Bulletin **18** (1), 32 (1993).

[236] A. Joshi, "Auger Electron Spectroscopy," in *Materials Characterization*, (ASM International, 1986), Vol. 10, pp. 549.

[237] D.E. Aspnes, W.E. Quinn, M.C. Tamargo, M.A.A. Pudensi, S.A. Schwarz, M.J.S.P. Brasil, R.E. Nahory and S. Gregory, "Growth of $Al_xGa_{1-x}As$ parabolic quantum wells by real-time feedback control of composition," Applied Physics Letters **60** (10), 1244 (1992).

[238] D.E. Aspnes, W.E. Quinn and S. Gregory, "Optical control of growth of $Al_xGa_{1-x}As$ by organometallic molecular beam epitaxy," Applied Physics Letters **57** (25), 2707 (1990).

[239] J. Koh, "The Sensitivity Limits of Spectroscopic Ellipsometry for the Characterization of Optical Coatings," M.S. thesis, The Pennsylvania State University, 1995.

[240] J.-P. Maria, B.J. Gibbons and S. Trolier-McKinstry, "Structural and optical analysis of $SrRuO_3$ epitaxial thin films and powders at elevated temperatures," to be submitted to Applied Physics Letters (1998).

[241] S. Trolier-McKinstry and J. Koh, "Composition profiling of graded dielectric function materials by spectroscopic ellipsometry," Thin Solid Films **313-314**, 389 (1998).

[242] M. Wakagi, B. Hong, H.V. Nguyen, R.W. Collins, W. Drawl and R. Messier, "Characterization of substrate temperature and damage in diamond growth plasmas by multichannel spectroellipsometry," Journal of Vacuum Science and Technology A **13** (4), 1917 (1995).

[243] P. Lautenschlager, M. Garriga, L. Viña and M. Cardona, "Temperature dependence of the dielectric function and interband critical points in silicon," Physical Review B **36** (9), 4821 (1987).

[244] R. Goettler, J.-P. Maria and D.G. Schlom, "The origin of the (110) orientation of epitaxial Y_2O_3 and CeO_2 films grown on (100) silicon," submitted to Applied Physics Letters.

[245] R.A. McKee and F.J. Walker, patent 5,225,031, USA (1993).

[246] R.A. McKee and F.J. Walker, patent 5,482,003, USA (1996).

[247] G.A. Niklasson, C.G. Granqvist and O. Hunderi, "Effective medium models for the optical properties of inhomogeneous materials," Applied Optics **20** (1), 26 (1981).

[248] J. Haeni, personal communication.

[249] Y. Nigara, "Measurement of the optical constants of yttrium oxide," Japanese Journal of Applied Physics **7** (4), 404 (1968).

[250] A. Feldman, X. Ying and E.N. Farabaugh, "Optical properties of mixed yttria-silica films," Applied Optics **28** (24), 5229 (1989).

[251] D.F. Bezuidenhout and R. Pretorius, "The optical properties of evaporated Y_2O_3 films," Thin Solid Films **139**, 121 (1986).

[252] M. Swarnalatha, A.F. Stewart, A.H. Guenther and C.K. Carniglia, "Optical and structural properties of thin films deposited from laser fused zirconia, hafnia, and yttria," Applied Physics A **54**, 533 (1992).

[253] D. Basak and S.K. Sen, "Electrical, dielectric and optical properties of $M/Y_2O_3/M$ devices," Thin Solid Films **254**, 181 (1995).

[254] V. Matijasevic, P. Rosenthal, K. Shinohara, A.F. Marshall, R.H. Hammond and M.R. Beasley, "Reactive coevaporation of YBaCuO superconducting films," Journal of Materials Research **6** (4), 682 (1991).

[255] H.E. Kissinger, Analytical Chemistry **29**, 1702 (1957).

[256] T. Ozawa, Journal of Thermal Analysis **2**, 301 (1970).

VITA

Brady J. Gibbons was born in Syracuse, New York, on July 15th, 1970. He spent the first eighteen years of his life there. In Syracuse, he attended John T. Roberts elementary school, James A. Shea junior high school and Thomas J. Corcoran senior high school. He began his collegiate studies at Rensselaer Polytechnic Institute in Troy, New York, in 1988. There, he received a Bachelor of Science degree in Materials Engineering in May of 1992. Thereafter, he entered the graduate program in Ceramic Science at the Pennsylvania State University. He received his Master of Science degree in May of 1995 and won the Xerox research award for his work. Subsequently, he continued his graduate studies at Penn State toward a Ph.D. in the Intercollege Graduate Program in Materials. At Penn State, his research was mainly conducted at the Materials Research Laboratory and the Materials Research Institute. He is a member of the Materials Research Society, the American Ceramic Society, Keramos and the phi kappa phi national honor society.

His father (John), mother (Barbara) and sister (Sarah) reside in Syracuse. Brady will be married to Heather Hawkins on September 5th, 1998. They will live in Los Alamos, NM.

IMAGE EVALUATION
TEST TARGET (QA-3)

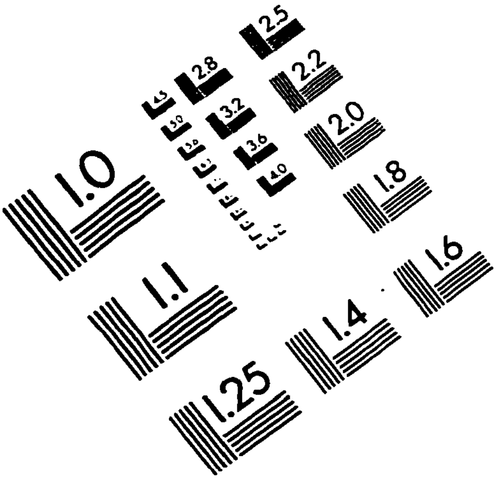

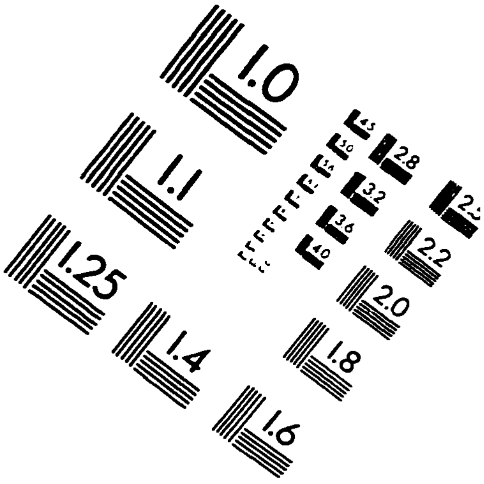

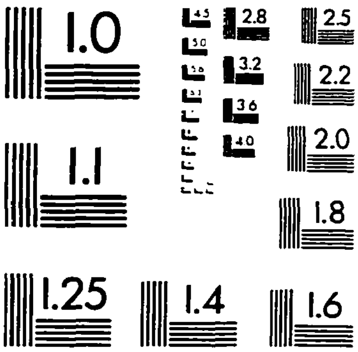

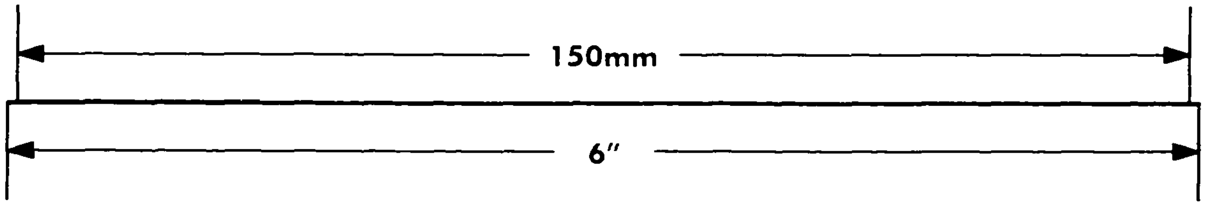

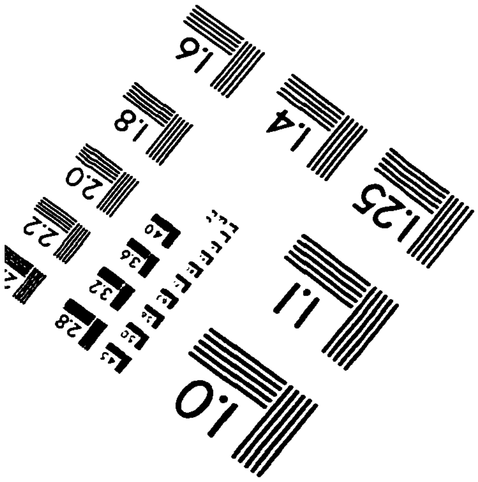

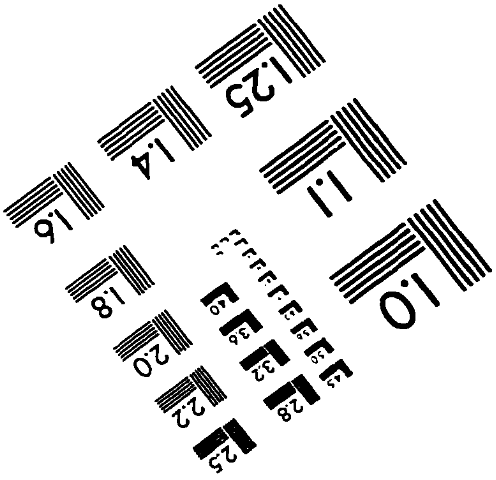

APPLIED IMAGE, Inc
1653 East Main Street
Rochester, NY 14609 USA
Phone: 716/482-0300
Fax: 716/288-5989